PEA Method Space Charge Measurement

Modeling & measurement of applied pulsed-voltage in different setups for MV mini-cable

By

AMIR GHASSEMI

Electrical Engineering, Mathematics and Computer Science, Electrical Sustainable Energy, DC Systems, Energy Conversion & Storage
DELFT UNIVERSITY OF TECHNOLOGY

Student Number:	4418158	
Supervisor:	Prof. ir. Peter Vaessen	
Daily Supervisor:	Dr. ir. Armando Rodrigo Mor	
Thesis committee:	Prof. ir. Peter Vaessen	TU Delft
	Dr. ir. Armando Rodrigo Mor	TU Delft
	Dr. ir. Simon Tindemans	TU Delft

A dissertation submitted to the Delft University of Technology in accordance with the requirements of the degree of **MASTER OF SCIENCE** *in the Faculty of Electrical Engineering, Mathematics, and Computer Science, to be defended publicly on Nov* 13^{th}*, 2020 at TU Delft*

NOVEMBER 2020

To our beloved Phuong, the embodied pure love

"Of aught beyond, and yet two worlds agree -
A mighty partnership - to furnish thee.
By nature first, in order last, art thou;
Hold not thyself then lightly. I have known"

Ferdowsi, The Book of Kings, 1010 A.D

Translated to English By K. E. Eduljee, Zoroastrian Heritage, 2005-2017

Abstract

Destructive consequences of trapped space charges within HVDC coaxial cable insulation, such as accelerated aging, degradation, and breakdown, are some of the most significant challenges that manufacturers and users usually come up with. Pulsed Electro-Acoustic (PEA) method is a widely-used method for space charge detection and measurement, in which the space charge profile is mapped through acoustic waves that are excited by applied pulsed-voltage. There are a few practices for pulse application into PEA circuit. Pros and cons of the different injection practices have been remained unknown due to limited accessibility to the critical points like the core conductor. Modeling of the pulse injection setups can help us with simulating the essential parameters, like voltage and current, at the unreachable spots.

The way how the circuit can be modeled, selecting adequate software and transmission line model, strengths and weaknesses of the injection practices and the changes required for possible optimization in the practices are challenging questions that need to be answered.

This thesis develops frequency-dependent models for all the PEA injection setups that are usually deployed for Medium Voltage (MV) mini-cables geometry. It shows, through a validation process, that PSCAD/EMTDC phase model can yield sufficiently accurate results with reference to the lab measurements. In the next stage, the questioned strengths and weaknesses of each original design setup are determined through a series of lab tests and computer-aided simulations by utilizing of which the best setup is recognized. Seeking some approaches for further optimization of the setups is also another aim of this research.

This thesis proves that the PSCAD/EMTDC phase model is capable to present an acceptably exact model for the circuits, despite having some limitations that will be explained. Operational versions of all setups, in which the fundamental problems are cleared up, will also be proposed in this thesis. Among all the setups, Core Pulse Injection (CPI) and Table Pulse Injection (TPI) practices offer the best non-optimized (original design) and optimized results, in terms of quality of the delivered voltage across the target dielectric respectively, while the original design of Double Side Pulse Injection (DSPI) and Single Side Pulse Injection (SSPI) seem to be unreliable due to severe oscillatory behaviors. Nevertheless, two modified versions for DSPI and SSPI show quality results.

Keywords: Space, Charge, Coaxial,Mini, Cable, Medium, Voltage, MV, Length, PEA, Pulsed, Electro, Acoustic, HVDC, Detection, Measurement, PSCAD, EMTDC, Square, Rectangular, Pulse, Step, Injection, DSPI, SSPI, TPI, CPI, Voltage, Current, Optimization, Oscillation, Reflection, Peak, Comparison, Overshoot, Undershoot, Phase, Model, ULM, Universal, Line, Distributed, Lumped, Simulation, Termination, Test, Ground, Grounding, Screen, Table

ACKNOWLEDGEMENTS

I would like to express my sincere gratitude to prof. P. Vaessen, dr. A. Rodrigo Mor & G. A. Mier Escurra for their support, kindness & understanding, & pay my deep sense of appreciation to dr. M. Ghaffarian Niasar for his valuable guidance.
I also would love to extend my gratitude to my dear wife & parents for their patience & all the sacrifices they have made for me.

TABLE OF CONTENTS

List of Tables

Table **Page**

List of Figures

Figure **Page**

1

INTRODUCTION

1.1 Background

1.1.1 Space Charge problem in HVDC XLPE coaxial cables

The recent developments in power electronic energy conversion techniques and equipment as well as many privileges of High Voltage DC (HVDC) power transmission over High Voltage AC (HVAC) have provoked ever-increasing initiation of HVDC projects worldwide (refer section A.1).

Cabling systems are significant role-players in HVDC systems. In some cases, deployment of cabling systems instead of overhead lines is very advantageous, like elimination of negative visual impact of overhead lines, and even inevitable, such as long submarine power transmission (discussed in section A.2). Although still oil-based insulated coaxial cables are predominant cable types in HVDC cabling systems, polymer-based cable types are gradually opening their share in the market, because of many technical, environmental, and economical pros.

Cross-Linked Polyethylene (XLPE) together with Ethylene Propylene Rubber (EPR) are the most popular polymer dielectrics in HVDC coaxial cable manufacturing. XLPE dielectric materials that are usually applied in AC cables (XLPE-AC) have some properties like low charge carrier mobility that might be considered as drawbacks under DC stresses, for instance, it may lead to accumulation of space charges, therefore manufacturers developed a special type of XLPE for DC stresses (XLPE-DC). In spite the fact that XLPE-DC dielectric offers good functionality under DC stresses, producing an ideal material is practically impossible. Chemical and physical inhomogeneities inside the material such as the regions containing fillers, additives, by-products, defects, etc, as well as local change in morphological structure or crystallinity rate of the material, forming amorphous regions as well as interfaces between two material types (such as dielectric-dielectric or conductor-dielectric) at which conductivity and permittivity of the material experience an abrupt change all make the dielectric vulnerable to space charge accumulation. Some internal and external factors like temperature gradient created by conductor current-originated ohmic losses and electric field gradient formed by DC voltage application at electrodes, also facilitate space charge accumulation inside the material. The space charges trapped inside the dielectric

may change local electric field profile, initiate treeing and partial discharges, and can lead to accelerated aging, degradation and even breakdown in the cable insulation. The topic is explained in more detail Appendix A, section A.6.

1.1.2 Space charge detection & measurement methods

There are several destructive and non-destructive techniques to detect and measure space charges inside a piece of dielectric with any geometry. Selection of an appropriate technique is highly dependent on the geometry and type of the sample. Most of the methods follow one of the three principles of thermal, acoustic, optical, although there are still a few alternative methods that follow non of the mentioned principles. Pulsed Electro-Acoustic method (PEA), being one of two important acoustic methods for space charge detection and measurement, is the main focus of this thesis.

1.1.3 Acoustic methods for space charge detection

Ultrasonic acoustic wave diffusion in the bulk of a homogeneous dielectric material [1] is the main principle of these methods. Basically, the main difference between PEA and PWP is wave generation mechanism [1–3]. In fact acoustic wave in PEA is internally generated as a response to pulsed electric field application, while in PWP the acoustic wave is externally applied.

1. **Pulsed Electro-Acoustic method (PEA):** Affordability, convenience of applicability, and acceptable error make this method very popular in space charge detection and measurement [4, 5]. PEA method obeys the electric stress pulse technique principles which first introduced by *Takada et al.* in the late 80's [6]. This methods will be explained in more detail in the following sections of this chapter. The main variants of PEA are 2D and 3D, open upper electrode, portable/mountable, cable geometry and transient PEA methods.

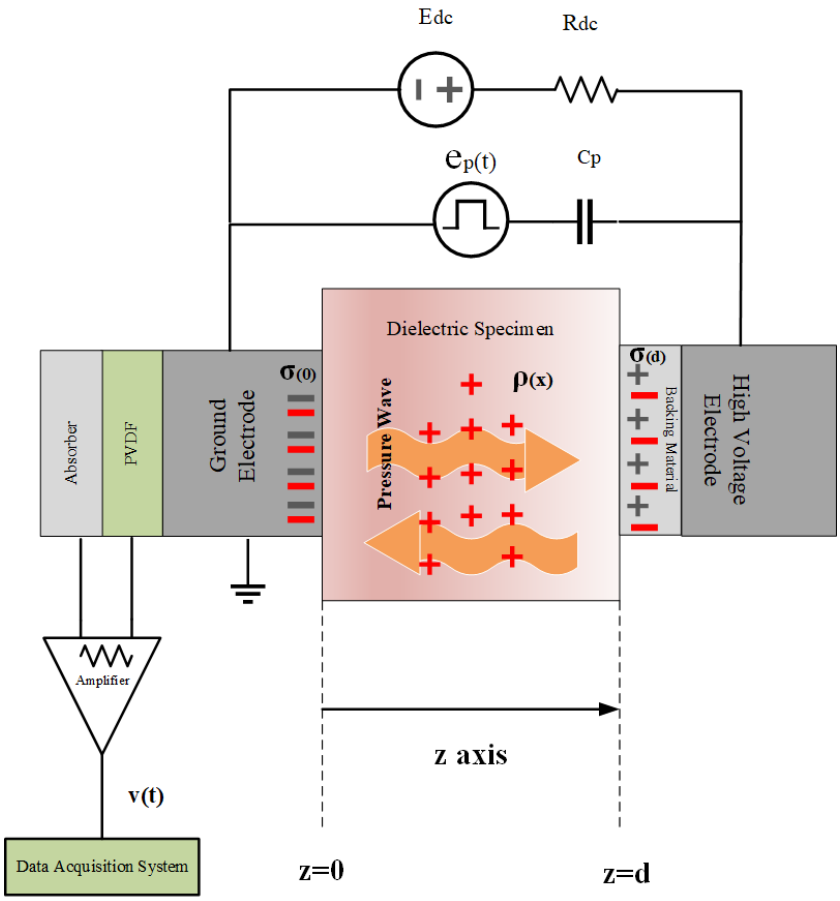

Figure 1.1: Principle of PEA method for flat specimen

2. **Pressure Wave Propagation method (PWP) or Pressure Pulse method (PPM):** According to the literature [1–3, 7, 8], a fast pressure wave is applied to the surface of the dielectric containing space charges. An acoustic wave starts propagating through the non-conductive homogeneous material leading to exertion of successive perturbation forces to the trapped space charges (ρ), geometric deformation of the dielectric as well as alteration in the dielectric permittivity. The resultant space charge displacement prompts changes in electric field distribution profile ($\vec{E}$) and surface charges (σ) at the both metal electrodes. A circuit is deployed to analyze the data extracted from the sensed current in order to locate the accumulated space charges and approximate their magnitude. The signal must be carefully amplified, calibrated and processed to achieve a result with acceptable accuracy. The figure 1.2 illustrates PWP method for a simple geometry (two parallel planes). Laser Induced Pressure Pulse Method (LIPP), Thermo-elastically LIPP, Piezo-electrically Induced Pressure Pulse, also named as PIPWP or Piezo-PWP (PIPP), and Non-Structured Acoustic Pulse Method (NSAPM) are the most important PWP method variants.

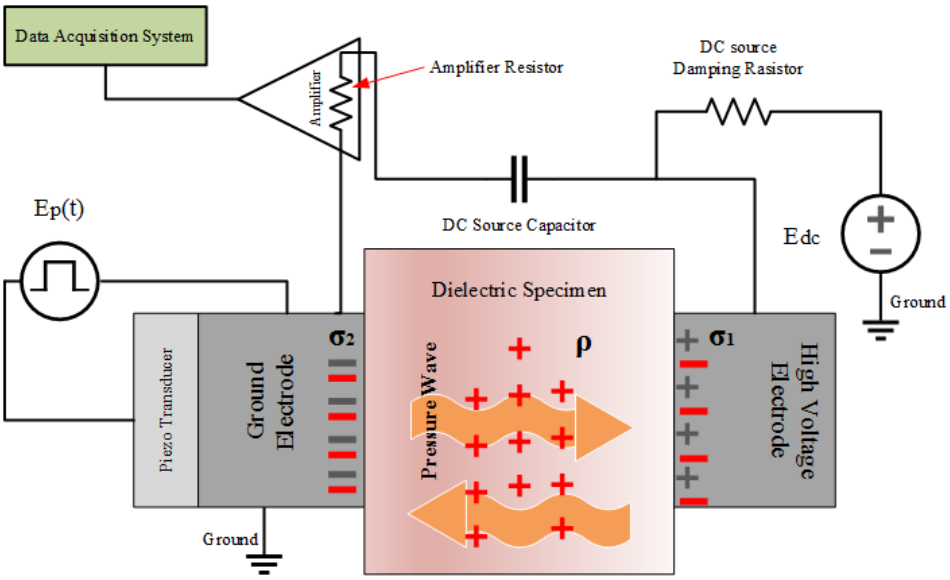

Figure 1.2: Principle of PWP method for flat specimen

1.1.4 PEA method principle

However both PEA and PWP methods are classified as acoustic methods, dissimilar to PWP, in which the acoustic wave is externally exerted to the dielectric, in PEA method the acoustic wave is originated from the space charge vibration trapped inside the material [9].
For better understanding, the PEA mechanism through the most basic geometry is explained. The flat sample is composed of two parallel electrodes whose middle gap is filled with dielectric material. Treatment by the electrode evaporation technique helps preventing acoustic wave propagation blockage and reflection at the interfaces [6]. The detected signal at the piezo-electric transducer includes both the original and the reflected signals.
Accumulation of the space charges $\left(\rho(z)\right)$ in the insulation bulk forms opposite polarity image or mirror surface charges (σ_1, σ_2) on the electrodes. Total amount of the trapped space charges can be approximated through equations 1.2 and 1.4 [9]. According to Coulomb's Law, the trapped space charges originate a net electric field E_1 at electrode A located at $z = d$ [6].

$$E_1 = -\frac{1}{\epsilon}\int_0^d \frac{d-z}{d}\rho(z)dz \tag{1.1}$$

Electric field E_1 together with a DC field (E_{DC}) ,which is generated by applying a DC voltage to the electrodes, form a layer of mirror surface charges (σ_1) on electrode A[9].

$$\sigma_1 = -\epsilon E_{DC} - \int_0^d \frac{d-z}{d}\rho(z)dz \tag{1.2}$$

Similarly, electric field E_2 appears at electrode B at $z = 0$.

$$E_2 = \int_0^d \frac{z}{d}\rho(z)dz \tag{1.3}$$

σ_2 represents the mirror charges at electrode B.

$$\sigma_2 = \epsilon E_{DC} - \int_0^d \frac{z}{d}\rho(z)dz \tag{1.4}$$

Consequently, by measuring the surface charges σ_1 and σ_2, the total bulk charge quantity (Q) and mean penetration depth ($\bar{x}$) can be recognized [6].

$$Q = S\epsilon(E_2 - E_1) \tag{1.5}$$

$$\bar{x} = \frac{E_1}{E_1 + E_2}d \tag{1.6}$$

S, ϵ and d represent the electrodes area, dielectric permitivitty and diameter respectively. A more accurate map of the trapped space charges inside the dielectric in obtained by applying a pulsed voltage to the electrodes [1]. The pulse excites a pulsed electric field $\left(e_p(t)\right)$ propagation along the dielectric that imposes electric stresses into the surface and trapped space charges[6] according to the Lorentz Force Law.

$$\vec{F} = q(\vec{E} + \vec{v} \times \vec{B}) \tag{1.7}$$

$\vec{F}$, $\vec{E}$, $\vec{v}$ and $\vec{B}$ are the Lorentz force, electric field, velocity and magnetic field density, respectively.

$$e_p(t) = \frac{V_p}{d}\Big|U(t) - U(t-\tau)\Big| \tag{1.8}$$

U(t) is the unit function and τ stands for the pulse width. By neglecting magnetic field in equation 1.7, the second term including cross vector product is dropped.

$$\vec{F} = q\vec{E} \tag{1.9}$$

The externally applied pulse-voltage, $U(t)$, generates a pulsed electric field of $e_p(t)$ inside the material, stimulating a time-varying perturbation forces, $f_1(t)$ and $f_2(t)$, onto the surface charges σ_1 and σ_2 [6].

$$f_1(t) = \left[\sigma_1 - \frac{\epsilon}{2}e_p(t)\right]e_p(t) \tag{1.10}$$

$$f_1(t) = \left[\sigma_2 + \frac{\epsilon}{2}e_p(t)\right]e_p(t) \tag{1.11}$$

[1] Instead of applying a sinusoidal wave with 1 MHz frequency, which is deployed in the older literature [10], in the newer methods a pulsed voltage is applied [6]. In this way the original and reflected waves can be more conveniently distinguished.

A space charge cloud located at $z = k$, with volume density λ_k, and width $\Delta\lambda$ is also subjected to another perturbation force Δf_3 under influence of $e_p(t)$.

$$\Delta f_3(\lambda_k, t) = \rho(\lambda_k) \cdot \Delta\lambda \cdot e_p(t) \tag{1.12}$$

This force causes a slight but fast location displacement of surface and bulk charges, producing acoustic waves of $p_1(t)$, $p_2(t)$ and $\Delta p_3(\lambda_k, t)$. The acoustic waves propagate in both directions through the sample. The acoustic waves are detected by a piezo-electric transducer mounted behind the rear electrode $\big($in our case made of PolyVnyliDene Fluoride (PVDF)$\big)$ [3] and are converted back into electric signals for further process. Takada found out that Ceramic Piezo-electric Transducer (PZT) could not cover the entire range of bandwidth, thus a portion of data is lost and the converted electric signal would not represent the actual space charge profile. For this reason, usually PVDF sensors are deployed to obtain more accurate results. In addition, some researches [11] showed better operational features of $LiNbO_3$ crystal, under high temperature conditions, compared to PVDF. A while later, through a few complementary techniques functionality problem of PVDF, in high temperatures, improved considerably [2]. Simple de-convolution process of signal and applicability to thin samples (in μm scale) as well as coaxial cables are also considered as the other advantages of this acoustic sensor type.
The total acoustic wave $p_3(t)$ reaches the transducer at each moment. The signal includes, in fact, all of the internally generated pressure waves. Finally after conversion of the acoustic signal into a voltage signal $v_3(t)$, it is analyzed by some de-convolution techniques in order to approximate location and magnitude of the trapped space charges[6].

[2] sample heating introduced by Chen [12], according to which the temperature gradient is tried to be kept as small as possible

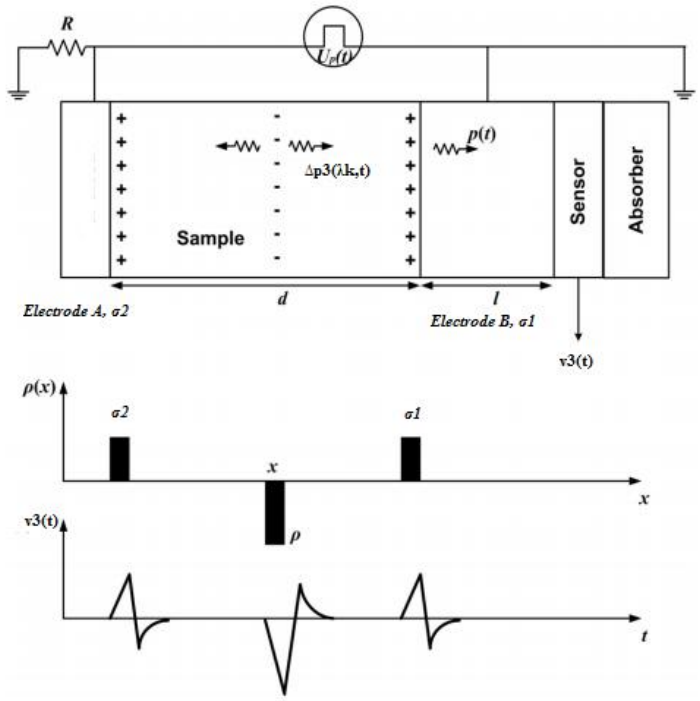

Figure 1.3: Principle of PEA method in a flat sample and in presence of a disc space charge, adapted from [13]

1.1.5 PEA method, pros & cons for cable geometry

According to the literature [14, 15], only a few methods are applicable to coaxial structures including TPM, TSM, LIMM, PWP, LIPP and PEA. *Mazzanti 2013* made a comprehensive comparison between functionality of the available detection methods for different power cable types and suggests TSM and PEA as the most accurate methods for space charge measurement in cables geometry. The early introduction of PEA method aimed solving the restrictions and shortcomings of PWP and TSM methods. Below some of the pros and cons of PEA method compared to its alternatives for space charge detection in cable samples are listed.

— Unlike in TSM method, in which cable must be fully decoupled from HV supply for testing purposes, PEA method can function under load.

— Unlike TSM and PWP, PEA method is applicable to thick samples, since the pressure wave is generated internally. This leads to higher time resolution for PEA compared to its alternatives.

— Fast space charge relocation, in response to a ultra fast applied pulse provides us with high spatial resolution. It is specifically advantageous in locating thin charge layers and narrow samples.

— Electric field profile mapping in PEA is easier and more accurate compared to TSM.

— A super-fast pulse created in PEA, in contrast to TSM, makes measurement with uninterrupted poling voltage possible[14].

— A super-fast pulse created in PEA, in contrast to TSM, makes measurement with uninterrupted poling voltage possible[14].

— PEA method demands for outer semicon layer exposure throughout measurement process restricts online testing usage as well as possibility for conveniently being mounted on full length cables due to destructiveness [16–18], although most of the alternatives also demand for the same demolishment.

— In the literature [14], obtaining a uniform electric stress distribution, being inappropriate in complex bulk charge detection and difficulties in pressure wave dispersion/reflection are cited as some drawbacks for PEA method, however the latter has recently become improved in some extent [9, 16].

1.2 Problem Statement

PEA method is a commonly-used approach to detect magnitude and location of space charges trapped inside the HVDC cable dielectric. Previous researches proposed a few different setups for pulse injection into the circuit. Lack of accessibility to the cable critical spots such as cable core conductor is one of the most problematic barriers in PEA test circuit enhancement, as one needs to know potential difference across the target dielectric material, in which the space charges are trapped, in order to select the best pulse injection practice or enhance the setups.
This research is dedicated to answer a set of essential questions regarding quality of the pulsed-voltage delivery in PEA testing method for space charge detection in medium voltage mini-cables as follows,

(i) How can the constraints imposed by lack of accessibility in the PEA setups be overcome? Is modeling of the circuit possible in practice? If frequency dependency of the circuit components has to get into consideration in the model? Which challenges might we face up to, in modeling procedure of the setups?

(ii) Is the commonly-used PSCAD/EMTDC phase model of transmission lines a good candidate for modeling of PEA testing setups? Is is able to yield sufficiently accurate results in our cases?

(iii) Which of the PEA pulse injection practices (into the core, PEA cell or screen conductor) would deliver a quality pulse across the target dielectric in terms of magnitude and resolution-related parameters?

(iv) What are the main issues with each setup and how can they be improved?

(v) After optimization, which setup would have the upper hand with respect to quality of the delivered voltage?

1.3 Objective

This thesis tries to achieve the following objectives,

(i) Assessment of applicability of PSCAD/EMTDC and its phase model for transmission lines to model different injection practices of PEA space charge detection method for medium voltage HVDC mini-cables

(ii) Comparing delivered voltage magnitude and resolution-related parameters like pulse width, rise time and slew rate of the injection practices by means of the developed model

(iii) Understanding the injection setups mechanism through lab tests, theoretical assessment and computer aided simulations and evaluation of different circuit components impact on the key parameters

(iv) Optimization of the original setups and comparing the pulsed-voltage delivered by the optimized setups once again in terms of magnitude and the resolution-related parameters

1.4 Approach & Layout

The summarized step-by-step approach to reach the goals is as follows:

- **Chapter 1 - Introduction:** The thesis starts with,
  - A short introduction about space charge accumulation problem in HVDC XLPE coaxial cables
  - The problems that are going to be solved are defined
  - The objectives of the research are introduced
- **Chapter 2 - PEA method for MV coaxial cable:**
  this chapter is dedicated to,
  - Introducing the PEA injection practices
  - Characteristics of different components of the injection practices that are deployed in the lab tests and simulations.
  - Important parameters of the mini-cable under test are calculated and frequency dependency of some of the is evaluated.
- **Chapter 3 - Test circuit modeling & validation:**

  - The best cable model is selected and the reasons for its selection is explained.
  - Models for SSPI and DSPI is built. The layout of the model and important input parameters are defined.
  - Through compering to a few lab experimental results, the model is validated.
  - The inaccuracies of the model and possible reasons are theoretically discussed.

- **Chapter 4 - Experiments & circuit analysis:**
  In this chapter we try to understand, different phenomena, interaction and interrelations between circuit components and to sum up mechanism of the setups,

  - After a short theory, reflections in the circuits and their origins are explained. A frequency-dependent figure of impedances and reflections are also provided.
  - Many tests are passed in the lab. The thesis tries to explained the circuit mechanism and interdependence of the phenomena and parameters through the empirical test results supported by computer aided simulations.

- **Chapter 5 - Setups comparison & enhancement:**
  this chapter focuses on,

  - Important parameters of the setups are compared to each other. Parameters like peak value of the output voltage, pulse width, rise time, front slew rate, energy storage capacity of the circuit, reflection at injection point and oscillations. The best practice from each aspect as well as in general will be introduced.
  - Sensitivity of the output results in response to change in different parameters are evaluated. Parameters such as mini-cable, exposed part and central electrode lengths, insulation permittivity, etc. are assessed in this part.
  - Grounding practices for both mini-cable screen and PEA table and their influences on the final results are also analyzed.
  - From step response of the circuits also important information about circuit characteristics are extracted.
  - In the next stage, effect of insertion parameters for both step and square voltage input are assessed.
  - Through our findings some optimizations are proposed for different setups.
  - The output voltage of the different optimized setups are compared and the best optimized setup is introduced.

- **Chapter 6 - Discussion & Conclusion:**

- First a summary of the important topics of the thesis is provided and the important points and challenges are discussed
- The findings and answers of the research questions are explained
- Finally, some recommendations for further researches on the topic are provided.

2

PEA METHOD FOR MV COAXIAL CABLE

In this chapter, the tests circuit and relevant components are briefly introduced and important parameters of the mini-cable are calculated.

2.1 Pulse injection approaches

There are four different approaches to inject pulsed-voltage into a piece of MV mini-cable geometry as mentioned below [8].

2.1.1 CPI (Core Pulse Injection)

When a pulse is applied to the core conductor, a rather large decoupling capacitor, in comparison with the cable capacitance, is suggested to be deployed in order to prevent any influence of the HVDC voltage on the pulse generator. If cable length is much longer than the pulse wavelength, the cable can not be considered as a lumped element anymore but distributed, as the pulse undergo attenuation and reflections during its propagation until reaching the aimed point [8].
In this setup, as a consequence of pulse application into inner conductor, while screen conductor is grounded through PEA unit, a pulsed electric field is generated, leading to mechanical stress exertion to the trapped space charges, resulting in pressure pulse creation that can be sensed.

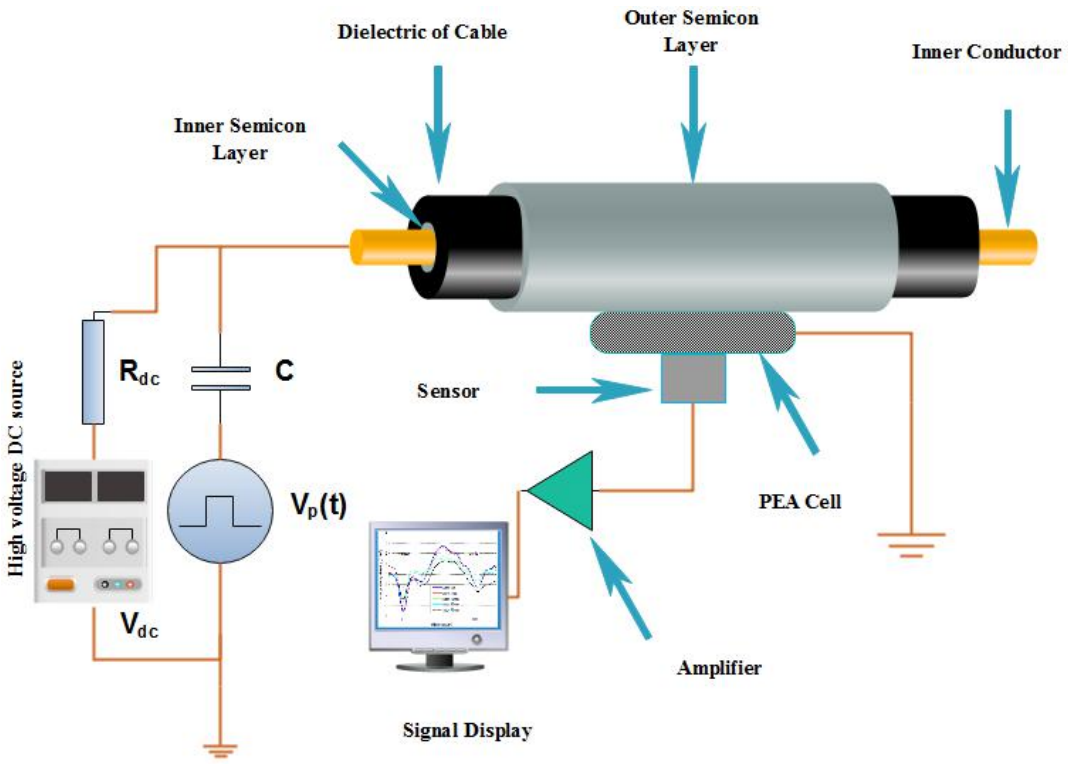

Figure 2.1: Pulse application to the core conductor[8]

2.1.2 DSPI (Double-side pulse injection)

In this approach, the pulsed-voltage is applied to screen conductors at both sides of the central exposed part (as indicated in figure 2.2) in order to create a pulsed-voltage across the insulation. This applied pulse generates transient electric field inside dielectric. In this case, the sample cable detaches the pulse generations/application circuit and HV source. In other words, the cable itself plays the role of decoupling capacitor. Because PEA cell is grounded, measurement device can be connected directly to piezo-sensor[8], which is very beneficial. The central cable part, must be uncovered from both jacket and outer screen conductor, enabling acoustic wave be propagated and sensed, except of the piece on which the PEA cell is mounted where screen conductor remains. This exposure also hinders pulse propagation along the screen conductor and helps its concentration towards the core.

There is one important difference between the DSPI setup suggested by *Bodega, 2006* and the setups tested in the lab. In this thesis, a capacitor parallel to HVDC source is deployed in order of nano-farads. Because the HVDC source is decoupled from the circuit by means of a very large resistance (3 $M\Omega$), the core conductor would have no path to earth in practice. Additionally, assuming the required path is provided by direct earth contact at the setup's termination, no DC voltage will be applied to the core conductor, since the termination point will be kept at zero potential.

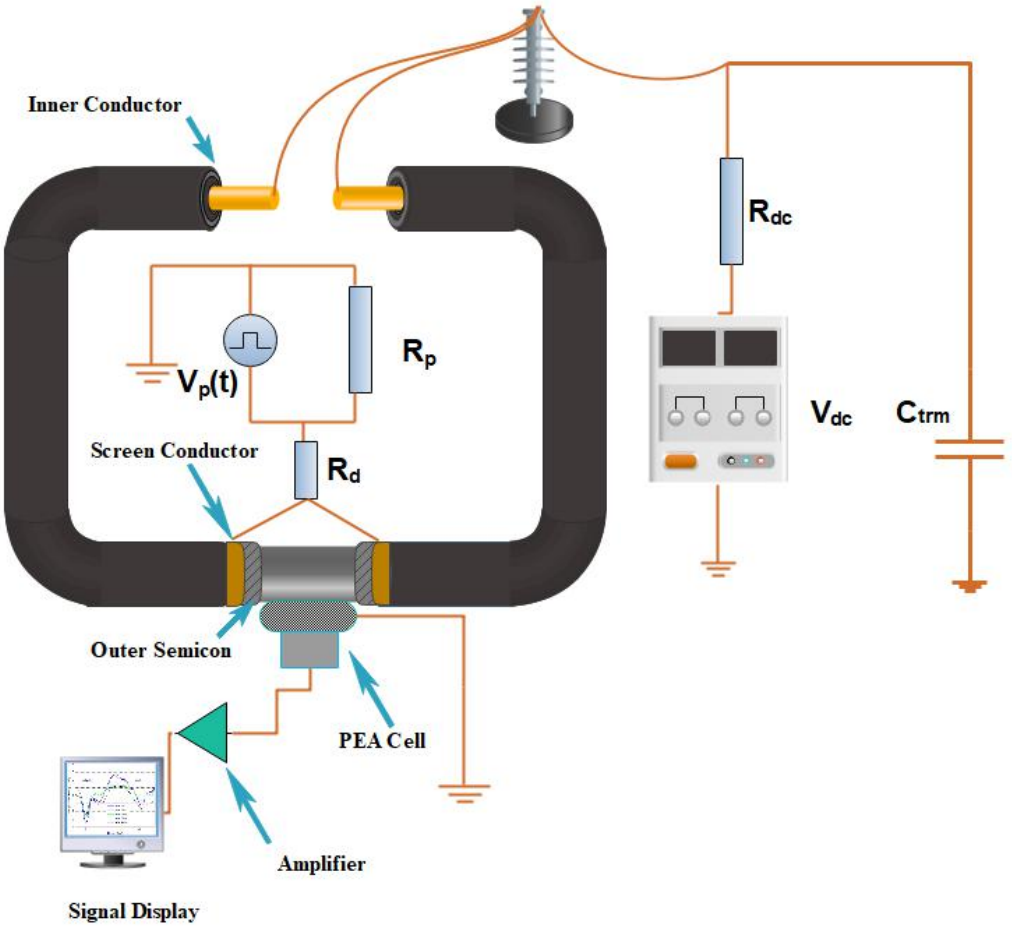

Figure 2.2: Pulse application to both sides of the screen conductor (DSPI)[8]

Beside the recommended DSPI practice, there is also another practice for DSPI [19] where ends of the screen conductors at the termination point are grounded while the PEA cell is left floated.

2.1.3 SSPI (Single-side Pulse Injection)

This method follows exactly the same principles as DSPI with one difference that the pulsed-voltage is applied only to one side of instead of both sides. This method is not introduced by any available literature. In fact it is deployed in this thesis in order to simplify the cable modeling by reducing the number of reflected waves. During this research some tests and simulations will be performed using this setup as well to assess its functionality.

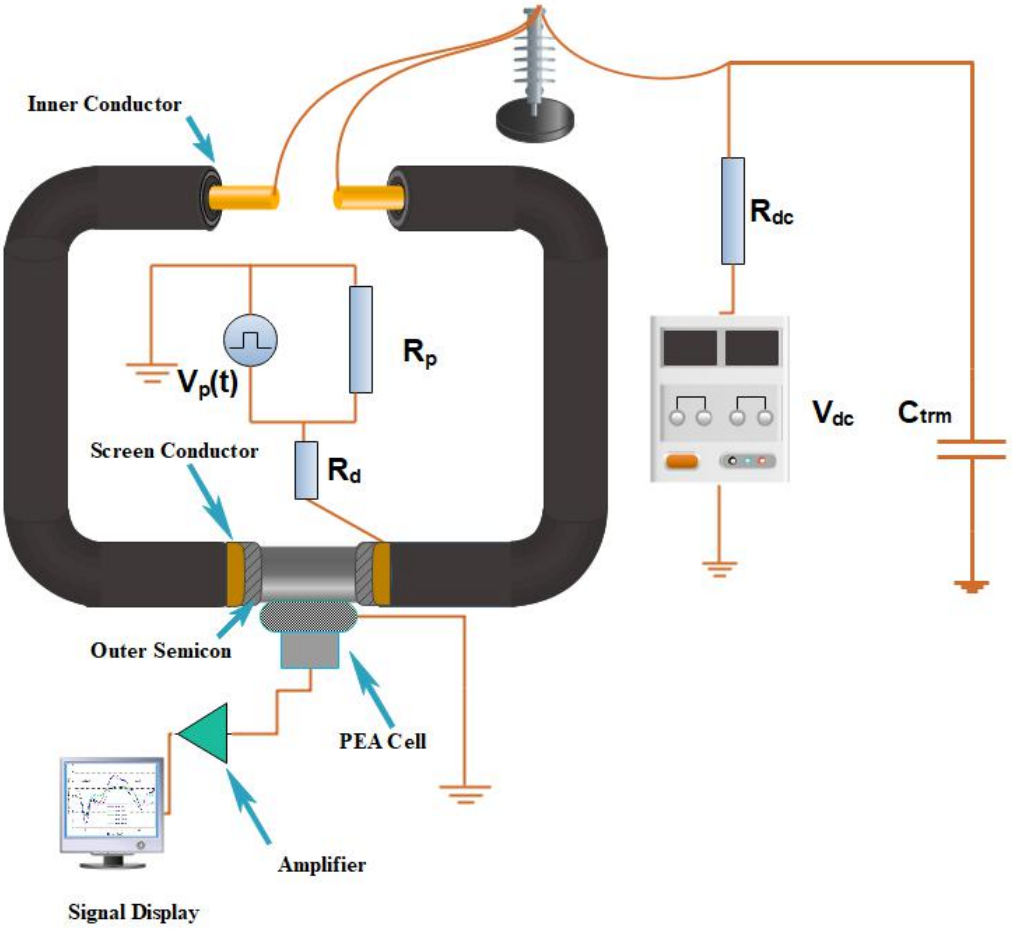

Figure 2.3: Pulse application to one side of the screen conductor (SSPI)

2.1.4 TPI (Table Pulse Injection)

In this method, the pulse is injected into the PEA cell (table), whereas the cell is left ungrounded. No need for a huge expensive decoupling capacitor, as the cable insulation acts as capacitor, can be considered as a major advantage for this method, however due to the same reasons stated for DSPI and in order to providing ground potential connection for the circuit, existence of shunt capacitor seems to be inevitable. In this setup, isolation from the piezoelectric sensor is fulfilled by means of an electro-optic converter, as the sensor's potential would be at the HV pulse level. The converter converts the signal received by the sensor into an optical signal and it is converted back into a low voltage analyzable signal in order to become processed and displayed [8].

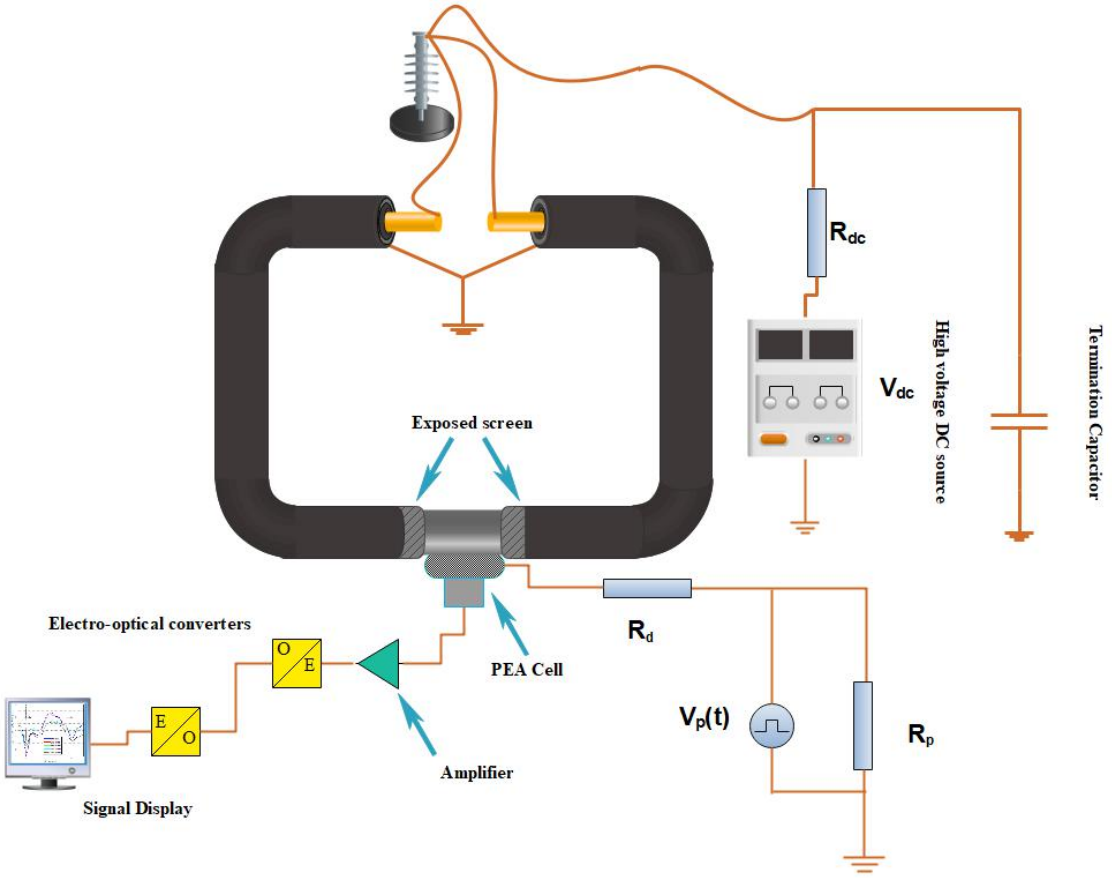

Figure 2.4: Pulse application to the PEA cell[8]

2.2 Components of measurement system for PEA test

This section introduces necessary circuit components regarding PEA approach for mini-cable space charge test.

2.2.1 PEA table and earth electrode

There are two typical ground configurations deployed in PEA Cable geometry setups that are explained below.

2.2.1.1 Curved Surface Electrode

In this type of electrodes a metal electrode is matched to semiconductor layer convexity in order to become adapted to cylindrical acoustic waveshape. Imperfect curvature and difficulties to attain smooth, well-polished interface between semiconductor layer and cast electrode, that may lead to incomplete faulty contact, are regarded as limitations for this structure. Imperfect contact may

also be formed at the electrode-piezoelectric sensor interface[1] or between anti-reflection absorber and sensor which all are designed in arc shape. Any imperfection would distort acoustic wave shape, hence space charge profile reproduction. A curved earth electrode is uniquely designed for a specific cable dimension and can not be used for other samples. This is considered as a drawback for this types of electrodes [8, 20–24]. A thin layer of silicon-oil is usually applied to improve roughness of the interfaces as much as possible, however achieving a perfect interface is practically impossible. In spite of the mentioned limitations, due to the curved structure, clamping force-driven deformation is not a major concern anymore [24].

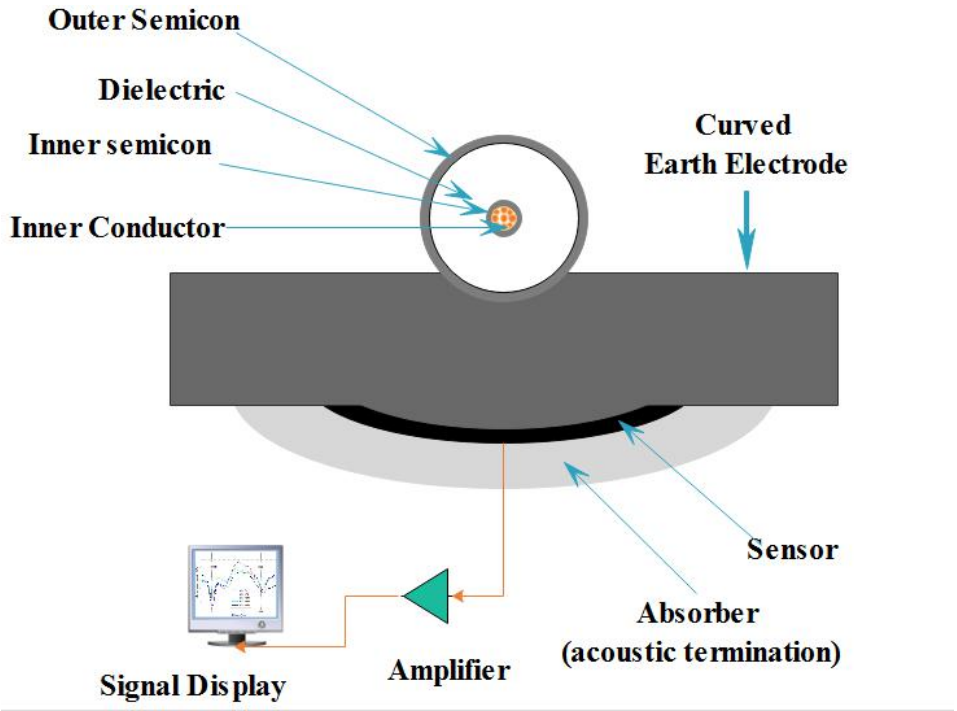

Figure 2.5: Curved earth electrode

2.2.1.2 Flat Electrode

The curved configuration troubles provoked idea of flat AL electrode [22]. The new structure cleared the problems up, however new restrictions arose, namely small capacitance of the piezoelectric sensor due to reduction in the sensor's interfacial area. The problem shows itself when low amplifier input impedance would lead to signal distortion [8, 24]. Linear contact between the electrode and the cable also results in dispersing the acoustic wave when penetrating through the rear Al-electrode [21]. Despite ever-changing test conditions and its consequent material deformation, such as thermal expansion, the clamping force must be kept constant during the test for calibration purposes which is not easy at all [24].

[1] usually PVDF-TrFE film

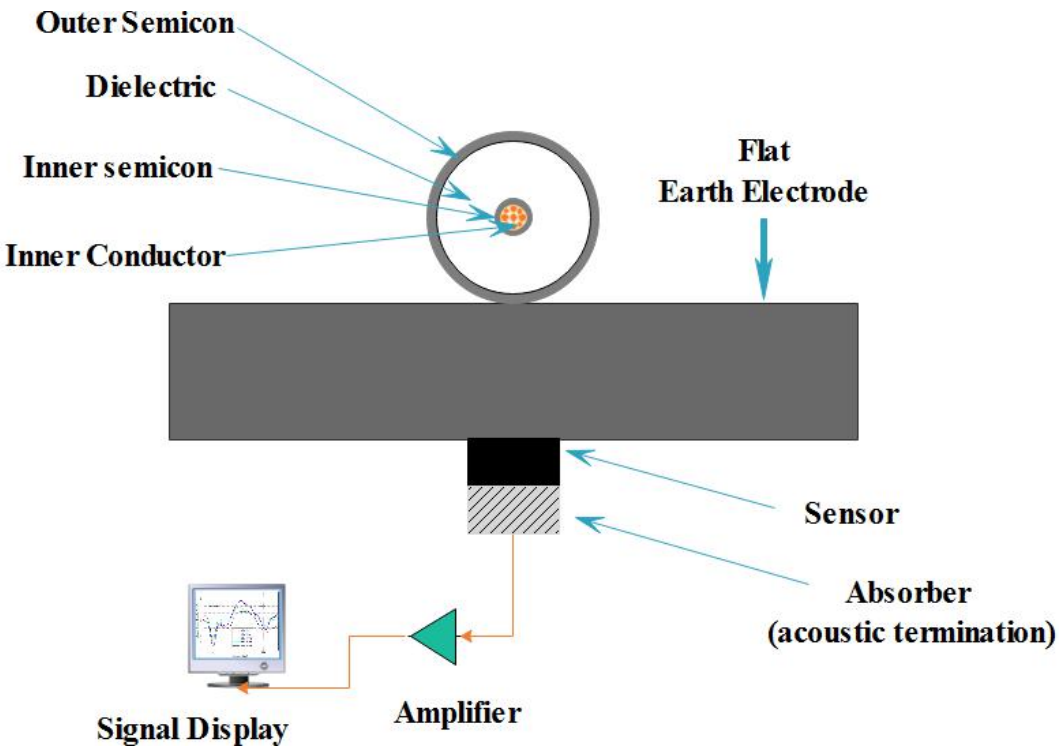

Figure 2.6: Flat earth electrode design

In this research, an Aluminum structure on which different accessories like a combination of PEA cell, bottom electrode, piezoelectric cell and anti-reflection rear material at one side and a cable holder on the other side are mounted.

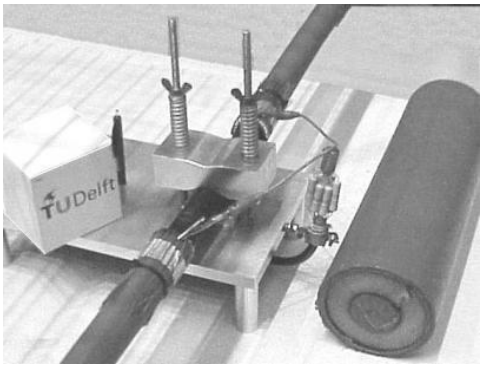

(a) TU Delft design for Al table

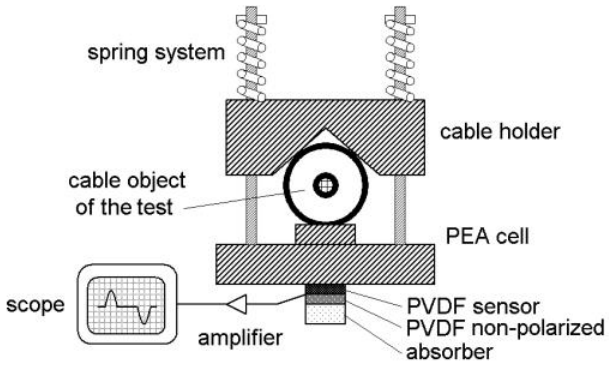

(b) Al table typical structure

Figure 2.7: Al table in PEA measurement setup for coaxial cable
[8, 25]

2.2.2 High Voltage DC Supply

The required HVDC voltage for online testing is provided by a programmable HVDC source (Sorensen 1101), which supplies a voltage level in order of 50 kV_{dc} into the circuit.

2.2.3 Pulse Generator

When an array of shunt capacitors is fully charged by a DC source, it is discharged through an ultra-fast transistor switch (Behlke HTS 80-20-UF [26, 27]) into a resistive load, in this way a square pulse is shaped [28] (figure 2.9).

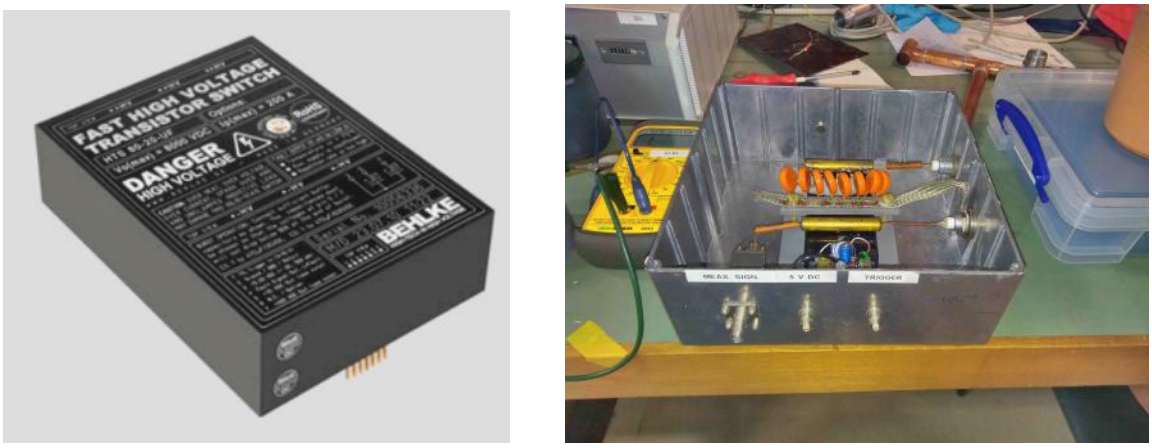

Figure 2.8: Pulse generator

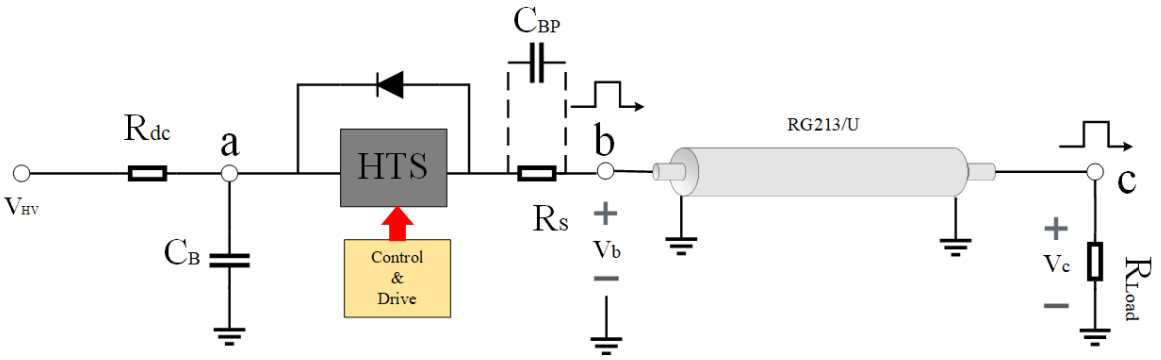

Figure 2.9: Pulse injection circuit

If HTS switch conducts in $t_{on} < t < t_{off}$, where t_{on} is assumed to be zero, assuming

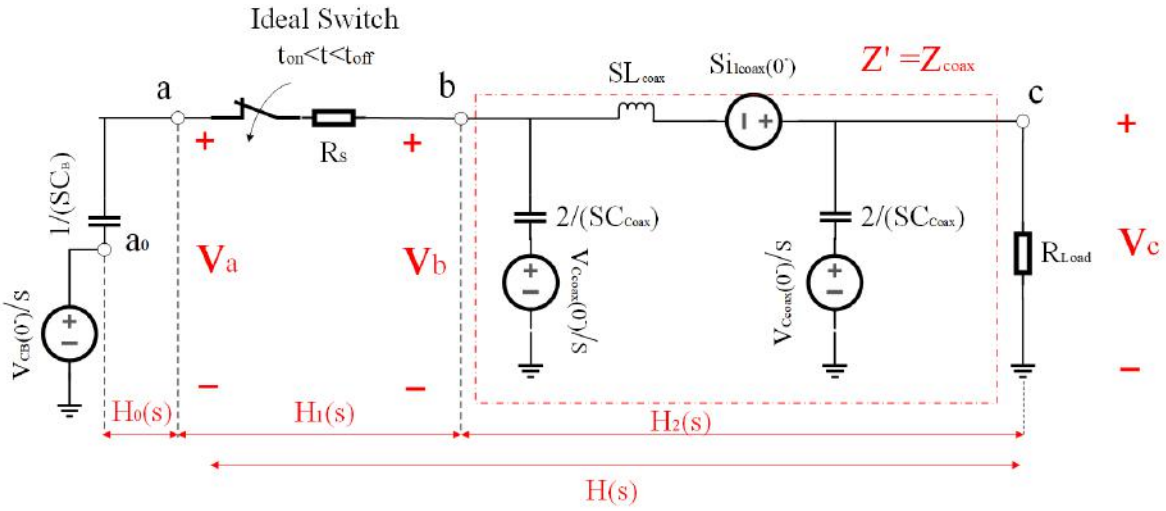

Figure 2.10: Equivalent circuit - Laplace domain

C_B, C_{BP} and R_S are energy storage, by pass capacitors and series resistor.

$$H(s) = \frac{V_c(s)}{V_b(s)} \tag{2.1}$$

If we assume the pulse arrived at point b to be an ideal trapezoidal function with rise time $3\,ns$, pulse width of $81\,ns$ and fall time of $62\,ns$, the wave equation is,

$$v_b(t) = (304t)u(t) - (608t)u(t-3) + (288t)u(t-84) + (16t)u(t-143) \tag{2.2}$$

in Laplace domain,

$$\begin{aligned} V_{b,s} = & \frac{304}{s} + \\ & e^{-3s}\left[\frac{608}{s^2} + \frac{1824}{s}\right] + \\ & e^{-84s}\left[\frac{288}{s^2} + \frac{24192}{s}\right] + \\ & e^{-143s}\left[\frac{16}{s^2} + \frac{2288}{s}\right] \end{aligned} \tag{2.3}$$

According to the specifications, cut off frequency of RG213/U transmission line is calculated as follows,

$$f_c = \frac{1}{2\pi\sqrt{L'.C'}} \approx 1\,GHz \tag{2.4}$$

where L' and C' are per unit length inductance and capacitance of the cable respectively. The transfer function of a coaxial transmission line in Laplace domain for each velocity group is defined as [29],

$$\begin{bmatrix} V_c(s) \\ I_c(s) \end{bmatrix} = \begin{bmatrix} Cosh.\gamma(s).x & Z_0(s).Sinh.\gamma(s).x \\ Sinh.\gamma(s).x/Z_0(s) & Cosh.\gamma(s).x \end{bmatrix} \begin{bmatrix} V_b(s) \\ I_b(s) \end{bmatrix} \tag{2.5}$$

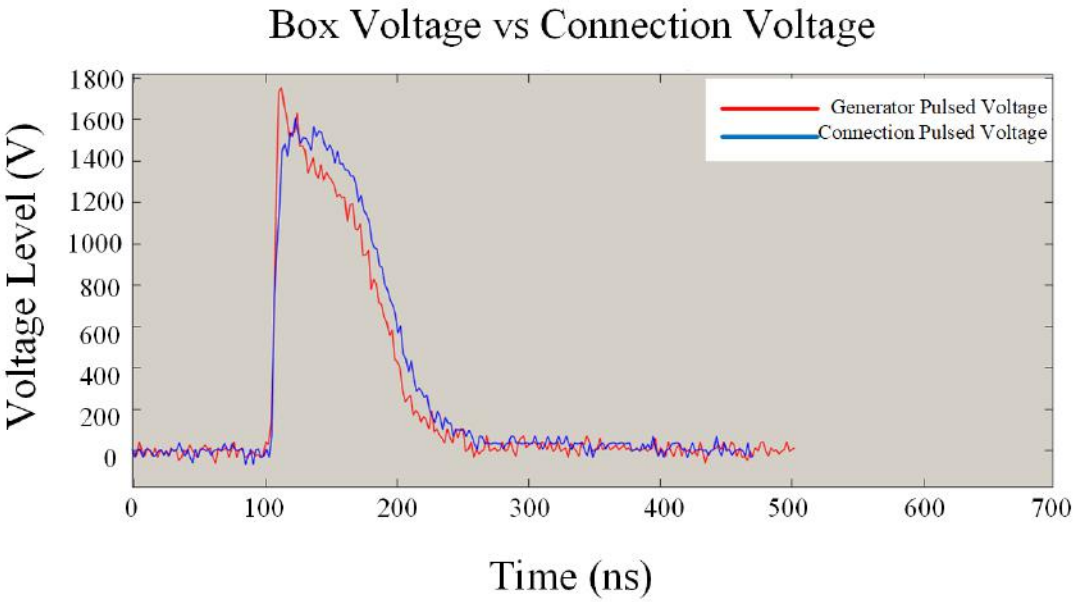

Figure 2.11: Pulse generator voltage vs connection voltage

Figure 2.11 shows the measured pulsed voltage before and after passing the coaxial cable. A turn-on current spike [30] can be detected in red-curve due to fast switching action, while the transmission line acts as a damping filter for this spike. The square pulse equation id defined as follows,

$$\begin{aligned} x(t) &= A\Pi\left(\frac{t}{T_0}\right) \\ &= \frac{1}{T_0}\left[u(t+\frac{T_0}{2}) - u(t-\frac{T_0}{2})\right] \end{aligned} \tag{2.6}$$

A and T_0 represent amplitude and wavelength. Assuming a continuous aperiodic ideal square pulse its Fourier transform is,

$$\begin{aligned} X(f) &= \int_{-\infty}^{+\infty} f(t)e^{-j2\pi ft}dt \\ &= \int_{-\infty}^{+\infty}\left[u(t+\frac{T_0}{2}) - u(t-\frac{T_0}{2})\right]e^{-j2\pi ft}dt \\ &= Sinc(\pi ft) \\ &= \frac{Sin(\pi ft)}{\pi ft} \end{aligned} \tag{2.7}$$

The frequency at which the single pulse has the highest power density can be derived from the wavelength of the pulse.

$$f_0 = \frac{1}{T_0} \approx 12.5\,MHz \tag{2.8}$$

This is the first zero crossing spot in the Sinc function, below which the most concentration of magnitude is observed [31] (figure 2.12).

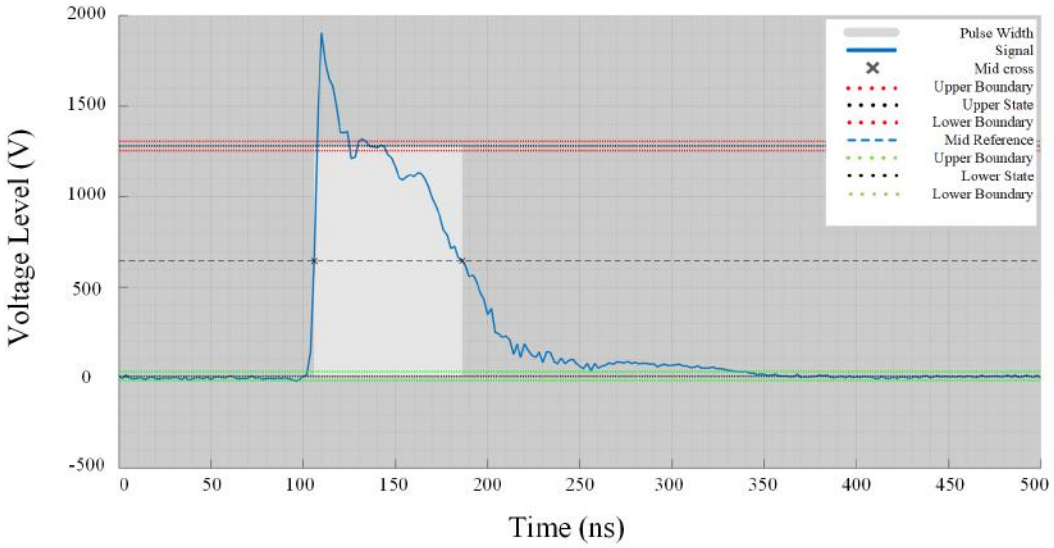

Figure 2.12: Applied pulse waveshape

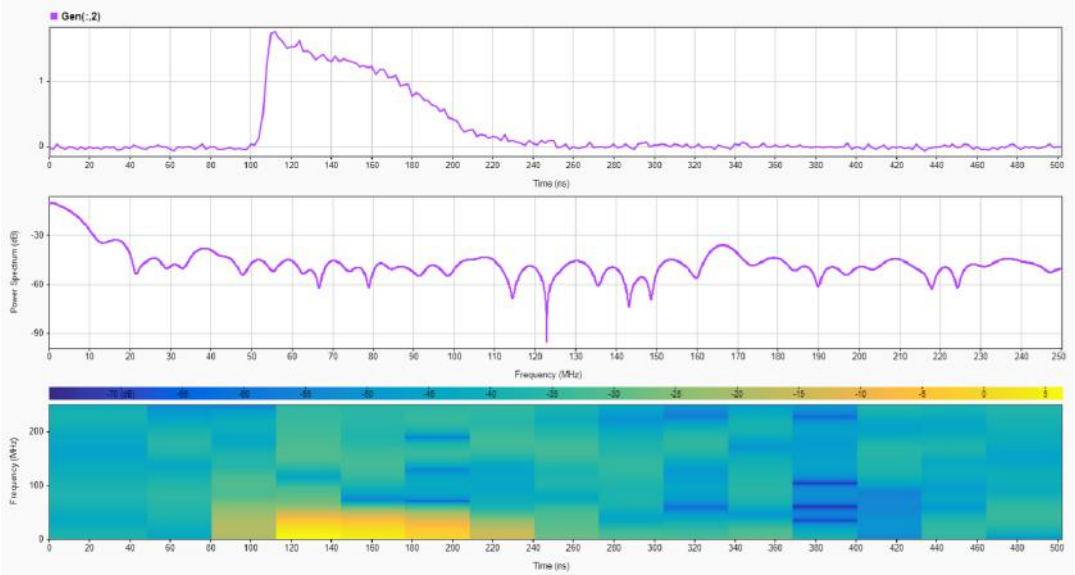

Figure 2.13: Power spectrum & spectrogram of applied pulse

Para.	Rise	Fall	PW	Rising Slew Rate	Falling Slew Rate	RMS	DC
Unit	ns	ns	ns	V/ns	V/ns	V	dBm
	3	62.1	80.6	303.77	-16.03	912.57	58.59

Table 2.1: Characteristics of applied pulsed voltage

Morshuis et al. 1997 [32] recommended a pulsed voltage with amplitude of $0.1-2\,KV$ having a pulse width of $5-200\,ns$ for this test. The more pulse width approaches to zero, the better PEA test resolution is achieved. In fact, The ideal resolution are obtained by applying an impulse voltage, however there is no compact and inexpensive commercially available device to produce such a wave.

2.2.4 Oscilloscope

Oscilloscope is responsible for output data display and storing the recorded data. In this research, the deployed oscilloscope is a Lecroy, WaveRunner 44Xi-a. The nominal analog bandwidth is 500 MHz and the sample rate is $5\,GS/s$. The full device's specifications are available in the device data sheet [33].

2.2.5 Amplifier

Since the generated electric signal is not strong enough in order to be processed by the oscilloscope, an amplifier is required. For this research one pre-amplifier with input impedance of 1-3 $k\Omega$ and two *Mini Circuit* $ZFL-500LN+$ low-noise amplifiers with approximately 28 dB gain, 50 Ω input impedance and a bandwidth of $0.1 \leqslant BW \leqslant 500\,MHz$ are deployed [8, 25].

Figure 2.14: Mini Circuit $ZFL-500LN+$ *amplifier*

2.2.6 Piezoelectric sensor

This sensor is a typical PVDF film with 25 μm thickness[8].

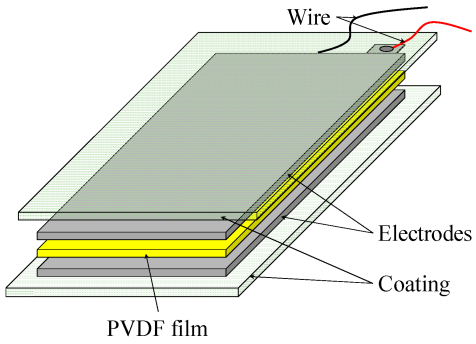

Figure 2.15: Example of a typical PVDF thin-film sensor[34]

2.2.7 Coupling transmission coaxial cable M-17/74-RG213/U

The same cable models are applied to this coupling cable whose duty is carrying the pulsed-voltage from the box output to the injection point (see figures 2.9 & 2.16). Some of the important specifications (according to the US standard of MIL-C-17 [35–39]) of this coaxial cable are mentioned in the table 2.2.

Symbol	Definition	value & Unit
-	Inner conductor dimension	$7 \times 0.7\,mm$
-	Outer conductor dimension	$192 \times 0.18\,mm$
-	Dielectric dimension	$\phi 7.25 \pm 0.18\,mm$
-	Sheath dimension	$\phi 10.3 \pm 0.18\,mm$
$V_{p,test}$	Peak test voltage	$10\ KV$
V_p	Peak operating voltage	$5\ KV$
Z_0	Characteristic impedance	$50 \pm 3\,\Omega$
L	Inductance	$253\ nH/m$
C	Capacitance	$101\ pF/m$
$R_{dc,in}$	DC resistance of core conductor @ 20°	$5.8\ m\Omega/m$
$R_{dc,out}$	DC resistance of shield conductor @ 20°	$5\ m\Omega/m$
R_{ins}	DC resistance of dielectric @ 20°	$2\ M\Omega/m$
v_p	Nominal velocity of propagation(velocity ratio)	66%
t_d	Nominal delay	$5.05274\ ns/m$
l	length of cable	$1.15\,m$

Table 2.2: Coaxial transmission connecting cable specifications

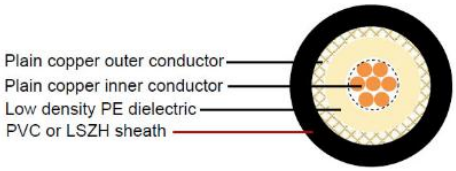

Figure 2.16: Scheme of RG-213 / U coaxial cable[40]

2.2.8 Current probe

A current probe coupled to a current transformer is used in this experiment in order to measure the current passing through the cable. The employed current transformer is De Dri Electronics 4.29.000.0280. T The point A and B (colored in red) in figure 3.1 are the locations where clamp-on current probe is installed for measurement purposes.

2.2.9 Voltage probe

For this test a voltage probe is required, being capable to measure not only low frequency high level voltages but also high frequencies at the same voltage rate. A Tektronix P6015A (see figure 2.17) is selected for this purpose whose full datasheet is available online [41]. This probe measures up to 20 kV DC and 40 kV peak pulse for max duration of 100 ms. The point A and B (colored in red) in figure 3.1 are the locations where HF voltage probe is installed for measurement purposes.

Figure 2.17: Tektronix P6015A high frequency high voltage probe - TU Delft

2.2.10 Other circuit components

- **Impedance Matching Resistor** (R_{pulse}): it is of importance to prevent the pulse reflection at the output of RG-213 transmission line (pulse injection circuit), hence a resistor (R_p) is used whose value is almost equal to the characteristic impedance of the mentioned cable piece [42], to be approximated 45.2 Ω in this case.

$$R_{pulse} = Z_{0,rg} \tag{2.9}$$

- **HVDC Resistor** (R_{dc}): in order to avoid invasion of the high voltage pulsed voltage into the HVDC source circuit and consequent loading of its small internal impedance, that

may lead to damages [8, 24], the source is connected through a large series oil resistor of $R_{hvdc} = 3\,M\Omega$ to the test circuit (see figure 2.18).

Figure 2.18: 3 $M\Omega$ resistor

- **Stray capacitances & inductances:** the setup makes special geometries that result in many unwanted stray parameters that might affect the simulations result.
  - ***Rectangular stray inductance:*** it is very difficult to approximate stray parameters that usually are shaped in complex geometries. In the setups, the cable together with the termination and pulse generation circuit form a long bent path that can be estimated by a rectangular inductance (see figure 2.19) whose value is derived from the equation 2.10[43].

$$L_{rect} = N^2 \frac{\mu_0 \mu_r}{\pi} \left[-2(w+h) + 2\sqrt{h^2+w^2} - h \ln \left[\frac{h+\sqrt{h^2+w^2}}{w} \right] \right. \\ \left. - w \ln \left[\frac{w+\sqrt{h^2+w^2}}{h} \right] + h \ln \left(\frac{2h}{a} \right) + w \ln \left(\frac{2w}{a} \right) \right] \tag{2.10}$$

  a represents radius of the conductor. In the equation 2.10, if values of w, which is rectangle width, are approximated 2.8 and 5.1 meters respectively, and h that shows the rectangle height would be assumed 1.5 meter, then the stray inductances are theoretically estimated to be in order of a few μH's, however simulation results shows that this value does not exceed a few hundreds of nH's. In fact at high frequencies, where the electrical length is higher than earth-to-earth path, no loop is formed to create inductance.

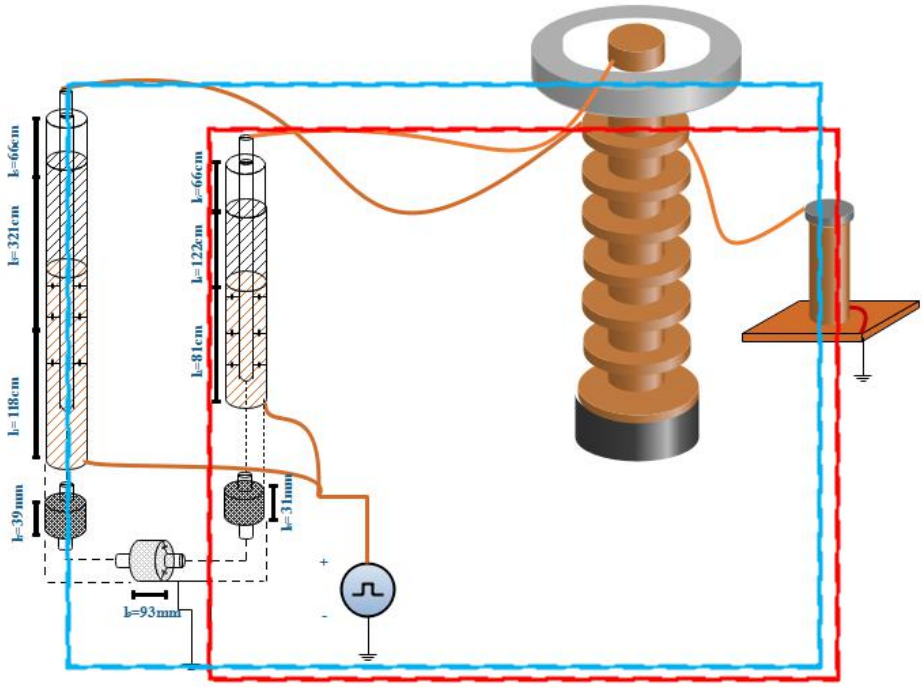

Figure 2.19: Rectangular stray inductance

– ***Triangular inductance at injection point (for DSPI):*** at the pulse injection point a quasi-triangular path is formed. A equilateral triangular inductance is approximated by the following equation [44],

$$L_{tri} \approx N^2 \frac{3\mu_0\mu_r s}{2\pi}\left[\ln\left(\frac{s}{a}\right) - 1.405\right] \tag{2.11}$$

where s, a and μ_r represent each side length of the triangle, conductor radius and the medium relative magnetic permeability respectively, and N is number of the wire turns to be equal to 1 in this case. Therefore, each triangle side is approximated to be in range of a few hundreds of nH's, however, according to the simulation results the value does not exceed a few tens of nH's.

– ***Circular inductance at termination capacitor grounding:*** if we assume ground connection of the termination capacitor to be a full circle, the equation below gives an estimation for the stray inductance at ground connection of termination capacitor[45] according to which the inductance value is in order of a few hundreds of nH's.

$$L_{circ} \approx N^2 R\mu_0\mu_r\left[\ln\left(\frac{8R}{a}\right) - 2\right] \tag{2.12}$$

in the equation above, N, R and a are number of the wire turns, radius of the circular route and radius of the conductor respectively.

– ***Stray capacitance between table and screen conductor:*** some parts of the coaxial cable screen is in proximity of the ground sheet and table. This would result in stray capacitances that is estimated as follows:

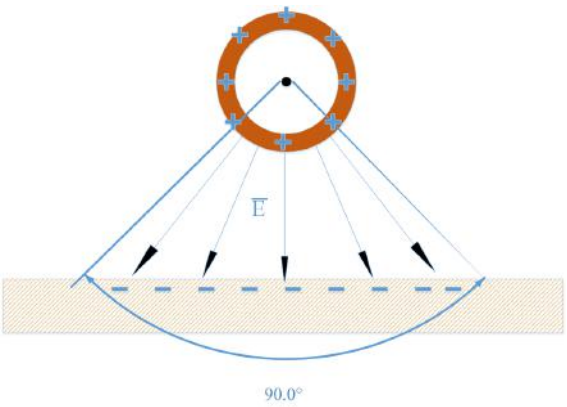

Figure 2.20: Stray capacitance between screen conductor and ground sheet

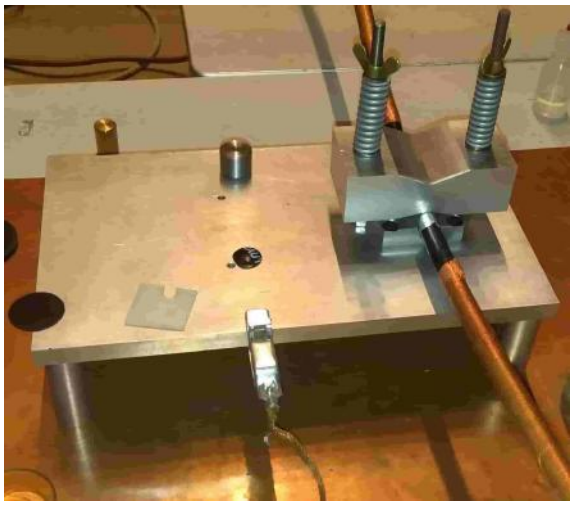

Figure 2.21: Table structure

if **a** is the mean radius of the screen conductor and **b** is radius of the assumptive circle at the ground sheet position, and assuming only $\frac{\pi}{2}$ of the contour contributes to the capacitance calculation as shown in drawing 2.20, the stray capacitance can be estimated using similar method used for coaxial cable capacitance. The cable-sheet capacitance would be,

$$C = \frac{\pi \epsilon_0 l}{2 \ln\left(\frac{b}{a}\right)} \tag{2.13}$$

and for the cable-table stray capacitance we would have,

$$C = \frac{\pi \epsilon_0 l}{\ln\left(\frac{b}{a}\right)} \tag{2.14}$$

Notice: the ground sheet is considered so small that only one quarter of an arbitrary contour would include the whole sheet.
If the cable is located 10 cm above the sheet and just 1.5 cm above the table. Considering the outer conductor mean diameter would be 7.85 mm, and due to the closeness of the cable to the measurement table we assume half and a quarter of the total charge participate in forming stray capacitances for cable-table and cable-ground structures, together estimated to be around 18 pF for each side. In the simulation 20 pF stray capacitance works well.

– ***Stray capacitance between cable holder structure and screen conductor:*** the holder structure is estimated by two rectangles as it is illustrated in the drawing 2.22.

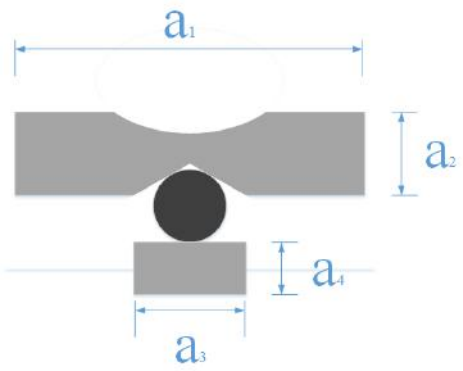

Figure 2.22: Stray capacitance between screen conductor and central cable holder structure

This structure is perpendicular to the cable screen conductor. This is a very complex geometry, however it can be estimated by two planes with the same length (l) and the the same thicknesses (e) according to the literature [46], as indicated in figure 2.23.

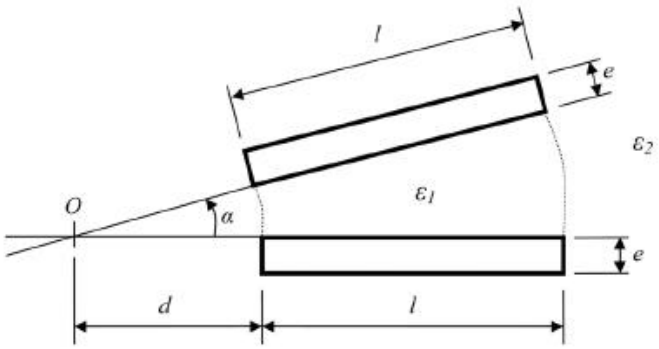

Figure 2.23: two perpendicular plate capacitance

Therefore the capacitance is derived from the following equation,

$$C = \frac{\epsilon_0 \epsilon_r}{\alpha} . \ln\left[1 + \frac{l}{d}\right] \tag{2.15}$$

If we assume half of the screen conductor to be perpendicular to the upper part of the holder and the other half to be perpendicular to the lower part of the structure then the total stray capacitance is calculated from the following equation,

$$C = \frac{2\epsilon_0}{\pi} . \left[\ln\left(1 + \frac{a_2}{d}\right) + \ln\left(1 + \frac{a_4}{d}\right)\right] \tag{2.16}$$

Therefore this yields a rough estimation of about 7 pF for longer side and 6 pF for shorter side of the circuit.

- **Damping Resistor (R_d):** A part of the incident pulsed-voltage reflects back towards pulse generator. In order to minimize unwanted disruptive impact of the reflected wave on the pulse generator a damping resistor with magnitude of 155.2 Ω is connected at injection point entrance [8, 47]. The main application of this, however, is flattening the pulse overshoot and disruptive oscillations, mostly originated form fast switching actions.

- **Termination capacitor:** this capacitor (figure 2.24), parallelly connected to HVDC source, to provide a earth connection for core conductor in order to close the circuit. For this case applied capacitor is approximated to be 1.2 nF.

Figure 2.24: Termination capacitor of 1.2 nF

2.2.10.1 Mini-cable layers

For this study, a single core Medium Voltage unarmoured coaxial mini-cable with stranded Aluminum wires as inner conductor and copper-tape screen is used that is composed of the following layers.

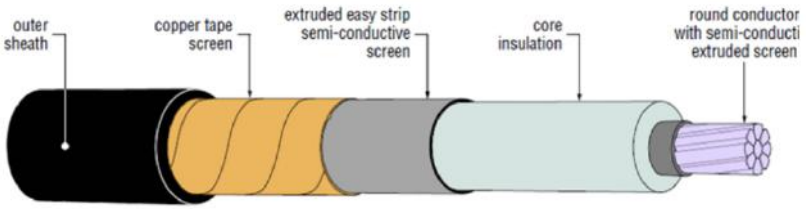

Figure 2.25: Layers of a MV stranded single-core, taped copper screen, XLPE insulated cable[48]

1. ***Inner conductor***: In this case inner conductor is a set of circularly stranded Aluminum wires. The inner conductor diameter (braiding neglected) is approximated to be 6 mm.

2. ***Dielectric***: The dielectric is XLPE with approximated thickness of 3.4 mm. XLPE Permittivity (relative to vacuum) and conductivity are considered to be 2.38 and 1 fS/m accordingly.

3. ***Inner*** & ***Outer semicon***:

   - **Reasons for use:** semi-conductive layers of cross-linked compound material are usually produced by adding *carbon black* as a filler into polymer lattice according to the literature [49–52] in order to smoothen rough interface between inner conductor and insulation on one hand and that between insulation and screen conductor on the other hand. This material contributes to achieving a rather gradual change of conductivity and permittivity values when electric field trespasses from a conductive to dielectric material. By injecting the CB additives, whose particle resistivity are in range of 0.1 to 100 $\Omega.cm$, the polymer resistivity plunges enormously. In this way an almost symmetric radial electric field profile is achieved, resulting in swift electrostatic charge dissipation, and preventing local field enhancement. This is major drive for treeing, partial discharges and even breakdown in the power cables [51, 52]. A barrier can be developed against externally induced voltages, unwanted hazardous electric shock and radio interference are also contributed to their application necessity [51]. The bedding layers thickness are approximated to be 0.7 mm and 0.5 mm respectively for inner and outer in this thesis.
     In addition to change in electrical properties, the composite mechanical characteristics like tensile strength, heat conductivity and material flexibility also changes due to CB injection [52, 53]. They might be advantageous, for example, in building a protective layer in order to limit any deterioration resulted by current carrying conductor(s) overheating during system faults (e.g short-circuit), ensuing heat conductivity alteration. A shield establishment against unwanted external phenomena, such as moisture, protrusions, etc. helps protecting the cable functionality and enduring its lifetime.
   - **Behaviour:** According to *M.E. Spahr et al 2017* [52], XLPE-CB composite shows a triple phase behaviour including insulating, percolation and conducting phases (figure 2.26). The main factor that determines XLPE-CB application is critical percolation threshold that varies as a function of concentration, structure and type of the filler added to the polymer lattice. For high voltage applications usually a smooth transformation zone is intended.

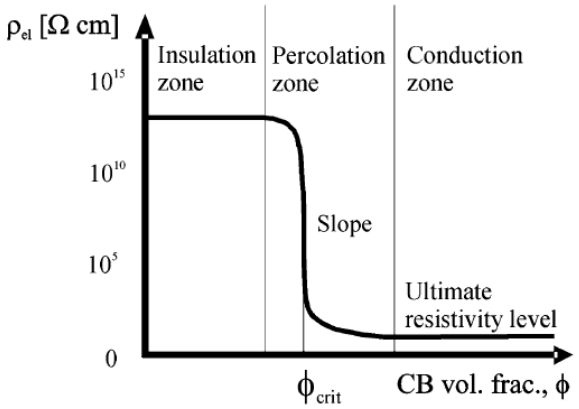

Figure 2.26: Resistivity alteration of a polymer-CB composite depending on filler concentration

- **Electrical modeling:** electrical model development for CB-polymer compound is immensely laborious and complicated, as multiple factors and disciplines are involved. In the most cases the material behaviour is usually not predictable. Any change in filler injection and processing procedure, resulting in different void dimension, crystallinity and CB conducting chain abundance and length. Type of the polymer dielectric itself is also another deterministic factor that affects the electrical properties of the composite significantly. In addition, external role-playing factors like frequency, heat, current and voltage density and mechanical stresses contribute to the material modeling complexity [52, 54]. The literature [54, 55] explains that despite the fact that the resistive current may follow one of the mechanisms including field emission, thermionic emission or tunneling effect, the first two can not be realized in practice, since usually the electric field can not reach to the threshold value, as the gap distance barely exceeds 10 Å.

  At low frequencies, tunneling between CB particles is considered to be dominant mechanism, hence the conductivity does not differ too much from σ_{dc}, however, above 1 MHz, the equivalent resistance declines, thus capacitance becomes increasingly influential and becomes leading mechanism and conductivity climbs rapidly.

  The other influential parameter on the semiconductor characteristics is current density. At low current densities, current-voltage curve shows almost linear behaviour. On the other hand, by increasing the current density, the curve starts behaving non-linearly. When a certain limit for current density is passed, the apparent resistivity collapses, that can be interpreted to inverse proportionality of the apparent resistivity across the material and the applied current density to the compound.

4. ***Metal screen***: this layer is used for electric field cancellation at the cable outside. By earthing the screen, unwanted currents like capacitive current and induced circulating current can be discharged into ground. Furthermore, draining zero-sequence current and

making a wall against humidity are other factors cited by the literature[49]. Screen also provides a return path for HVDC applications. In this research outer screen is added manually using a 0.25 mm thick copper strip.

5. ***Jacket***: cable outermost layer that acts as a protecting barrier against mechanical tensions and moisture. In the most cases, the layer is composed of Thermoplastic materials like PVC, Neoprene or Timbal Lead [56]. In this study jacket is completely removed.

6. ***Cable lug***: cable lugs are used to provide connections of the cable to other installations such as capacitor whose effect is neglected in this study.

2.3 Mini-cable dimensions

In order to attain accurate models for the whole setup, the layers dimensions are measured as it is demonstrated in figure 2.27.

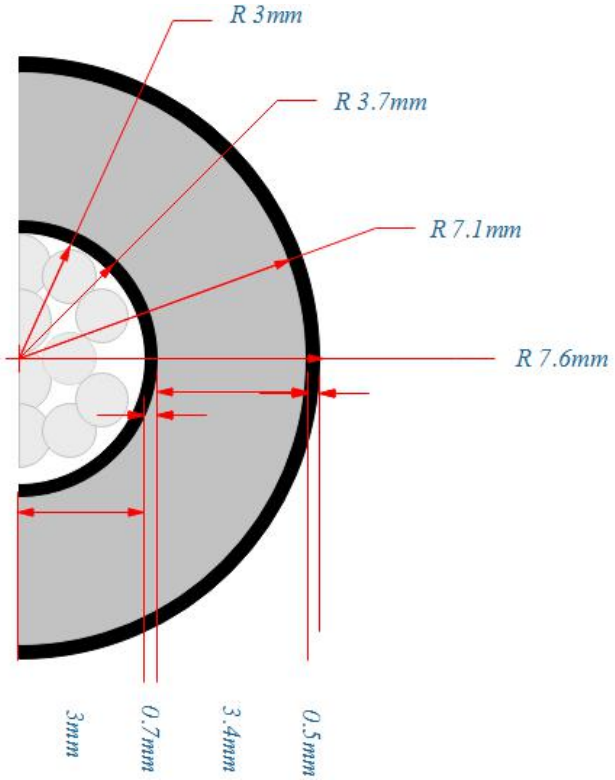

Figure 2.27: Cross-section of the cable under test

However the mini-cable measured characteristics do not precisely correspond to *IEC*[2] *60228-part II* [57, 58], as dielectric thickness is 3.4 mm and voltage rating is usually related to thickness

[2]International Electrotechnical Commission

of insulating material, its operational voltage level is approximated to be $6/10(12)\,kV$ [3], although the core is thinner than that of comparable standard cables [50, 58].
To achieve maximum pulse concentration at the exposed part not only screen conductor is shortened but also outer semicon layer at both ends are removed in order to prevent any probable leakage current through that as it is depicted in figure 2.28. Full dimensions of the cable are scoped and shown in table 2.3.

[3] Rated phase, rated line and max voltage respectively

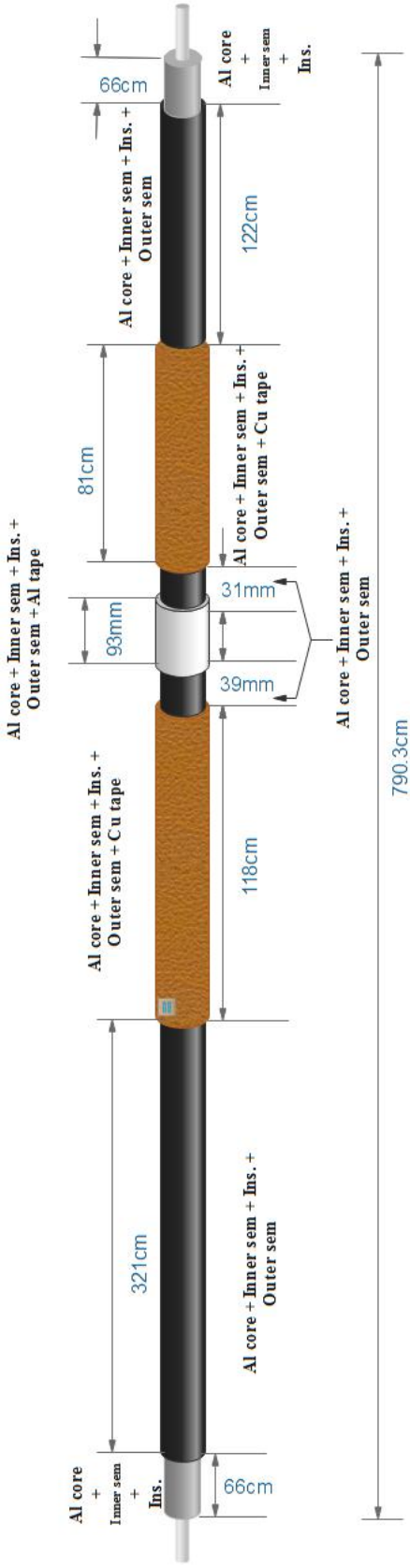

Figure 2.28: Actual configuration of sample MV cable

Symbol	Cross-sectional parameters	Magnitude	Unit
	Core conductor		
r_i	Aluminum inner conductor radius	3	mm
d_i	Aluminum inner conductor diameter of	6	mm
	Core + Inner Semicon		
r_{is}	Inner semiconductor outer radius	3.7	mm
d_{is}	Inner semiconductor outer diameter	7.4	mm
t_{is}	Inner semiconductor thickness	0.7	mm
	Core + Inner Semicon + Insulation		
r_{ins}	Insulation outer radius	7.1	mm
d_{ins}	Insulation outer diameter	14.2	mm
t_{ins}	dielectric thickness	3.4	mm
l''_1	Removed screen & outer semicon, shorter	66	cm
l''_2	Removed screen & outer semicon, longer	66	cm
	Core + Inner Semicon + Insulation + Outer Semicon		
r_{os}	Outer semiconductor outer radius	7.6	mm
d_{os}	Outer semiconductor outer diameter	15.2	mm
t_{os}	Outer semiconductor thickness	0.5	mm
$l'_{ctr,1}$	Removed screen, shorter, central	31	mm
$l'_{ctr,2}$	Removed screen, longer, central	39	mm
l'_1	Removed screen, shorter	122	cm
l'_2	Removed screen, longer	321	cm
	Core + Inner Semicon + Insulation + Outer Semicon + Screen conductor		
r_s	Metal screen (Cu or Al) outer radius	7.85	mm
d_s	Metal screen (Cu or Al) outer diameter	15.7	mm
t_s	Metal screen (Cu or Al) thickness	0.25	mm
l_1	Length of cable healthy part, shorter	81	cm
$l_{healthy}$	Length of cable healthy part, longer	118	cm
l_{cable}	Total cable length	790.3	cm
	Some Important Dimensions		
D	Mean diameter of screen	15.45	mm
A_{cu}	Cu-conductor cross-sectional area	12.134	mm^2
A_{al}	Al-conductor cross-sectional area	28.274	mm^2
A_{xlpe}	XLPE cross-sectional area	115.36	mm^2
$A_{sem,outer}$	Outer semicon cross-sectional area	23.091	mm^2

Table 2.3: Measured dimensions of MV cable

2.4 Mini-cable parameters

This section discusses the initial parameters used for modeling of the mini-cable. For further reading, one can refer Appendix, where the parameters calculation is discussed in detail. Figures 2.27 and 2.28 show cross-sectional and longitudinal configuration of the mini-cable under test.

2.4.1 Insulation properties

1. **Relative permittivity (ϵ_r):** the complex permittivity $\left(\epsilon^*(\omega)\right)$, referring to capacity of a dielectric material to be polarized when undergoing an external electric field, is a frequency dependent parameter, being composed of real $\left(\epsilon' = \epsilon_0 \epsilon_r'\right)$ and imaginary part $\left(\epsilon" = \epsilon_0 \epsilon_r"\right)$. The term relative stands for ratio of the material absolute permittivity $\left(|\epsilon|\right)$ to the vacuum permittivity $\left(\epsilon_0\right)$. As XLPE is a low-loss dielectric, ϵ_r" (equation C.5) is negligibly small $\left(\epsilon" \approx 6 \times 10^{-6}\right.$ in our case$\left.\right)$, while ϵ_r' starts at a static value of $\epsilon_s \approx 2.5$ dropping to $\epsilon_\infty \approx 2.38$ at sufficiently high frequencies in order of 100 MHz. Therefore in the most cases ϵ" is ignored and the relative permittivity is approximately by its real term $\left(\epsilon_r \approx \epsilon_r'\right.$, thus $\left.\epsilon \approx \epsilon'\right)$. By means of Debye (equation C.7) Cole-Cole (equation C.9), Davidson-Cole (equation C.10) or Havriliak-Negami (C.8) equations, frequency dependent behaviour ϵ_r can be explained (graph 2.29).

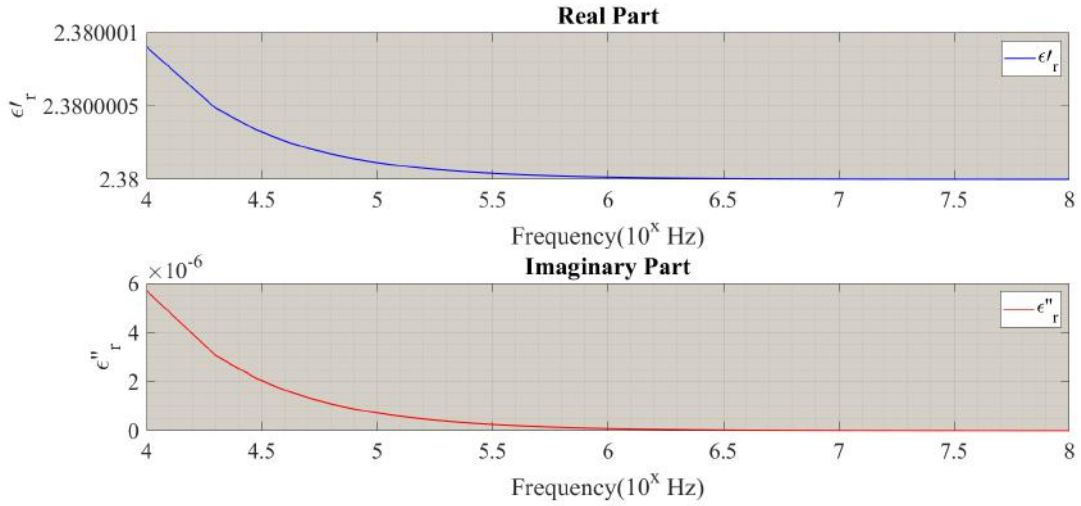

Figure 2.29: Real & imaginary parts of XLPE as a function of frequency (relative to vacuum permittivity ϵ_0)

Existence of semiconducting layers along radial axis is taken into account by multiplication of a geometrical correction factor Θ (equation 3.2) into ϵ_r. The resultant value is called effective relative permittivity $\epsilon_{r,eff}$ (equation 3.3). Applying a geometrical correction factor by PSCAD, in order to take CB-XLPE layers into account, gives rise to polarizability of the insulation (from $\epsilon_r \approx 2.38$ to $\epsilon_{r,eff} \approx 3.39$) in practice.

.

2. **Conductivity(σ_e):** Conductivity is a measure that defines how convenient charge carriers penetrate into a medium. Assessment of polymer conductivity is not easy at all. The dielectric conductivity is constructed by static (σ_s) and alternating (σ_a) terms (equation C.11). The latter is a complex number and heavily dependent on frequency, as at certain

frequency intervals a polarization mechanism (dipolar, atomic or electronic) is activated. Although the AC component rises almost thrice from frequencies in range of kHz to a few hundreds of MHz, in this thesis, change in conductivity is insignificant, as ***a)*** application of a fast pulse (pulse width in order of $\approx 80\,ns$), is much lower than polarization time of the dielectric (being in order of $\approx 1000\,s$ [59]) and ***b)*** even if we assume dielectric is fully polarized the pure AC conductivity (ignoring static term) would not exceed a few pS (see figure 2.30).

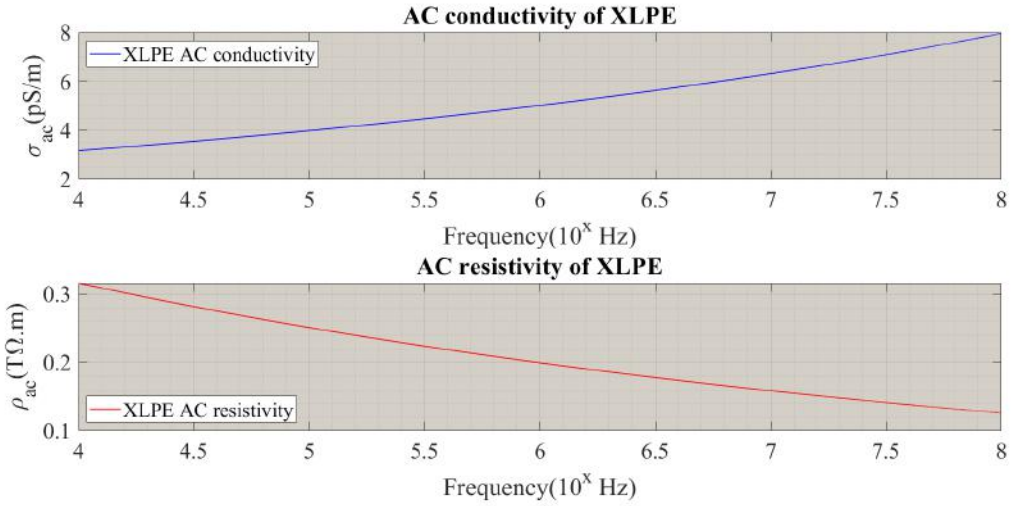

Figure 2.30: XLPE AC Conductivity & Resistivity

3. **Loss tangent (δ_e):** effective loss tangent (δ_e) is a measure to identify how lossy a dielectric material is and is derived from the following equation,

$$\begin{aligned} tan\delta_e &= tan\delta_{con} + tan\delta_{pol} \\ &= \underbrace{\frac{\sigma_s}{\omega\epsilon_0\epsilon'_r}}_{\text{Conduction}} + \underbrace{\frac{\epsilon''}{\epsilon'}}_{\text{Polarization}} \end{aligned} \tag{2.17}$$

where $tan\delta_e$, $tan\delta_{con}$, $tan\,\delta_{pol}$ and σ_s stand for effective, conduction and polarization loss tangents and DC or static conductivity. At $12.5\,MHz$, $tan\,\delta_{con}$ and $tan\,\delta_{pol}$ are in order of 10^{-13} and $tan\,\delta_e$ is in order of 10^{-12}, hence the polarization in the insulation, in practice can be neglected.

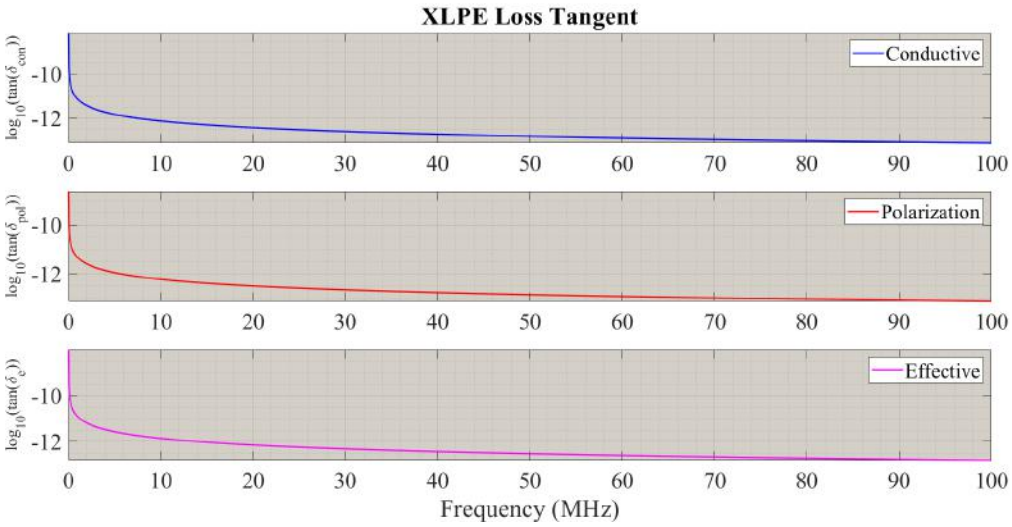

Figure 2.31: XLPE conduction, polarization & effective loss tangents

2.4.2 XLPE-CB compound properties

1. **Permittivity (ϵ_{sem}):** as it is already discussed in this chapter, in XLPE-CB compound the percolation region can be manipulated. This is an ultra-sensitive process throughout which the material characteristics may alter enormously. This thesis does not dig very deeply into XLPE-CB properties, since **a)** it needs a deep knowledge into polymer science, **b)** it requires proper facilities especially very accurate measurement devices, **c)** obtaining exact results is not guaranteed as manufacturing XLPE-CB with uniformly distributed CB particles is nearly impossible and also insignificant in cable manufacturing and finally **d)** it is far beyond the scope of this research.
   Relative permittivity of XLPE-CB is a non-linear function of frequency. One of the proposed straightforward frequency-dependent models for CB-XLPE compound consists of two CB resistances (R_{cb}) in series to a capacitor-resistor set ($C_{p,xlpe}$, $R_{p,xlpe}$) , which are parallelly connected to each other, representing a polymer gap between CB particles [55] (figure 2.32).

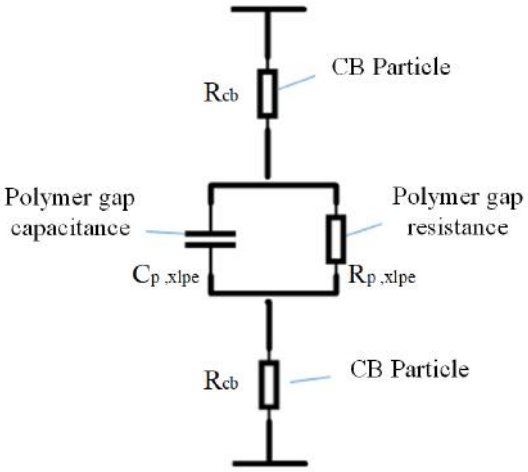

Figure 2.32: Equivalent circuit for CB particles and polymer gap

In this thesis, we intend to understand current flowing towards the central part on which the PEA measurement set is assembled. Influence of semiconductor in the sound parts of the cable where the screen conductor is not removed is simply taken into account by applying a correction factor. The complex apparent permittivity $\epsilon_{r,sem}$, taking only the parallel elements into account is approximated based on Debye equation as follows,

$$\epsilon^*_{r,sem}(\omega) = \epsilon_\infty + \frac{\epsilon_s - \epsilon_\infty}{1 + j\omega\tau_{sem}} \tag{2.18}$$

Considering high frequency permittivity to be $\epsilon_\infty \approx 500$, static permittivity to be $\epsilon_\infty \approx 2700$ and time constant (τ_{sem}) be equal to 4.5 ns, as suggested in literature [60], real and imaginary components of the complex permittivity alters as indicated in graph below as a function of frequency.

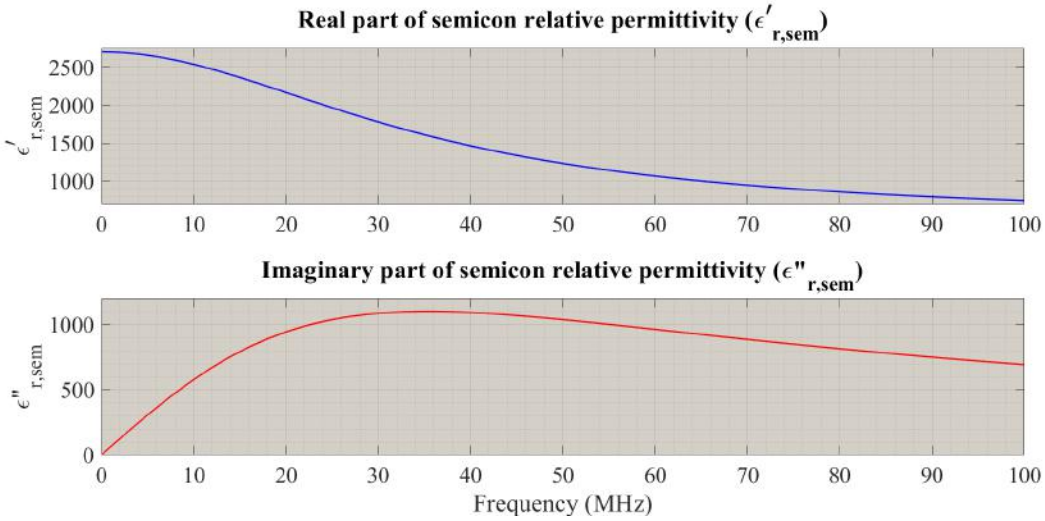

Figure 2.33: Apparent relative permittivity (relative to vacuum permittivity ϵ_0) of outer semiconductor as a function of frequency

2. **Conductivity (σ_{sem}):** having ϵ'_{sem} and ϵ''_{sem}, the effective complex semiconductor conductivity is also computable (equation 2.19).

$$\sigma^*_{sem}(\omega) = \left(\sigma'_{sem}(\omega) + \sigma_{dc,sem}\right) + j\sigma''_{sem}(\omega) \tag{2.19}$$

In order to observe very low voltage and DC resistivity of the semiconducting material $\sigma_{dc,sem}$ (quasi-DC), a set of measurements are performed at lab, according to which an ascending set of DC voltages, ranged between $0.1\,V$ to $2.245\,V$ (figure 2.35), are applied across a semiconductor sheet and penetrated current is measured as the first test. Possible impact of high current densities and frequency dependency of semiconductor resistivity is ignored in this test to avoid complexity. The sample is held between two cylindrical Al electrodes (figure 2.34), both having diameter of $40\,mm$. Graph below 2.36 shows changes in penetrated current and resistivity by voltage increase.

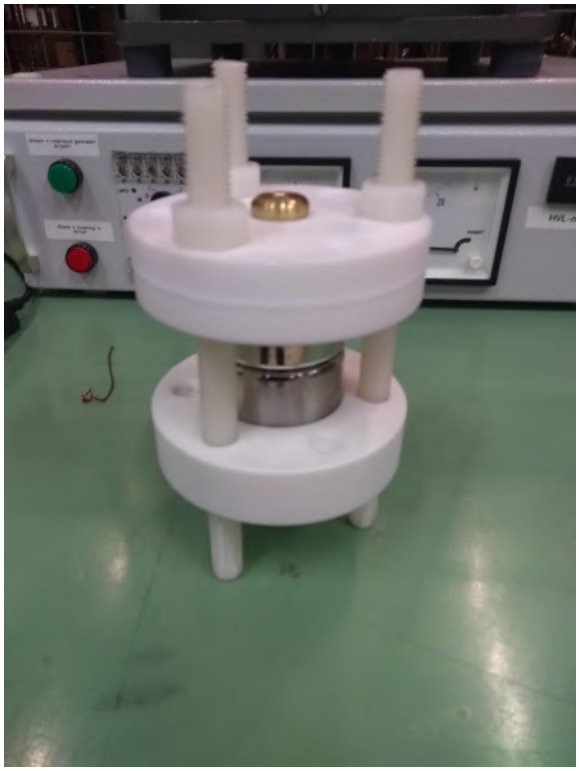

Figure 2.34: Electrodes for DC measurement

Figure 2.35: DC supply for DC measurement

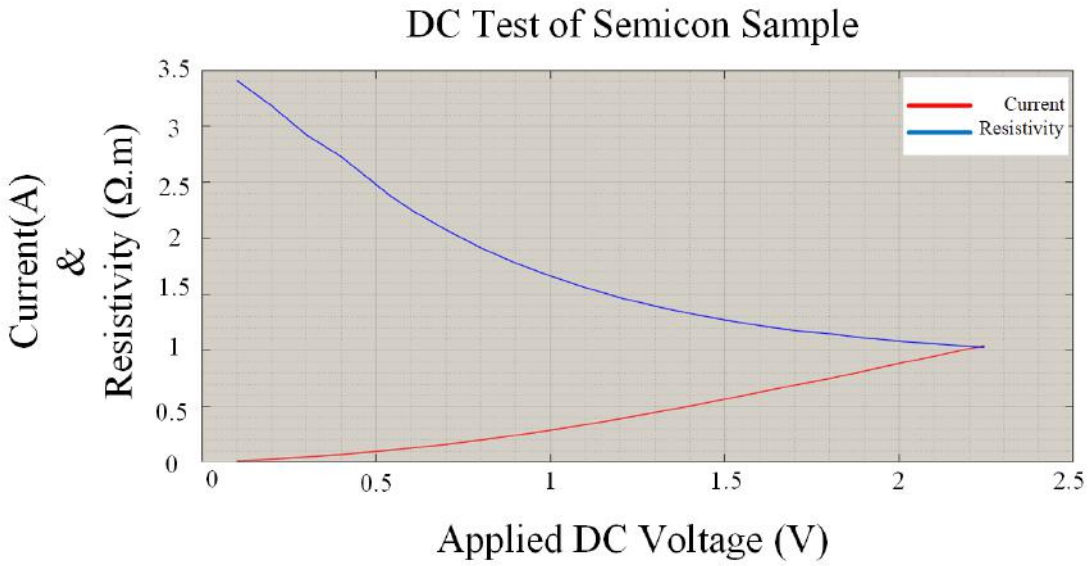

Figure 2.36: DC Semicon behaviour at low voltages

Graph 2.36 concludes that the semiconductor resistivity acquires a stable value around $1\,\Omega.m$ at a few volts that is equal to $100\,\Omega.cm$. At low frequencies and DC if sufficiently

high voltage is applied, conductivity/resistivity of semicon layer stays more or less stable, as tunneling is the only mechanism that drives the phenomenon. Therefore, in this research DC resistivity of the material is assumed to be $100\,\Omega.cm$.

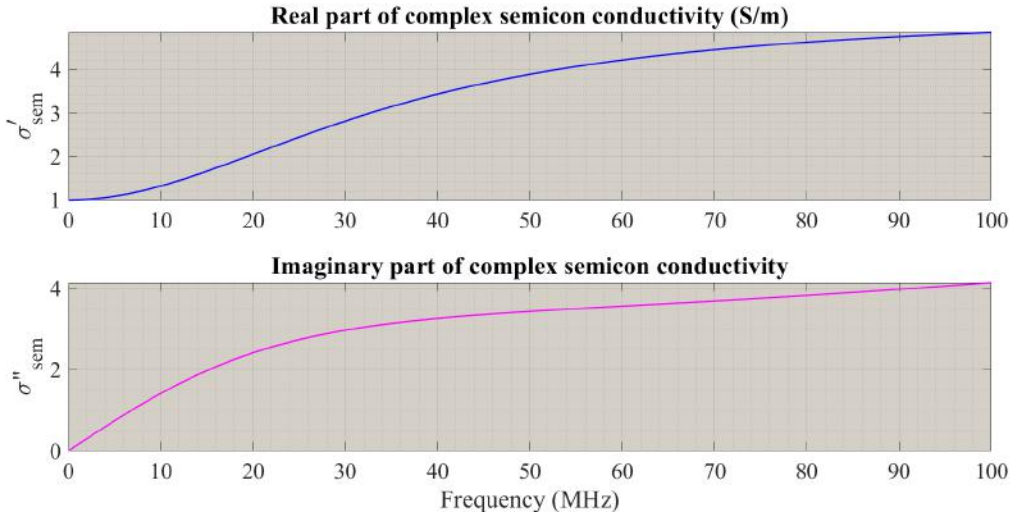

Figure 2.37: real and imaginary part of semicon complex conductivity

2.4.3 Conductor's frequency-dependent effects

1. **Skin effect:** at high frequencies in a piece of current carrying conductor, electrons tend to concentrate at the surface of the conductor, giving rise to current density at that region. This parameter is very influential in some primary line parameters like conductors resistance and inductance (equation 2.20 & graph 2.38).

$$\delta = \sqrt{\frac{2}{\omega\mu\sigma}} = \frac{1}{\sqrt{\pi f \mu\sigma}} \tag{2.20}$$

Graph 2.38 show collapse of the skin depth δ_{skn} by frequency rise. For the core and screen conductors of the subjected mini-cable the skin depth falls from 2.7 mm and 2.1 mm at 1 kHz to 24.1 μm and 18.5 μm at 12.5 MHz respectively.

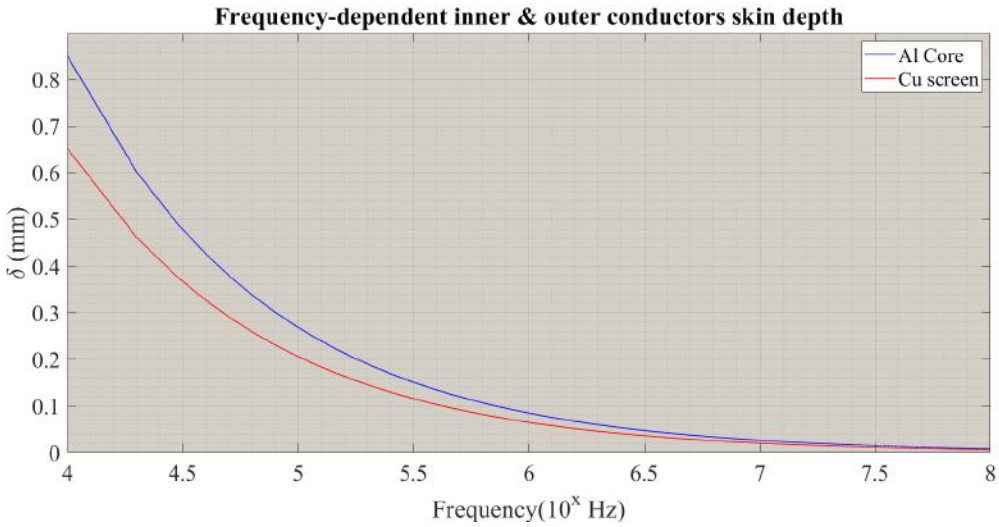

Figure 2.38: Al core vs Cu screen frequency-dependent skin depth

2. **Proximity effect:** in the adjacent conductors, in case of AC current, the current flowing through the first conductor generates a magnetic field round it, inducing eddy currents inside the second conductor and changes the current density profile. PSCAD/EMTDC phase-model of transmission line includes this factor in its calculations.

2.4.4 Primary transmission line constants

Primary transmission line parameters describe physical characteristics of the line that are derived based on Telegrapher's equations and identified as per unit length values. However they usually referred as "constants", this term is ambiguous and misleading as the values changes with frequency. However, The π-section model of cable, in practice, is inapplicable in case of high-frequency and transients, these values are used as initial values in frequency-dependent models of transmission lines.

1. **Series resistance (R'_{sr}):** the cumulative resistance R_{sr} of the cable is sum of the resistances of the core (R_{core}) and screen conductors (R_{scr}), each of which are inversely proportional to radius, skin depth and conductivity of the conducting material according to equation 2.21.

$$\begin{aligned} R_{sr} &= R'_{sr}.l_{cable} \\ &= \left(R'_{core} + R'_{scr} \right).l_{cable} \\ &= \left(\underbrace{\frac{1}{2\pi r_{is}\delta_{Al}\sigma_{Al}}}_{\text{Core Ohmic Losses}} + \underbrace{\frac{1}{2\pi r_{ins}\delta_{Cu}\sigma_{Cu}}}_{\text{Screen Ohmic Losses}} \right).l_{cable} \quad (\Omega) \end{aligned} \tag{2.21}$$

Per unit length resultant resistance of the cable (R'_{ser}), thus, increases considerably with frequency rise reaching to around 200 $m\Omega.m$ at very high frequency in order of 100 MHz as shown in figure 2.39. Influence of skin depth in the series parameters is internally calculated in PSCAD/EMTDC phase model of cable.

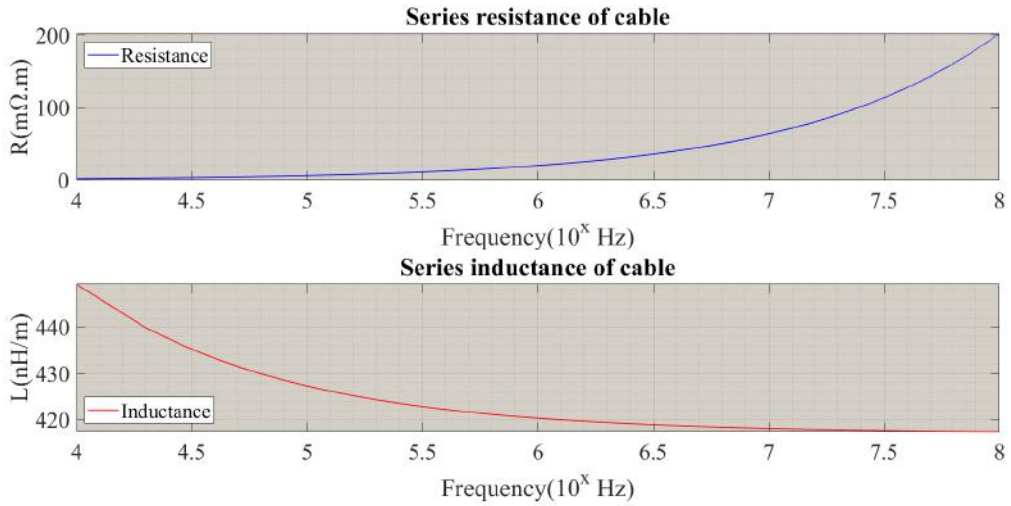

Figure 2.39: Frequency-dependency of series impedance parameters

2. **Series inductance (L'_{sr}):** per unit length inductance is summation of three elements, including the conductors self-inductances (L'_{sc} for core & L'_{ss} for screen) and the mutual inductance L'_m between two current carrying conductors.

$$\begin{aligned} L_{sr} &= L'_{sr}.l_{cable} \\ &= \left(L'_m + L'_{sc} + L'_{ss}\right).l_{cable} \\ &= \left(\underbrace{\frac{\mu_0\mu_r}{2\pi}\ln\frac{r_{ins}}{r_{is}}}_{\text{Mutual}} + \underbrace{\frac{\mu_0\mu_r\delta_{Al}}{4\pi}\left(\frac{1}{r_{is}}\right)}_{\text{Core}} + \underbrace{\frac{\mu_0\mu_r\delta_{Cu}}{4\pi}\left(\frac{1}{r_{ins}}\right)}_{\text{Screen}}\right).l_{cable} \quad (H) \end{aligned} \tag{2.22}$$

Despite the fact that the mutual inductance is independent of frequency, the self-inductances, are functions of frequency, as they are directly proportional to the skin depth, and according to graph 2.39 in contrast to series resistance increase with frequency rise.

3. **Shunt conductance (G'_{sh}):** as ϵ" in XLPE is very small, in most cases the shunt conductance can be ignored. In spite of being a function of frequency (equations 2.23 &2.40), even at high frequencies its value scarcely exceeds a few hundreds of pS/m. At 12.5 MHz, per unit length XLPE conductance is approximately 1.76×10^{-14}.

$$G_{sh} = G'_{sh}.l_{cable} = \frac{2\pi\sigma_e}{\ln\frac{r_{ins}}{r_{is}}}l_{cable} = \frac{2\pi\omega\epsilon_0\epsilon''}{\ln\frac{r_{ins}}{r_{is}}}.l_{cable} \quad (S) \tag{2.23}$$

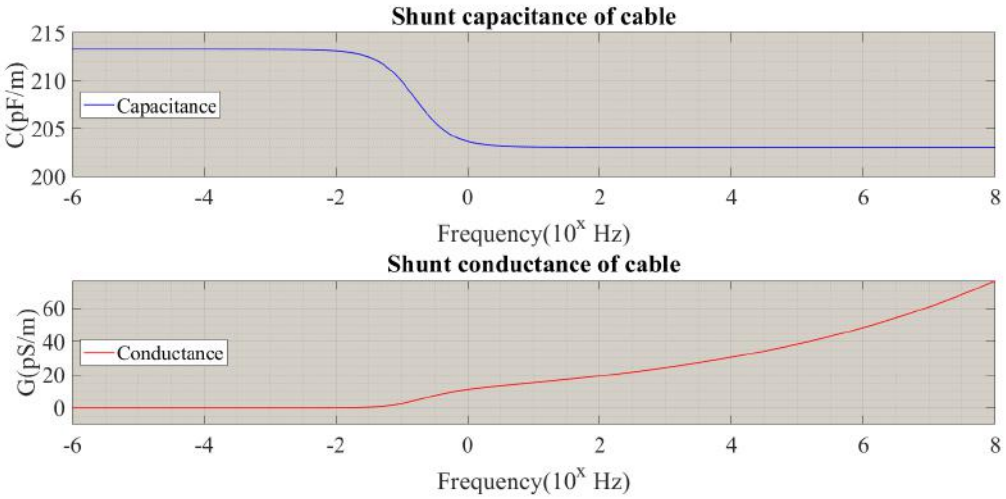

Figure 2.40: Change in shunt admittance by frequency rise

4. **Shunt capacitance (C'_{sh}):** per unit length shunt capacitance is practically independent of frequency if it is subjected to fast pulses (as depicted in graph 2.40), because ϵ'_r, to which C'_{sh} is directly proportional, stays almost stable with frequency rise (graph 2.29 & equation 2.24).

$$C_{sh} = C'_{sh}.l_{cable} = \frac{2\pi\epsilon'}{\ln\frac{r_{ins}}{r_{is}}}.l_{cable} \quad (F) \tag{2.24}$$

2.4.5 Secondary transmission line constants

these are propagation-related coefficients, which are strongly dependent on frequency of propagating wave along the transmission line.

1. **Characteristic impedance (Z_c):** According to the transmission line theory, when a travelling wave propagates through a transmission line, the instantaneous voltage and current at each position along the propagation axis ($x-axis$) can be decomposed into forward ($V^+(x,t)$, $I^+(x,t)$) and backward ($V^-(x,t)$, $I^-(x,t)$) components. The ratio between the forward voltage and current flowing towards single direction remains constant and is known as characteristic impedance and is defined as follows,

$$Z_c = \frac{V^+(x,t)}{I^+(x,t)} = \frac{V^-(x,t)}{I^-(x,t)} = \frac{Z_0}{2\pi}\sqrt{\frac{\mu_r(\omega)}{\epsilon_r(\omega)}}\ln\frac{r_{ins}}{r_{is}} = \sqrt{\frac{R'_{sr}(\omega)+j\omega L'_{sr}(\omega)}{G'_{sh}(\omega)+j\omega C'_{sh}(\omega)}} \tag{2.25}$$

Vacuum Permeability	μ_0	H/m
Relative Permeability	μ_r	-
Initial Characteristic Impedance	Z_0	Ω
Frequency-dependent characteristic Impedance	Z_c	Ω

However the characteristic impedance is usually considered constant, the literature [61] argues that it changes with frequency due to permittivity and permeability changes.

$$Z_c(\omega) = \frac{1}{2\pi}\sqrt{\frac{\mu_0}{\epsilon_0 \epsilon_r(\omega)}.\ln\left(\frac{r_{os}}{r_i}\right).\ln\left(\frac{r_{ins}}{r_{is}}\right)} \quad (\Omega) \tag{2.26}$$

The effective characteristic impedance $Z_{c,eff}\,(\omega)$, taking effective permittivity and semiconductor effect into account is derived according to equation 2.26 [62]. Based on the calculations, low frequency values for $Z_c(\omega)$ and $Z_{c,eff}(\omega)$ are approximately 41.75 Ω and 30.26 Ω accordingly, while at 12.5 MHz the values decline to 37.64 Ω and 30.26 Ω.

2. **Propagation constant (γ):** this is a frequency-dependent complex parameter that describes per unit length changes that an electromagnetic wave experiences in terms of amplitude and phase when travelling along a transmission line.

$$\begin{aligned}\gamma(\omega) &= \sqrt{Z'_{sr}(\omega).Y'_{sh}(\omega)} \\ &= \sqrt{(R'_{sr}(\omega) + j\omega L'_{sr}(\omega)).(G'_{sh}(\omega) + j\omega C'_{sh}(\omega))} \\ &= \alpha(\omega) + j\beta(\omega)\end{aligned} \tag{2.27}$$

In the PEA testing circuit, when the device under test (DUT) is a mini-cable, due to very low loss it can be approximated through equation that ignores attenuation along the cable. Hence, $\gamma(\omega)$ is directly proportional to the angular frequency (ω) of the propagating wave and square root of multiplication of the per unit length inductance and capacitance of the cable.

3. **Attenuation constant (α):** this parameter determines per unit length rate of attenuation in voltage or current magnitude when the wave travels from the sending port to receiving port of the transmission line.

$$\alpha(\omega) = Re\left(\gamma(\omega)\right) = \frac{1}{2}\left(R'_{sr}.\sqrt{\frac{C'_{sh}}{L'_{sr}}} + G'_{sh}.\sqrt{\frac{L'_{sr}}{C'_{sh}}}\right) \tag{2.28}$$

It is usually calculated in natural logarithmic scale. As $\alpha \propto C'_{sh}$, $C'_{sh} \propto \epsilon'_r$ and $\epsilon'_{r,eff} > \epsilon'_r$, its effective value is slightly higher than geometrical value. At 12.5 MHz, its original value is equal to $9.5 \times 10^{-4}\, N/m$, whereas its effective value slightly rises to $1.1 \times 10^{-3}\, N/m$. Attenuation constant increases with frequency rise as illustrated in graph 2.41.

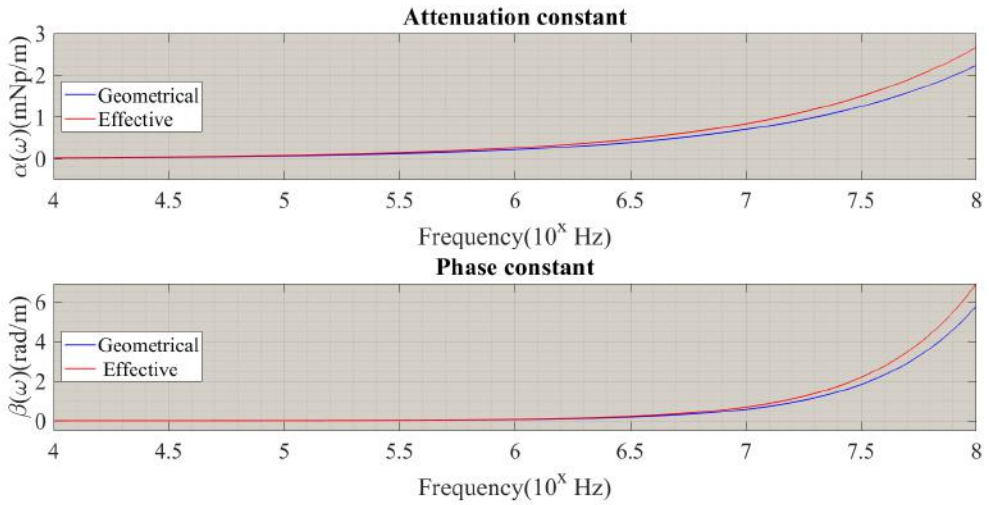

Figure 2.41: Frequency dependent attenuation & phase constants - Geometrical vs Effective

4. **Phase constant (β):** similar to α, β also increases with frequency (graph 2.41) and the effective value is higher than geometrical value. The phase constant is imaginary term of the propagation constant. This parameter explains how phase of a sinusoidal wave alters along the line.

$$\beta(\omega) = Img\Big(\gamma(\omega)\Big) = \omega\sqrt{L'_{sr}.C'_{sh}} \tag{2.29}$$

5. **Velocity of propagation (v_p):** velocity of propagation of an electromagnetic wave through cable is also directly proportional to the frequency, and shows how fast the electromagnetic wave travels through the transmission line.

$$v_p(\omega) = \frac{\omega}{\beta(\omega)} = \frac{1}{\sqrt{L'_{sr}(\omega).C'_{sh}(\omega)}} \quad (m/s) \tag{2.30}$$

In many cases for convenience the wave velocity is defined as a percentage of the light speed (c). This parameter is known as velocity factor (VF). At $12.5\,MHz$, the velocity factor of the sample mini-cable is approximated to 65%, while its effective value is lower, to be around 54% of the light speed.

Symbol	Description	Value	Unit
	Conductivity		
σ_{Cu}	Cu conductivity	59.5	MS/m
σ_{Al}	Al conductivity	35	MS/m
$\sigma_{xlpe,dc}$	XLPE DC conductivity	1	fS/m
$\sigma_{xlpe,ac}$	XLPE AC conductivity	82.38	aS/m
$\lvert\sigma^*_{sem}\rvert$	XLPE-CB absolute conductivity	1.77	S/m
$\angle\sigma_{sem}$	XLPE-CB absolute conductivity	1.3	rad
$\sigma_{dc,sem}$	XLPE-CB DC conductivity	1	S/m
σ'_{sem}	XLPE-CB real conductivity	0.48	S/m
$\sigma"_{sem}$	XLPE-CB imaginary conductivity	1.71	S/m
	Permittivity		
ϵ_0	Vacuum electric permittivity	8.8542	pF/m
$\epsilon_{\infty,xlpe}$	XLPE Infinite frequency permittivity	2.38	–
$\epsilon_{s,xlpe}$	XLPE Static permittivity	2.5	–
$\epsilon'_{r,xlpe}$	XLPE real relative permittivity	2.38	–
$\epsilon'_{r,xlpe,eff}$	XLPE real effective relative permittivity	3.39	–
$\epsilon"_{r,xlpe}$	XLPE imaginary relative permittivity	1.19×10^{-12}	–
$\epsilon_{\infty,sem}$	XLPE-CB Infinite frequency permittivity	500	–
$\epsilon_{s,sem}$	XLPE-CB Static permittivity	2700	–
$\epsilon'_{r,sem}$	XLPE-CB real relative permittivity	2456	–
$\epsilon"_{r,sem}$	XLPE-CB imaginary relative permittivity	691	–
	Loss tangent		
$tan(\delta_{s,xlpe})$	XLPE conduction loss tangent	6.05×10^{-13}	–
$tan(\delta_{a,xlpe})$	XLPE conduction loss tangent	5×10^{-13}	–
$tan(\delta_{e,xlpe})$	XLPE effective loss tangent	1.1×10^{-12}	–
$tan(\delta_{s,sem})$	XLPE-CB conduction Loss tangent	0.59	–
$tan(\delta_{a,sem})$	XLPE-CB conduction Loss tangent	0.28	–
$tan(\delta_{e,sem})$	XLPE-CB conduction Loss tangent	0.87	–
	Permeability		
μ_0	Vacuum permeability	$4\pi \times 10^{-7}$	H/m
$\mu_{r,Cu}$	Cu permeability	0.999994	–
$\mu_{r,Al}$	Al permeability	1.000022	–
$\mu_{r,xlpe}$	XLPE relative permeability	2.5	–
μ	XLPE Permeability	31.425×10^{-7}[63, 64]	H/m
	Skin depth		
δ_{cu}	Screen skin depth	18.455	μm
δ_{al}	Core skin depth	24.062	μm

Table 2.4: Calculation constants at 20°C & 12.5 MHz

Parameters	Calculation	Unit
	Resistance	
R'_{core}	51.1	$m\Omega$
R'_{scr}	20.4	$m\Omega$
R'_{sr}	71.5	$m\Omega$
$R_{sr,1}$	58	$m\Omega$
$R_{sr,2}$	84	$m\Omega$
$R_{sem,ctr,1}$	219	$G\Omega$
$R_{sem,ctr,2}$	276	$G\Omega$
$R_{sem,lng,1}$	8.64	$T\Omega$
$R_{sem,lng,2}$	22.73	$T\Omega$
	Inductance	
L'_m	287	nH
L'_{sc}	650	pH
L'_{ss}	260	pH
$L_{snd,1,eff}$	232	nH
$L_{snd,2,eff}$	338	nH
$L_{ctr,exp,1}$	385	pH
$L_{ctr,exp,1,eff}$	1111	pH
$L_{ctr,exp,2}$	526	pH
$L_{ctr,exp,2,eff}$	1439	pH
$L_{exp,1}$	35.78	nH
$L_{exp,1,eff}$	64.35	nH
$L_{exp,2}$	108	nH
$L_{exp,2,eff}$	184	nH
$L_{exp,sem,1}$	17.49	nH
$L_{exp,sem,1,eff}$	32.95	nH
$L_{exp,sem,2}$	17.49	nH
$L_{exp,sem,2,eff}$	32.95	nH

Table 2.5: Mini-cable series impedance parameters - values at 12.5 MHz & 20°C

Parameters	Calculation	Unit
	Capacitance	
$C'_{sh,geo}$	@ DC 213 — @ 12.5 MHz 203	pF/m
$C'_{sh,eff}$	@ DC 304 — @ 12.5 MHz 290	pF/m
$C_{ctr,geo}$	@ DC 20 —- @ 12.5 MHz 19	pF
$C_{ctr,eff}$	@ DC 28 —- @ 12.5 MHz 27	pF
$C_{snd,1,geo}$	@ DC 304 — @ 12.5 MHz 290	pF
$C_{snd,1,eff}$	@ DC 246 — @ 12.5 MHz 235	pF
$C_{snd,2,geo}$	@ DC 240 — @ 12.5 MHz 252	pF
$C_{snd,2,eff}$	@ DC 359 — @ 12.5 MHz 342	pF
$C_{sem,ctr,1}$	16	pF
$C_{sem,ctr,2}$	13	pF
$C_{sem,xp,1}$	0.4	fF
$C_{sem,xp,2}$	0.2	fF
	Conductance	
$G_{snd,1}$	14.2	fS/m
$G_{snd,2}$	20.7	fS/m

Table 2.6: Mini-cable shunt admittance parameters - values at 12.5 MHz & 20°C

Symbol	Value	Unit
	Propagation constants	
γ	$0.0009 + 0.6003j$	$-$
γ_{eff}	$0.0011 + 0.7169j$	$-$
	Attenuation constant	
α	0.008249	dB/m
α_{eff}	0.009851	dB/m
	Phase constant	
β	0.6003	rad/m
β_{eff}	0.7169	rad/m
	Velocity of propagation	
v_p	1.3084×10^8	m/s
$v_{p,eff,ctr}$	1.5388×10^8	m/s
$v_{p,eff,snd,1}$	1.6271×10^8	m/s
$v_{p,eff,snd,2}$	1.6277×10^8	m/s
	Velocity factor	
VF_{steady}	64.82	%
$VF_{12.5MHz}$	54.28	%
$VF_{eff,ctr}$	51.2942	%
$VF_{eff,snd,1}$	54.2351	%
$VF_{eff,snd,2}$	54.2577	%
	Cut-off frequency	
$f_{cut-off,eff}$	≈ 3.2583	GHz

Table 2.7: Secondary parameters of mini-cable- values at 12.5 MHz & $20^\circ C$

3

Test Circuit Model & Validation

For main purposes of this research that are ***a)*** comparison of different pulse injection practices in terms of the pulsed voltage quality and ***b)*** enhancement of the delivered pulse from different aspects, including magnitude, fluctuations, resolution, etc. designing of a model is crucial. The parameters can not be measured at every desired location of the circuit due to following reasons,

- Lack of accessibility
- Possible damages to device under test (DUT)
- Experiments need money, time and facilities
- All desired tests are not possible in practice

The MV coaxial mini-cable is considered as DUT in this thesis. As it is already discussed, a fast pulse whose pulse width is in order of 80 ns is applied to the cable for space charge detection purposes. All the coaxial cable models does not yield accurate results when undergone high-frequency electromagnetic waves. In this thesis, DUT is model based on Universal Line Model (ULM) or Phase Model, which is a type of well-known distributed model, by means of PSCAD/EMTDC software. The followings are being discussed in this chapter.

(i) A brief introduction to applicability of some commonly used transmission line modeling methods, align with their cons and pros

(ii) The logic behind selection of ULM

(iii) Explication of the developed PSCAD model

(iv) Validation of the model by means lab experiments

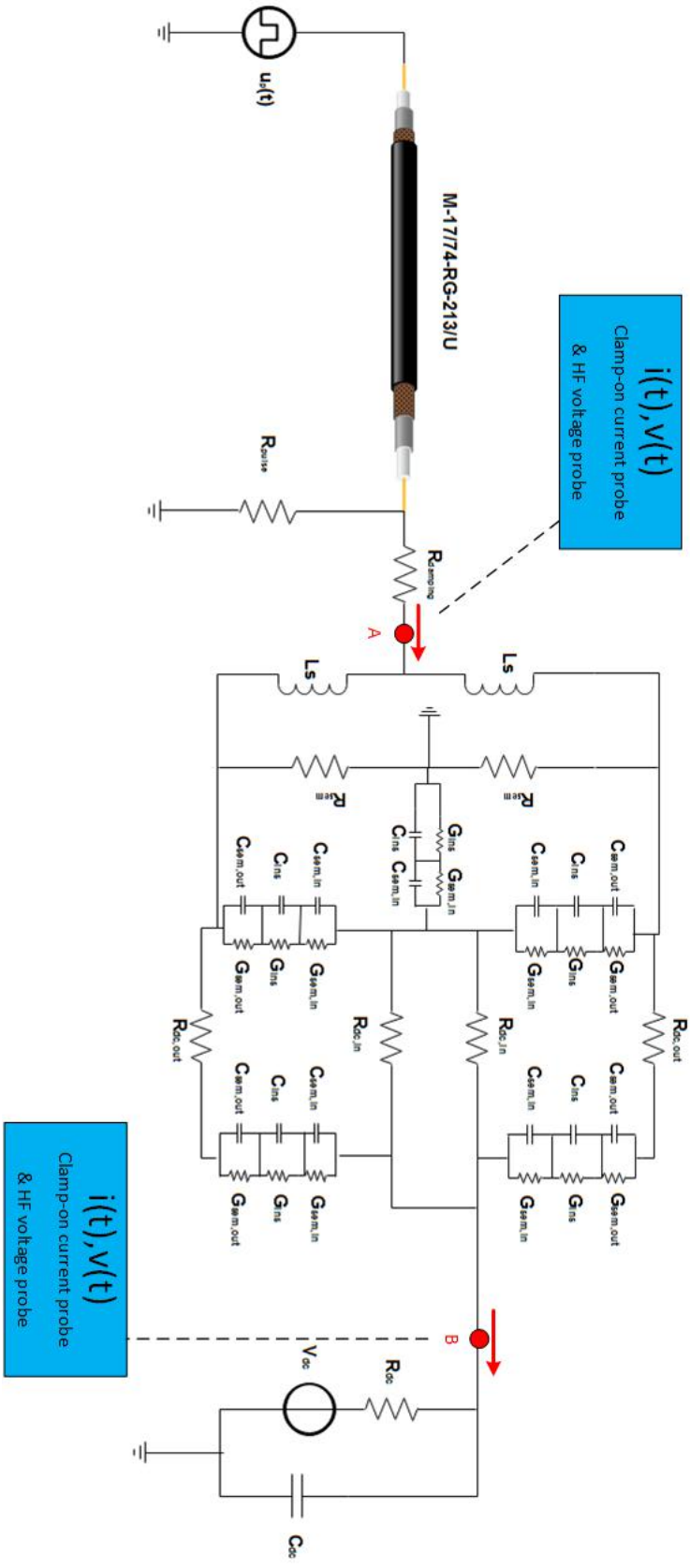

Figure 3.1: Full circuit and components for simulation, pulse injection to screen

3.1 Coaxial cable models

The cable models are categorized into two main categories of lumped and distributed as indicated in the tree diagram 3.2.

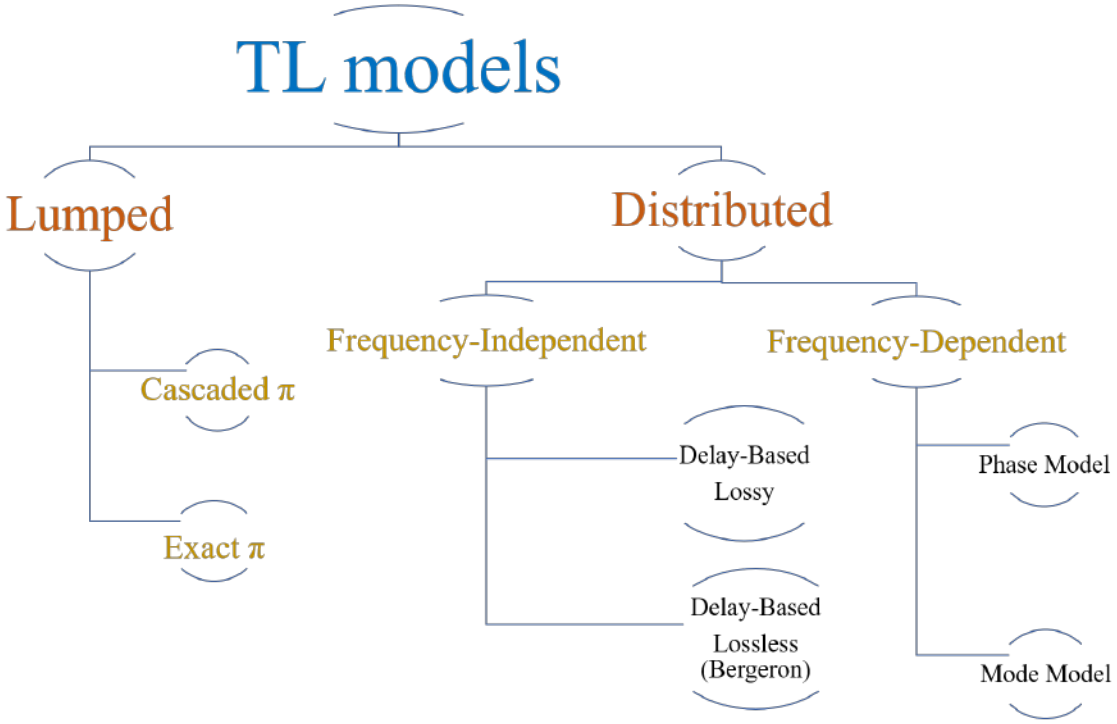

Figure 3.2: Models of transmission line

According to the cable modeling background information appendix B, the shortcomings of lumped element models, especially cascaded π-model can be summarized as follows [65]:

(a) Limited to steady state condition

(b) Frequency-independence

(c) Inapplicability in transient analysis

(d) Unwanted oscillations originated from cascading

(e) Influence of frequency electric field and permittivity, skin and proximity effects are all ignored

Table 3.1 below puts significant features of the most important transmission line models in a nutshell.

Model	Pros & Cons
$\pi-$section Cascaded & Exact	• Simple ✓ • Applicable for steady state analysis ✓ • Frequency-dependency: – ***Cascaded:*** frequency-independent ✗ – ***Exact:*** only small frequency range ✗ • Inapplicable for transient analysis ✗ • Ignored skin & proximity effect ✗ • Ignored propagation constant ✗
Bergeron Lossless & Lossy	• Propagation delay is taken into account ✓ • Only forward component is considered ✗ • Calculation based on fixed frequency ✗ • Oscillatory behaviour in transient & high frequency analysis ✗ • Ignored skin & proximity effect ✗ • Ohmic losses: – ***Lossless:*** excluded ✗ – ***Lossy:*** through a lumped resistor, non-accurate at high frequencies ✗
Mode Model	• Propagation function is included ✓ • Frequency-dependent (FD) ✓ • Different propagation modes are included ✓ • Appropriate for balanced systems ✓ • Modal transformation matrices are calculated once for each delay group. Changes due to time-variation of the parameters is ignored ✗
Phase Model	• Propagation function is included ✓ • Fully frequency-dependent (FD) ✓ • Most accurate commercially available model ✓ • Different propagation modes are included ✓ • Appropriate for balanced & unbalanced systems, ideal & non ideal conductor transposition ✓ • Transformation matrices are directly calculated in phase domain by curve fitting techniques, hence they change during the simulation. ✓

Table 3.1: Comparison of most important models for coaxial cable

3.2 PSCAD/EMTDC PEA circuit model

In order to validate this model, the simulation results of SSPI and DSPI setup configurations are compared to the measurements. The reference measures for this comparison are considered to be injection voltage (Point *A* in figure 3.1) and capacitors current (Point *B* in figure 3.1) due to the fact that those are the only accessible points whose parameters can be scoped experimentally. Figure 3.3 shows the block diagram of DSPI setup of PEA circuit.

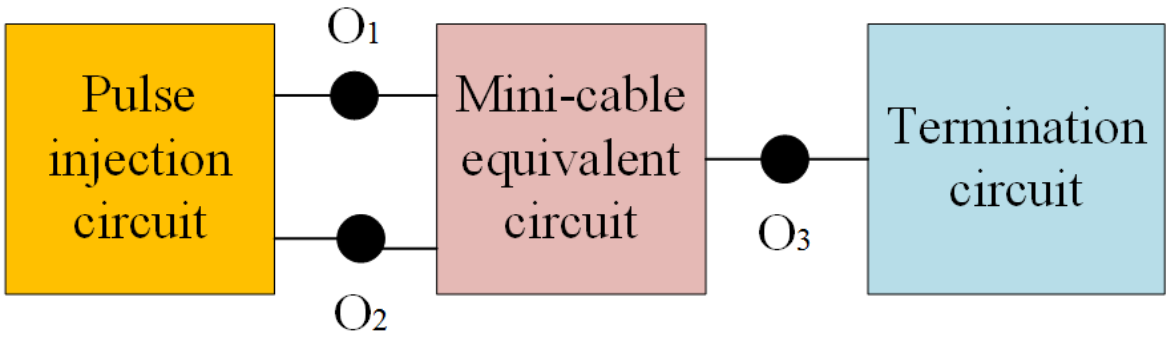

Figure 3.3: PSCAD circuit

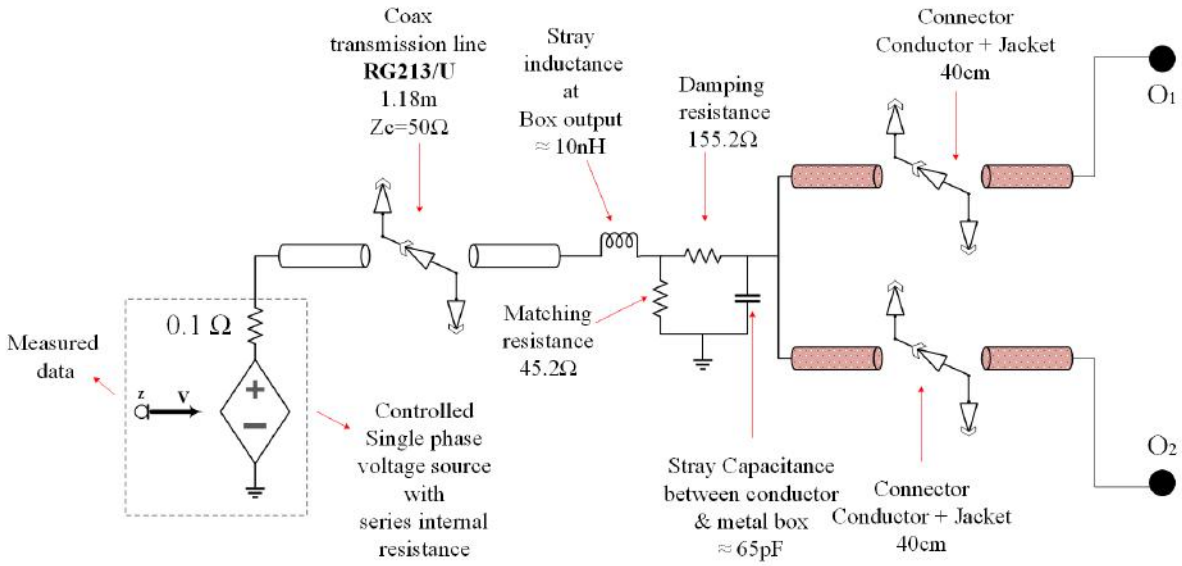

Figure 3.4: Pulse injection section equivalent circuit

The pulse injection block content of figure 3.3 is indicated in figure 3.4. The points $O_{1,2}$ are the coupling spots between the pulse injection and mini-cable blocks (or injection point). Figure 3.5 demonstrates the cross sectional view and dimensions of RG213/U coaxial cable transmission line.

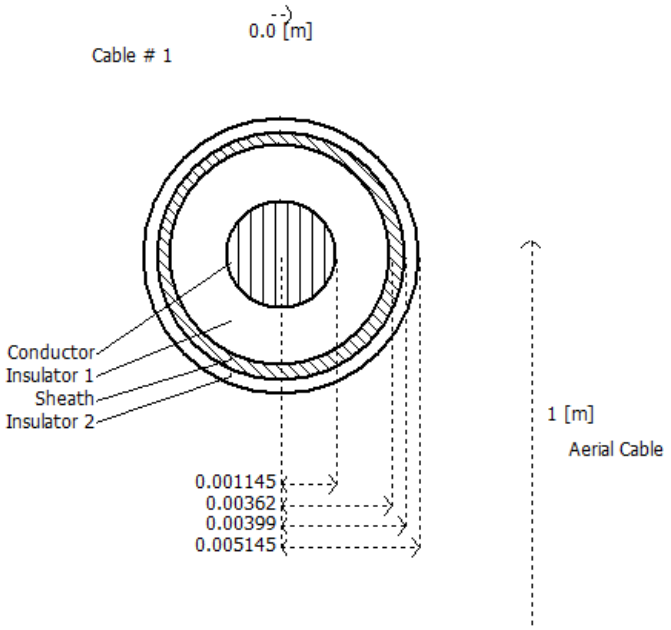

Figure 3.5: Defined cross section of RG213/U

In the same manner, the mini-cable equivalent circuit is shown in figure 3.6. A combination of an arrow and its adjacent cylindrical shapes in figure 3.6 represent a different cable section with different characteristics. The cable setting values are illustrated in figures 3.7 and 3.10.

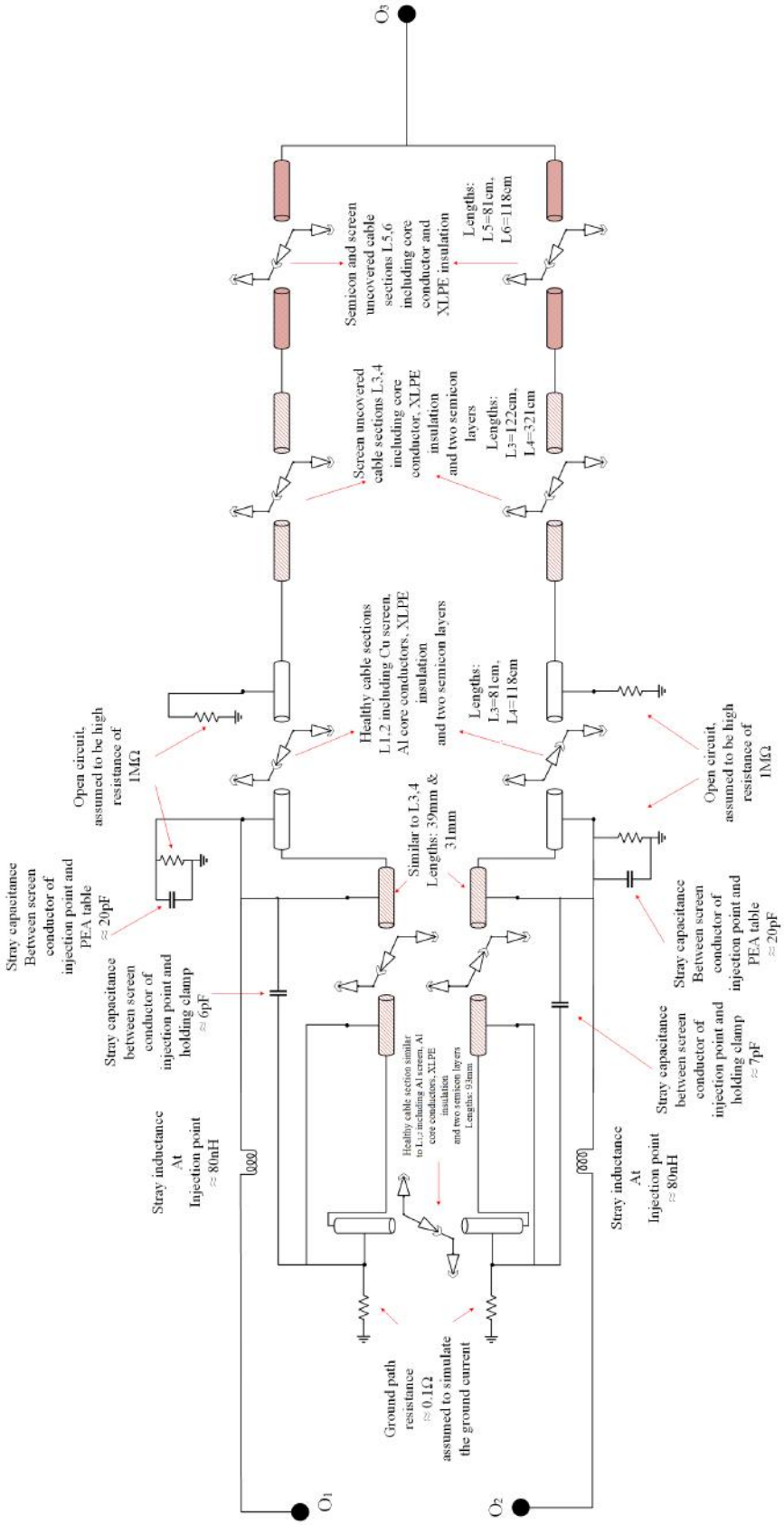

Figure 3.6: Mini-cable section equivalent circuit, for equivalent circuit of the cables shown with arrows refer to B.0.1

The cross sections of the transmission lines $L_{1,2}$, $L_{3,4}$, $L_{5,6}$ in figure 3.6 are illustrated in figures 3.7 - a, b and c respectively.

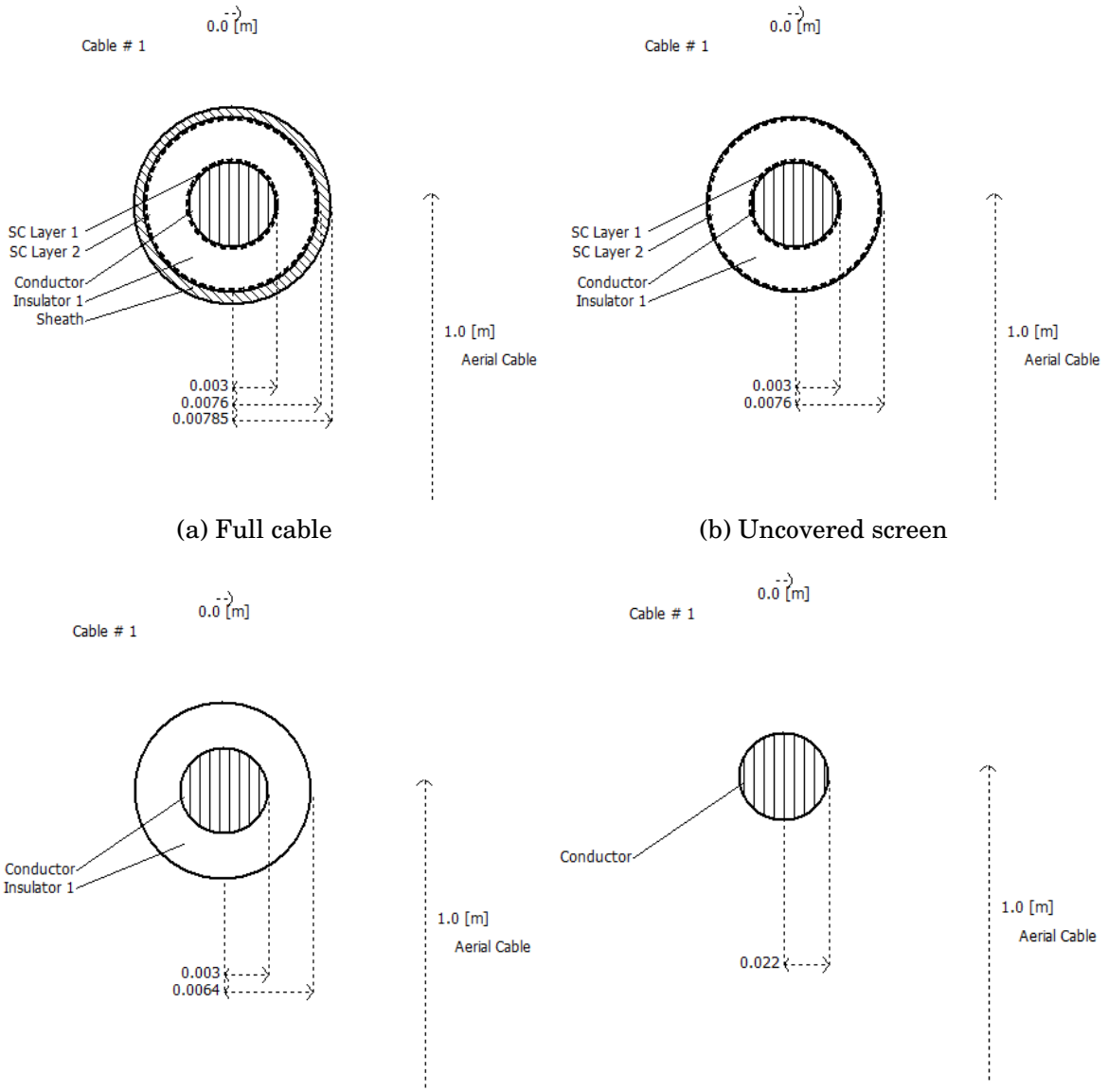

(a) Full cable

(b) Uncovered screen

(c) Uncovered screen and outer semicon

(d) Braided Cu connector

Figure 3.7: Cross section of different parts of mini-cable transmission line

Finally, the termination block is indicated in figure 3.8. The Cu braided connector is assumed to be round in order to make the use of transmission line model of PSCAD possible, however in practice the cross section has a rectangular dimension.

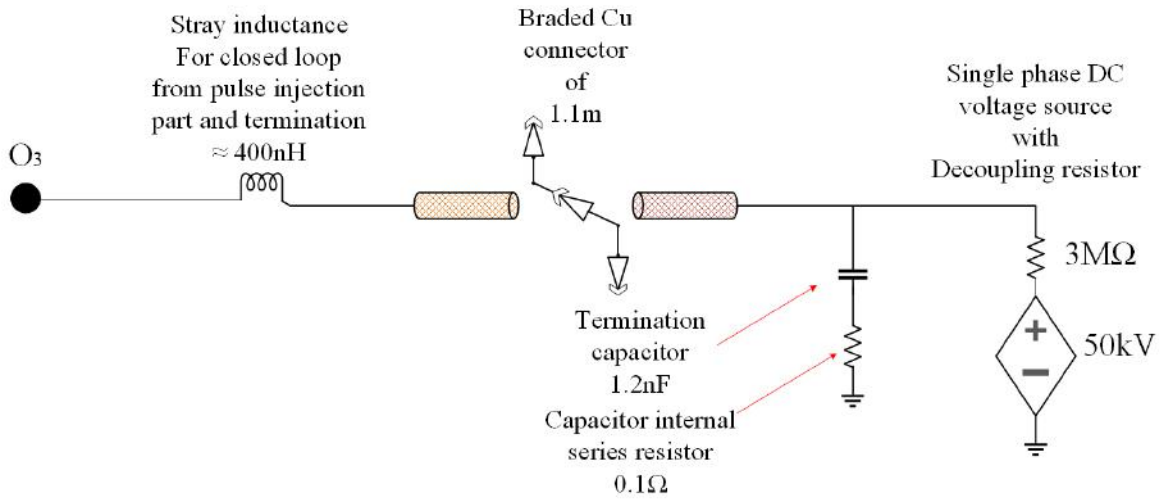

Figure 3.8: Termination section equivalent circuit

The cable model type can be selected in PSCAD/EMTDC including Phase, Mode or Bergeron model as depicted in figure 3.10. Curve fitting starting and end frequency are chosen from approximately DC to 100 MHz. Characteristics of each cable layer are defined whether those are conductors or insulation. Absence or presence of semiconducting layers is one important issue in this analysis. In PSCAD/EMTDC, semi-conducting layer's resistance is considered very high (in order of the insulation resistance) and the layer's capacitance is derived by means of the insulation's permittivity modification [66] (see equations 3.9, 3.1 & 3.2). In this approach, an effective permittivity is defined based on the geometrical data that can help improving the cable parameter approximation [62].

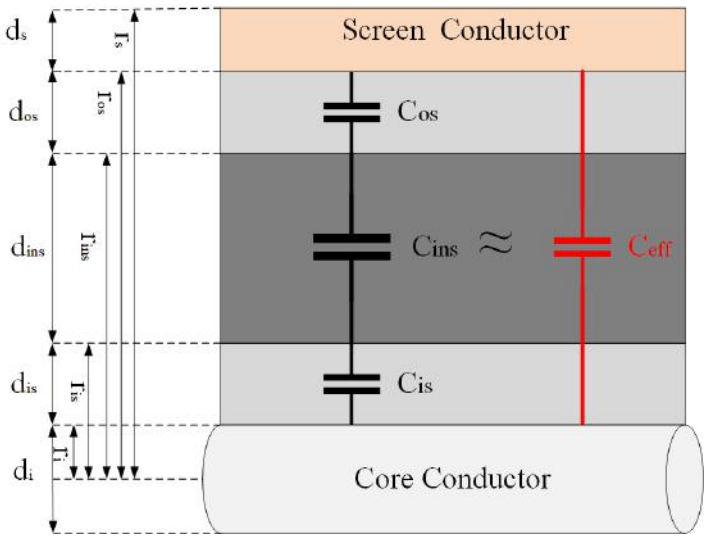

Figure 3.9: Effective permittivity

$$\frac{2\pi\epsilon_0\epsilon'_{r,ins}(\omega)}{\ln(\frac{r_{r_{ins}}}{r_{is}})} = \frac{2\pi\epsilon_0\epsilon_{r,eff}(\omega)}{\ln(\frac{r_{r_{os}}}{r_i})} \tag{3.1}$$

The equation above yields a geometrical correction factor (Θ), in order to calculate the effective permittivity ($\epsilon_{r,eff}$),

$$\Theta = \frac{\ln(\frac{r_{os}}{r_i})}{\ln(\frac{r_{ins}}{r_{is}})} \tag{3.2}$$

$$\epsilon_{r,eff}(\omega) \approx \Theta \cdot \epsilon'_{r,ins}(\omega) \tag{3.3}$$

$$\epsilon_{r,sem} = \epsilon_{r,ins}\frac{ln\frac{r_{os}}{r_i}}{ln\frac{r_{ins}}{r_{is}}} \tag{3.4}$$

$$C_{sem} \gg C_{ins}$$

hence,

$$C_{eq} \approx C_{ins}$$

In our case, the fixed value of conductivity does not yield desired results, especially at high frequencies where the conductivity drops considerably. On the other hand, the semiconducting layer's capacitance in series to the insulation capacitance is practically eliminated. In order to simulate the semiconducting layers more accurately, this layer is considered as a conducting layer whose resistivity is approximated by matching the simulation result to the lab measurements. According to the DC tests, that is already discussed in the previous chapters, at low frequencies close to DC, the semiconducting layer's resistivity reaches $1\,\Omega.m$ while at high frequencies in order of $12.5\,MHz$, the value climes to around $1.77\,\Omega.m$.

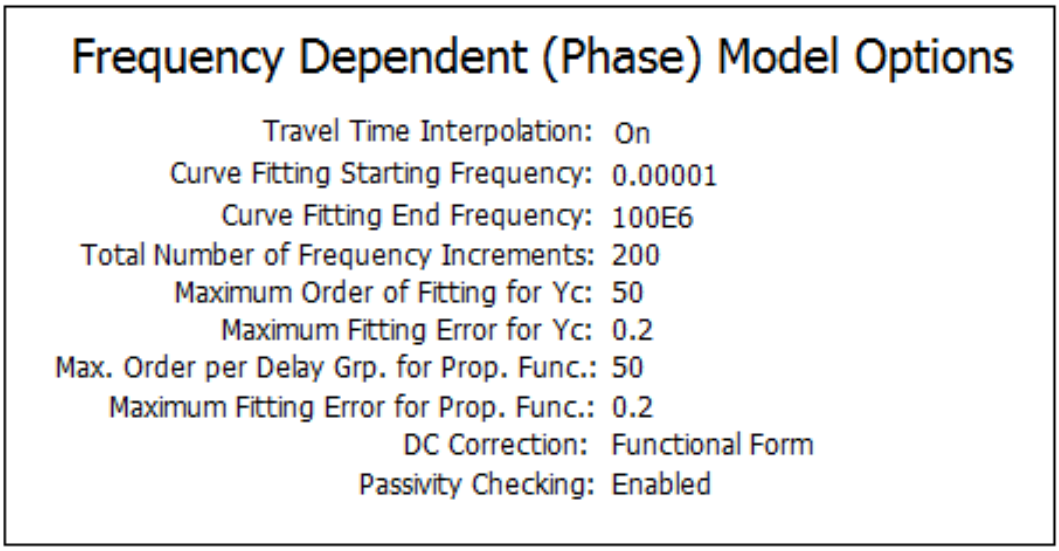

Figure 3.10: PSCAD/EMTDC model selection

As indicated in figure 3.10, the model is assessed for a frequency range between DC and 100 MHz. Figure 3.10 gives the initiations for rational function approximation for fitting of the characteristic admittance ($\boldsymbol{Y_c}$) and propagation function ($\boldsymbol{H}$) curves.

3.3 Model Validation

3.3.1 No cable simulation

In this part, the cable and related accessories are all eliminated from the circuit and the simulation results are compared to the measurements as indicated in the graph 3.11.

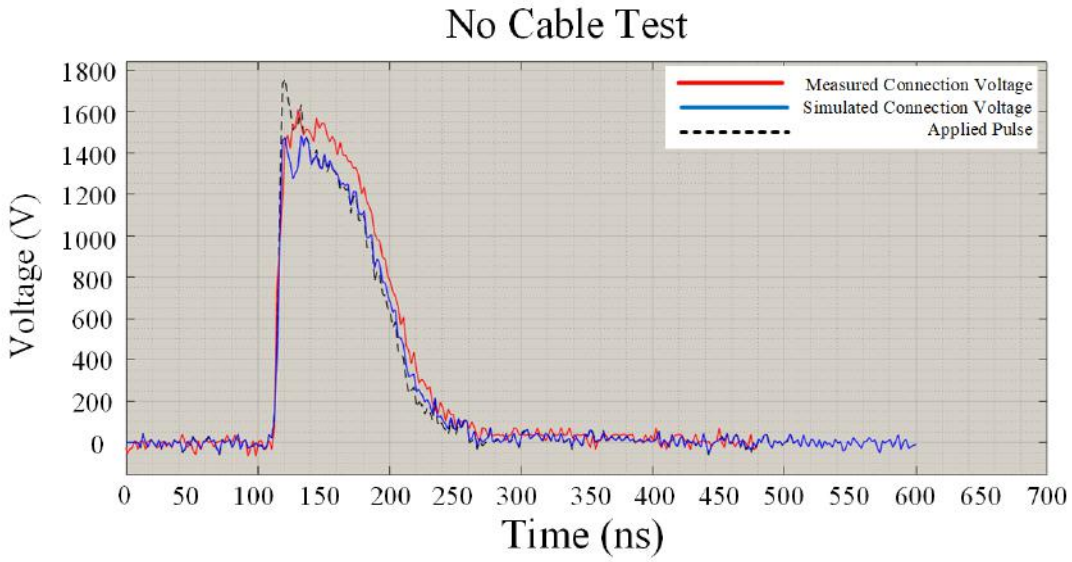

Figure 3.11: No cable test - lab measurement vs simulation

Figure 3.11 shows that when RG213/U transmission coaxial cable, having the length of 1.18 m, is modeled by means of the universal line model (phase model), and in absence of mini-cable. The damping resistor (R_d) is removed and the transmission line is grounded through the pulse or matching resistor R_p that is shown in figure 3.12, The actual pulse (point **b** in drawing 2.9, dashed black line in graph 3.11) is is applied to the cable and the voltage at receiving end of the cable is measured (point **c** in drawing 2.9). $R_1$and R_2 are earth path resistances that in our case are ignored.

Figure 3.12: Pulse resistor $R_p \approx 50\,\Omega$

However, the output pulsed-voltage resembles the measured pulse in the lab, there are minor differences. The simulated pulse has slightly lower amplitude compared to the real case, being in order of $1400\,V$ while the real case is in order of $1500\,V$ in average. The pulse width in the simulation is also moderately lower than that of the measured case.
However, it is not easy to inspect the error origins, a few possible reasons spring to mind.

- *Propagation constant error:* According to diagram 3.23, ignoring the core braiding can lead to higher phase (β) and attenuation (α) constants in the simulated pulse compared to the actual case.
- *Tolerance in standard values:* standard tolerance in standard dimensions and characteristic parameters can be other source for error in the simulation of RG213 coaxial cable.
- *Inaccuracy in actual route approximation:* in the calculation, the distance travelled by the pulse inside the devices and where accessibility were limited, all ignored. These may contribute to net delay in actual pulse measurement.

3.3.2 Capacitor behaviour

The pulse is applied directly to two different capacitors of $1.2\,nF$ (figure 3.15) and $2\,nF$ (figure 3.14). Both resistors of R_p and R_d remain in the system, while the mini-cable is disconnected. Actual capacitor is not ideal and owes stray parameters including a series branch (ESL & ESR) and a shunt conductance (EPR) as depicted in sketch below.

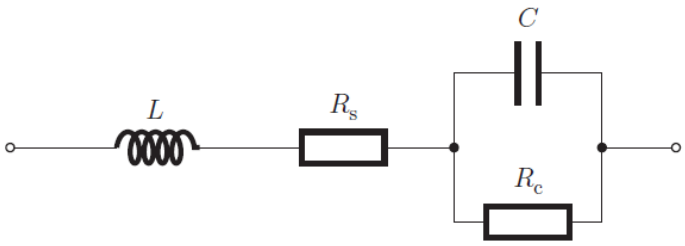

Figure 3.13: Real component model of capacitor for high frequencies [67]

The equivalent circuit of the capacitor is defined as,

$$\begin{aligned} Z_{c,eqv} &= Z_{sr} + Z_{sh} \\ &= \left(R_s + j\omega L_s\right) + \frac{1}{G_c + j\omega C} \\ &= \left(R_s + j\omega L_s\right) + \frac{j\omega R_c C}{R_c + j\omega C} \end{aligned} \tag{3.5}$$

If we neglect the shunt conductance ($G_c = 1/R_c$), the natural frequency (ω_0,), attenuation factor (α) and damping factor (ζ) are derived from the following equations [68],

$$\omega_0 = \frac{1}{\sqrt{L_s C}} \tag{3.6}$$

$$\alpha = \frac{R}{2L_s} \tag{3.7}$$

$$\zeta = \frac{\alpha}{\omega_0} = \frac{R}{2} \cdot \sqrt{\frac{C}{L_s}} \tag{3.8}$$

The initial high voltage spike observed in figures are attributed to a high reflected wave superimposed into leakage inductances voltage.

$$V_0 = j\omega L_s I_0 \tag{3.9}$$

$s = j\omega$ in frequency domain is analogous to time differential d/dt in time domain. Therefore, at high frequencies, where current changes rapidly in time unit, a large voltage is formed in the capacitor in initial moments of injection. Additionally at high frequencies above ω_0 (or ω_r) the load becomes inductive, reflecting a portion of the incident power back at the same polarity. The reflected wave overlay the high initial inductive voltage resembling a spike on the voltage curve.Thus, the voltage spike is proportional to sum of the capacitor leakage (due to the metal foil and bushing), earth-to-earth loop and connector stray inductances $L_{s,sum}$.

Figure 3.14: 2nF capacitor

Figure 3.15: 1.2nF capacitor

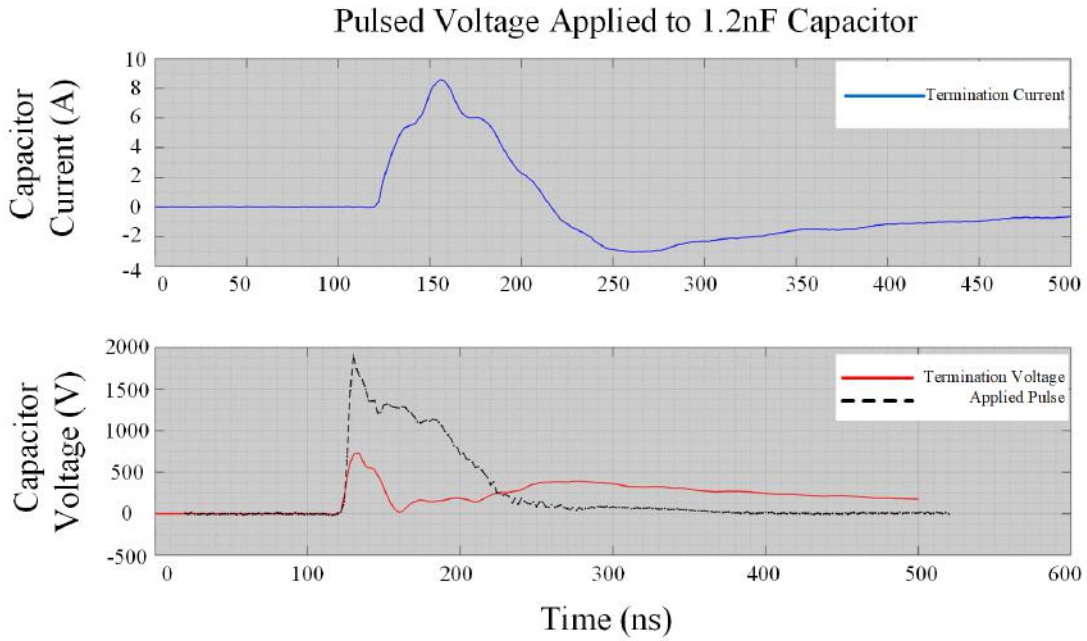

Figure 3.16: Direct pulse application into 2nF capacitor (lab measurements)

$\approx 9\,A$ and $\approx 700\,V$ current and voltage spikes for $2\,nF$ capacitor gives an inductance in order

of 990 nH, however in longer lines the loop inductance practically becomes ineffective. .

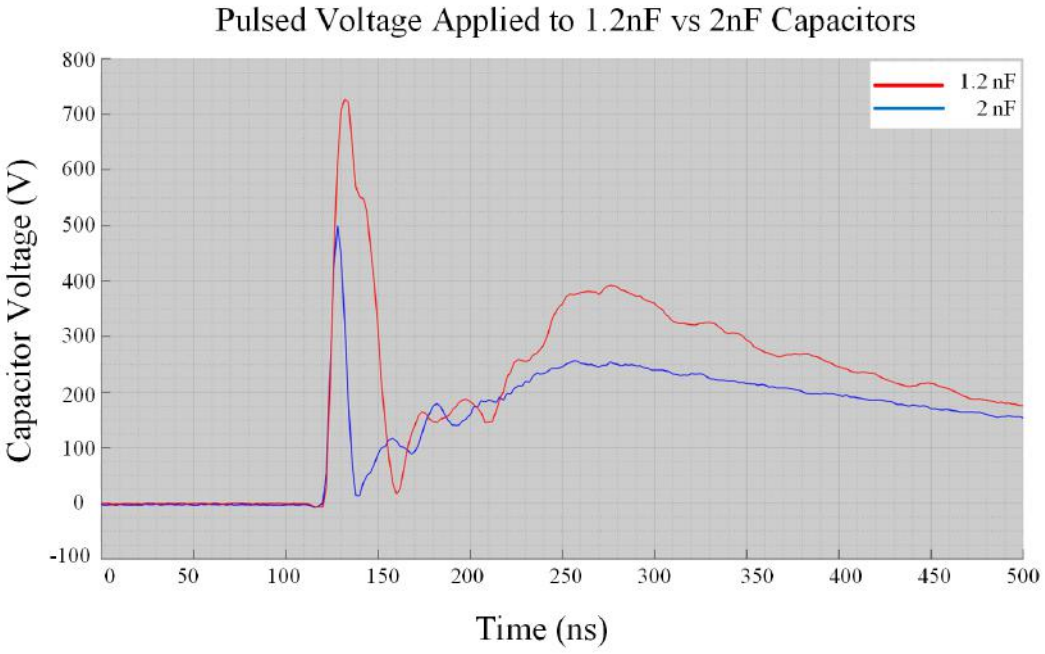

Figure 3.17: Voltage of 1.2 nF *vs* 2 nF *cap (lab measurements)*

After the initial spike, the voltage first rises and subsequently drops following the double exponential function of RLC circuits. Imperfect parameters of the capacitor contributes to the oscillation [67] (equation 3.5 & figure 3.13), specifically on the leading edge of the waveform, as the actual model of capacitor contains also stray inductance. In addition, higher damping and less oscillations is seen when applying 2 nF capacitor instead of 1.2 nF. The higher damping in case of higher capacitance can be justifies knowing that ζ is directly proportional to R_s and $\sqrt{C}$. On the other hand, no significant change in oscillation frequency (peak to peak) is observed, however ω_0 is inversely proportional to $\sqrt{C}$. The reason can be decrease in the stray inductance in case of 2 nF capacitor with respect to its alternative, due to smaller physical size.

3.3.3 SSPI - FLT termination - Injection voltage

If we disconnect the capacitive termination , whereas the measurement table stays grounded, evaluation of termination influence can be better understood (scheme 3.18).

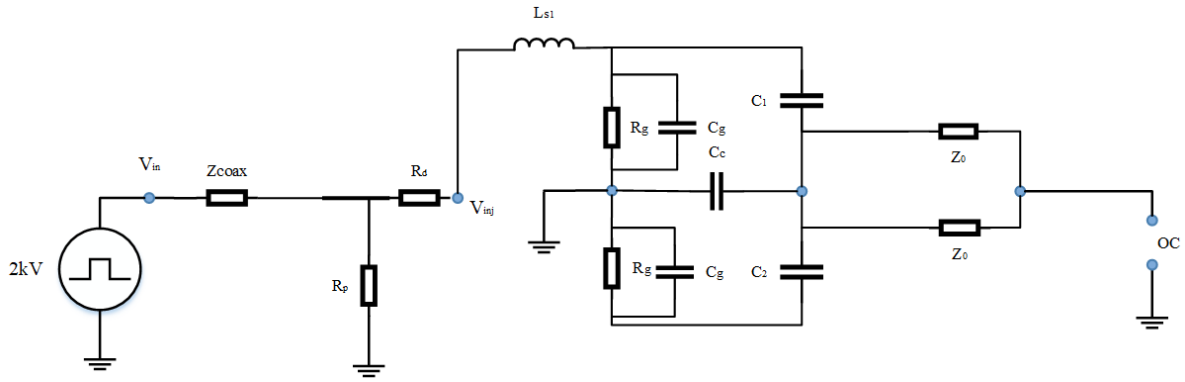

Figure 3.18: SSPI - Circuit configuration - floated termination - GND table

For the rest of the research, the terms floated and grounded are represented by acronyms as FLT and GND respectively.

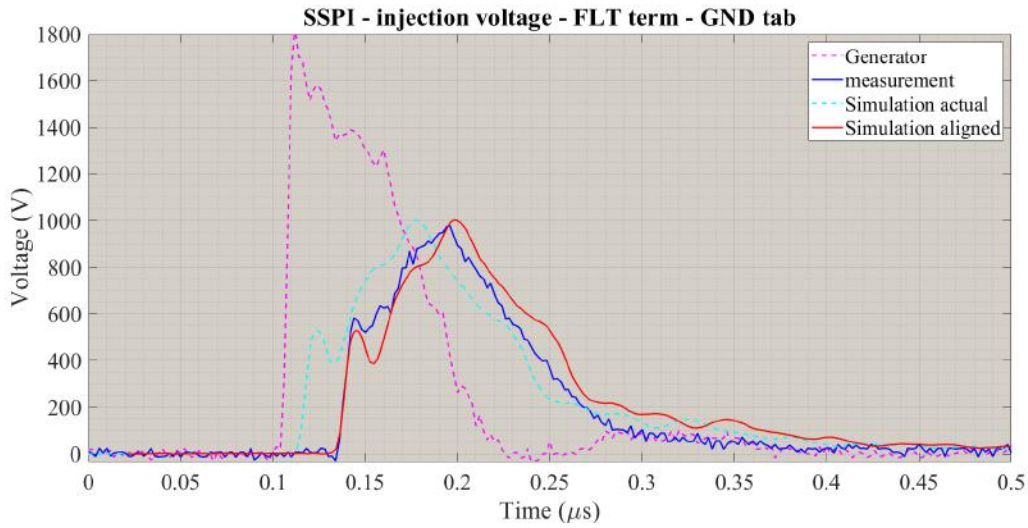

Figure 3.19: SSPI- FLT termination - grounded table - lab measurements vs simulations

As illustrated in graph 3.19, the crest value in the both cases are very close, with the simulated case being slightly higher ($\hat{V} \approx$ 1003 to 984 V, for simulated and measured cases accordingly). As it can be observed, the leading edge undershoot digs deeper in simulation. According to the simulations, the voltage drop on the front edge is originated from immediate pulse reflection when confronting the screen conductor of the mini-cable. Moreover, high frequency noises on the measured pulse bulk are observed that are absent in simulation. Imperfect adherence of the screen conductor to the mini-cable semiconductor layer is the main source of the noises. It is possible that the delay difference between the non-shifted simulated (cyan) and measured (red) curves is because of faster propagation velocity in the modeled $RG-213$ compared to the actual case. As current flowing towards the termination reduces by its disconnection from earth, the

dominant error source should be misapproximation of the cable capacitance by the software (see diagram 3.24).

3.3.4 SSPI - Connected termination - GND table - Injection voltage

In this case the termination including a capacitor of 1.2 nF is connected to the circuit, while the measurement table is grounded (see scheme 3.20). Simulations show that the termination cumulative inductance, $L_{s,sum}$ and resistance $R_{s,sum}$ (Capacitor series resistance and ground connection) are in order of 400 nH and 15 Ω.

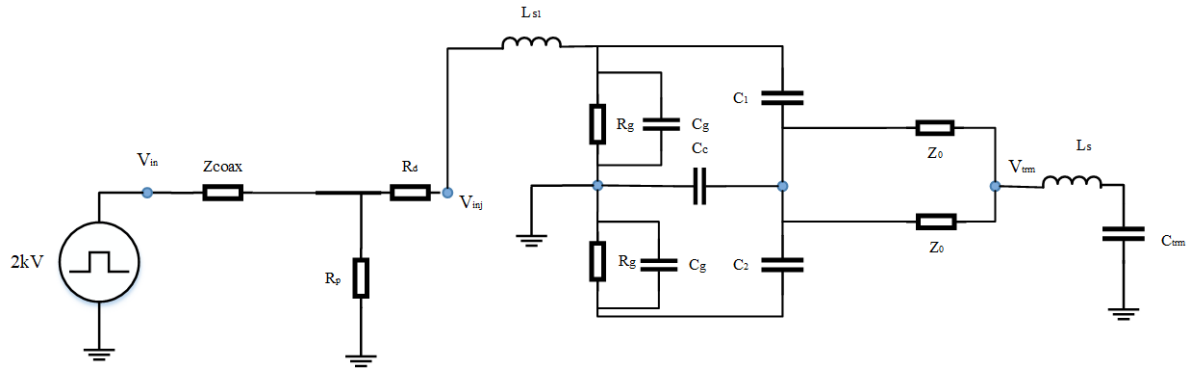

Figure 3.20: SSPI - Circuit configuration - connected termination - GND table

The model seems to overestimate effect of reflections when the travelling wave enters to a medium with different properties. As, in contrary to the previous case, current conveniently flows towards the termination, the braiding error becomes more important. Rise in the characteristic impedance (see diagram 3.23) leads to a general increase in voltage (graph 3.21) and drop in current (graph 3.22) magnitudes, for simulated case compared to the actual measurement. Improvement of this error might be one of the topics for future researches.

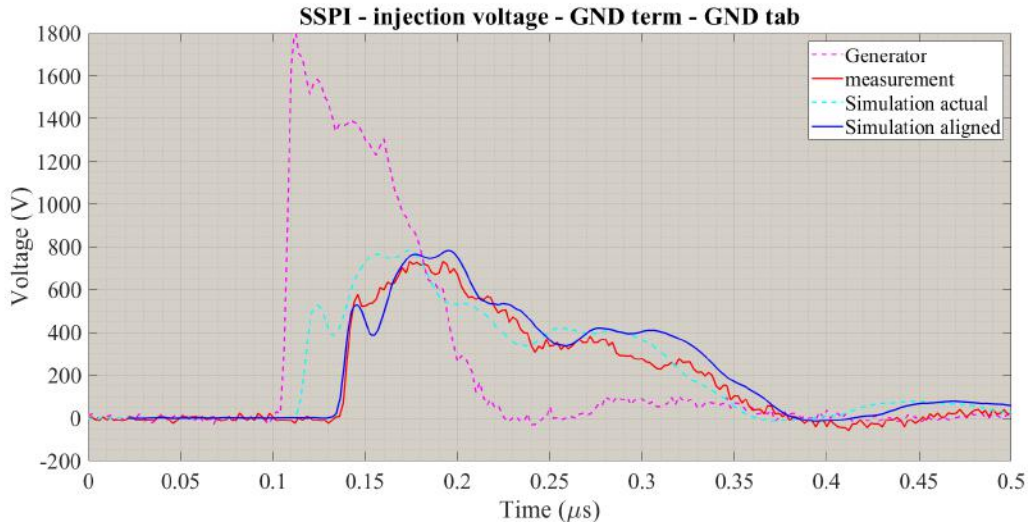

Figure 3.21: SSPI - Injection voltage - connected termination - GND table

Graph 3.22 shows that the simulated termination current resembles the measurements with minor differences. The dashed cyan curve represents the originally simulated current, that leads the red curve by 21 ns. However, a part of this time offset is mainly related to the pulse injection circuit as already discussed. Diagrams 3.21 and 3.22 expose contribution of the mini-cable in the propagation constant approximation inaccuracy. Similar to the termination voltage, a slightly exaggerated reflected wave at the termination show itself on the current curve (on the first peak trailing edge).

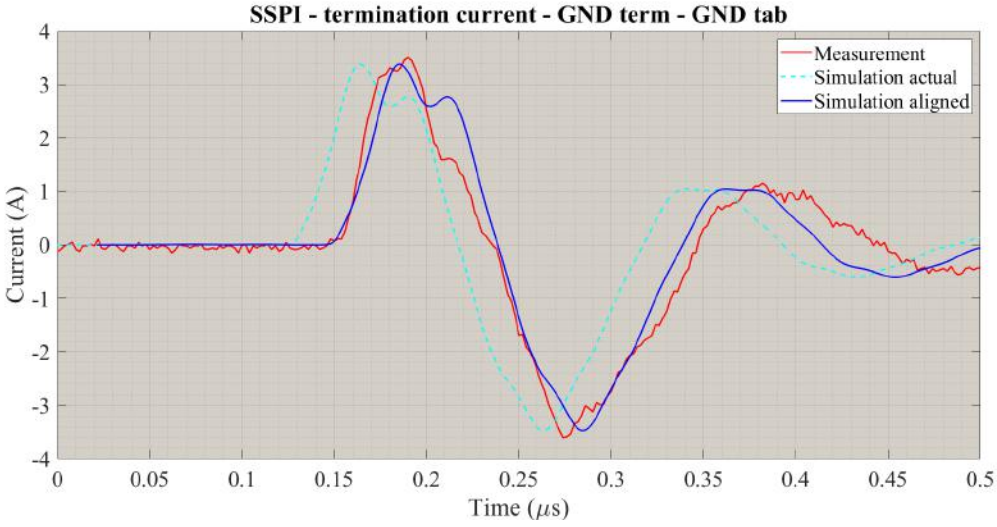

Figure 3.22: SSPI - termination current - connected termination - GND table

Diagrams 3.23 and 3.24 summarize influence causality of braiding of the core conductor and approximation of effective permittivity on inaccuracy in the cable parameter calculation, hence

error in the simulations.

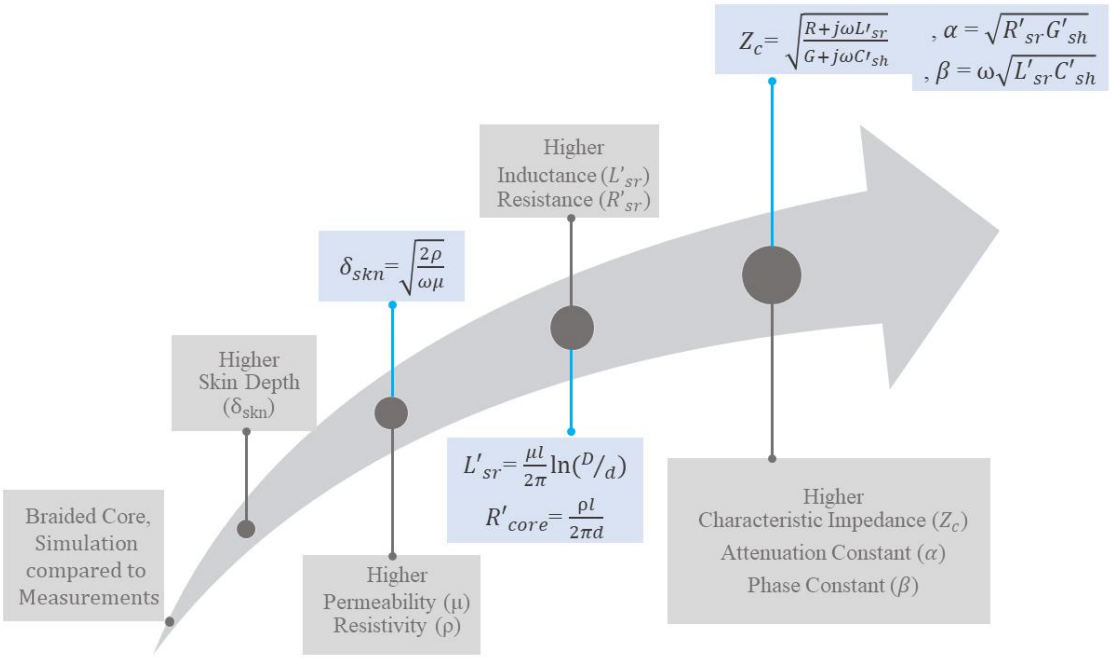

Figure 3.23: Influence of ignoring braided core by model on cable parameter

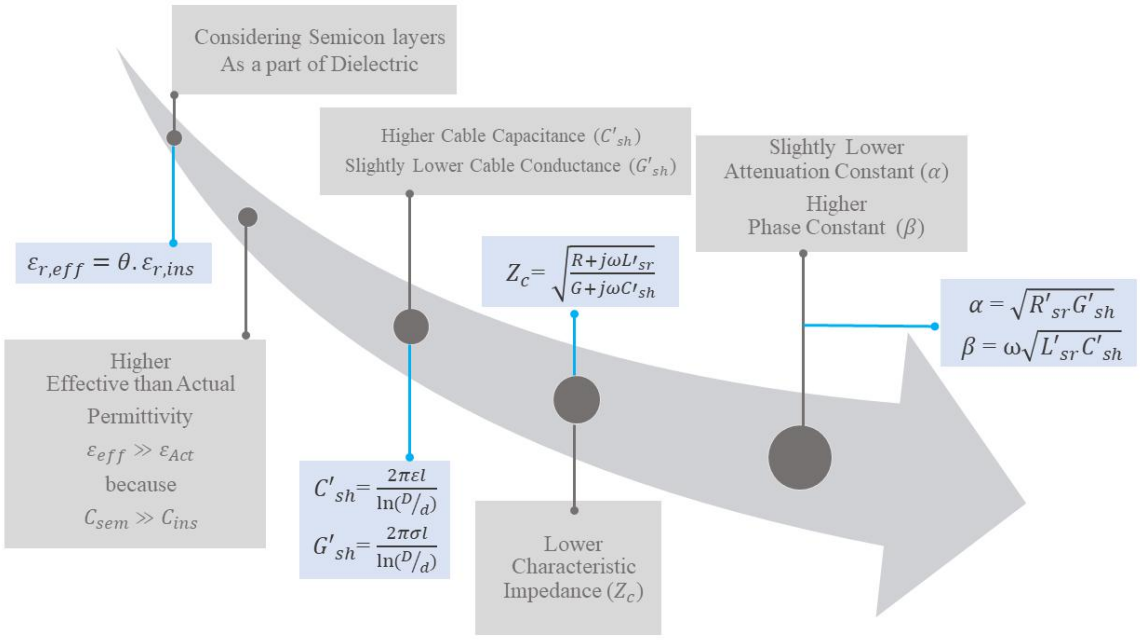

Figure 3.24: Influence of effective permittivity approximation by model on cable parameter

3.3.5 SSPI - Connected termination - FLT table - Injection voltage

By disconnecting the measurement table ground connection, we effectively force the injected current towards the termination (see figure 3.25).

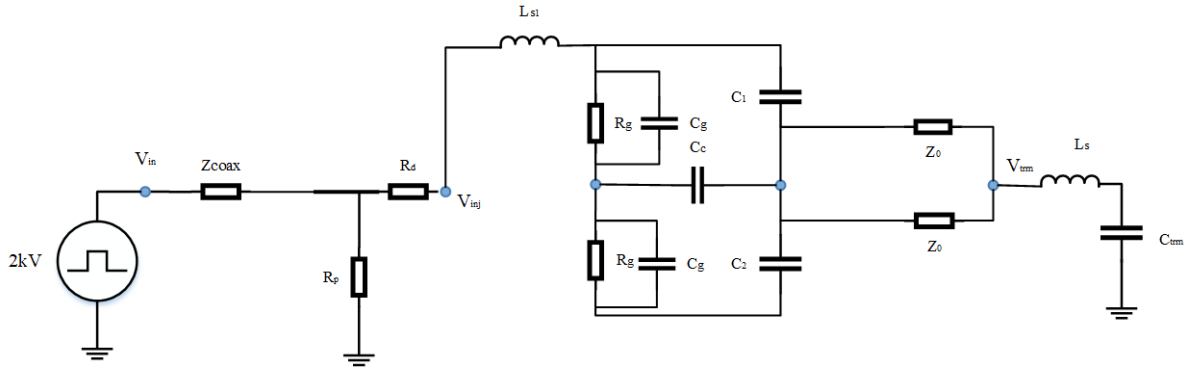

Figure 3.25: SSPI - Circuit configuration - connected termination - FLT table

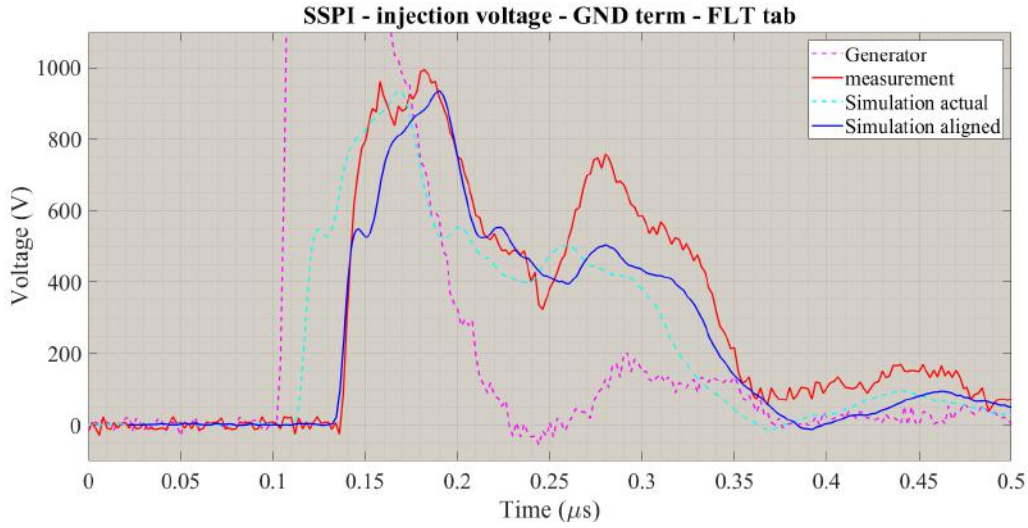

Figure 3.26: SSPI- connected termination - floated table

Graph 3.26 proves that as soon as the current flows more intensively towards the termination, higher error emerges. The reflected wave collapses suddenly in the simulated case with reference to the actual measurement, as overestimation of the cable characteristic impedance would result in underestimation of the cable-termination impedance mismatch. An error in the incident wave leading edge is also observable, that might be due to higher reflection at the injection point.

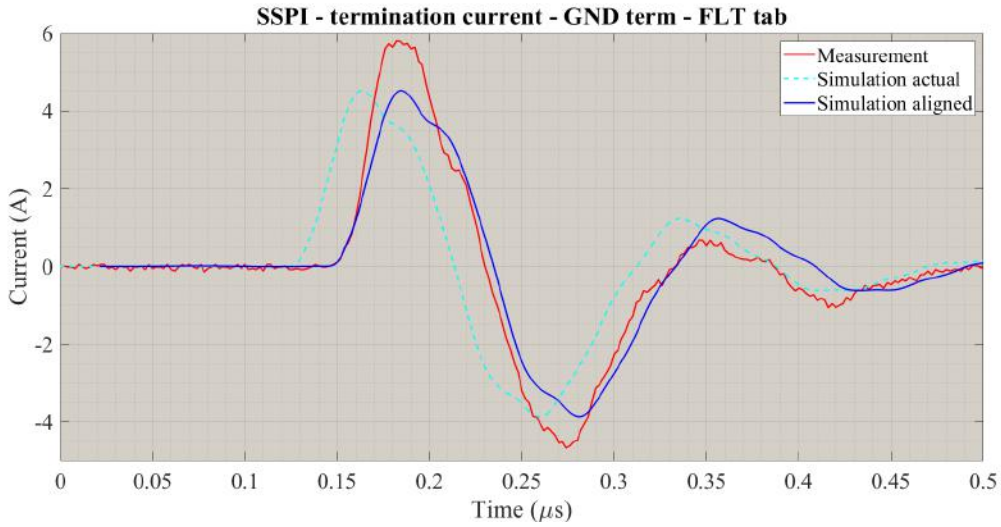

Figure 3.27: SSPI - termination current - GND termination - FLT table

Figure 3.27, also agrees our findings. It can be seen that higher current, in terms of peak magnitude, arrives to the termination.

3.3.6 DSPI - Connected termination - GND table - Injection voltage

In DSPI practice, the pulsed voltage is injected into both sides. In this test, the termination is connected to the circuit while table is grounded (scheme 3.28). In DSPI, in comparison with SSPI practice, current density flowing through each injection spot reduces compared to SSPI as it is split into two parts. Graph 3.29 shows lower velocity of propagation in DSPI compared to SSPI, since the second peak is shifted forward. In addition, the voltage magnitude error increase in DSPI compared to that of SSPI, while the simulated current magnitude error is improved. The reason should be change in configuration of the circuit. Capacitance of two half cables are connected in parallel that is inversely proportional to velocity of wave propagation if we consider the circuit as lumped. The larger value of capacitance is contributed to importance of effective permittivity error (diagram 3.24). Additionally, by current drop, influence of skin effect (diagram 3.23) becomes less important and less ohmic dissipation occurs that leads to higher voltage magnitude. diagram 3.30 shows indicates the similar trend compared to SSPI. however, compared to SSPI, the phase shift deviation from the measured value is marginally higher.

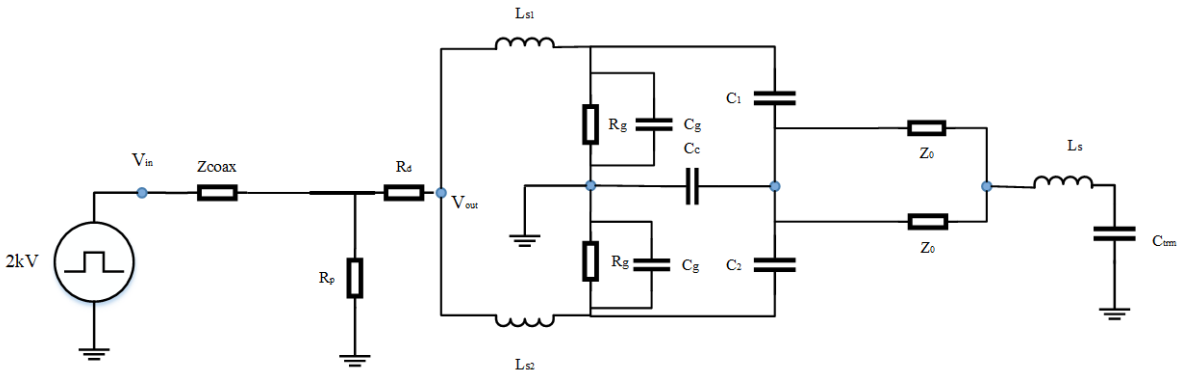

Figure 3.28: DSPI - Circuit configuration - connected termination - GND table

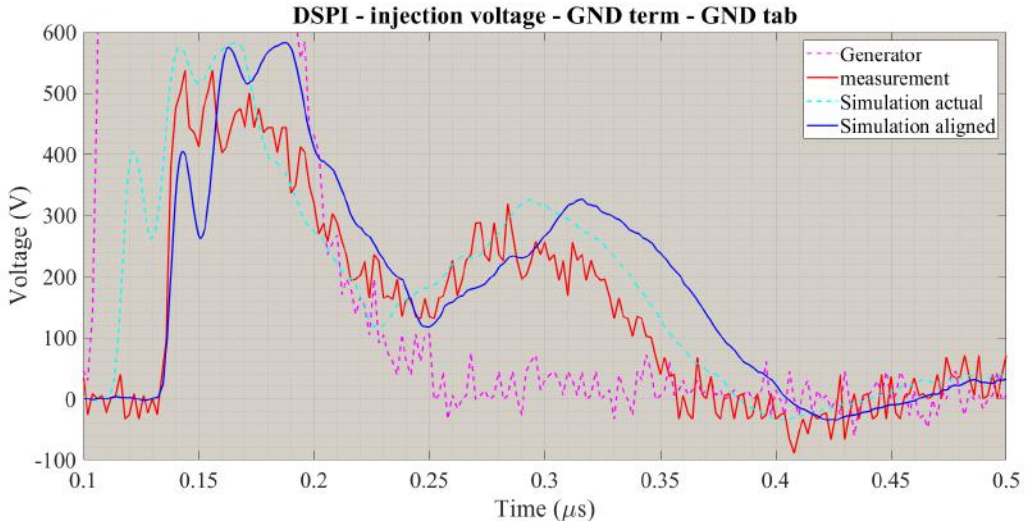

Figure 3.29: DSPI- Injection Voltage - Connected Termination - Grounded Table

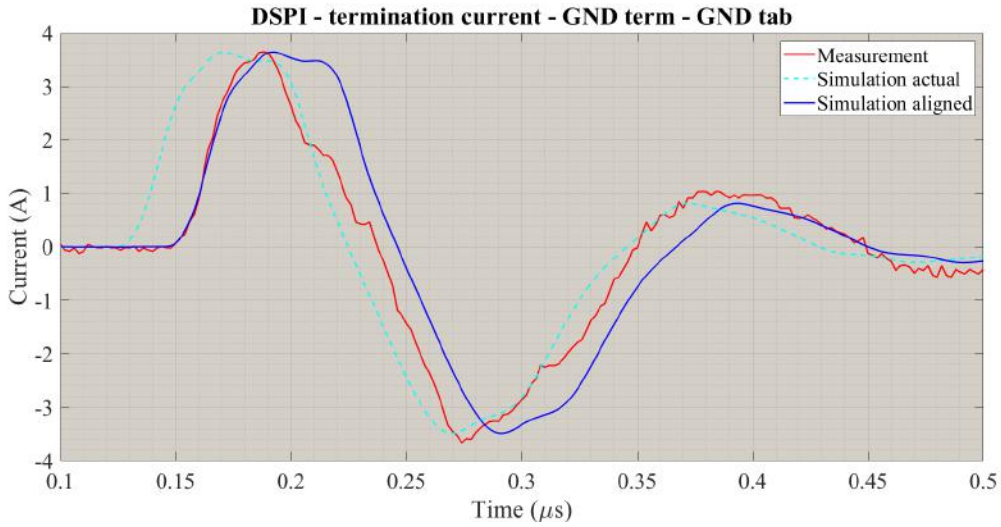

Figure 3.30: DSPI- termination current - connected termination - GND table

3.3.7 DSPI - Connected termination - FLT table - Injection voltage

According to sketch 3.31, the table is left disconnected from earth while termination is coupled to the circuit.

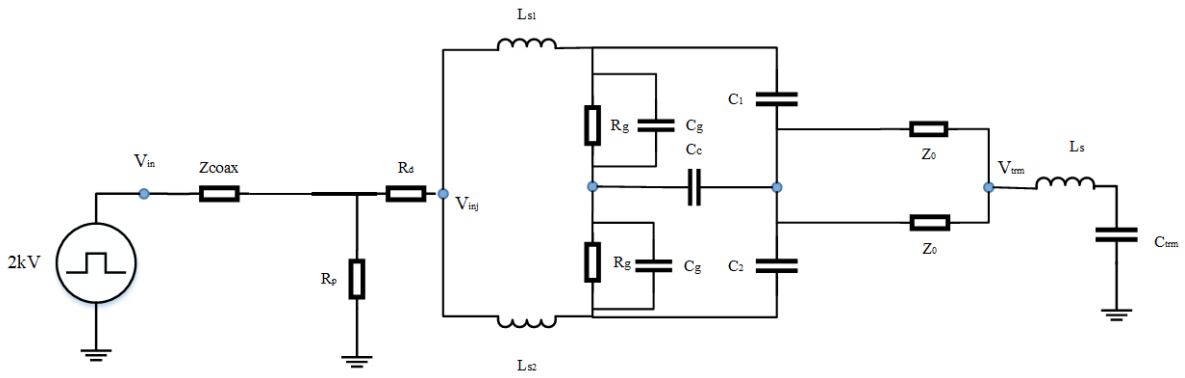

Figure 3.31: DSPI - Circuit configuration - connected termination - FLT table

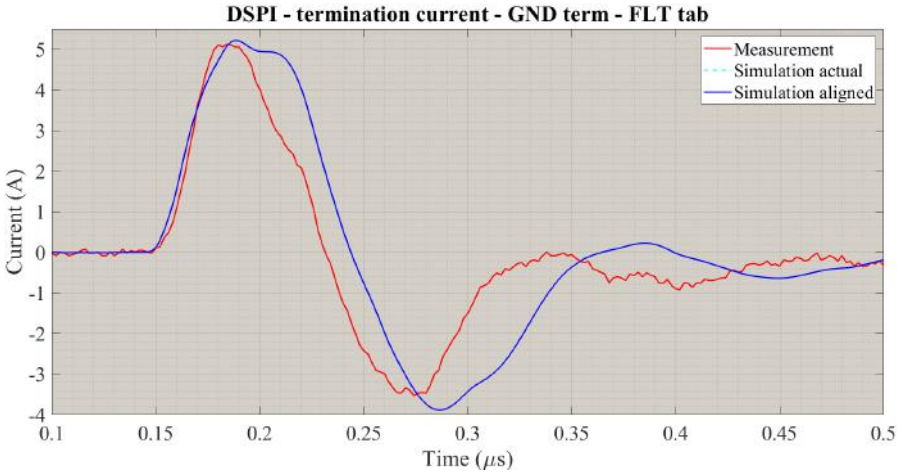

Figure 3.32: DSPI- termination current - connected termination - FLT table

Figure 3.32, similar to SSPI, implies higher frequency shift when more current density propagates towards the termination load.

All the simulated curves by our PSCAD/EMTDC model resembles the same trend as the scoped values in lab, with some differences. In this chapter it tried to discuss the possible reasons behind the observed inaccuracies. In the next chapters, the developed model will be used to explain behavior of the different practices. This model will also be deployed to enhance some features of the four main practices for pulse injection.

4

EXPERIMENTS & CIRCUIT ANALYSIS

In this chapter influence of different parameters on behaviour of the circuit is evaluated. For this purpose a set of tests are arranged (listed in the tables 4.1 & 4.2, mainly focused on DSPI & SSPI, & a few test regarding TPI) in order to achieve better understanding of the testing circuit.

4.1 Theoretical Background

For analyzing such a complex circuit, one has to acquire a profound knowledge on some principle theories, such as voltage/current divider at high frequencies, reflection coefficient and bifurcation rule that are briefly explained in this thesis.

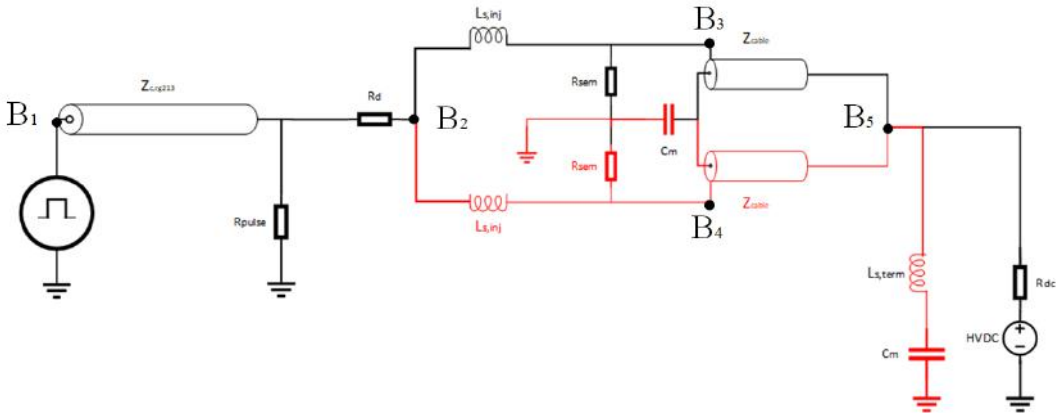

Figure 4.1: Lumped simplified equivalent circuit of SSPI (red path) & DSPI (black & red paths)

- **Cable input impedance ($Z_{in,c}$):**
  When the signal reaches the injection point starts propagating in different directions. Tracking the signal in a complicated circuit with many imperfections and non-linearity's is not easy, specially when the circuit is not lumped anymore and propagation function must

be taken into account in the calculations. At spots B_3 and B_4 (figure 4.11), for both DSPI and SSPI injection practices, the pulse finds two main routes to start propagating.

— A part of the current flowing through the semiconducting layer. After reaching the table, it can either go into the earth (the ground impedance is included) or penetrate capacitively into the cable through C_m, in the latter case a delay is expected due to charging time of C_m though, which is proportional to its time constant τ_{cm}.

— Another part of the current flows through the sound sections capacitance into the core and is split up into two. The first signal split sees characteristic impedance of the cable until reaching the termination load, however along defected parts of the cable (in our case), only the core self-inductance and ohmic losses must be encountered. The second split, again, penetrates capacitively to the table and earth.

Input impedance of the cable is derived as follows (refer to drawing 4.11),

$$Z_{in,c} = Z_c \frac{1+K}{1-K} \tag{4.1}$$

$$\begin{aligned} K = &\left[\Gamma_1 . e^{-2\gamma l_{c1}} + \Gamma_2 . e^{-2(\gamma l_{c1} + \gamma' l_{c2})} + \Gamma_5 . e^{-2\left(\gamma l_{c1} + \gamma'(l_{c2}+l_{c5})\right)} \right] \\ &+ \left[\Gamma_3 . e^{-2\gamma l'_{c3}} + \Gamma_4 . e^{-2(\gamma l'_{c3} + \gamma' l_{c4})} + \Gamma_6 . e^{-2\left(\gamma l'_{c3} + \gamma'(l_{c4}+l_{c6})\right)} \right] \end{aligned} \tag{4.2}$$

in the equation above,

— γ and γ' stands for propagation function along sound cable and uncovered parts.

— l' represents sum of the original length and length of the central part.

$$l'_{c3} = l_{c3} + l_{ctr}$$

— change in propagation velocity in the central part is ignored.

— propagation the propagation velocity inside the sound parts is assumed to be the effective value,

$$\begin{aligned} v_{p,eff} &\approx 1.63 \times 10^8 \, m/s \\ VF_{eff} &\approx 54\% \quad @12.5\, MHz \end{aligned}$$

— propagation velocity along the uncovered parts is assumed to be equal to light speed ($v'_p = c$ or $VF' = 100\%$)

— at fundamental frequency of the injected pulse ($f_0 = \frac{1}{T_0} \approx 12.5\, MHz$), the signal wavelength inside a piece of sound cable is,

$$\lambda_0 = \frac{v_{p,eff}}{f_0} \approx 13\, m$$

while the wave length alters inside solid wires,

$$\lambda_0' = \frac{c}{f_0} \approx 24\,m$$

— electrical length of the circuit at f_0 is calculated as,

$$\begin{aligned} l_{e,s} &= \frac{l_{c1}}{\lambda_0} + \frac{l_{c2}+l_{c5}}{\lambda_0'} \approx 0.14\,m \quad \text{For shorter half} \\ l_{e,l} &= \frac{l_{c3}}{\lambda_0} + \frac{l_{c4}+l_{c6}}{\lambda_0'} \approx 0.25\,m \quad \text{For longer half} \end{aligned} \tag{4.3}$$

— Wave bounce back at the PEA measurement table is ignored.

— The second reflections (marked in red in figure 4.11)

- **Complex reflection coefficient:**
  Impedance mismatches along propagation path of a travelling wave are considered as the main source for multiple reflections. If the source and/or load impedances are complex numbers, according to *Kurogawa 2014* [69] reflection coefficient is calculated as,

$$\Gamma = \left[\frac{Z_l - Z_s^*}{Z_l - Z_s} \right] \tag{4.4}$$

  Therefore a part of the incident wave's power, is reflected back, whose magnitude is obtained from equation 4.5 [70, 71],

$$\Gamma_{pwr} = |s^2| = \left| \frac{Z_l - Z_s^*}{Z_l + Z_s} \right|^2 \tag{4.5}$$

- **Bifurcation rule:**
  When the incident wave collides with a *bifurcation* the following relationships are valid (see drawing 4.2) [72].

$$\begin{aligned} T = \frac{E''}{E} &= \frac{\frac{2}{Z}}{\frac{1}{Z} + \frac{1}{Z_1} + \frac{1}{Z_2} + \frac{1}{Z_3} + \ldots + \frac{1}{Z_n}} \\ &= \frac{2Z_1Z_2}{Z_1Z_2 + ZZ_1 + ZZ_2} \quad \text{(for T-junction)} \\ &= \frac{2Z''^2}{Z''^2 - 2Z''Z} \quad \text{(for T-junction if } Z_1 = Z_2 = Z'') \end{aligned} \tag{4.6}$$

$$\Gamma = \frac{E'}{E} = T - 1 \tag{4.7}$$

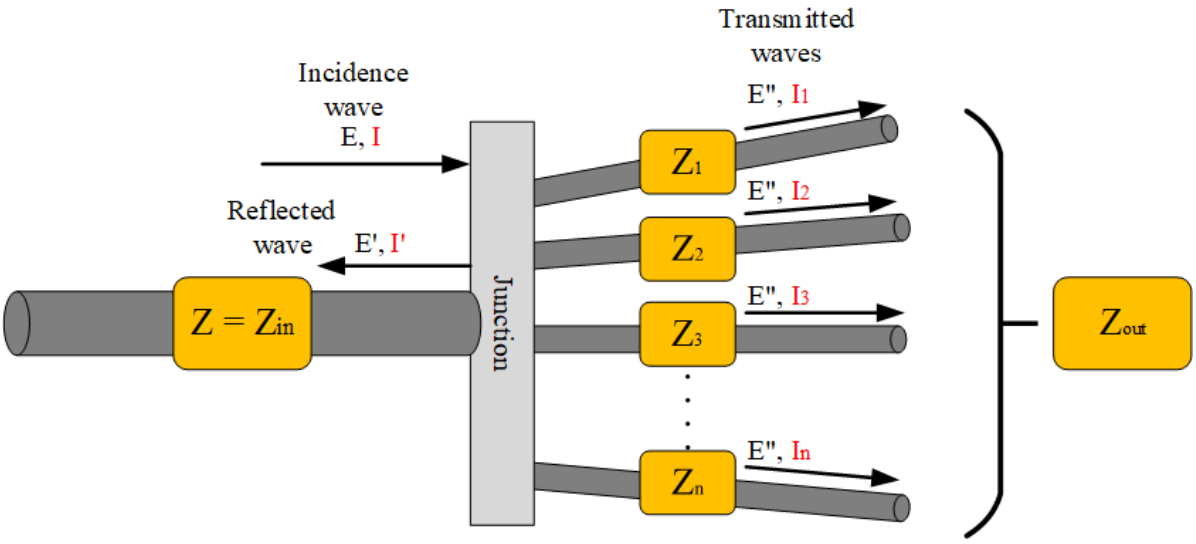

Figure 4.2: Reflection & refraction at a bifuraction

4.2 System Reflections & Oscillations

In order to understand the circuit behaviour first the reflection and transmission coefficients at critical points need to be computed.

1. **HTC transistor switch (B_1):**
   this switch is assumed to work ideal, meaning that after pulsed-voltage creation it acts instantaneously as an open circuit (OC). The reflection (Γ_{B1}) and transmission (T_{B1}) coefficients for the wave reflected back towards the source are,

$$\begin{aligned} \Gamma_{B1} &= 1 \\ T_{B1} &= 2 \end{aligned} \tag{4.8}$$

   it means no voltage is transmitted through the open switch and the entire pulse is reflected back, with the same magnitude and polarity as original incident wave arriving B_2 and it contributes to distortions on the recorded injection pulsed voltage.

2. **Injection point before stray inductance (B_2):**
   assuming the stray inductances to be $L_s \approx 80\,nH$,

   (i) **DSPI:**

$$\begin{aligned} T_{B2} &= \frac{2\,(j\omega L_s)^2}{(j\omega L_s)^2 + 2j\omega R_d L_s} \\ &= 0.0008 + 0.0405j = 0.0405\angle 1.5506 \quad @12.5\,MHz \\ T_{B2} &= 1 + \Gamma_{B2} \\ &= -0.9992 + 0.0405j = 1\angle 3.1011 \quad @12.5\,MHz \end{aligned} \tag{4.9}$$

where Γ and T stand for reflection and transmission coefficients accordingly.

(ii) **SSPI:**

$$\begin{aligned}\Gamma_{B2} &= \frac{j\omega L_s - R_d}{j\omega L_s + R_d} \\ &= -0.9967 + 0.0808j = 1\angle 3.0607 \quad @12.5\,MHz \\ T_{B2} &= \frac{2j\omega L_s}{j\omega L_s + R_d} \\ &= 0.0033 + 0.0808j = 0.0809\angle 1.5303 \quad @12.5\,MHz\end{aligned} \tag{4.10}$$

3. **Injection point at cable screen entrance (B_3 & B_4):**
At B_3 and B_4 reflection and transmission coefficients for DSPI and SSPI are derived as follows,

$$\Gamma_{B3,B4} = \frac{\frac{2}{Z_{Ls}}}{\frac{1}{Z_{Ls}} + \frac{1}{Z_0} + \frac{1}{Z_{sem}}} \tag{4.11}$$

All the below values are calculated, as an example for $12.5\,MHz$ frequency.

(i) **For DSPI:**

$$\begin{aligned}\Gamma_{B3} &= 0.9968\angle -3.1416 \\ T_{B2} &= 0.0032\angle -3.3561 \times 10^{-4} \\ \Gamma_{B4} &= 0.9974\angle -3.1416 \\ T_{B4} &= 0.0026\angle -2.6685 \times 10^{-4}\end{aligned} \tag{4.12}$$

(ii) **For SSPI:**
the configuration only has one injection connection B_3 as depicted in figure 4.11. The values for Γ and T are exactly same as those of DSPI

4. **Termination point (B_5):**
The reflection and transmission coefficients at the point $B5$, where the wave sees an impedance of $Z_{trm} = j\omega L_{trm} + \frac{1}{j\omega C_{trm}} + R_{trm}$ is frequency dependent (see figure 4.4). L_{trm} combination of the capacitor leakage inductance, probable ground loop inductance and coupling wire and bushing self-inductance (ESL). R_{trm} represents ohmic losses of the capacitor (ESR), ground and couplings. The combination is considered as a series resonator RLC circuit [71, 73, 74].

$$\begin{aligned} Z_{trm} &= R_{trm} + j\left(\omega L_{trm} - \frac{1}{\omega C_{trm}}\right) \\ &= R\left[1 + jQ_{sr}\left(\frac{\omega}{\omega_r} - \frac{\omega_r}{\omega}\right)\right] \\ &= R\left[1 + j\theta Q_{sr}\left(\frac{2+\theta}{1+\theta}\right)\right] \end{aligned} \tag{4.13}$$

where θ and Q_{sr} signify per unit deviation from the resonance frequency (ω_r or ω_0) and series resonator quality factor. At resonance frequency where the inductive and capacitive reactances become equal ($X_L = X_C$), the input impedance is purely resistive ($Z_{trm,r} = R_{trm}$) and known as dynamic impedance of the system (figure 4.3).

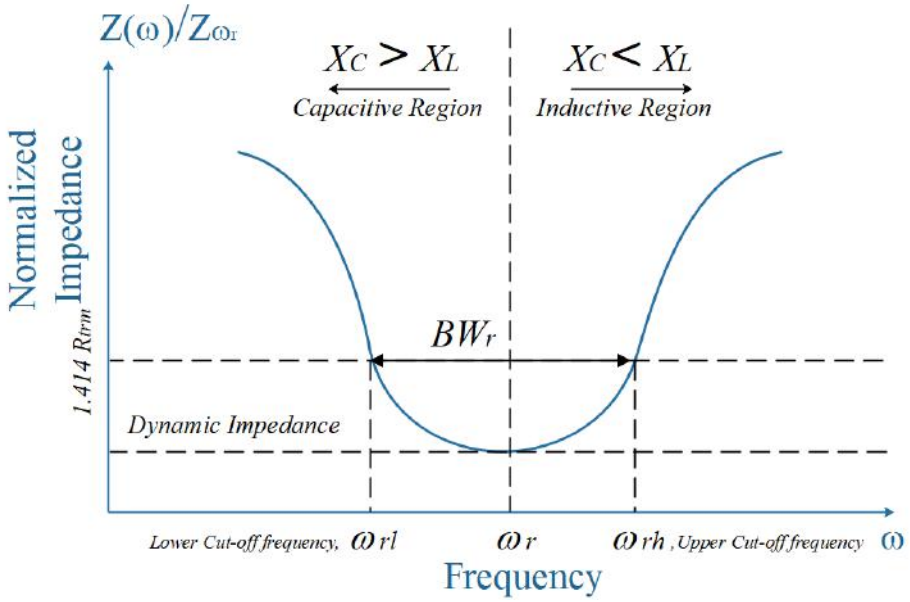

Figure 4.3: Series RLC resonance

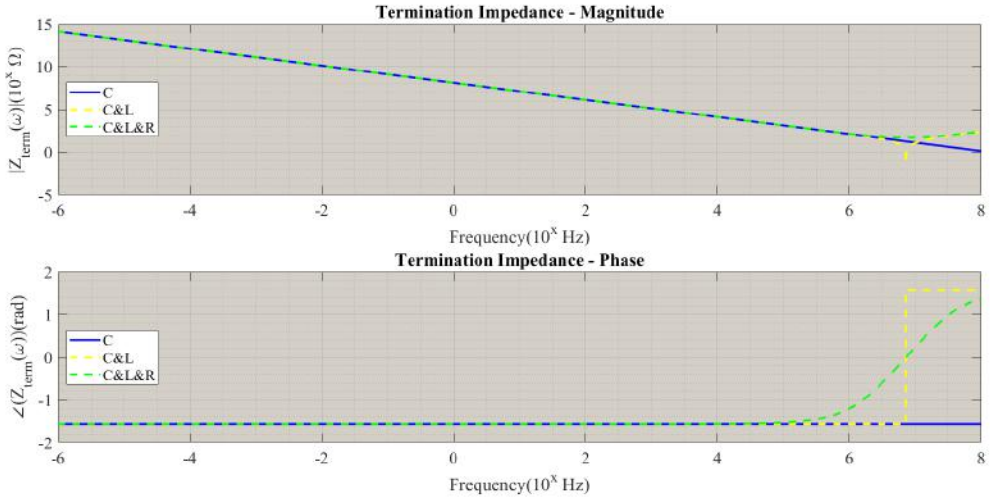

Figure 4.4: Termination Load, ***a)*** *C=1.2 nF,* ***b)*** *C=1.2 nF, L=400 nH,* ***c)*** *C=1.2 nF, L=400 nH, R= 50 Ω (MATLAB Simulations)*

The termination branch initially acts capacitive in lower frequencies up to resonance frequency where it sees a dig being equal to dynamic impedance of the RLC system. After trespassing the border of ω_r the impedance enters the inductive region and impedance amplitude starts rising at higher frequencies in range of tens of MHz up to GHz. As the applied pulse is composed of a wide range of high frequency components, the termination tends to behave inductively. Graph 4.4 reveals that:

— In absence of inductance, no resonance occurs and accordingly the inflection point of the convex disappears. Therefore the line continues falling down, approaching zero at high frequencies.

— Adding a resistance to the electrical mesh, pushes the local minimum spot upwards, as it is governed by dynamic impedance of the system.

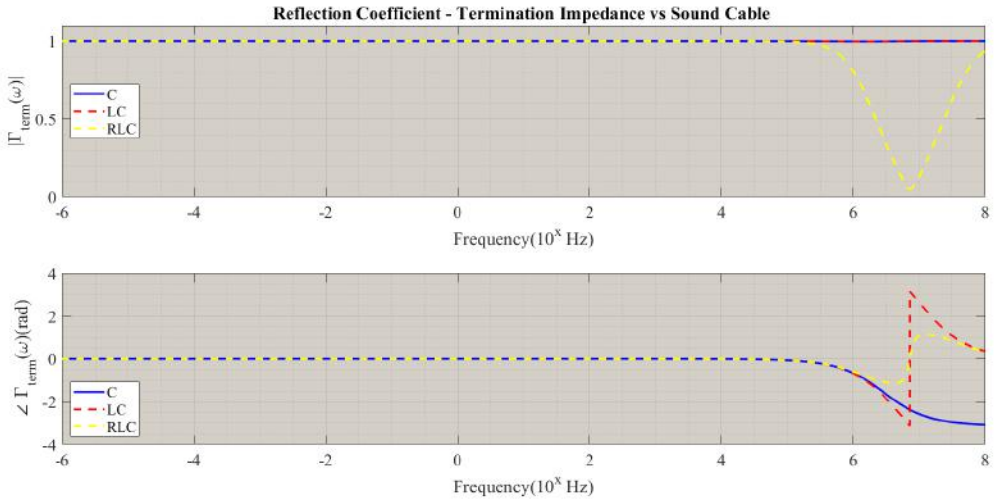

Figure 4.5: Termination Load, ***a)*** *C=1.2 nF,* ***b)*** *C=1.2 nF, L=400 nF,* ***c)*** *C=1.2 nF, L=400 nF, R=50 Ω*

Reflection at the termination, is very dependent on the load nature and source impedances as depicted in figure 4.5. In existence of pure inductance and/or capacitance, full reflection takes place at the spot travelling back towards the injection and scope loci. Polarity of the reflected voltage is defined by the impedance phase. The yellow line implies a considerable reduction in reflection coefficient, specially at high frequencies, when a resistance is added to the termination.

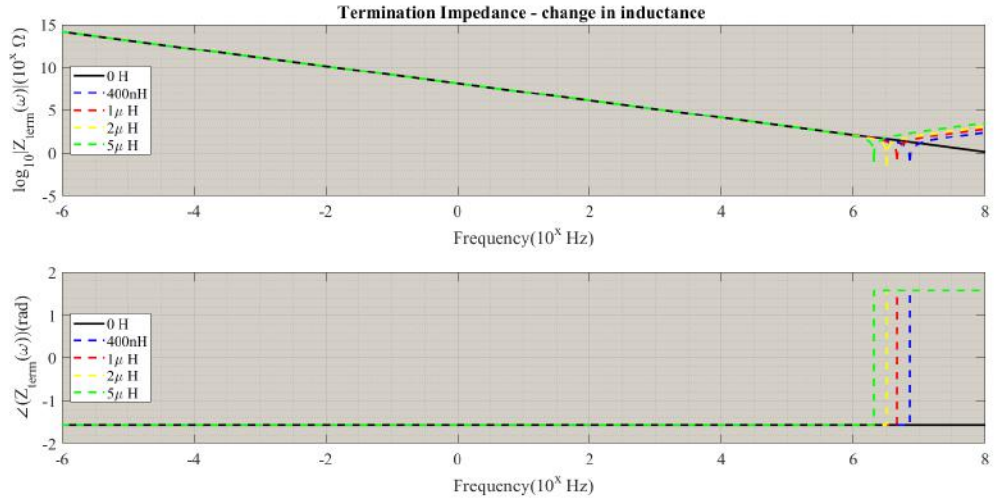

Figure 4.6: Termination impedance at different inductance values, ***a)*** *0 H,* ***b)*** *400 nH,* ***c)*** *1 μH,* ***d)*** *2 μH,* ***e)*** *5 μH (MATLAB Simulations)*

Higher inductive termination leads to a back-shift in ω_r as it is inversely proportional to $\frac{1}{\sqrt{L_{trm}}}$ (see diagram 4.6). The same result is observed for reflection coefficient plus more radical change at higher inductances.

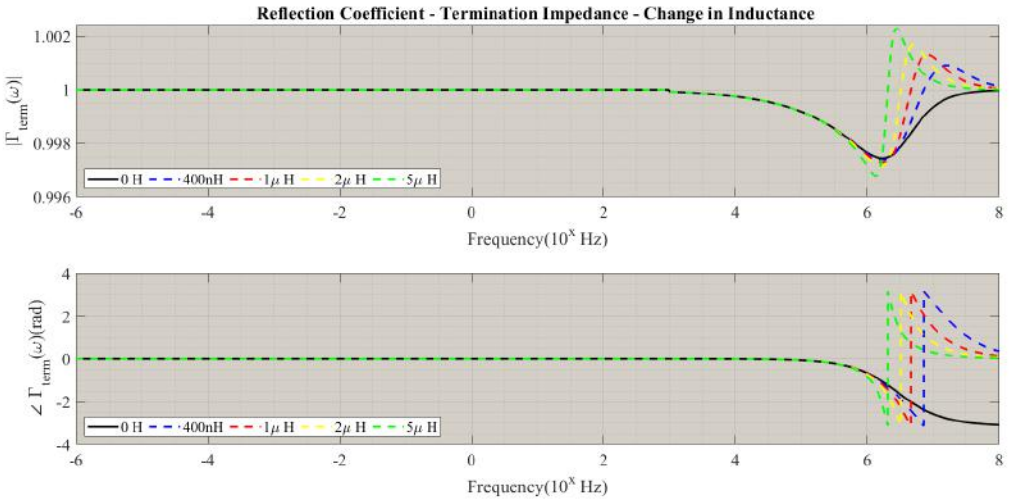

Figure 4.7: Termination reflection at inductance values, ***a)*** *0 H,* ***b)*** 400 *nH,* ***c)*** 1 *μH,* ***d)*** 2 *μH,* ***e)*** 5 *μH (MATLAB Simulations)*

Figure 4.7 and 4.6 declares that when the an electromagnetic wave containing wide range of AC components with different frequencies is applied to an RLC circuit, depending on the frequency, the components are reflected back towards the source at different polarities with reference to the incident wave.

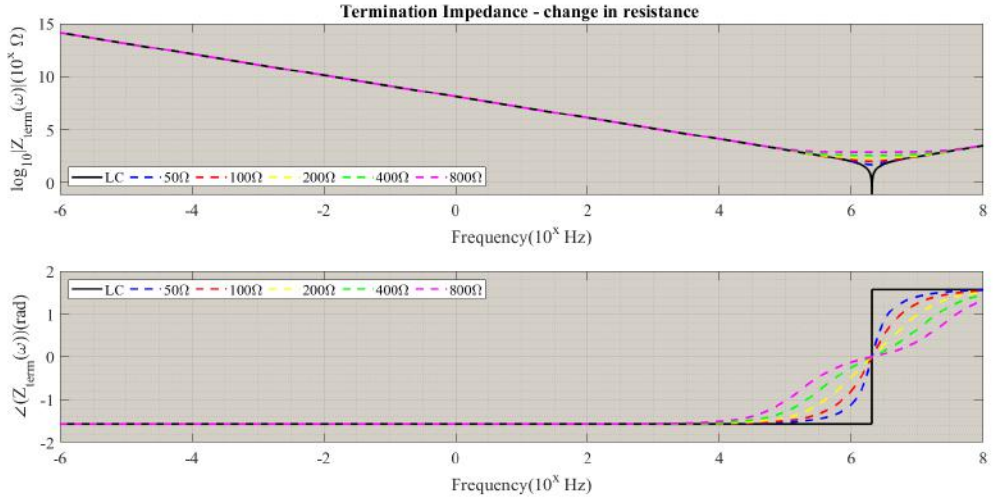

Figure 4.8: Termination Load - Change in resistance, ***a)*** *C=1.2 nF, L=4 μH,* ***b)*** *C=1.2 nF, L=4 μH, R=50 Ω,* ***c)*** *C=1.2 nF, L=4 μH, R=100 Ω,* ***d)*** *C=1.2 nF, L=4 μH, R=200 Ω,* ***e)*** *C=1.2 nF, L=4 μH, R=400 Ω,* ***f)*** *C=1.2 nF, L=4 μH, R=800 Ω (MATLAB Simulations)*

According to graph 4.8, deploying sufficiently large resistance, hence the system damping factor, the transition from capacitive to inductive phase occur smoothly and the local minimum nearly is disappeared.

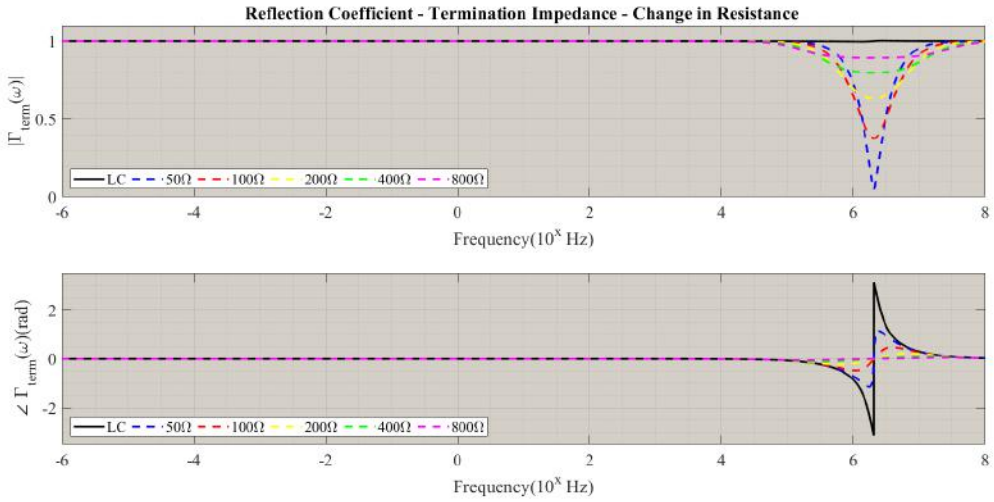

Figure 4.9: Reflection at termination Load - change in resistance, ***a)*** *C=1.2 nF, L=4 μH,* ***b)*** *C=1.2 nF, L=4 μH, R=50 Ω,* ***c)*** *C=1.2 nF, L=4 μH, R=100 Ω,* ***d)*** *C=1.2 nF, L=4 μH, R=200 Ω,* ***e)*** *C=1.2 nF, L=4 μH, R=400 Ω,* ***f)*** *C=1.2 nF, L=4 μH, R=800 Ω (MATLAB Simulations)*

The gradual phase change is also observed in reflection coefficient (figure 4.9), hence the reflected wave magnitude around ω_r collapses to much lower value. In addition, a wider resonance band width (BW_r) acquired when R_{trm} grows, since lower and upper cut-off frequencies are functions of the system resistance,

$$\omega_{lr,hf} = \mp\frac{R_{trm}}{2L_{trm}}\sqrt{\left(\frac{R_{trm}}{2L_{trm}}\right)^2 + \frac{1}{L_{trm}C_{trm}}} \tag{4.14}$$

Quality factor of the resonator Q_{sr} is inversely proportional to BW_r. Considering Lower Q_{sr} is targeted, as less stored energy and more dissipation is desirable. Diagram 4.10 show simulated reflection coefficient at the termination by PSCAD/EMTDC for DSPI pulse injection practice. The uncovered cable acts as inductive series coupling to which a load (termination) is connected in series. It means at very low frequencies we X_c is very high while X_L is very low. Therefore multiple reflection occurs between the termination and exposed part.

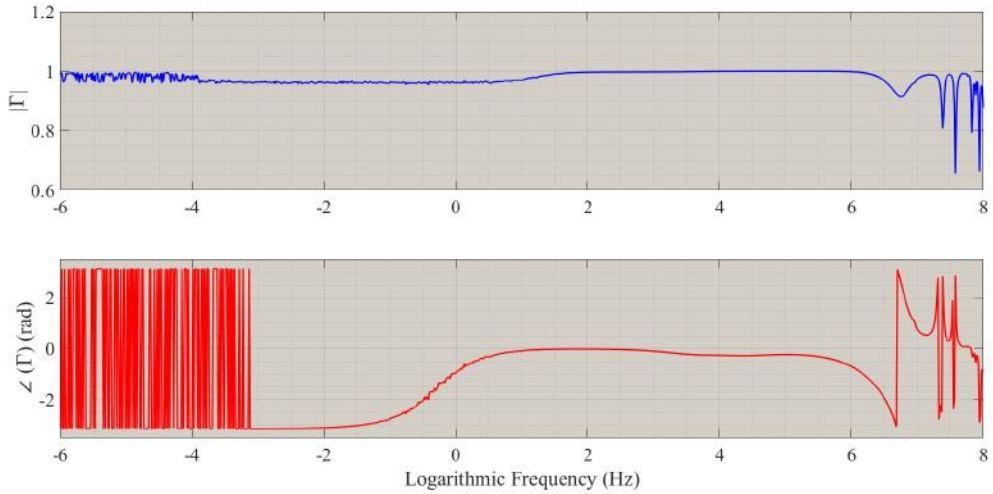

Figure 4.10: Reflection at termination - shorter half- DSPI (PSCAD Simulations)

5. **Uncovered sections:**

In addition to the mentioned junctions, the circuit defected sections can be other sources for reflection(see figure 4.11). The first group include intersection between Z_{c3} and Z_{c4} along longer half and between Z_{c1} and Z_{c2} along shorter half of the mini-cable (Γ_1 & Γ_3 in figure 4.11). Abrupt change in the cable impedance, due to uncovering the screen conductor, is the principle cause for such partial reflections. In fact, in ideal condition where no current penetrates into the outer semiconducting layer, the incident travelling wave observes the peeled part as a wire or inductive discontinuity with very small series ohmic dissipation. The reflected wave appears as an overshoot on the probed values at the injection spot or central section (PEA measurement location). The reflected wave with a pulse width being proportional to $\frac{Z_{c2}}{Z_{c1}+Z_{trm}}$ (if we neglect Z_{c5}) travels back at moment $2\tau_{c1}$ and is superimposed on the recorded waves at injection point[75]. If the inductive is accompanied by a stray capacitance a pre- or post-pulse undershoot is also expected on the recorded waves.

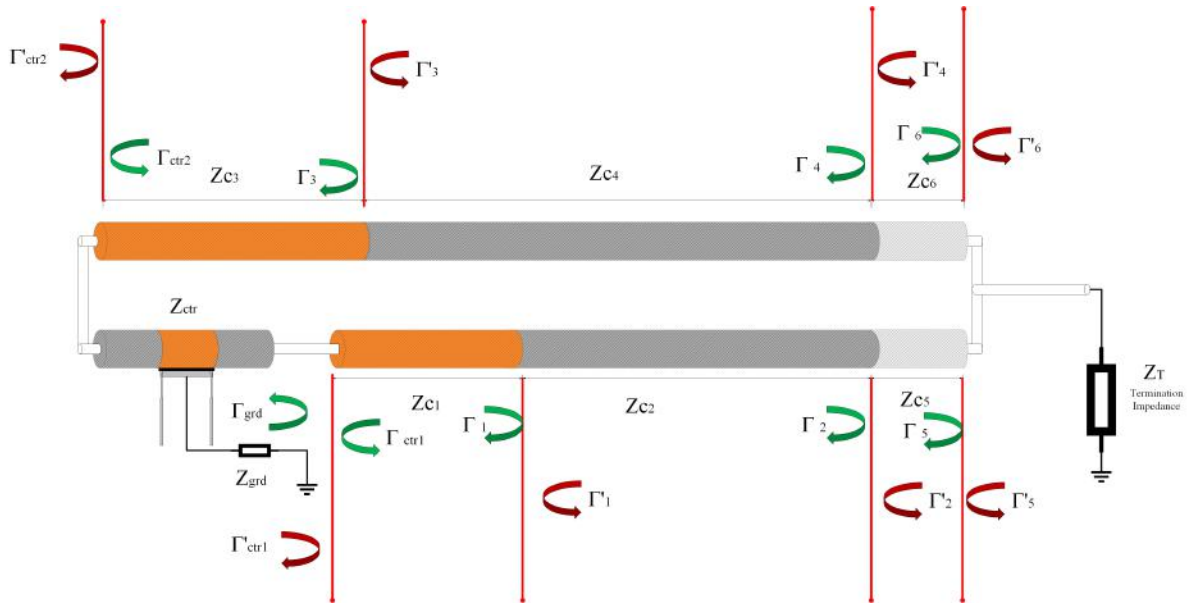

Figure 4.11: Reflections in test circuit

Figure 4.12 describes reflection coefficients at $Z_{c1} - Z_{c2}$ intersection as a function of frequency. The results imply emergence of high and fast oscillation in form of noises and sharp flexes on the probed waves.

The second group of reflected waves include Γ_2 and Γ_4 in figure 4.11. Separating traces of the mentioned reflection with that originated from the termination (figure 4.10) is very difficult due to proximity. As infinitesimally low or zero current is expected to propagate through the outer layer of the exposed part, sections $Z_{C,5}$ and $Z_{C,6}$ can be assumed as a part of $Z_{C,2}$ and $Z_{C,4}$.

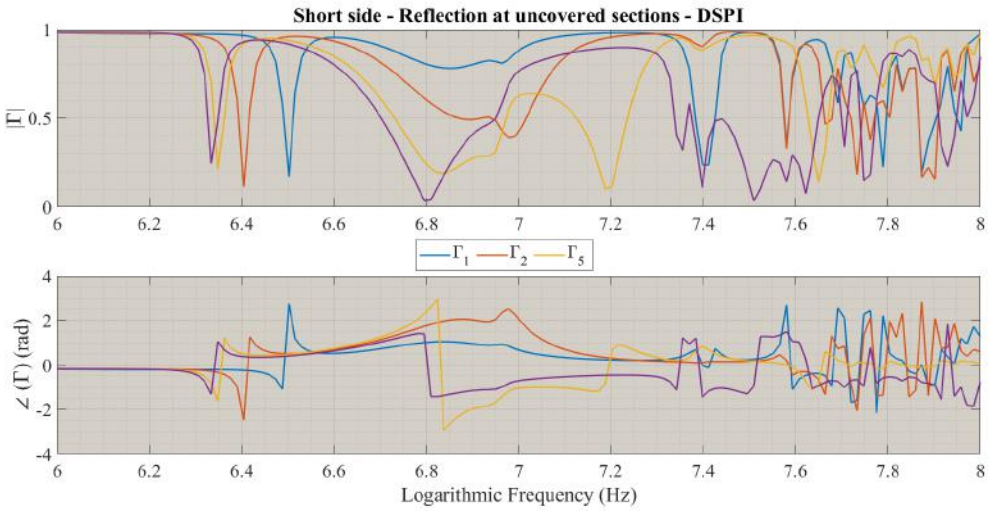

Figure 4.12: Reflection due to screen and semicon removal - shorter half- DSPI (PSCAD Simulations)

Concludingly, distortions on the voltage waveform recorded at the injection cross-point are originated form superposition of many different reflections at different spots of the circuit.

4.3 Experiments at Lab & circuit behaviour explanation

In this section, a group of lab tests are organized in order to understand influence of each element on the circuit behavior as listed in tables 4.1 and 4.2.

No.	Injection	Terminatic	Ext. Screen	Tab. Gnd.	HVDC	HVDC Res.	Voltage	Current
1	NC	✗	✗	✗	✗	✗	Term.	✗
2	DSPI	✓	✗	✓	✓	✓	Inj.	✗
3	SSPI	✓	✗	✓	✗	✗	Inj.	✗
4	SSPI	✗	✗	✓	✗	✗	Inj.	✗
5	SSPI	✗	✗	✓	✗	✗	Term.	✗
6	SSPI	✗	✓	✓	✗	✗	Term.	✗
7	SSPI	✓	✓	✓	✗	✗	Inj.	✗
8	SSPI	✗	✓	✓	✗	✗	Inj.	✗
9	SSPI	✗	✗	✓	✗	✗	Inj.	✗
10	SSPI	✗	✗	✓	✓	✓	Inj.	✗
11	SSPI	✗	✓	✓	✓	✓	Inj.	✗
12	SSPI	✗	✓	✗	✓	✓	Inj.	✗
13 (R.7)	SSPI	✓	✓	✓	✗	✗	Inj.	✗
14 (R.8)	SSPI	✗	✓	✓	✗	✗	Inj.	✗
15	SSPI	✗	✓	✗	✗	✗	Inj.	✗
16	SSPI	✓	✓	✗	✗	✗	Inj.	✗
17	SSPI	✓	✗	✓	✗	✗	Inj.	✗
18	SSPI	✓	✗	✗	✗	✗	Inj.	✗
19 (R.9)	SSPI	✗	✗	✓	✗	✗	Inj.	✗
20	SSPI	✗	✗	✗	✗	✗	Inj.	✗
21	SSPI	✓	✗	✓	✗	✗	Term.	Term.
22	SSPI	✓	✗	✓	✗	✗	✗	Term.1^{st}
23	SSPI	✓	✗	✓	✗	✗	✗	Term.2^{nd}
24	SSPI	✓	✗	✗	✗	✗	Term.	Term.
25(R.21)	SSPI	✓	✗	✓	✗	✗	Term.	Term.
26	DSPI	✓	✗	✓	✗	✗	Term.	Term.
27	DSPI	✓	✗	✗	✗	✗	Term.	Term.
28	TPI	✓	✗	✗	✗	✗	Term.	Term.
29	TPI	✓	✗	✗	✗	✗	Inj.	Term.
30	TPI	✓	✗	✗	✗	✗	✗	Inj.

Table 4.1: Test results at lab

No.	Injection	Termination	Ext. Screen	Tab. Gnd.	HVDC	HVDC Res.	Voltage	Current
31	NC	✓2 nF	✗	✗	✗	✗	Inj.	✗
32	DSPI	✓1.2 nF	✗	✓	✗	✗	Inj.	Inj.
33	DSPI	✗	✗	✓	✗	✗	Inj.	Inj.
34	DSPI	✓1.2 nF	✗	✗	✗	✗	Inj.	✗
35	DSPI	✗	✗	✗	✗	✗	Inj.	Inj.
36	DSPI	✓2 nF	✗	✗	✗	✗	Inj.	Inj.
37	DSPI	✓2 nF	✗	✓	✗	✗	Inj.	Inj.
38	DSPI	✓SG Term.	✗	✓	✗	✗	Inj.	Inj.
39	DSPI	✓SG Term.	✗	✗	✗	✗	Inj.	Inj.
40	DSPI	✓2 nF	✗	✗	✗	✗	Inj.	Inj.
41	DSPI	✓2 $nF + 50\,\Omega$	✗	✗	✗	✗	Inj.	Inj.
42	DSPI	✓2 $nF + 50\,\Omega$	✗	✓	✗	✗	Inj.	Inj.
43	DSPI	✓50 Ω	✗	✓	✗	✗	Inj.	Inj.
44	DSPI	✓50 Ω	✗	✗	✗	✗	Inj.	Inj.
45	DSPI	✓1.2 nF	✓center	✓	✗	✗	Inj.	Inj.
46	DSPI	✓1.2 nF	✓center	✓	✗	✗	Inj.	Inj.
47	DSPI	✗	✓center	✗	✗	✗	Inj.	Inj.
48	DSPI	✗	✓center	✗	✗	✗	Inj.	Inj.
49	DSPI	✗	✓center	✓	✗	✗	Inj.	Inj.
50	NC	✓1.2 nF	✗	✗	✗	✗	Inj.	Inj.

Table 4.2: Test results at lab

4.3.1 Injection voltage - DSPI vs SSPI

The cable input impedance is already discussed in *Theoretical Background Section* of the current chapter. The injection point (B_2) input impedance of SSPI and DSPI practices are compared in diagram 4.13.

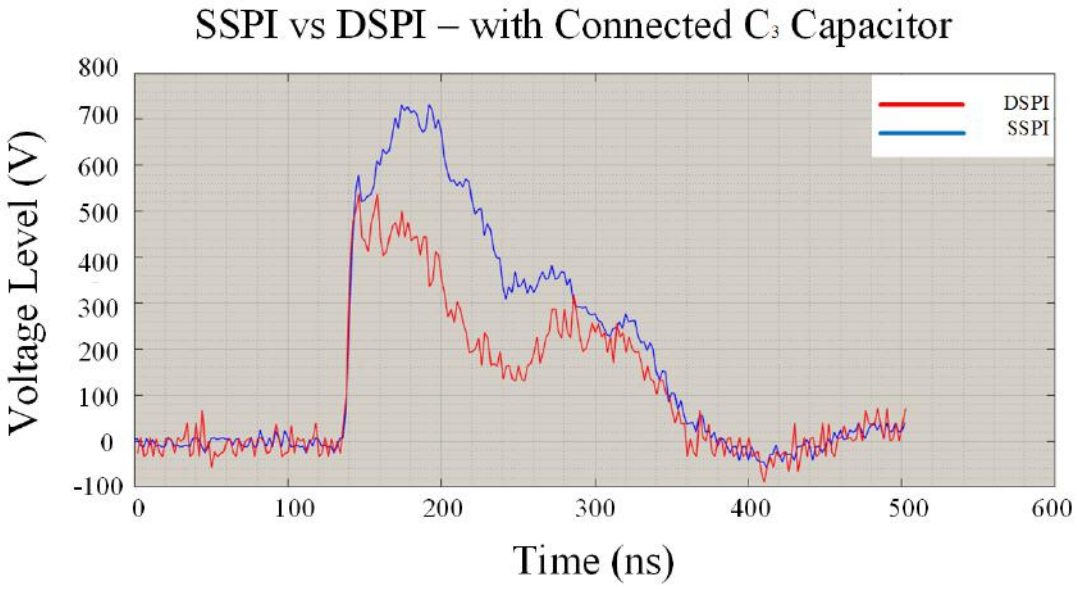

Figure 4.13: SSPI vs DSPI - injection voltage - terminated with cap C_3 (lab measurements)

Considering the same incident current for injection practices of SSPI and DSPI, higher amplitude of SSPI recorded voltage is interpreted to larger input observed impedance for it (diagram 4.14).

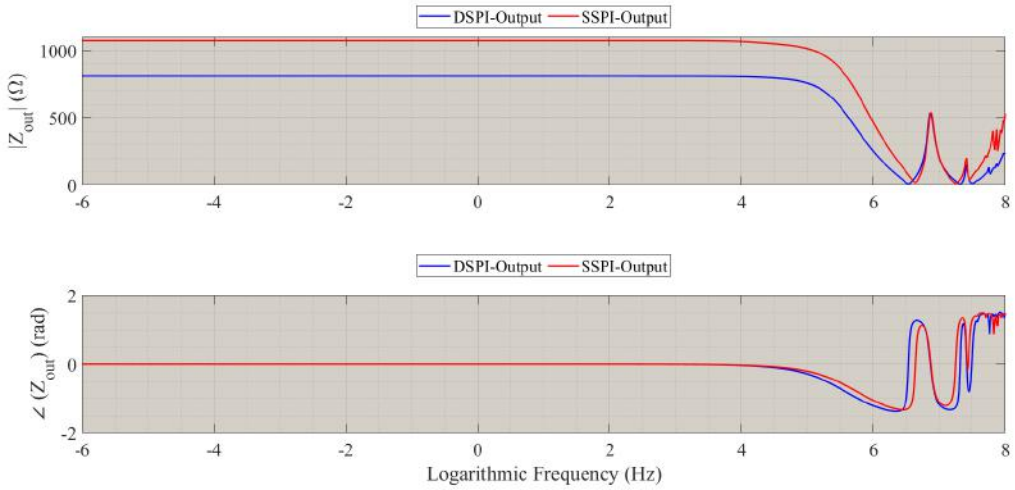

Figure 4.14: Input impedances seen from injection spots (PSCAD simulations)

Capacitive nature of the impedance is changed into inductive around fundamental frequency of the system. It means a large portion of the reflected wave at both cases must have positive polarity, being contributed the recorded voltage crest.

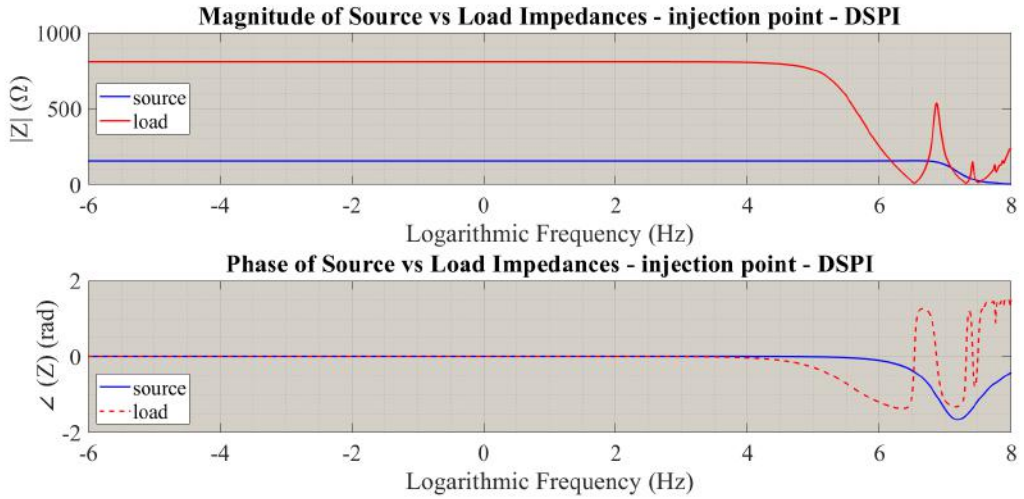

Figure 4.15: Logarithmic frequency dependent magnitude & phase of source & load impedances at injection point - DSPI (PSCAD simulations)

Diagram 4.15 compares DSPI source and load impedances seen from injection point by means of which reflection coefficient is calculated.

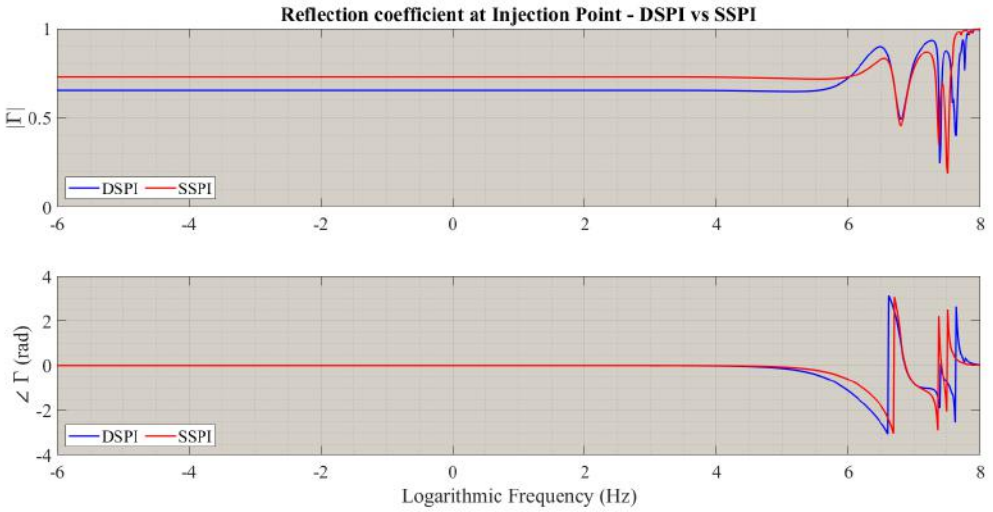

Figure 4.16: Reflection coefficient at power splitter - DSPI vs SSPI (PSCAD simulations)

Figure 4.16 shows reflection coefficients of SSPI and DSPI at injection spot. The figure shows that not all the frequency components reflected back at the same polarity, specially at high frequencies. Although in most frequencies DSPI hold higher reflection amplitude compared to SSPI, at high frequencies DSPI shows a better matching, lower reflection but more resonance quantity at the injection point.

4.3.2 HVDC voltage source

The branch including 50 kV HVDC source and its 3 $M\Omega$ resistor is ignored for most of the tests in this paper. Thus an experiment must be organized in order to show ineffectiveness of the HVDC source existence on the test results. The voltage at the injection point is scoped for SSPI setup (see figure 4.17).

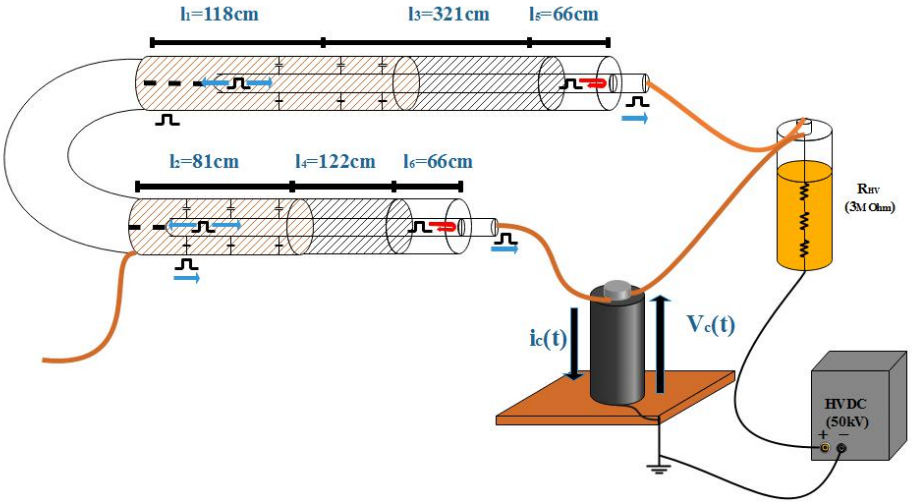

Figure 4.17: SSPI in presence of 50 kV *HVDC source (lab measurement)*

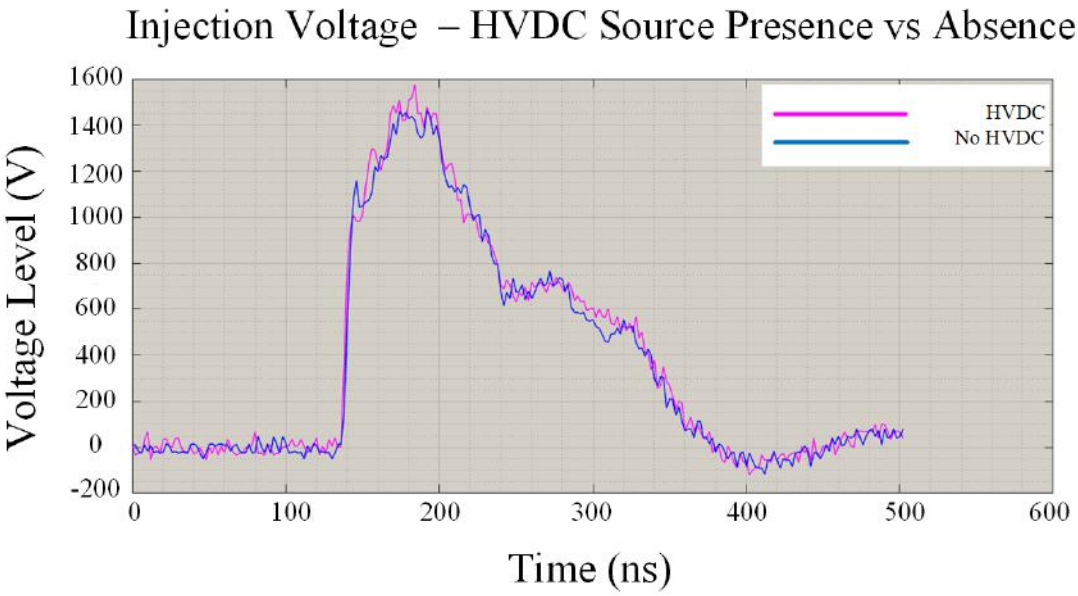

Figure 4.18: Effect of HVDC source on injection point voltage (lab measurements)

It is apparent that by decoupling the HVDC source and its series 3 $M\Omega$ from the circuit, no considerable change is recorded in the injection voltage.

Diagram 4.31 recommends 115 and 174 Ω for the termination and mini-cable (for both DSPI & SSPI) absolute impedance at 12.5 MHz. Applying the well-known current divider formula, only 0.0023% of the current flows through 3 $M\Omega$ resistor, which is negligible. Very similar results obtained when voltages and currents measured at other accessible circuit spots of the circuits. Therefore, all the lab experiments are set in absence of the HVDC source and coupled big resistor.

4.3.3 Screen Extension

As the graph 4.28 illustrates, a wrapped Cu strip plays the role of screen conductor along parts l_1 and l_2. In the sections l_3 and l_4, this conductor is absent. The the main XLPE insulating layers in parts l_5 and l_6 are also exposed. In this stage, effect of shield extension on pulse shape, which is extended one extra meter manually to l_3 and l_4, is assessed. Principally, by the screen layer extension, the capacitance between screen and core conductors through which the injected voltage penetrates capacitively is manipulated. The test is performed for SSPI setup, in presence and absence of the capacitor (figure 4.19).

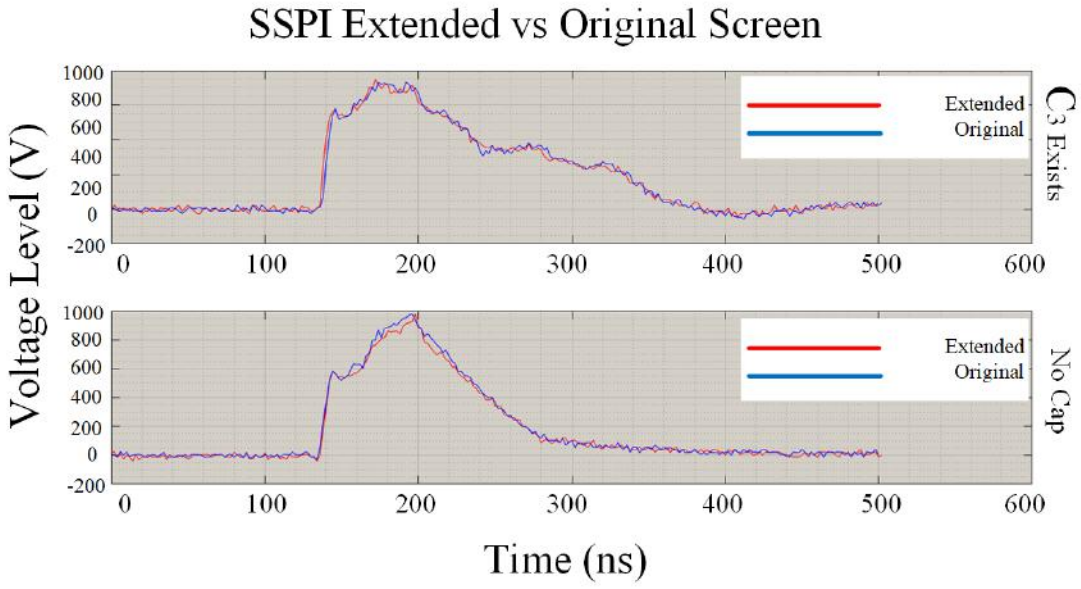

*Figure 4.19: SSPI- Injection Voltage - Effect of extra screen conductor - **a)** with & 4.20 without termination capacitor (lab measurements)*

According to the experiments performed in lab (see diagram 4.19), effect of screen conductor extension is almost negligible in injection point voltage for both connected or disconnected termination.

If the termination is decoupled and the core voltage at the disconnected spot is measured. Diagram 4.20 reveals a voltage rise in case of screen extension. This can be even intensified when the capacitors is connected to the circuit.

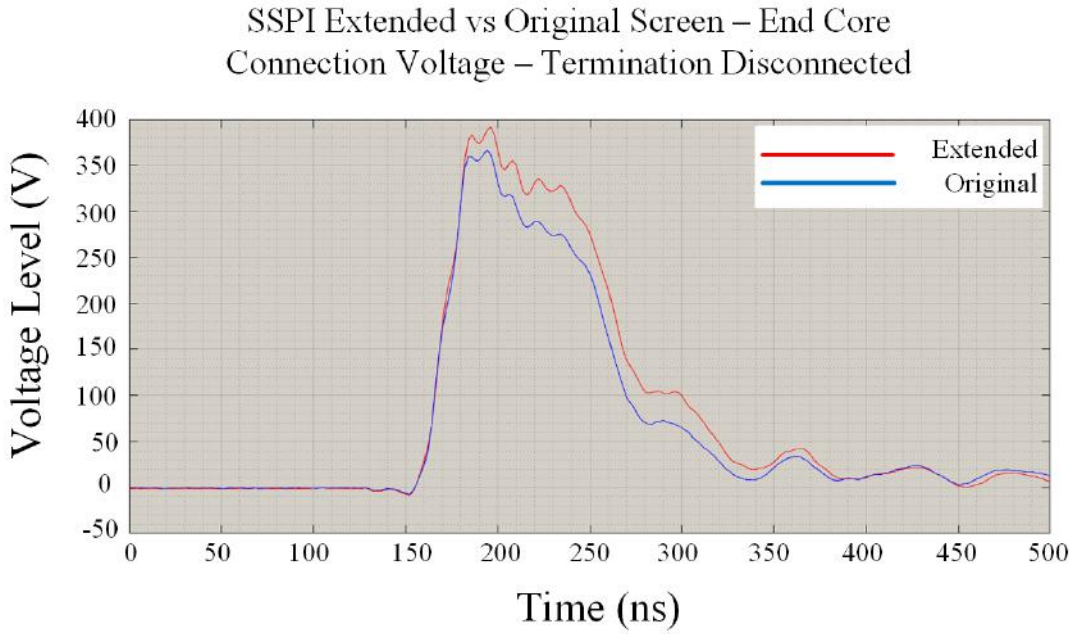

Figure 4.20: Effect of extra screen conductor on pulse measured at core assembly point (lab measurement)

With 1 m screen extension we practically add up a 304 pF capacitance to the cable, while mutual (L_m) and screen self (L_{ss}) inductances grow by 287 nH and 260 pH respectively. This means 3.591 Ω and 0.0038 Ω rise for X_L and X_C respectively at $\omega_0 \approx 12.5\ MHz$. Because cumulative reactance of the cable is derived as $X_L - 1/X_C$ and the inductive reactance growth predominates the capacitive one, impedance magnitude goes up, leading to less current, but higher voltage be formed through the cable.

4.3.4 Central exposed part length

As it is already pointed out, pulsed voltage prohibited from affecting the measurement unit by cutting the outer screen off and exposing the semicon layer, however there will inevitably be remained a minor leakage current propagated through the semicon layer towards the unit. If the gap is sufficiently short, the leakage current can not be considered insignificant anymore. In this part, the influence of the gap's length on injection voltage will be evaluated, by expanding the screen conductor to the center (by shortening the uncovered parts lengths to each 15 mm).

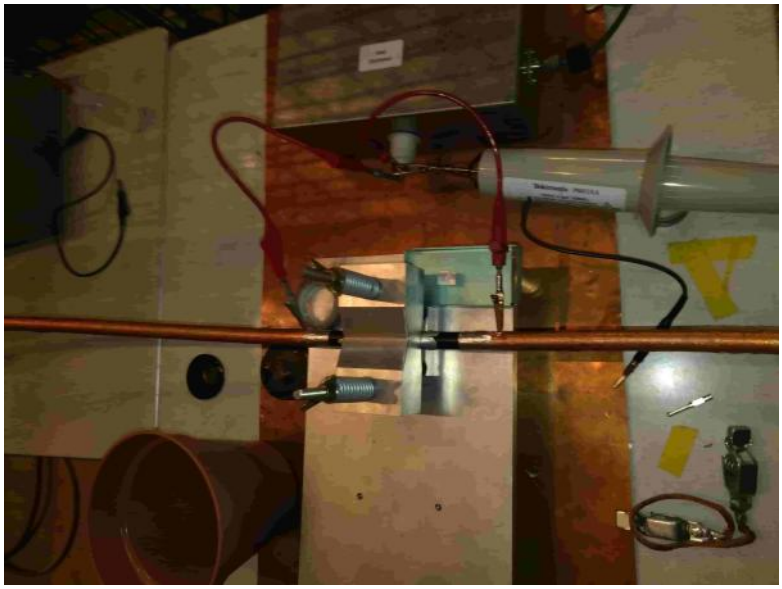

Figure 4.21: Change in center semicon length, lab test

Diagrams 4.22 and 4.23 state that by shortening the central semicon sections,

— Injection voltage descends, whether the cable is terminated or not. The drop is slightly higher decoupled termination.

— High frequency partial oscillations (ringing) appear on the injection voltage front edge.

— Injection current ascends whether the cable is terminated or not. The rise is slightly higher decoupled termination.

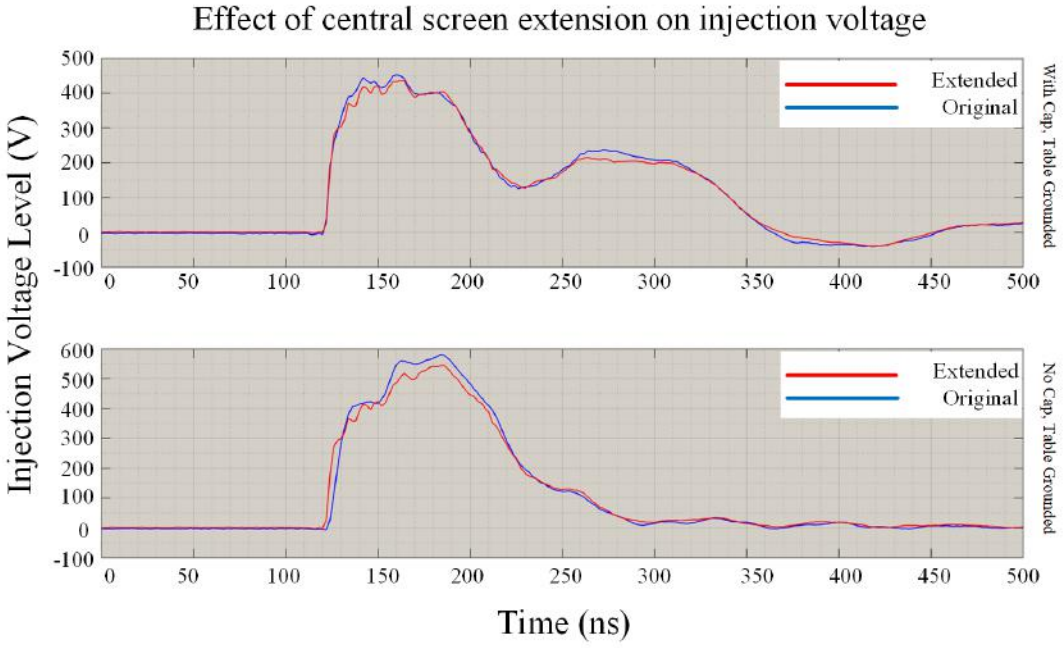

Figure 4.22: Change in center semicon length, injection point voltage, DSPI setup (lab tests)

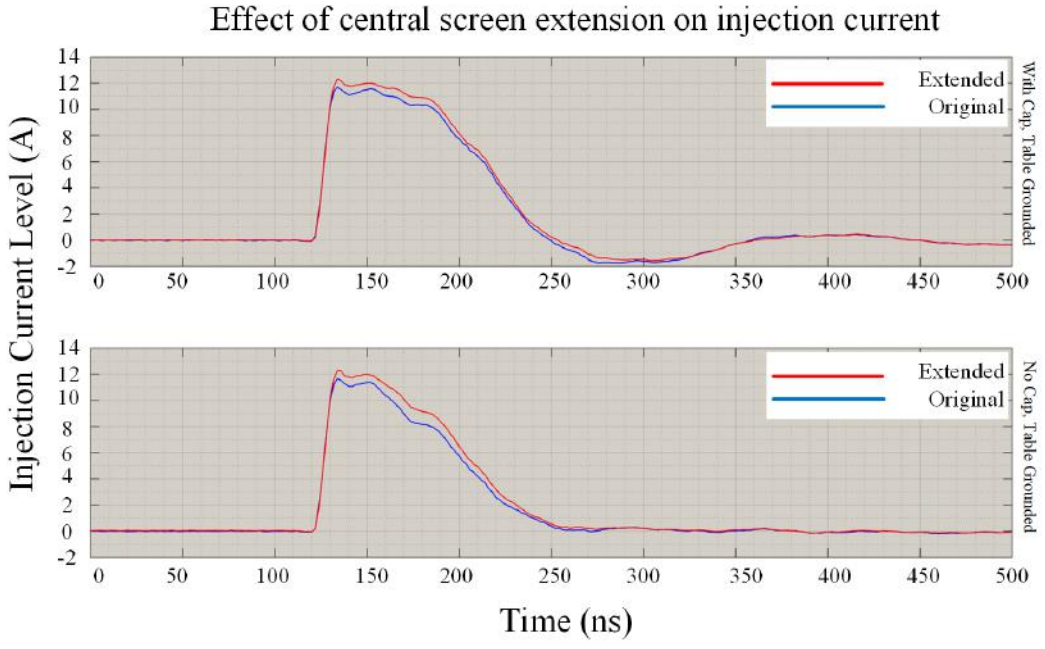

Figure 4.23: Change in center semicon length, injection point current, DSPI setup (lab tests)

The semicon layer acts as a RC parallel circuit, whose impedance changes with frequency. It is charged and discharged with time constant $\tau_{sem} = R_{sem}.C_{sem}$, leading to creation of an oscillating leakage current. Simulation 4.24 proves that at very low frequencies the semiconductor

impedance is resistive, having rather high magnitude, although by increasing the frequency $|Z_{sem}|$ collapses exponentially, so that at frequency span from 10 MHz to 30 MHz, it becomes almost purely capacitive. As it is already discussed, the non-linear behaviour of Z_{sem} is due to frequency-dependence of permittivity and conductivity of XLPE-CB (graphs 2.33 & 2.37).
Diagram 4.24 also reveals that impedance value is directly proportional to the exposed parts length. In this manner, both drop in the injection voltage (graph 4.22) and rise in the injection current (graph 4.23) can be explained. It is also notable that beyond 30 MHz the semiconducting layer resistive behaviour starts being recovered, the impedance magnitude does not differ too much though.

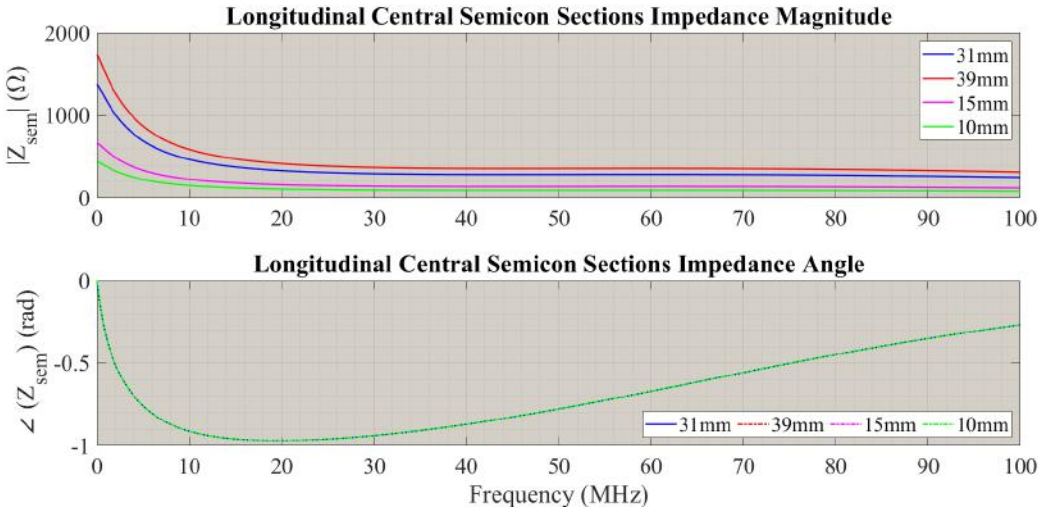

Figure 4.24: Change in center semicon impedance by changing its length (PSCAD simulations)

4.3.5 Termination

As it is already discussed, the termination is considered as the most important origin for reflections, oscillations and wave distortions in the recorded waves. Therefore, multiple lab experiments and simulations are arranged in order to evaluate its behaviour in more detail.

4.3.5.1 Floated termination

As it is observed in figures 4.25 and 4.13, voltage amplitude increases by eliminating one connection, whether the circuit is terminated or not. The reason is the fact that in spite of impedance elevation by disconnecting the termination (see figure 4.26), we limit the current penetration into the mini-cable in practice.

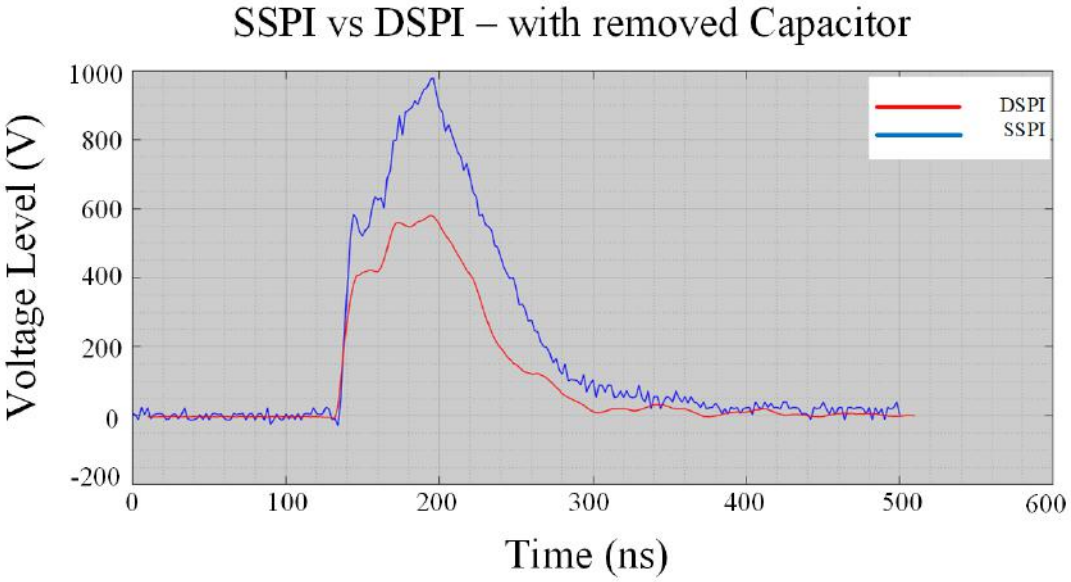

Figure 4.25: SSPI vs DSPI - injection voltage- removed cap (lab measurements)

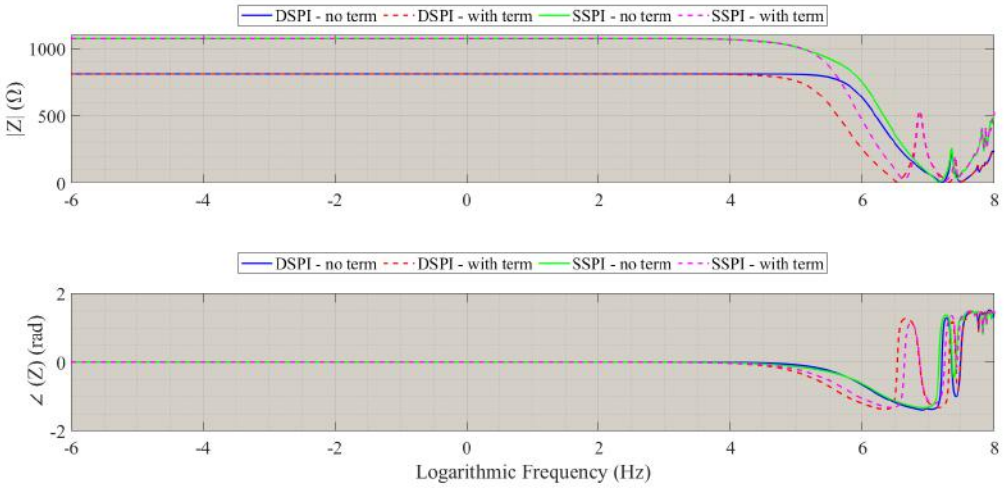

Figure 4.26: Change in input impedance seen from injection point - terminated vs non-terminated (PSCAD simulations)

The second peak disappears by termination removal, proving that the reflection is originated from the mini-cable and its discontinuities. Direction of voltage and current waves inside the mini-cable is simulated as shown in figure 4.27 for SSPI.

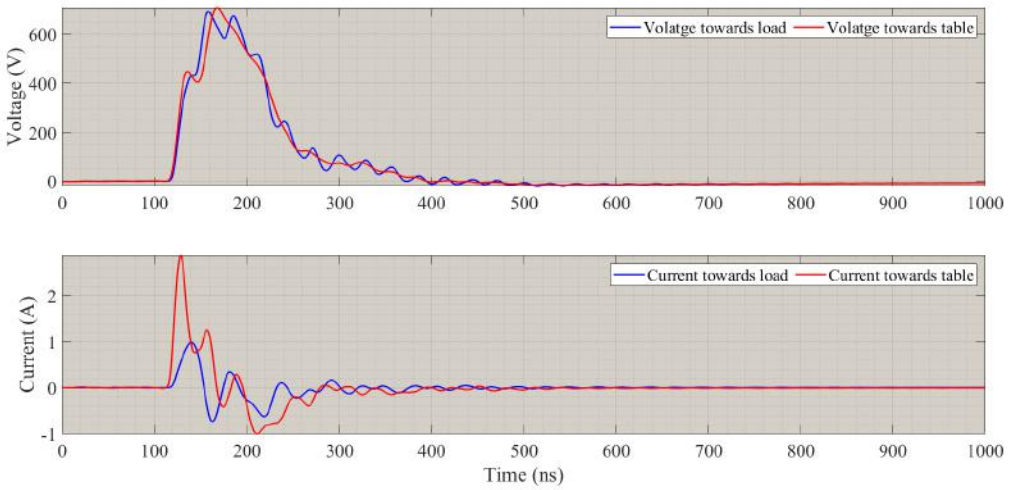

Figure 4.27: SSPI - voltage & current directions- removed cap (PSCAD simulations)

Figure 4.27 states that despite the termination removal, current and voltage waves still propagate into both directions, however current towards table is considerably higher. As a result of the current magnitude slump, the reflected wave is totally vanished.
Figure 4.26 evidences resonance amplitude intensification and quantity growth by terminating the circuit through a capacitor. The other remarkable result is relocation of the fundamental resonance frequency to higher frequencies.

4.3.5.2 Oscillation

Figure 4.28 shows the circuit configuration and directions of injection and termination currents as well as termination voltage. Layers $l_{1,2}$ represent sound cable parts including Cu screen conductor, while in $l_{3,4}$ the screen conductor, and in $l_{5,6}$ the outer semiconducting layer are also uncovered.

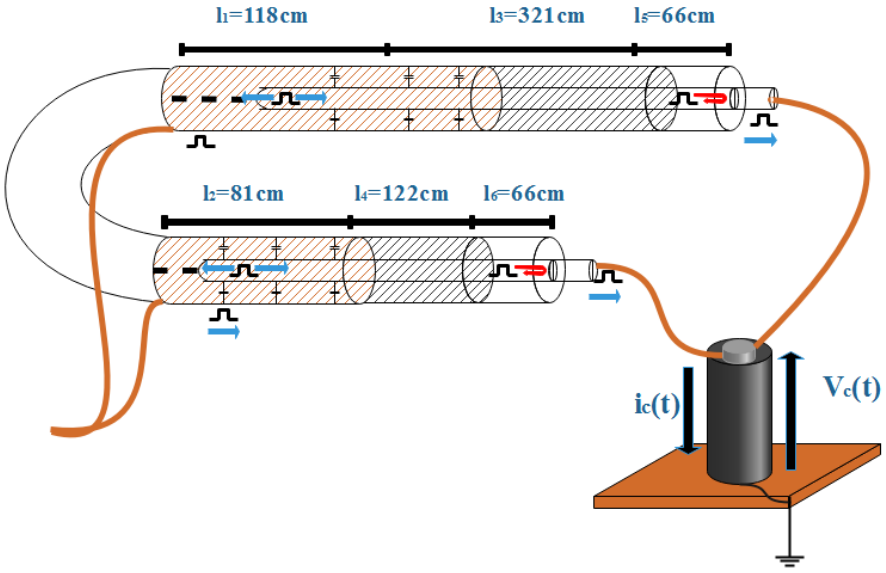

Figure 4.28: Capacitive current flow

When $i_c(t)$ (figure 4.28) enters the termination, an inductive voltage starts being developed, leading the current in phase ($150 < t < 190\,ns$, diagram 4.30 & 4.29). Accumulation of electric charges in the inductance gives rise to the voltage that tops at $\widehat{V}_L$ ($180 < t < 190\,ns$, figure 4.29). The crest value is a function of the termination inductance (L_{trm}) and the current gradient in time domain ($di_c(t)/dt$). As the applied square pulse can be decomposed into infinite number of sinusoidal components, one has to consider contribution of different frequencies in the resultant voltage. According to the superposition theorem, all the voltages can be summed up. Subsequently, the current starts charging the capacitor, where slope of the injection current is revered ($190 < t < 275\,ns$, diagrams 4.30 & 4.29).

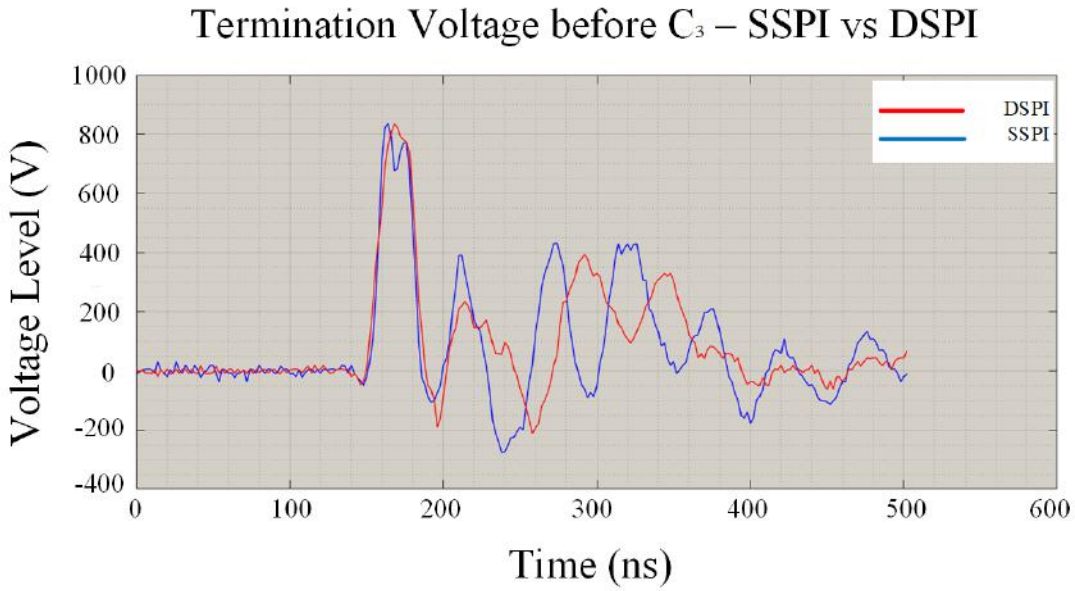

Figure 4.29: Termination capacitor voltage, SSPI vs DSPI - table grounded (lab measurement)

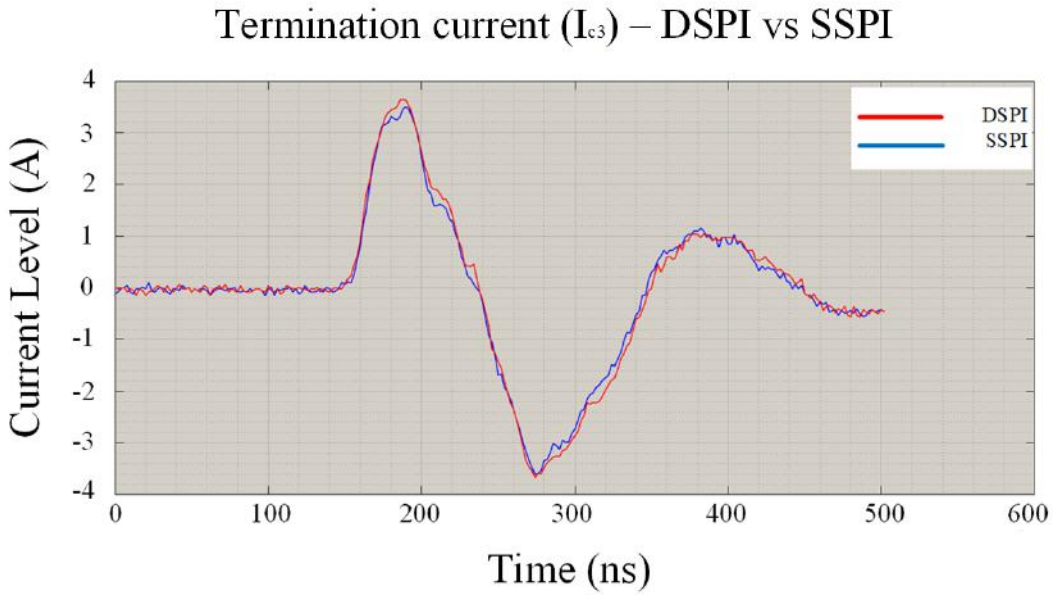

Figure 4.30: SSPI vs DSPI - capacitor current (lab measurement)

Figure 4.29 exhibits oscillation of the termination voltage in presence of a capacitive load for both SSPI and DSPI. The both configurations have under-damped oscillatory behaviour, with DSPI having higher damping frequency [76]. The unloaded (no connected cable) damping of the

termination is approximated as follows,

$$\zeta_{trm} = \frac{R_{trm}}{2}\sqrt{\frac{C_{trm}}{L_{trm}}} \approx 0.411 < 1 \quad \text{Underdamped} \tag{4.15}$$

ζ_{sys} represents damping factor of the entire system when the mini-cable is connected to the termination.

$$\omega_D = \omega_r\sqrt{\left|\zeta_{sys}^2 - 1\right|} \tag{4.16}$$

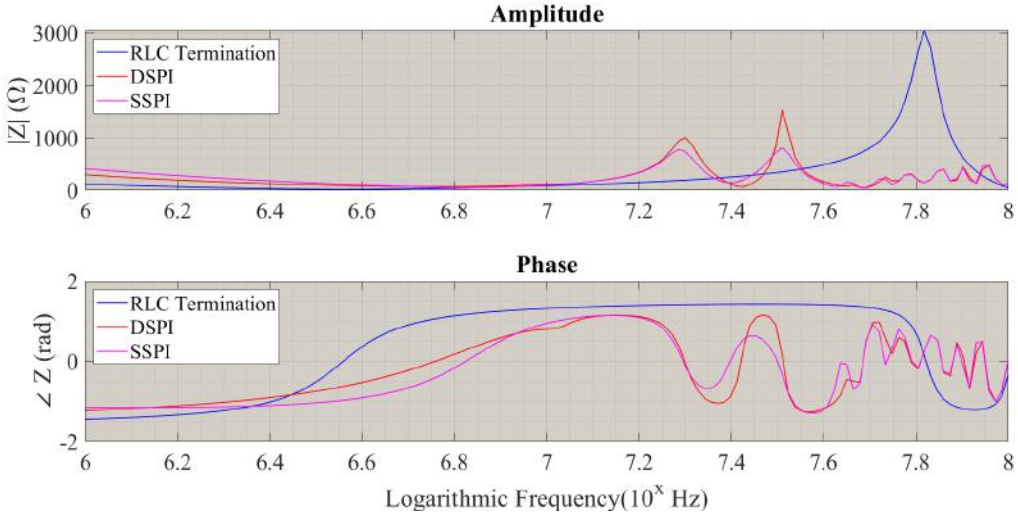

Figure 4.31: Thevenin Impedance seen from termination connection (PSCAD simulation)

Simulation 4.31 infers that DSPI holds higher impedance magnitude, compared to SSPI, around the fundamental frequency component of the applied pulse. Polarities of the impedances resemble each other, fluctuating between inductive and capacitive in wide region. The higher Z_{sys} implies higher equivalent system capacitance C_{sys} gives rise to ζ_{sys}, as $\zeta_{sys} \propto \sqrt{C_{sys}}$. Consequently, according to equation 4.16 damping frequency increases. On the other hand, oscillation frequency drops $\left(\omega_r \propto \frac{1}{\sqrt{C_{sys}}}\right)$ when C_{sys} grows, due to which peak-to-peak distance of the oscillation is extended. To sum up, higher damping and lower oscillation frequency are observed for DSPI as depicted in diagram 4.29. Nevertheless, diagram 4.29 illustrates more distorted curve for the DSPI termination voltage, due to the fact that by splitting the incoming current at B_2, **a)** a part of the signal arrives B_5 with a delay and **b)** number of partial reflections significantly increases.

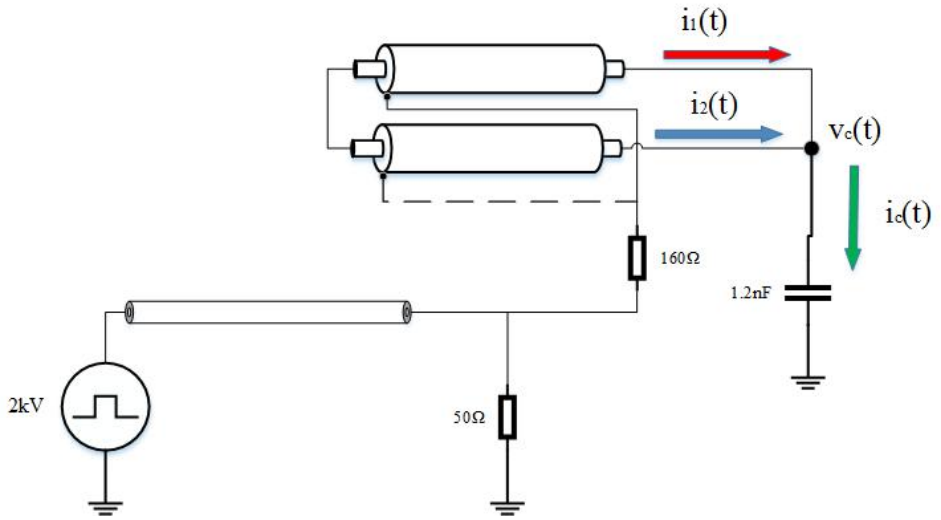

Figure 4.32: Configuration of circuit

Diagram 4.33 shows the lab measurement records for currents along longer and shorter half of the mini-cable. Generally, current magnitude through the longer half sustains higher magnitude than that of the shorter half, which are colored in blue and red accordingly in figure 4.32. The figure shows that $i_2(t)$ reaches a peak in order of $\widehat{i_2} \approx 1.75\,A$, whereas $\widehat{i_1}$ does not exceed $1.25\,A$. The ratio between the peaks is repeated between the digs as well, to be approximately $-1.9\,A$ and $-1.3\,A$ for $i_2(t)$ and $i_1(t)$ respectively.

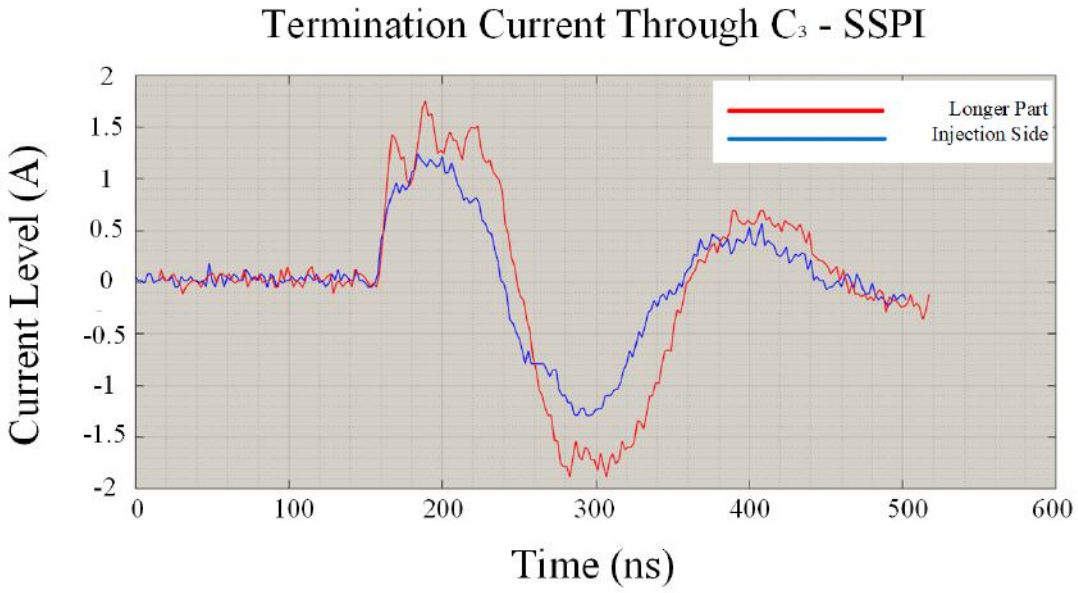

Figure 4.33: cable current at both sides of capacitor (lab measurements)

4.3.5.3 Capacitor value

A 2 nF capacitor, with less leakage inductance, is connected, to the termination path in place of 1.2 nF capacitor to assess the impact of capacitor value on the wave shapes (see figure 4.34).

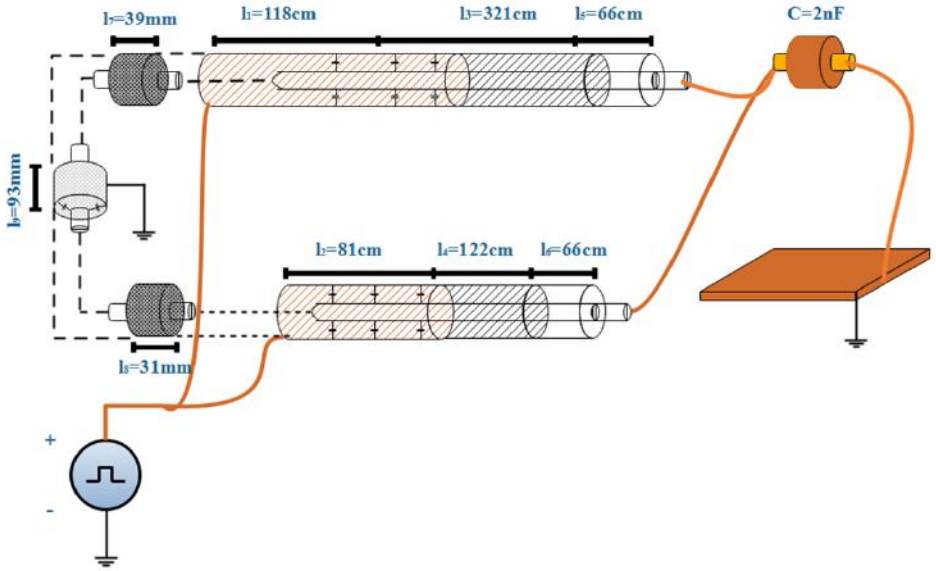

Figure 4.34: DSPI Circuit with grounded termination through 2 nF capacitor

From the graph 4.35, it is understood that when the table is floated and current flow towards the termination rises, change in capacitor value leads to more intense impact on the injection voltage and current. By increasing the capacitor value,

— The injected voltage drops

— The reflected voltage rises slightly and shifted backwards„

— Injection voltage ascends,

— The reflected current is also marginally shifted back.

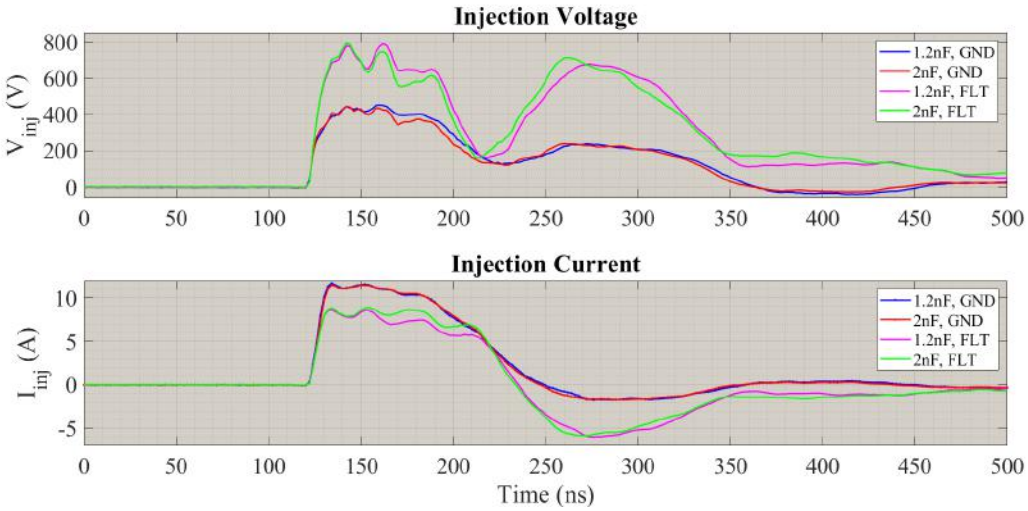

Figure 4.35: DSPI- 2 nF vs 1.2 nF capacitor termination, with GND vs FLT table (lab experiments)

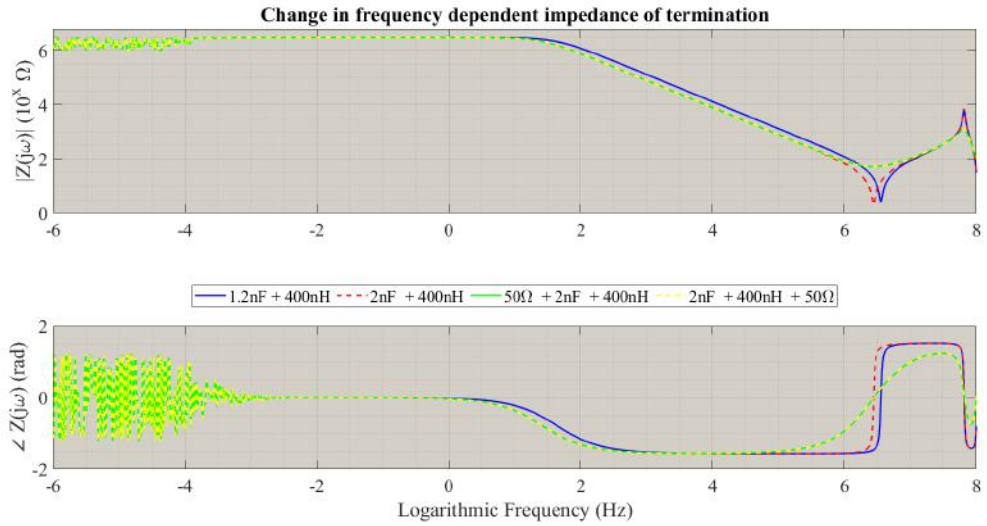

Figure 4.36: Change in termination load impedance (PSCAD simulations)

Simulation 4.36, shows change in the observed from the termination spot. In case of $C_{trm} = 2\,nF$, a back-shift in resonance locus is observable, while the upper cut-off frequency remains the same. This means higher resonance bandwidth when a $2\,nF$ capacitor is deployed. By adding a $50\,\Omega$ resistor, as it is already discussed, the phase transition becomes smooth and resonance intensity declines. Simulation 4.37 implies the same outcomes for the reflection coefficient at the termination spot. Since leakage inductance of the $2\,nF$ capacitor is lower than that of its alternative, small change in reflected wave infers dominance of the couplings and grounding inductance in reflection process, rather than leakage inductance of the capacitor itself.

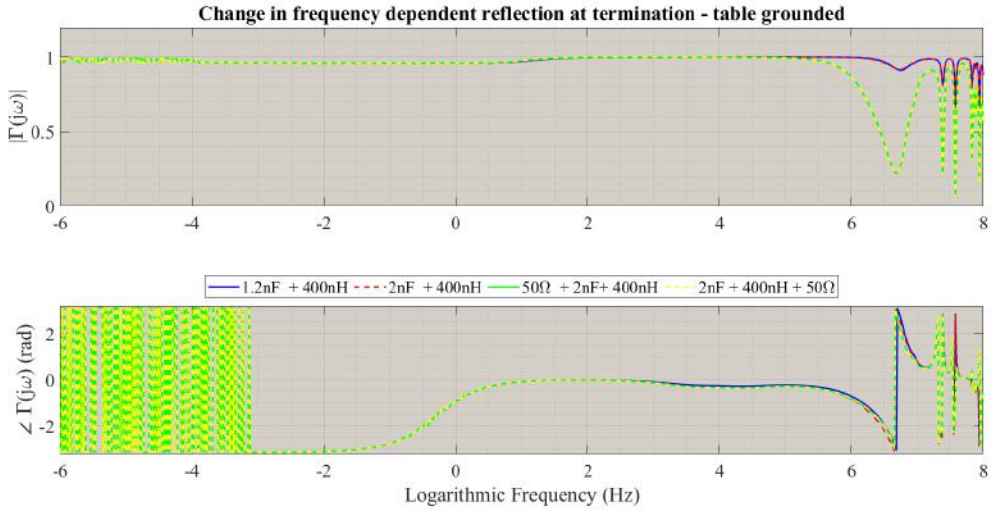

Figure 4.37: Change in termination load - reflection coefficient (PSCAD simulations)

4.3.5.4 Inductive termination (Solidly grounded termination)

In order to understand the circuit behaviour, the capacitor is detached from the circuit and its path is solidly grounded. The test is performed with and without earth connection at the table (see figure 4.38). In fact, the table ground disconnection forces current to flow towards the termination. Although the capacitor can not be eliminated from the circuit in real setup, since the HVDC voltage must be retained in the circuit in order to generate a constant electric field across the DUO, this test practically clarifies the termination inductance contribution in the reflected wave(s) and distortions.

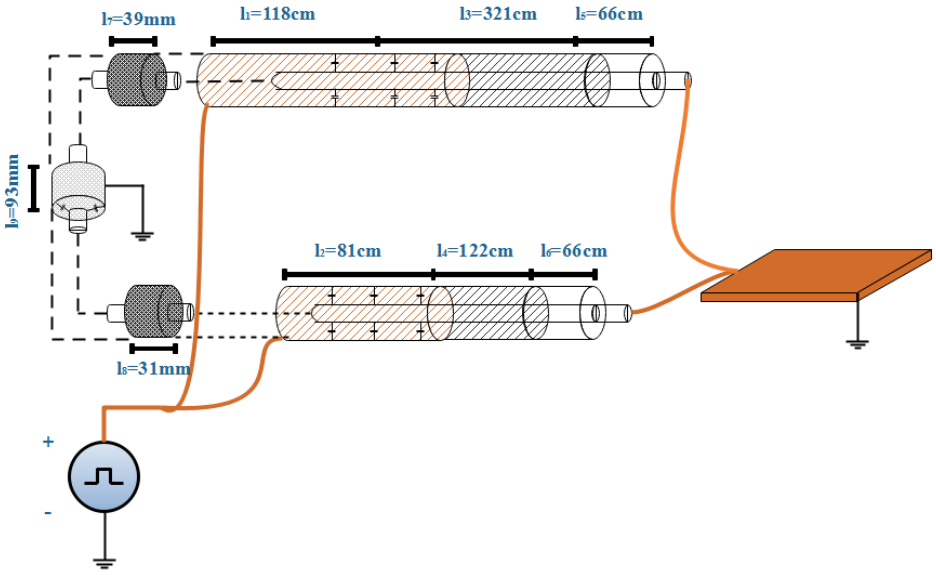

Figure 4.38: DSPI Circuit with grounded termination

Graph 4.39 implies a fall in the injection voltage and rise in the injection current by solidly grounding of termination (red lines) in comparison with the original configuration where the circuit is grounded through 1.2 nF HV capacitor (blue lines).

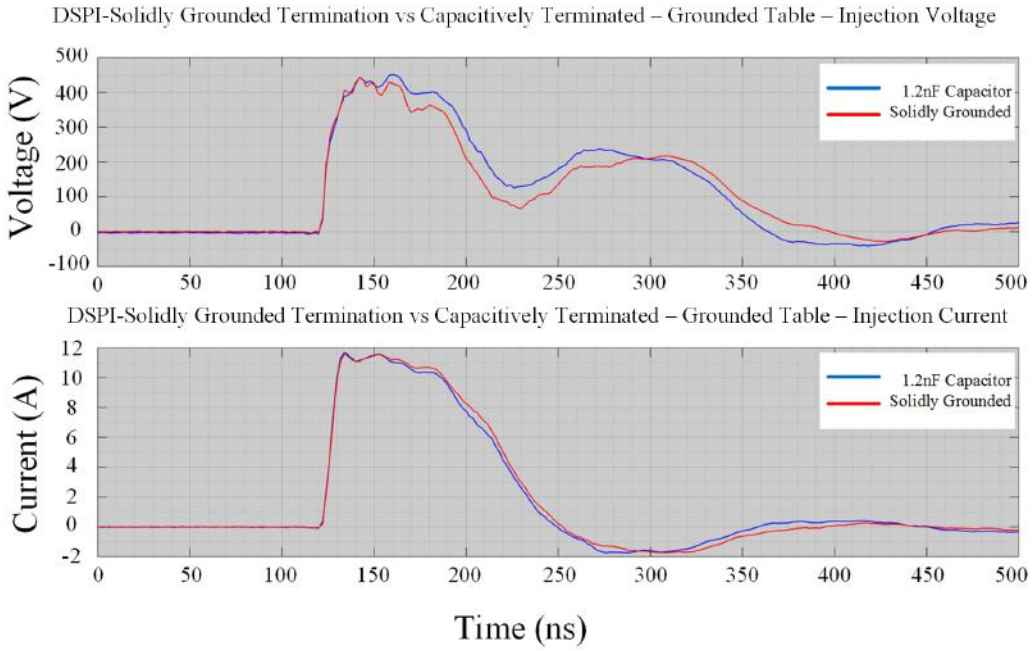

Figure 4.39: Solidly grounded termination vs earthing through 1.2 *nF capacitor- grounded table (lab measurements)*

Graph 4.40 simulates the Thevenin impedance observed from the injection point as a function of frequency for the both cases. Decrease in the Thevenin impedance magnitude, specially at frequencies lower than ω_0, seen from the injection spot, is apparent in figure 4.39. It is worthy to know that, as we already discussed, the impedance magnitude and phase curves are shifted back by the capacitor elimination.

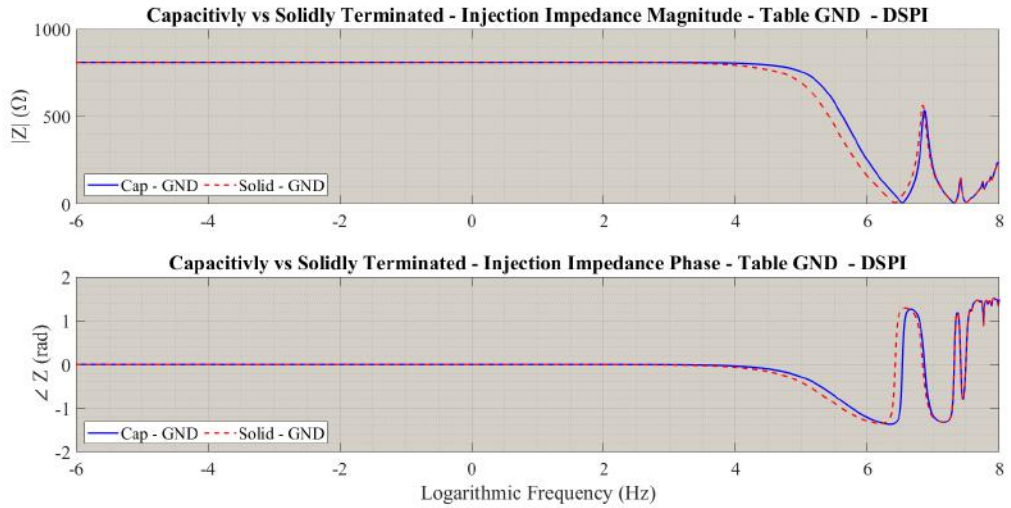

Figure 4.40: Injection spot Thevenin impedance - Solidly grounded termination vs earthing through 1.2 *nF capacitor - grounded table (PSCAD simulations)*

The measurements and simulations are repeated for the case where table is floated (Figures 4.41 & 4.42). Leaving the PEA set floated, intensifies the deviations. Graph 4.42 shows that the table disconnection, makes the cited shift of the impedance curves larger.

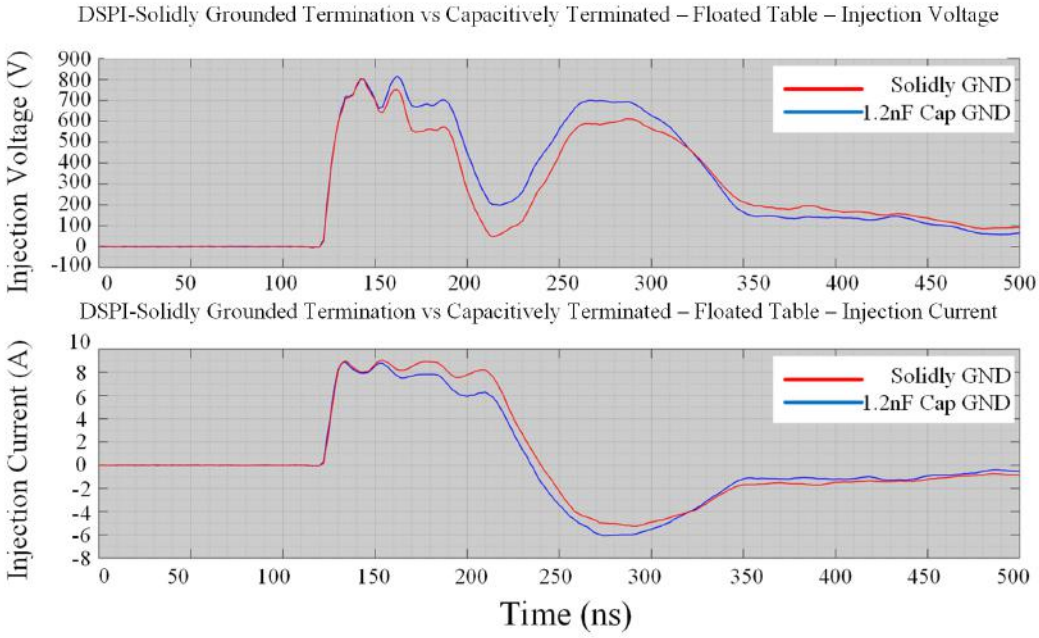

Figure 4.41: Solidly grounded termination vs earthing through 1.2 *nF capacitor - floated table (lab measurements)*

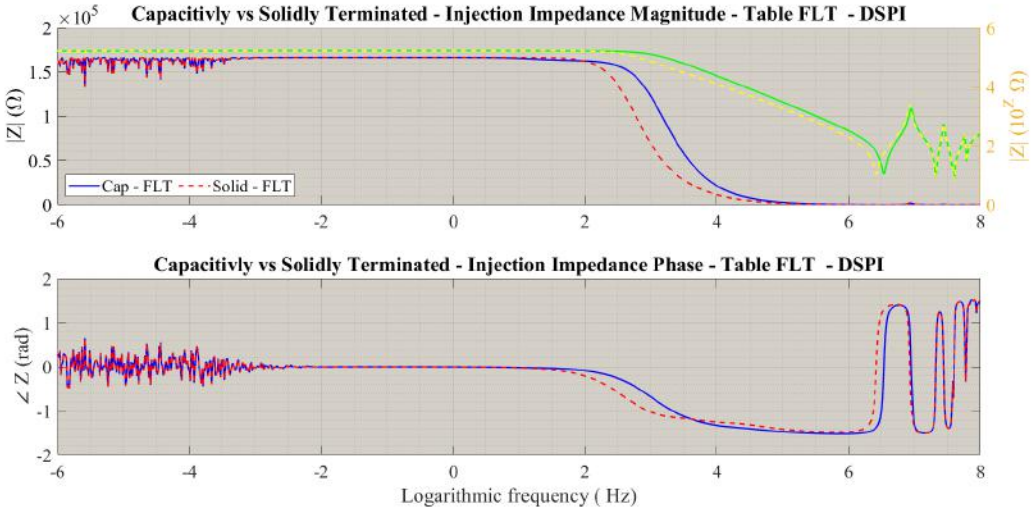

Figure 4.42: Injection spot Thevenin impedance - Solidly grounded termination vs earthing through 1.2 *nF capacitor - floated table (PSCAD simulations)*

By means of this experiment, other valuable findings are obtained as mentioned below,

— By amplifying the current flow into the termination, the low frequency noises escalate.

— Purely inductive inductance intensifies the high frequency oscillations.

— Existence of the termination capacitor contributes to the system damping.

4.3.5.5 Resistive termination

As indicated in figures 4.8 and 4.9, by increasing the termination resistance, the resonance oscillations drop in magnitude considerably. If the termination capacitor is replaced by a 50 Ω resistor, rise in the system damping can be observed clearly (as shown in scheme 4.43). The experiment is repeated for both grounded and ungrounded PEA measurement table cases.

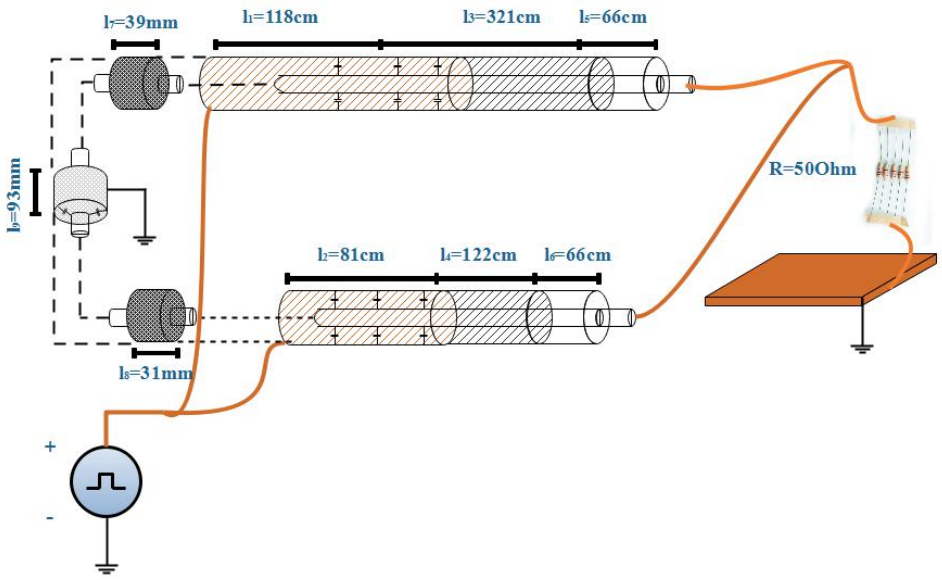

Figure 4.43: DSPI Circuit with grounded termination through 50 Ω *resistor*

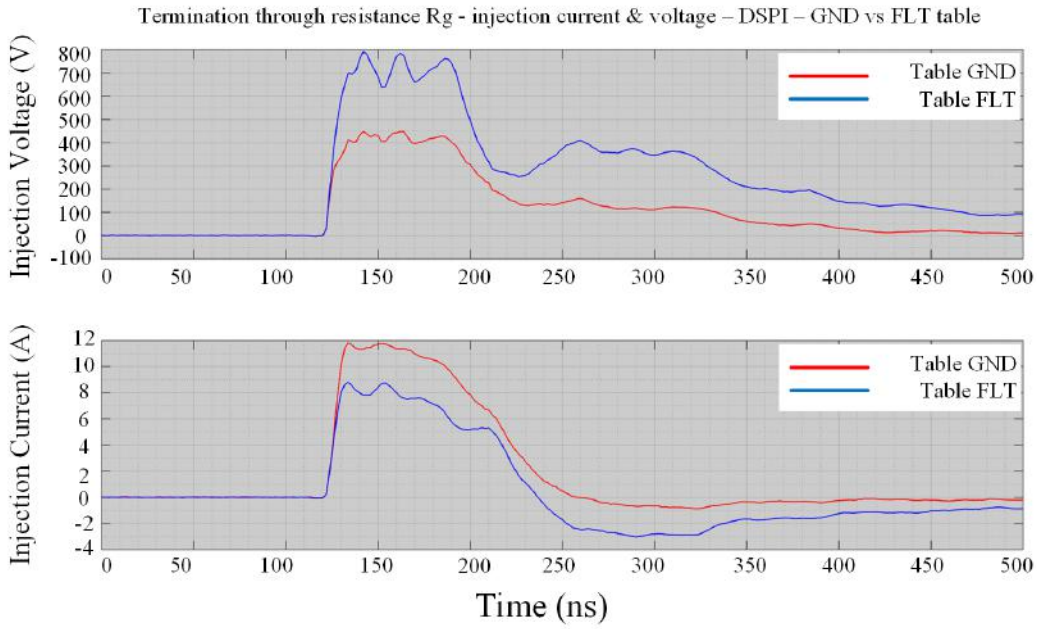

Figure 4.44: Injection voltages & currents, termination grounding through 50 Ω *resistor, with grounded vs floated table*

The test is performed on DSPI setup. Comparing graphs 4.44 and 4.41, it is revealed that the bounced back waves are effectively damped almost to half value for the both grounded and floated table cases, however a long standing DC-offset seems to maintain in the system. For the injection current, as long as the table is left ungrounded, a post-pulse undershoot appears in the system that continues existing with gradual attenuation rate.

4.3.5.6 Resistive-capacitive termination

Graph 4.45 shows the performed experiment in the lab where the table is grounded and the circuit is terminated by a $2\,nF$ capacitor and $50\,\Omega$ resistor. The goal is to observe the effect of manipulation in damping feature of the circuit when the termination capacitance is magnified.

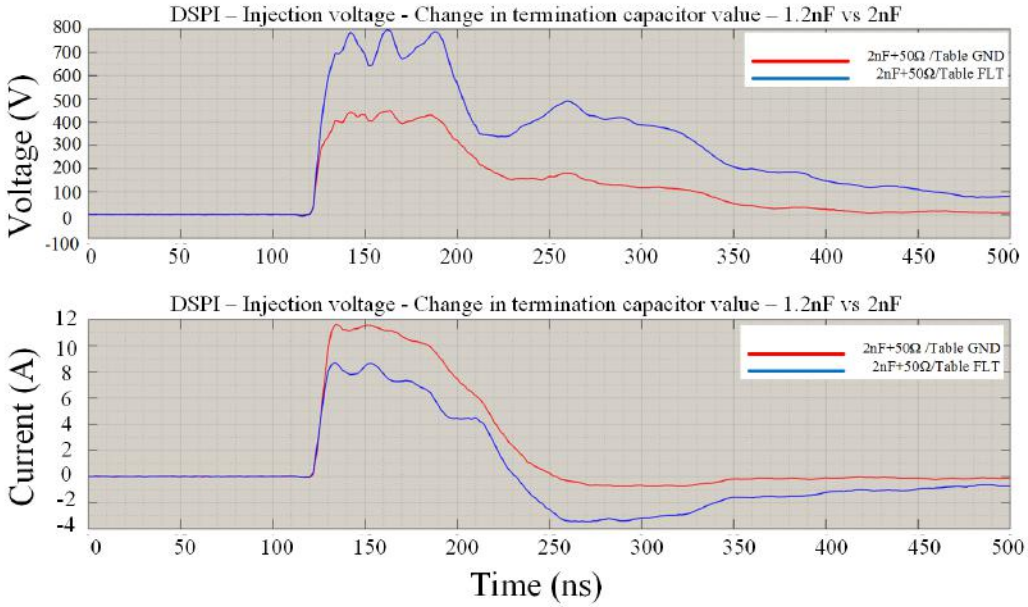

Figure 4.45: DSPI- terminated by series $2\,nF$ cap. and $50\,\Omega$ resistor, table is grounded (lab measurements)

Similar to the previous cases, As it can be seen the added resistor contributes to damping of the unwanted reflection/oscillation on the injection voltage. For instance, comparing graphs 4.45 and 4.35 it is concluded that the reflected wave amplitude falls down from just above $650\,V$ peak to around $500\,V$. The same happens for the grounded table cases, however the damping effect is much more sensible when current is higher. Figures 4.37 and 4.47 clearly indicate frequency dependent impedances of the termination impedances for the floated and grounded measurement table.

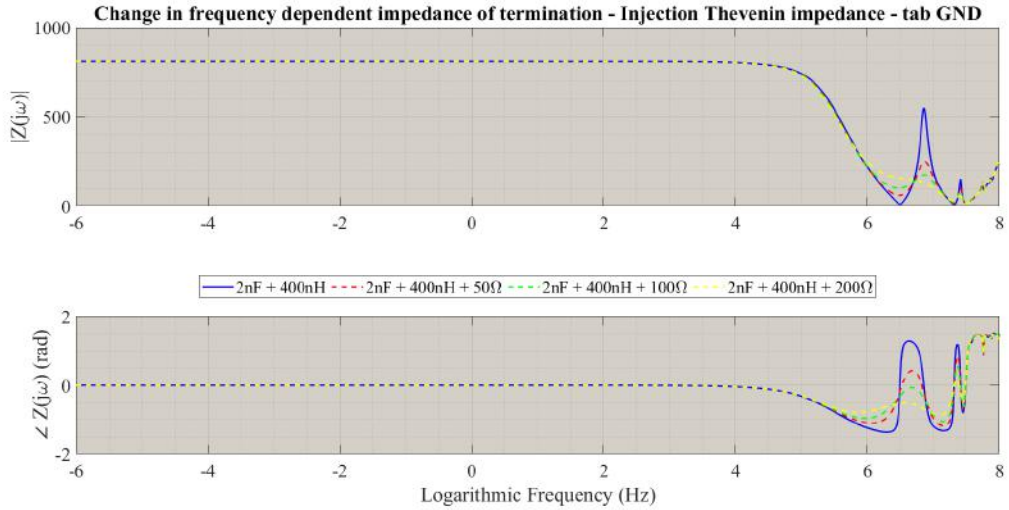

Figure 4.46: DSPI- Change in termination resistance - Grounded table (PSCAD simulations)

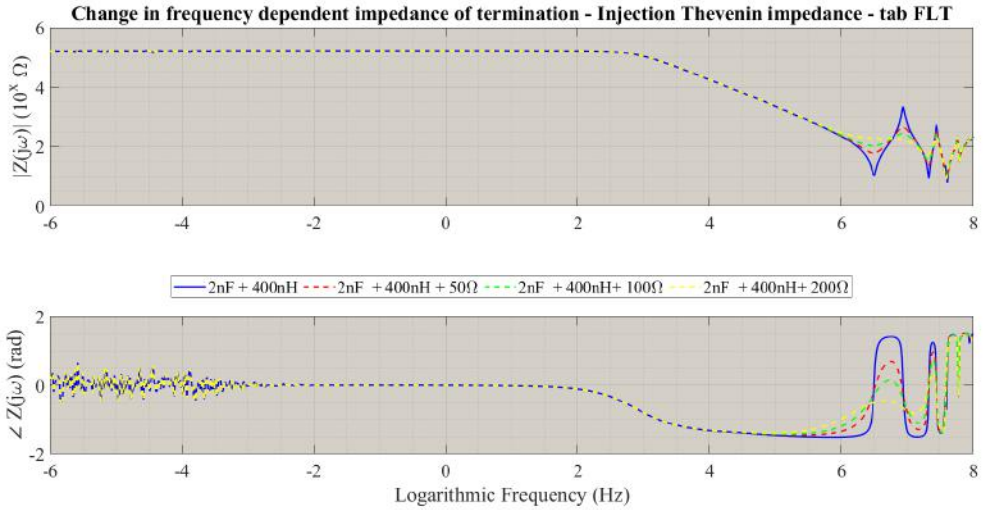

Figure 4.47: DSPI- Change in termination resistance - Floated table (PSCAD simulations)

4.3.6 Table pulse injection (TPI)

TPI setup is already introduced in section 2.1. In this setup, the pulsed-voltage is directly injected into the table or measurement unit, while the table is left ungrounded.

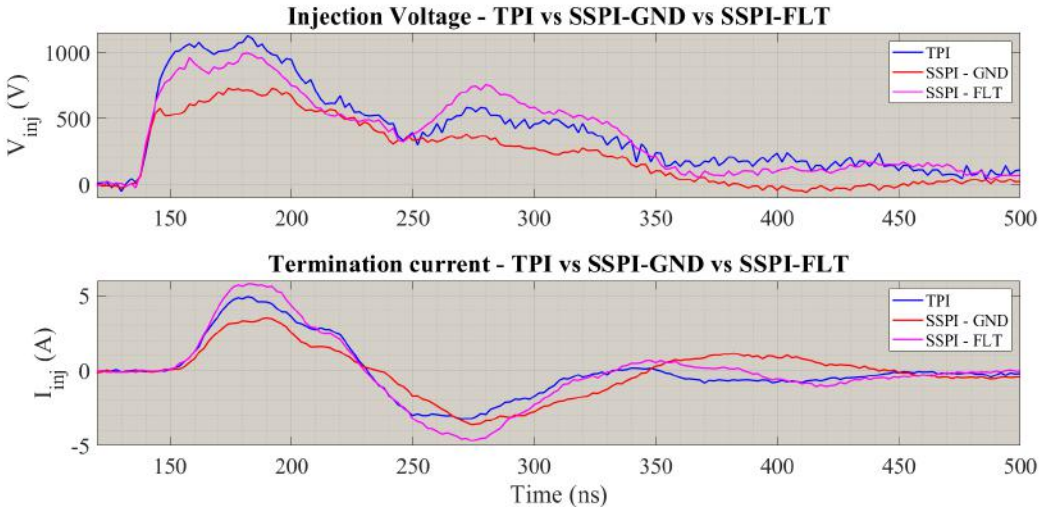

Figure 4.48: TPI vs SSPI - $C_{trm} = 1.2\,nF$, $L_{trm} = 400\,nH$ - Injection voltages & termination currents (lab measurements)

Diagram 4.48 implies that:

— The injection voltage in TPI is generally higher than that of SSPI whether the table is grounded or not,

— Compared to SSPI setup with the floated table, the reflected voltage has lower magnitude, however SSPI with grounded table has better performance from this aspect,

— The recorded injection voltage for TPI contains more high frequency noises.

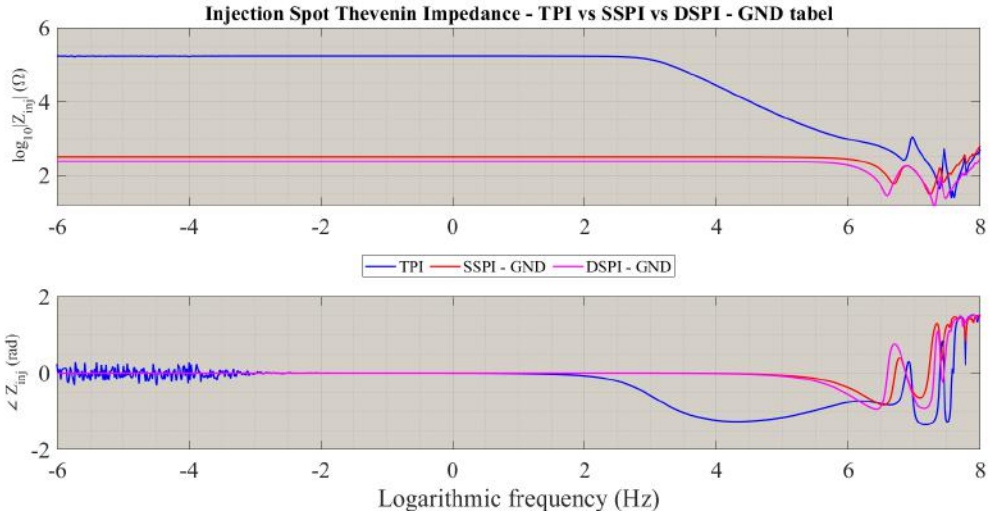

Figure 4.49: TPI vs SSPI vs DSPI - Injection Thevenin Impedance - Grounded table for two latter (PSCAD simulations)

Simulation 4.49 illustrates the impedances seen from the injection spot for TPI, SSPI and DSPI, where the two latter setups have the original configuration (PEA unit is grounded). The followings are resulted,

— Generally TPI impedance magnitude is far higher than the other two, which justifies higher magnitude of the injection voltage in TPI.

— Beyond 1 kHz, TPI impedance collapses, reaching a dig, less than DSPI and SSPI impedances at very high frequencies in order of 80 MHz.

— At low frequencies close to DC, TPI impedance is very oscillatory. One of the probable origins for more noises on the TPI recorded voltage pulse bulk might be these low frequency partial reflections.

— The figure shows more intense resonances at frequencies higher than ω_0 for TPI, that might be other source for the bulk noises.

— In frequency span between 100 Hz to almost 10 MHz, where the first resonance occurs, The TPI impedance is highly capacitive. Furthermore, at the first resonance, a minor inductive behaviour is observed for TPI compared to the other two.

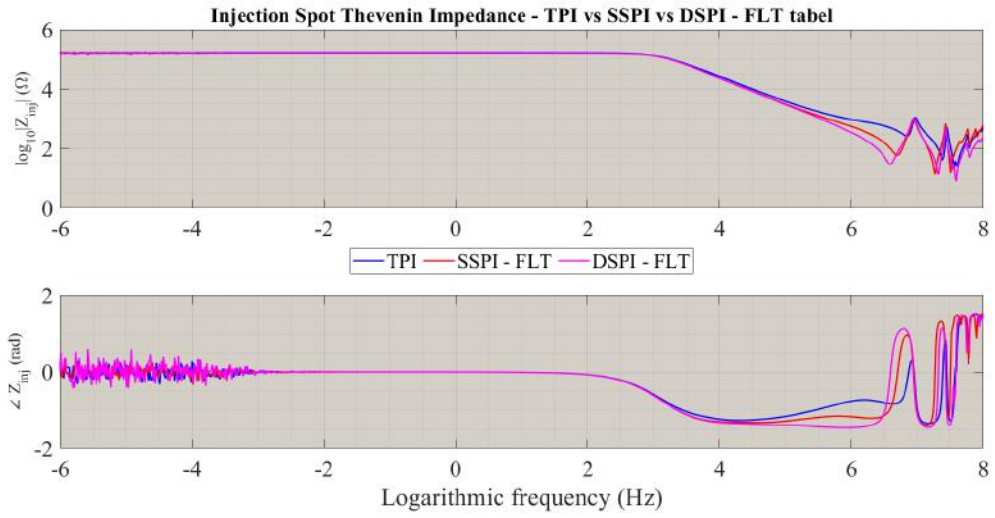

Figure 4.50: TPI vs SSPI vs DSPI - Injection Thevenin Impedance - Floated table for two latter

Now, we disconnect the table earth connection in DSPI and SSPI setups and simulate the injection impedances again (graph 4.50). In this case,

— The DSPI and SSPI injection impedances start approaching TPI values.

— At low frequencies, DSPI and SSPI become slightly more noisy than TPI.

— Still at high frequencies around ω_0, $|Z_{inj}|$ is higher for TPI, although DSPI and SSPI seem to be more oscillatory.

— Floating the table has the most severe impact on DSPI.

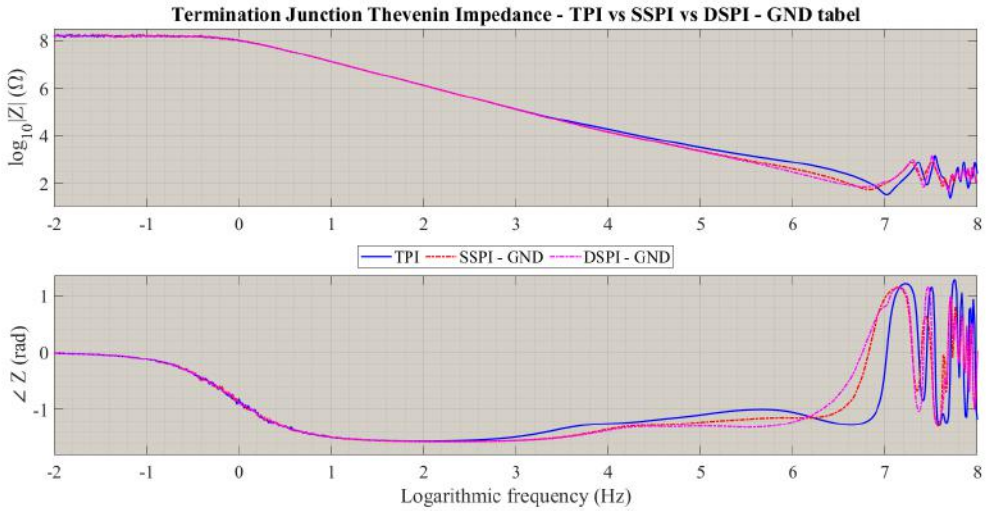

Figure 4.51: TPI vs SSPI vs DSPI - Termination Thevenin Impedance - Grounded table for two latter (PSCAD simulations)

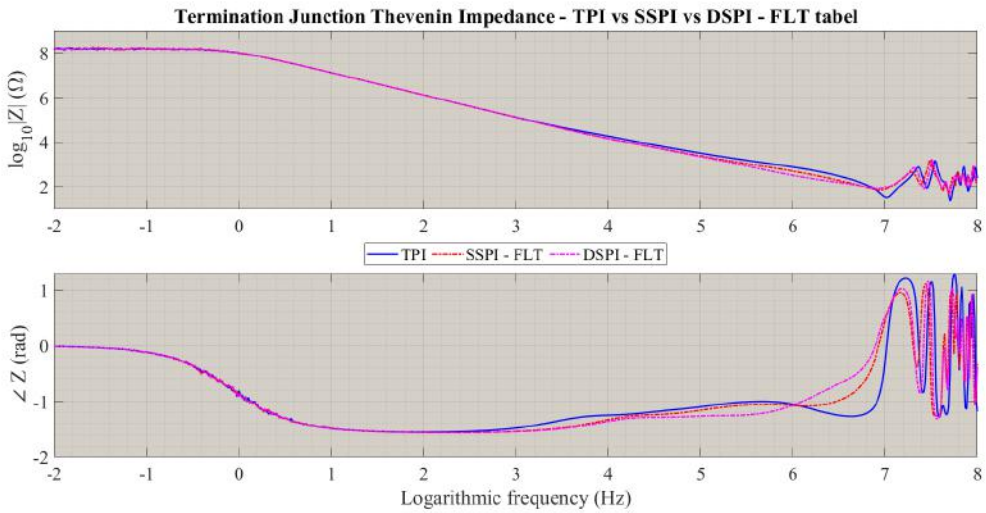

Figure 4.52: TPI vs SSPI vs DSPI - Termination Thevenin Impedance - Floated table for two latter (PSCAD simulations)

Graphs and illustrate the impedance seen from the termination junction towards the source. The graphs prove that floating the table is less influential in these Thevenin impedances rather than the Thevenin injection impedances, however the TPI impedance is still higher than those of DSPI and SSPI, especially in the cases where DSPI and SSPI are grounded at the table. It is

also worthy to note that at high frequencies, the TPI impedance experiences more abrupt phase alteration than the other two.

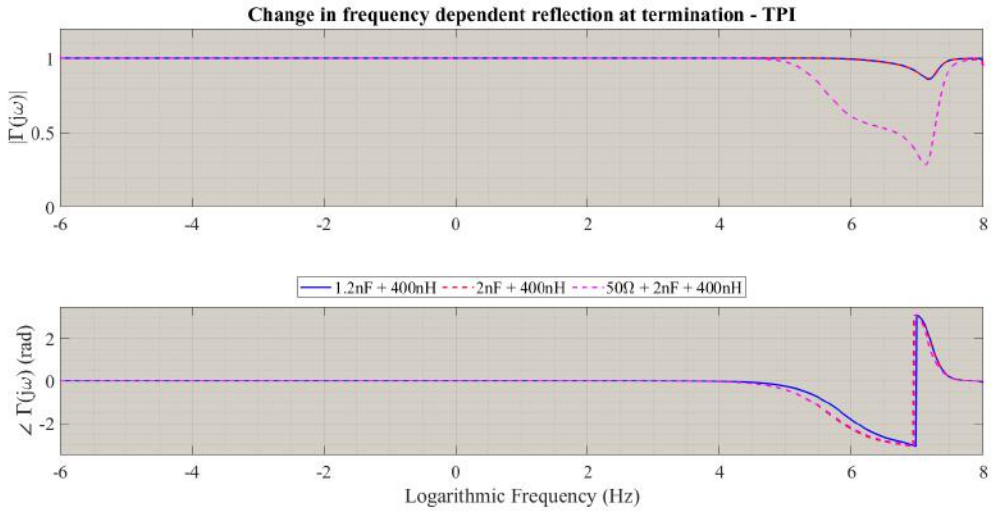

Figure 4.53: TPI - change in termination - reflection coefficient

figure 4.53 shows that similar to the other configurations, increase in the system damping by an additional resistor can help reducing amplitude of the bounced-back wave at the termination.

4.4 Chapter Highlights & Discussion

- **Reflection sources:** main sources for reflected signals (mismatches) are **a)** injection point **b)** termination spot and **c)** uncovered sections **d)** power splitter. The reflected waves appear as disturbances on the measured parameters at the injection point.
- **Uncovered sections:** the parameters such as impedance, velocity of propagation, velocity factor, wavelength, reflected signal waveshape, quantity and magnitude, electrical length of the circuit and so forth are changed by exposing the cable outer layers. Hence, futile screen removal must be avoided as it would give rise to disturbances.
- **Termination:** the circuit termination through a capacitor also includes stray inductances and leakage and grounding resistances. The termination inductance is composed of the capacitor leakage inductance, coupling wire self-inductance and ground loop inductance. The graphs on pages 85 to 88 evaluate change in Z_{trm} and Γ_{trm} by changing the termination parameters as a function of frequency.
- **Injection spot - DSPI vs SSPI:** the frequency-dependent Thevenin impedance seen from the injection spot holds a higher value in entire frequency span compared to DSPI, this leads to higher injection voltage but lower injection current for SSPI. Magnitude of the reflected signals at high frequencies above $1\,MHz$ is higher for DSPI.

- **HVDC source:** due to very high HVDC source series resistor, elimination of the HVDC branch is almost ineffective on the voltage waveshape seen from the injection point. Thus all the rest tests/simulations are executed in absence of them.
- **Screen extension:** The mini-cable screen extension (in order of 1 m) has minor effect on the injection voltage, but gives rise to the core voltage.
- **Central semicon gap:** cutting the central semicon gap down leads to reduction in the injection voltage, rise in the injection current and extra ringing at the front edge of the injection voltage. The results are also valid when the termination is disconnected from earth.
- **Floated termination:** by decoupling the termination from earth, the second peak on the injection voltage disappears both for SSPI and DSPI. Additionally, in the Thevenin impedance frequency scan no major resonance is observed anymore, except of a small resonance at very high frequency. The main share of the injected current, in this case, will flow towards the table.
- **Termination oscillation:** in both SSPI and DSPI the termination voltage show an under-damped oscillatory behaviour. Lower oscillation frequency and higher damping but more distortion is observed for DSPI compared to SSPI. The measurements also have shown higher current peak with more crest oscillations for the current flowing through the longer half compared to those of the shorter one.
- **Termination capacitance:** back shift of the resonance frequency, slight drop and rise in the first and second crests of the measured injection voltage accordingly and precisely opposite trends for the injection currents are observed by rising the capacitor value.
- **PEA table ground connection:** floating of the table gives radical rise to the injection voltage, while the injection current decreases.
- **Solidly grounding of termination:** Injection voltage lab measurements with solidly grounded termination indicate similar trends as grounding through a capacitor for both grounded and floated PEA table. The second peak remains on the curve, implying that the reflection is principally related to the inductance of the termination. An overall descent in voltage and jump in the current is also resulted by direct earth connection at the termination. The deviations become more significant when the table is ungrounded. Low frequency disturbances become more apparent when the table is left floated while solid grounding of the termination amplifies high frequency oscillations. The measurements prove that terminating the circuit through a capacitor contributes to the system damping.
- **Resistive & resistive-capacitive termination:** the resistive termination helps damping of the second crest of the injection voltage while it is ineffective on the main pulse magnitude.

The same is resulted when a resistor is added to the capacitive termination. Leaving the table ungrounded leads to rise in energy stored in the system.

- **TPI:** Compared to SSPI with GND and FLT table, higher injection voltage is resulted as Input impedance of TPI is very high. The recorded waveshapes contain both low frequency and high frequency oscillations.

5

PEA SETUPS COMPARISON & ENHANCEMENT

In this chapter, a couple of simulations are arranged, based on which different setups are compared to each other. Subsequently, impact of some important parameters on the output voltage is evaluated. The simulations also assist us with understanding the role of different grounding patterns in the resultant waveshape. Step responses of the setups are also passed, since in this way, many valuable system characteristics can be known. A short introduction on the system interference and their possible reasons come in the next stage, more accurate and vast assessments are still needed in this field, which is out of this research scope, though. Eventually, based on our findings some recommendations are given in order to improve quality of the output pulsed voltage (V_{pea}). All the simulations are performed by means of our PSCAD/EMTDC model that was already introduced in chapter 3.

5.1 Injection setups comparison - 10 m mini-cable

The injection setups are compared from different aspects,

a) Higher peak voltage ($\widehat{V}_{pea}$) across the central cable insulator (e.g. C_m in drawing 5.1 for, DSPI), which contains space charges, is favourable, as more intense electric field is created (equation 1.8).

b) Lower pulse width and sharper rise time (front slew rate) implies higher detection resolution and more accurate space charge profile mapping (equation 1.8).

c) Lower quality factor represents higher system damping, lower stored energy in the system, lower DC offset in V_{pea} and more convenient space charge detection.

d) Less mismatches and refraction at the injection and termination spots are advantageous.

e) Lower oscillatory behaviour contributes to more precise diagnosis.

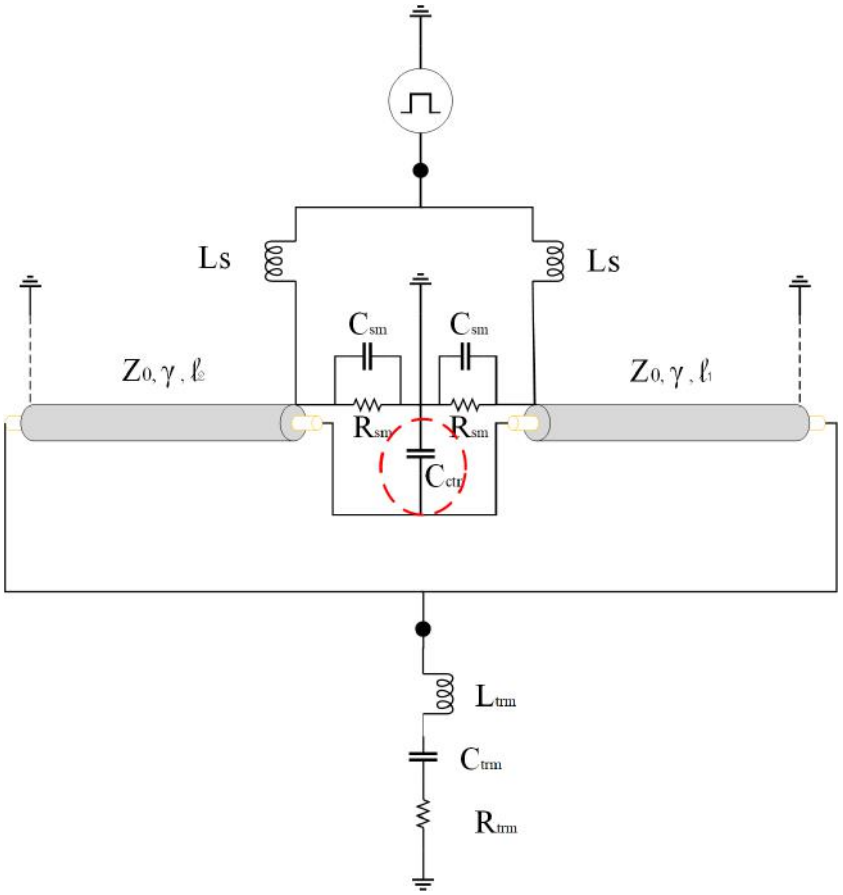

Figure 5.1: DSPI simplified model

Both cable halves (DUT) of each $5m$ long are considered to be sound, it means all discontinuities caused by screen conductor and semiconductor layer removals, are neglected. A non-ideal pulse, measured from output of the pulse generator box is deployed in the simulations. The termination is assumed to include a capacitor of $C_{trm} = 1.2\,nF$ and a stray inductance of $L_{trm} = 400\,nH$. The HVDC voltage source and its series resistor are also kept decoupled from the circuit.

5.1.1 Peak voltage ($\widehat{V}_{pea}$)

$\widehat{V}_{pea}$ represents instantaneous potential difference between core and screen conductors across C_m. The core and screen are considered as positive and negative electrodes. This means for TPI in which the pulse is directly applied to the negative electrode, the voltage polarity is reversed in comparison with the rest. Hence, for this special setup, the reversed voltage $\left(\widetilde{V}_{pea} = -V_{pea}\right)$ is taken into account for comparison purposes. The values of $\widehat{V}_{pea}$ for DSPI, SSPI, TPI and CPI are measured and compared to each other as depicted in graph 5.2.

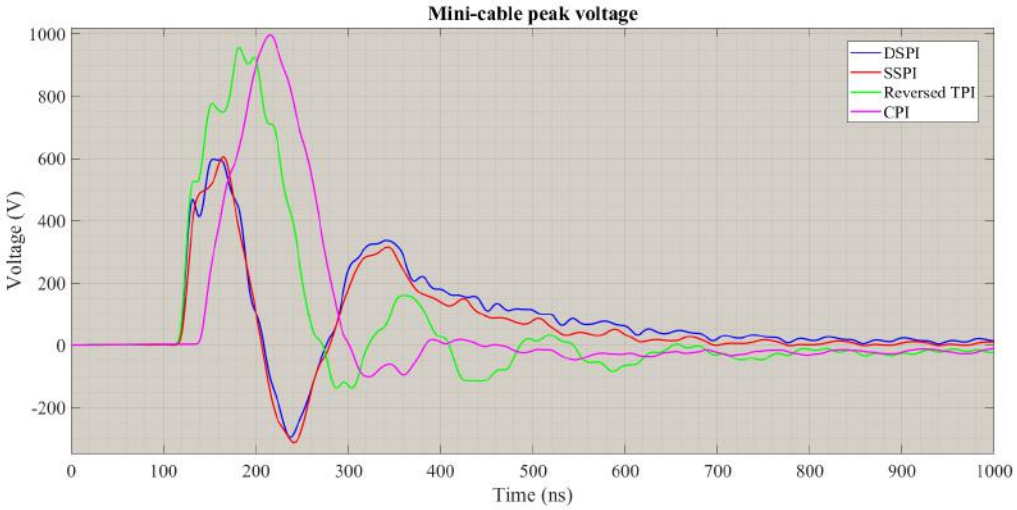

Figure 5.2: Different setups - applied voltage across insulation at center part - 10 meter cable

Table 5.1 ranks $\widehat{V}_{pea}$ in a descending order, according to which CPI with 995 V shows the best results among all. The other important finding is that $\widehat{V}_{pea,sspi}$ is slightly higher than $\widehat{V}_{pea,dspi}$. Therefore, the need for pulsed voltage application into both sides must be questioned.

10 m Sound mini-Cable (Two 5 m halves)				
Rank	Setup	Peak Voltage ($\widehat{V}_{pea}$)	Polarity	Unit
1.	CPI	995	Positive	V
2.	TPI	956	Negative	V
3.	SSPI	605	Positive	V
4.	DSPI	598	Positive	V

Table 5.1: Setups comparison, Peak voltage $\widehat{V}_{pea}$, 10 m mini-cable (PSCAD Simulations)

5.1.2 Pulse width (PW_{pea})

According to table 5.2, SSPI shows the narrowest pulse width among all, while DSPI, CPI and TPI stand on the next ranks. Having said that, as figure 5.2 shows, there are two significant undershoots attached to the main body of pulses that make the inspection very difficult. Therefore, the voltage pulse width, solely, can not be appropriate criterion for PEA measurement resolution.

10 m Sound mini-Cable (Two 5 m halves)			
Rank	Setup	Pulse width (PW_{pea})	Unit
1.	SSPI	58	ns
2.	DSPI	63	ns
3.	CPI	95	ns
4.	TPI	104	ns

Table 5.2: Setups comparison, $50-50\%$ pulse width PW_{pea}, 10 m mini-cable (PSCAD Simulations), ***Notice:*** *zero crossings are taken into account*

5.1.3 Rise time ($\tau_{r,pea}$) & slew rate (SR_{pea})

As mentioned before, rise time ($\tau_{r,pea}$) is an important factor for the PEA test resolution assessment. As the recorded pulses have different magnitudes, the rise times can not be compared to each other, hence the front slew rates are calculated and compared in order to assess quality of the setups. The setups are sorted according to descending slew rates in table 5.3.

10m Sound Cable						
Rank	Setup	$\tau_{r,pea}$	30% $\widehat{V}_{pea}$	90% $\widehat{V}_{pea}$	SR_{pea}	Polarity
		ns	V	V	V/ns	-
1.	DSPI	24.0	179	538	14.96	Positive
2.	CPI	45.6	298.5	895.5	13.1	Positive
3.	SSPI	31.2	181.5	544.5	11.63	Positive
4.	TPI	50.8	287	861	11.3	Negative

Table 5.3: Setups comparison, $30-90\%$ rise time RT_{pea} & SR_{pea}, $10\,m$ mini-cable (PSCAD Simulations)

TPI, despite having the highest $\widehat{V}_{pea}$, seems to have low slew rate with $11\,V/ns$. It means the voltage rises slowly in time. The reason for low slew rate is oscillations on the leading edge, in spite of fast initial rise. Smoothening of the oscillations might help achieving a better slew rate in TPI. However, DSPI does not offer acceptable peak voltage, in terms of resolution it offers the best results, with approximately $15\,V/ns$.

5.1.4 Energy storage & dissipation

In contrary to common applications of quality factor, in our case lower quality factor, seen from the central point, is beneficial, due to the fact that the instantaneous electric field determines the setups functionality. In fact, low quality factor means more dissipation and less stored energy in the system.

$$\text{Quality Factor} = \omega \quad \frac{\text{Average energy stored in the system}}{\text{Average dissipation power}}$$

Figure 5.3 shows that above $1\,MHZ$ multiple series and parallel resonances occur in the systems measured,

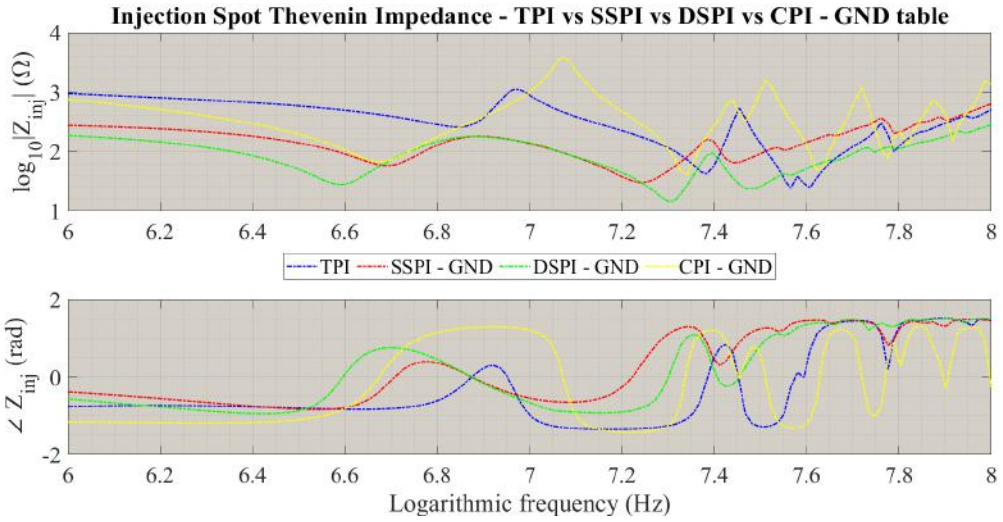

Figure 5.3: Different setups - Injection impedance & resonance - 10 meter cable

As quality factor is a inversely proportional to resonance bandwidth, higher bandwidth is beneficial that leads to higher damping of the system for that specific resonance frequency. The quality factors are sorted in an ascending order in table 5.4.

$f_{r,0}$	$BW_{r,0}$	Q_0	$f_{r,1}$	$BW_{r,1}$	Q_1	$f_{r,2}$	$BW_{r,2}$	Q_2	Q_{eq}
MHz	ns	–	MHz	ns	–	MHz	ns	–	–
DSPI	10 m	GND	Table						
7.59	4.7	10.15	25	2.9	54.17	54.2	4	85.14	7.77
SSPI	10 m	GND	Table						
7.83	4	12.31	24.21	2.6	58.51	57.8	8	45.4	8.31
TPI	10 m								
9.4	1.55	38.1	28.44	1.5	119.13	57.8	3.8	91.77	21.56
CPI	10 m	GND	Table						
11.91	1.1	68.03	32.36	2	101.66	52.48	2.3	143.37	31.74

Table 5.4: Setups comparison, Quality factor, 10 m mini-cable (PSCAD Simulations)

5.1.5 Injection point reflection

Diagram compares Return- (RL) and Insertion Losses (IL) of the four setups at different frequencies.

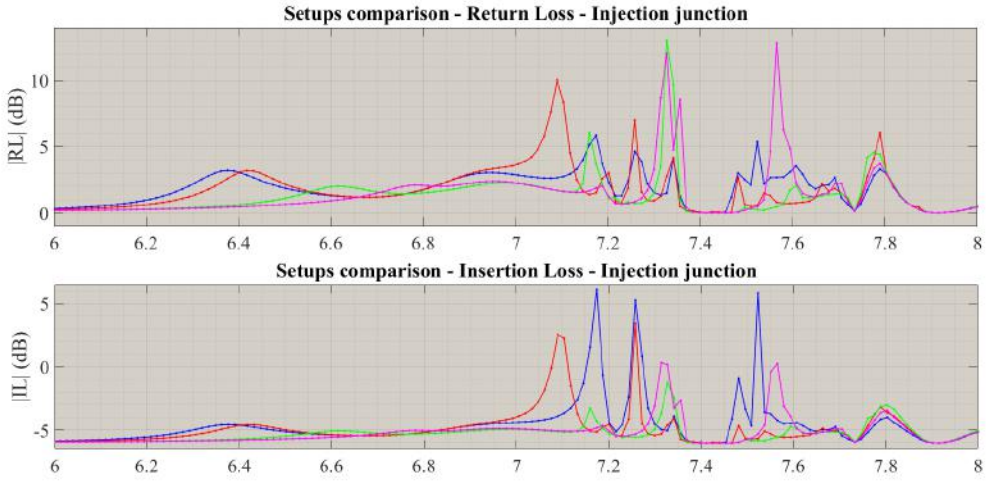

Figure 5.4: Different setups - Return Loss (RL) & Insertion Loss (IL) - 10 meter cable (PSCAD simulations)

In table 5.5, quadratic average of the return and insertion losses for first the frequency range between DC and 100 MHz and secondly for the frequencies above 1 MHz are ascensively ranked. The order is set based on the average of RL in entire frequency range.

10 m Sound Cable					
Rank	Setup	RL	IL	RL_{hf}	IL_{hf}
		dB	dB	dB	dB
1.	CPI	0.7792	5.8978	2.0497	5.3498
2.	DSPI	0.8372	5.834	2.1962	4.9912
3.	TPI	0.9086	5.8909	2.3938	5.2912
4.	SSPI	0.9216	5.8502	2.4219	5.1179

Table 5.5: Setups comparison, Average frequency-dependent Return- & Insertion-Losses, for $0 < f < 100\,MHz$ & $1MHz < f < 100\,MHz$, 10 m mini-cable (PSCAD Simulations)

5.1.6 Oscillations

Graph 5.5 compares unit step response of the setups. In these set of simulations, a unit standard Heaviside voltage is applied to the circuits and the output voltages are scoped across the target insulation (V_{pea}).

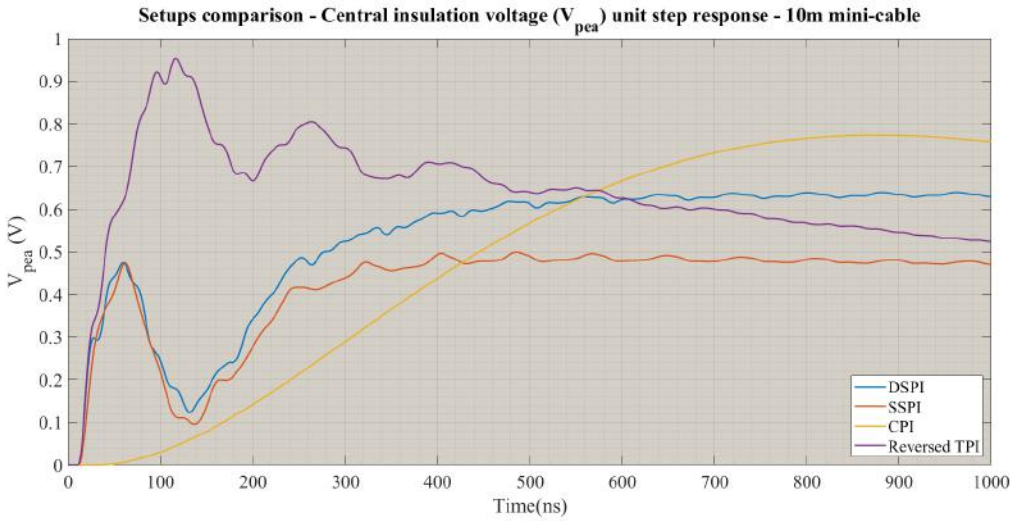

Figure 5.5: Different setups - Unit step responses - 10 meter cable (PSCAD simulations)

The followings are resulted,

— TPI performs like an underdamped RLC circuit.

— CPI response seems to be overdamped.

— After an initial overshoot, an abrupt fall is observed for both DSPI and SSPI, whose cause must be investigated.

— The post-undershoot charging voltage of DSPI is higher than SSPI.

5.1.7 Non-optimized setups comparison

Table 5.6 summarizes results of the simulations for mini-cable scale ($10m$ long) that compared the setups with original configuration (before optimization).

Setup	$\hat{V}_{pea}$	PW_{pea}	τ_r	SR_r	Under/Overshoot	Oscillation	RL
	V	ns	ns	V/ns	V		dB
DSPI	598	63	24	14.96	Severe (-300/+340)	Moderate	0.8372
SSPI	605	58	31.2	11.63	Severe (-320/+310)	Moderate	0.9216
CPI	995	95	45.6	13.1	Low (-100/+20)	Low	0.7792
TPI	956	104	50.8	11.3	Moderate (-130/+150)	Oscillatory	0.9086
Worst ✗	DSPI	TPI	TPI	TPI	S- & DSPI	TPI	SSPI
Best ✓	CPI	SSPI	DSPI	DSPI	CPI	CPI	CPI

Table 5.6: Comparison of most important parameters - Setups before optimization

5.2 Sensitivity Analysis

In this section effect change in different circuit parameters on the results are evaluated.

5.2.1 Cable length

By cable length extension to 20, 40 and 80 m, the waveform undergoes changes. According to graph 5.6, both the highest voltage peak (1285 V) and the longest pulse width (84 ns) among all belong to CPI. TPI stands on the second place in both metrics, with -1220 V and 82 ns respectively. DSPI and SSPI show similar trends, having approximately the same peak values (710 V) and pulse widths 70 ns.

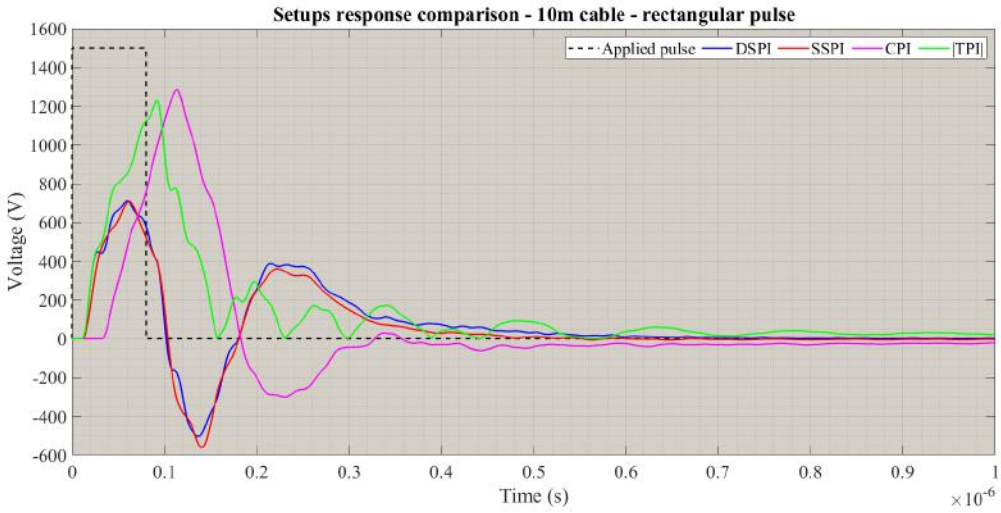

Figure 5.6: Response of 10 m cables against ideal pulse injection (PSCAD simulations)

In 20 m cable simulation (graph 5.7), CPI experiences a large drop in voltage peak, while DSPI and SSPI with the least voltage drop, almost equally show the best results. The values for voltage crest are recorded to be 984 V, 814 V, 774 V and 740 V for TPI, CPI, DSPI and SSPI respectively. However, the prolonged cable length leads to pulse width enlargement for the all cases, the highest belongs to CPI, with 144 ns, which is almost double the value of TPI, the second in ranking, with 82 ns. DSPI and SSPI also experience negligibly gentle rises in pulse width, showing the minimum dependency to the cable length.

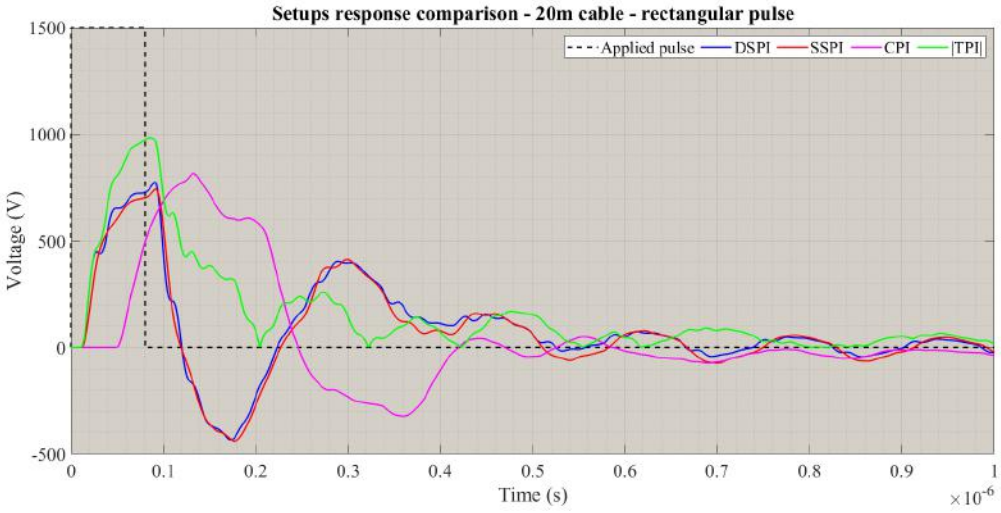

Figure 5.7: Response of 20 m cables against ideal pulse injection (PSCAD simulations)

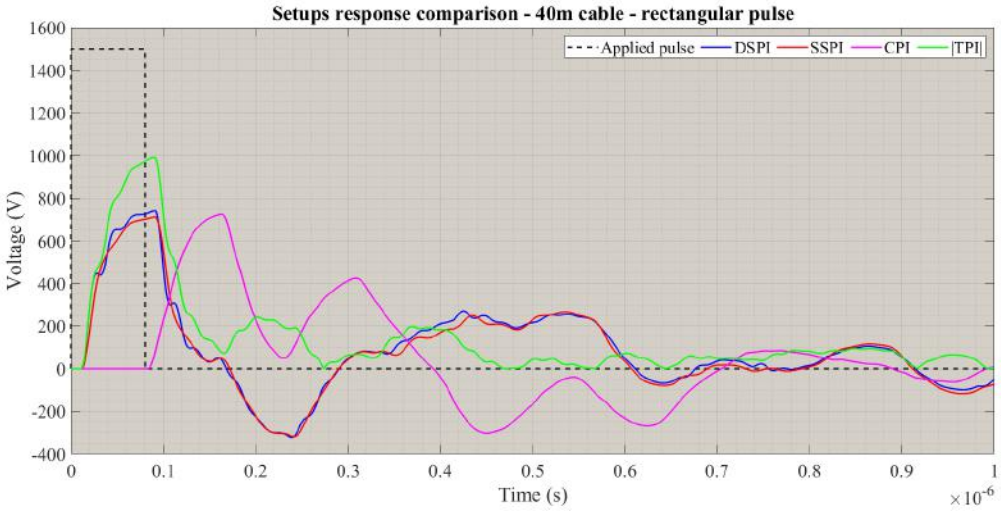

Figure 5.8: Response of 40 m cables against ideal pulse injection (PSCAD simulations)

By further increase in the cable length the undershoots/overshoots start separating from the main body (figures 5.8 & 5.9). Naturally, CPI, in which pulse is injected to the core, gives more fall in magnitude, such that in 80 m cable test, its magnitude equals those of DSPI and SSPI. Nevertheless, CPI is still free of noises that is desirable.

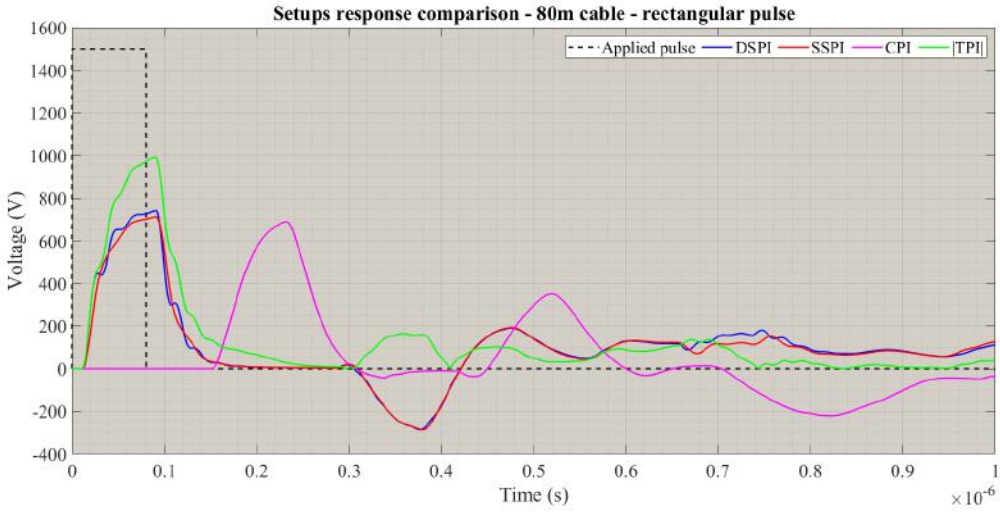

Figure 5.9: Response of 80 m cables against ideal pulse injection (PSCAD simulations)

In this stage change in output metrics like pulse width (up to first zero crossing) and voltage peak for each setup by cable length extension is evaluated.

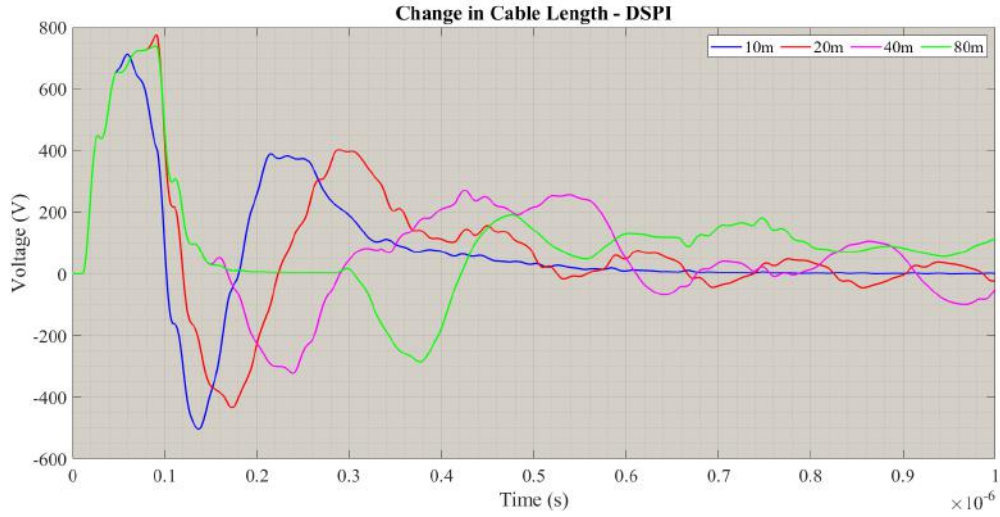

Figure 5.10: DSPI - change in cable length (PSCAD simulations)

According to graphs 5.10 and 5.11, in DSPI and SSPI, by the cable length expansion,

— Pulse width increases

— The pulse crest remains almost the same

— Damping capacity of oscillations declines

— Tail oscillation frequency drops, since the second peak is shifted forth

— The post pulse local maximum and minimum, are lifted upwards

— Further length expansion to 40 m and 80 m does not impact the pulse width

— If the length is sufficiently long, the post pulse undershoot is detached

— SSPI has lower high frequency partial oscillations than DSPI

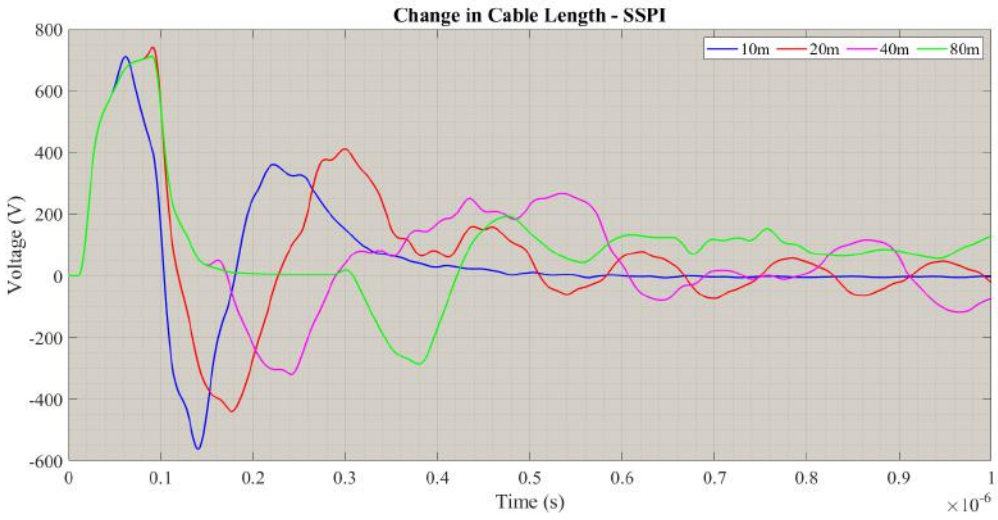

Figure 5.11: SSPI - change in cable length (PSCAD simulations)

Graph 5.12 shows simulations for CPI, the followings are concluded,

— $\widehat{V}_{pea}$ is inversely proportional to the cable length

— Exceeding a certain cable leads to polarity reversal of the post pulse oscillations

— The oscillations are decoupled if the cable length is sufficiently extended

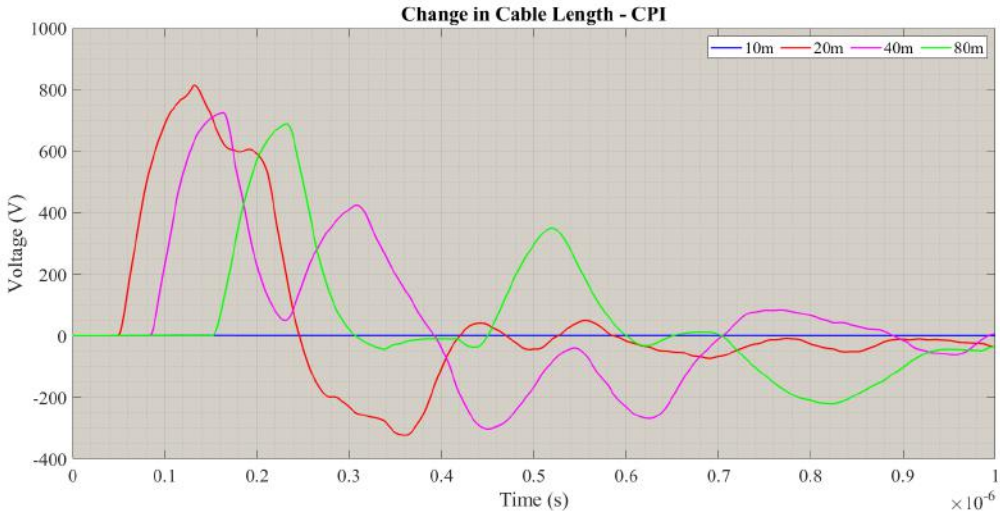

Figure 5.12: CPI - change in cable length (PSCAD simulations)

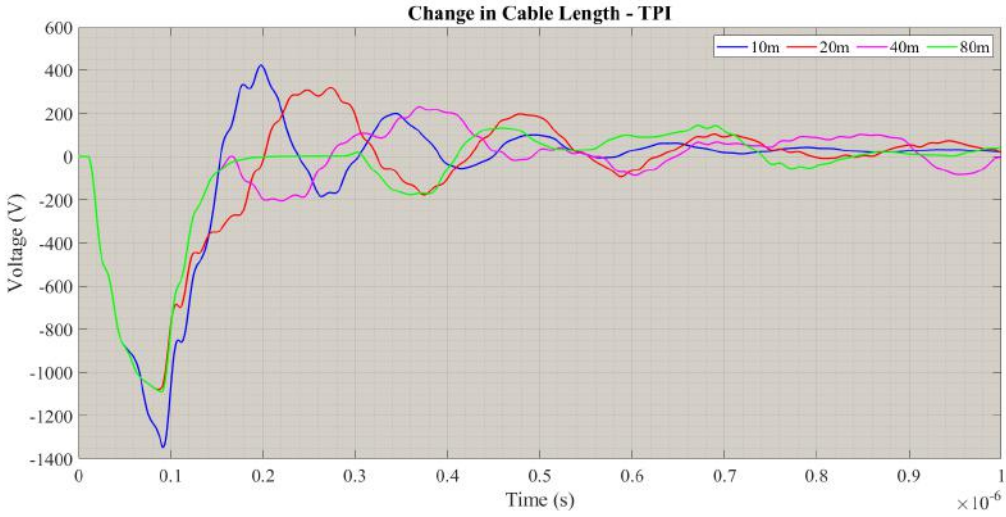

Figure 5.13: TPI - change in cable length (PSCAD simulations)

The followings are concluded from graph 5.13,

— $\widehat{V}_{pea}$ drops by approximately 150 V when the cable extension to 20m, although further enlargement is uninfluential as it remains stable

— The highest voltage gain belongs to TPI

— Among all, TPI contains the most high frequency partial oscillations, whose reason might be decoupling the table from earth and higher input impedance at the injection spot

— The oscillations are decoupled if the cable length is sufficiently extended

— Further simulations imply more smoother pulse shape at higher termination inductances

— Slightly less damping ratio and lower lower oscillation frequency are observed for expanded cables

— It seems the oscillations peaks are not detached from the main pulse by the cable extension, but they change the pulse shape, for instance the pulse widths becomes wider to an extent. Therefore, it can be concluded that the oscillations are not attributed to the termination reflections.

5.2.2 Central uncovered sections length

Figure 5.14 expresses frequency and length dependency of the outer semiconducting layer impedance.

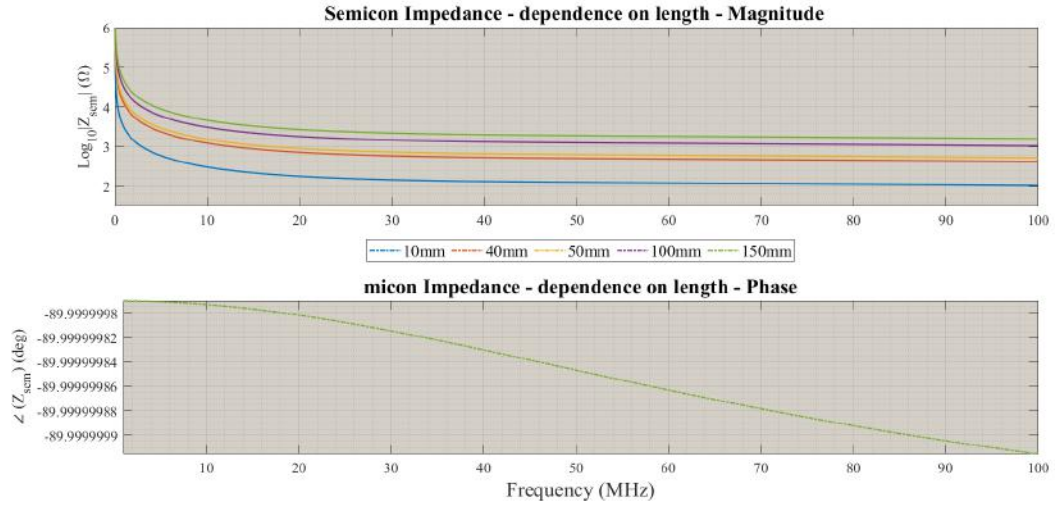

Figure 5.14: Length-dependency of longitudinal semicon impedance(PSCAD simulations)

Due to the fact that the pulsed voltage is injected in adjacency of these sections, every change in their length might change the injected current flux pattern. Hence, an ideal rectangular pulse, with 1500 V peak, is applied to the practices at different semicon section lengths to assess changes in V_{pea}. In the simulations the lengths are assumed to be 40 mm each side. Graphs 5.15, 5.16, 5.17 and 5.18 reveal changes in V_{pea} for both shrunk length to 10 mm and expanded length to 100 mm. The simulations findings are listed below.

— Higher section length lifts $\widehat{V}_{pea}$ in all cases

— Higher sections length leads to higher post pulse undershoot/overshoot for all practices

— Oscillation frequency remains the same by changing the sections length

— The section enlargement intensifies TPI post pulse oscillations, despite the fact that it contributes damping of the high frequency partial oscillations simultaneously.

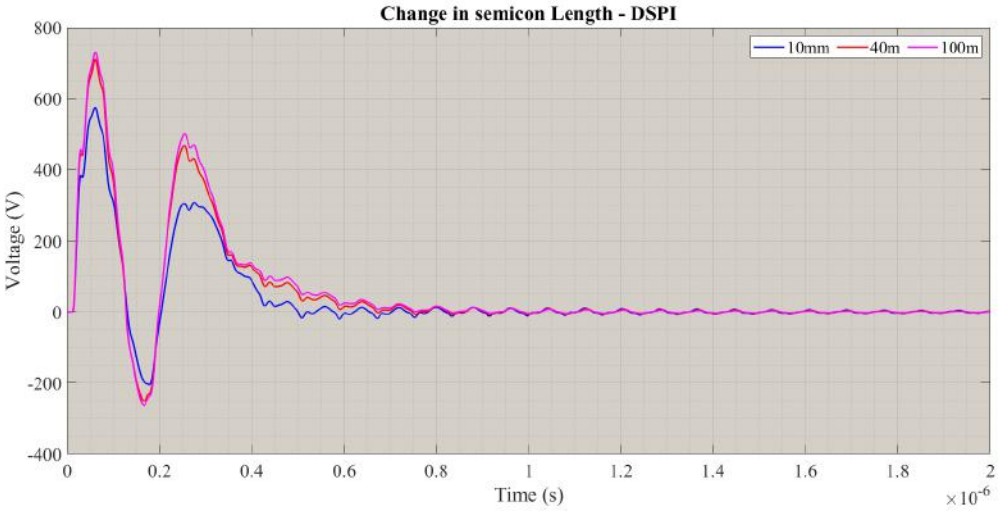

Figure 5.15: DSPI - change in central semicon length (PSCAD simulations)

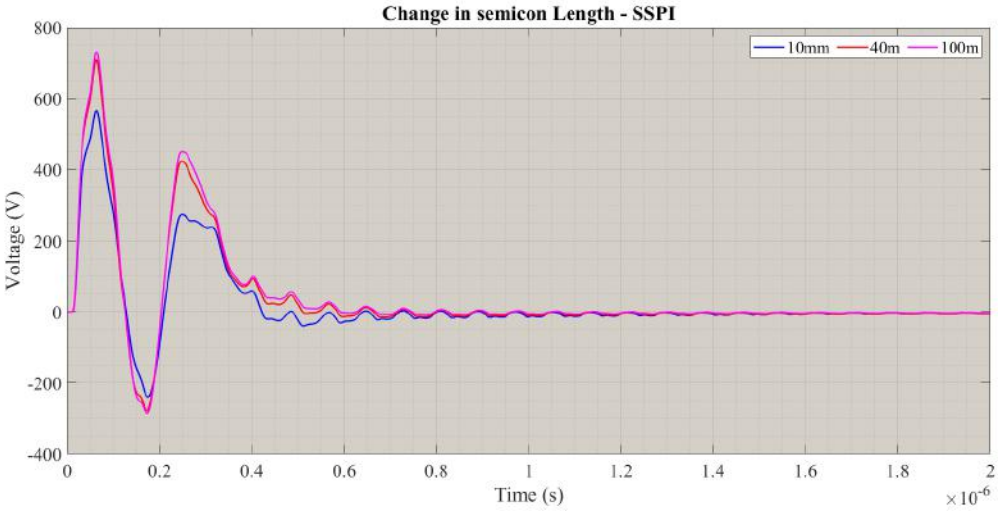

Figure 5.16: SSPI - change in central semicon length (PSCAD simulations)

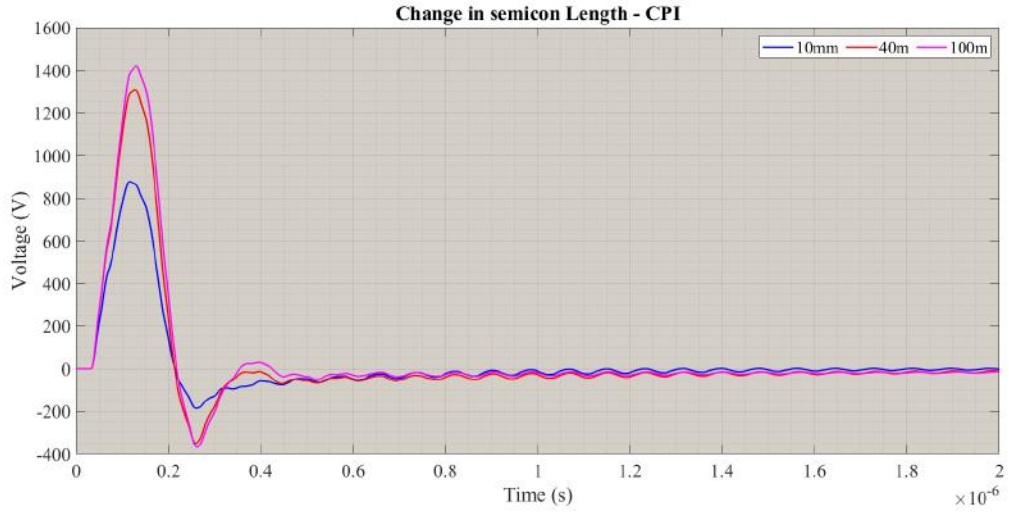

Figure 5.17: CPI - change in central semicon length (PSCAD simulations)

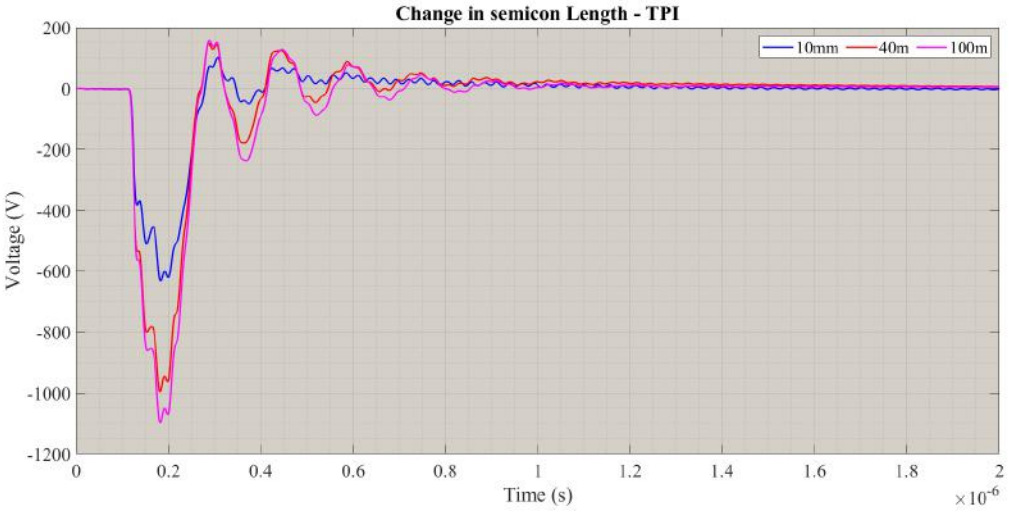

Figure 5.18: TPI - change in central semicon length (PSCAD simulations)

5.2.3 Measurement electrode length

Similar to the previous case an ideal square pulse is applied to the circuits at different lengths for the measurement electrode and V_{pea} is scoped. The simulations are repeated for the case where the screen conductor of the mini-cable samples are grounded (except for CPI).

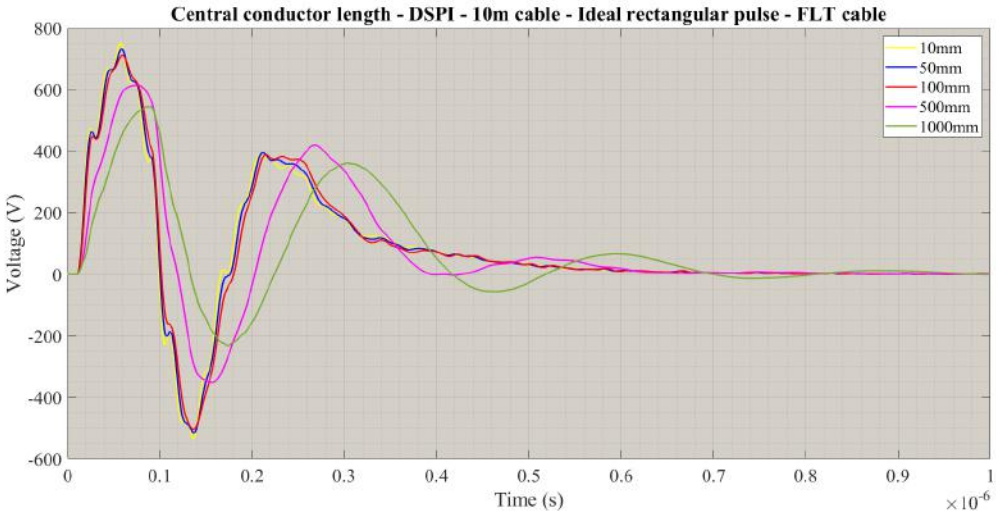

Figure 5.19: DSPI - length of measurement segment - 10 m mini-cable - FLT cable screen (PSCAD simulations)

From graphs 5.19, 5.20, 5.21 and 5.22 it is concluded that by the section enlargement for the all setups, as long as the screen conductors are decoupled from earth.

— The voltage across the central insulation ($\hat{V}_{pea}$) drops

— The pulse width is stretched

— Rise time of the pulse escalate, thus the slew rate collapses

— The peak-to-peak oscillation frequency declines

— High frequency partial oscillations are almost cleared out.

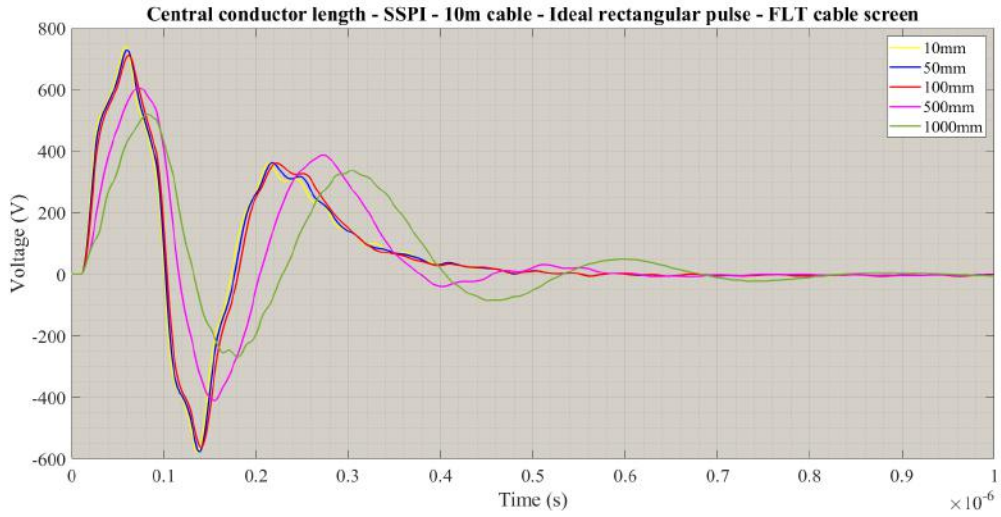

Figure 5.20: SSPI - length of measurement segment - 10 m mini-cable - FLT cable screen (PSCAD simulations)

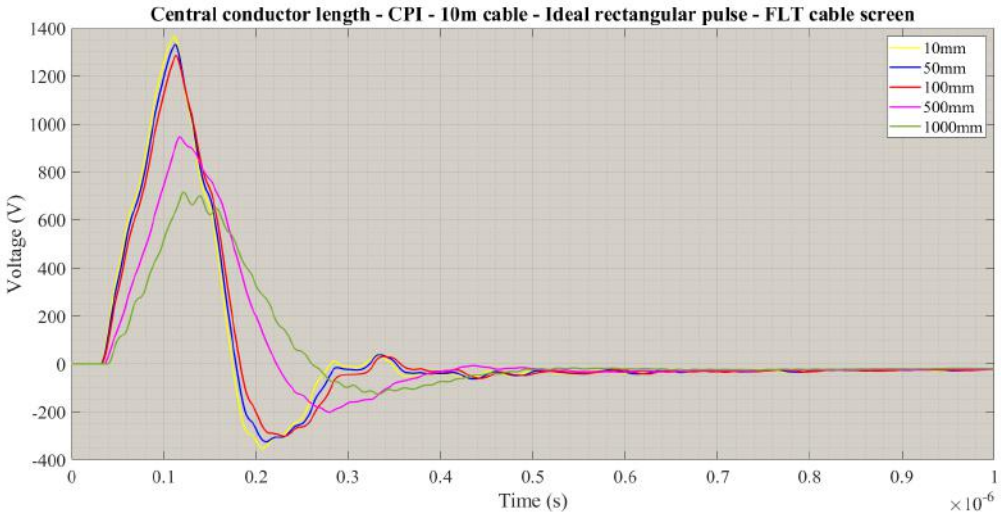

Figure 5.21: CPI - length of measurement segment - 10 m mini-cable - FLT cable screen (PSCAD simulations)

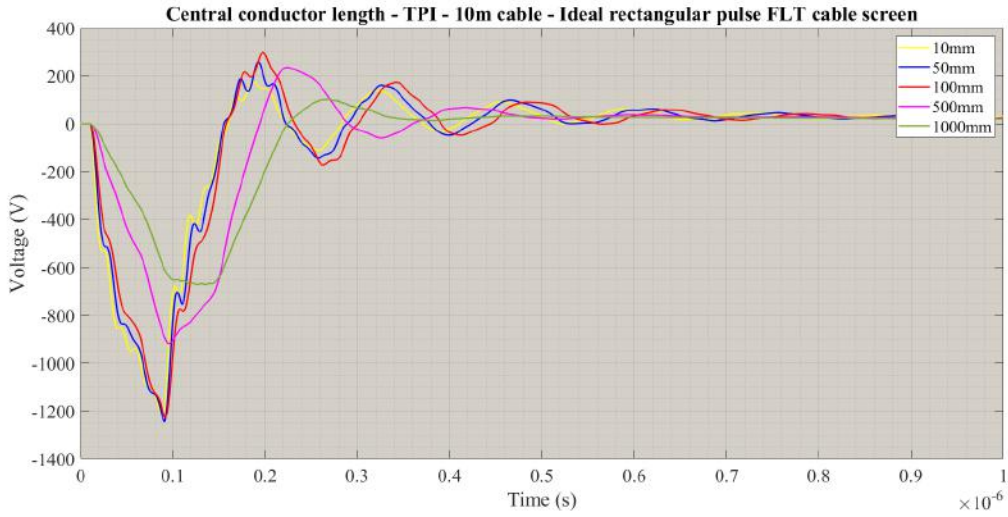

Figure 5.22: TPI - length of measurement segment - 10 m mini-cable - FLT cable screen (PSCAD simulations)

It is also noteworthy that for DSPI and SSPI oscillation damping ratio decreases slightly by at longer lengths of the section (figures 5.19 & 5.20). In other words the oscillation remains unsettled for a longer time. When CPI setup (graph 5.21) is test object, the segment expansion shows much more intensive consequences, by collapsing of the peak to less than half and vibrations on the crest, while pulse width become even wider. Further simulation shows that enlarging to the central cable part, makes the setup entirely inapplicable. By grounding of the cable screen (one side) in SSPI and DSPI also exactly the same results come out (Graphs 5.23 & 5.23).

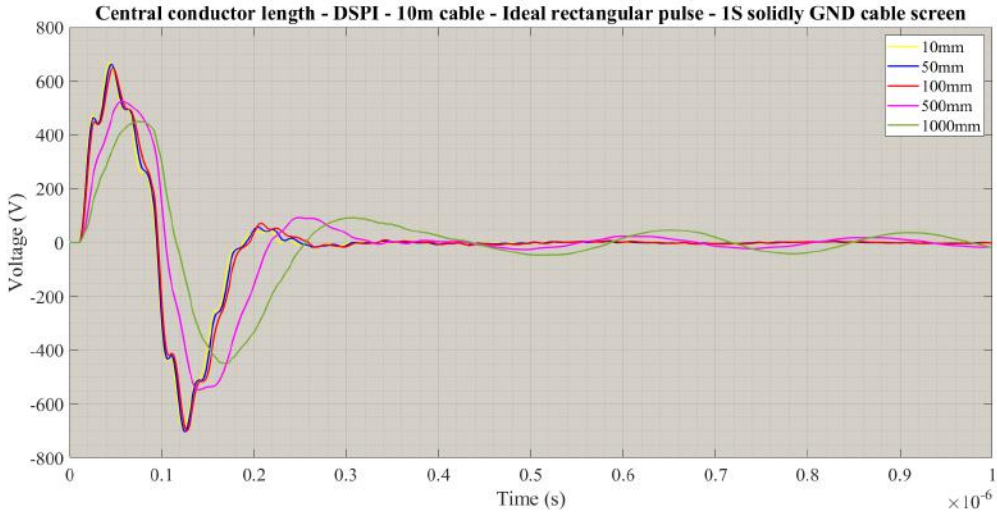

Figure 5.23: DSPI - length of measurement segment - 10 m mini-cable - single side solidly grounded cable screen (PSCAD simulations)

Figure 5.24: SSPI - length of measurement segment - 10 m mini-cable - single side solidly grounded cable screen (PSCAD simulations)

As graph illustrates, by grounding the mini-cable screen through a 400 Ω resistor (as the best found grounding practice), also similar results as those for the ungrounded case are achieved.

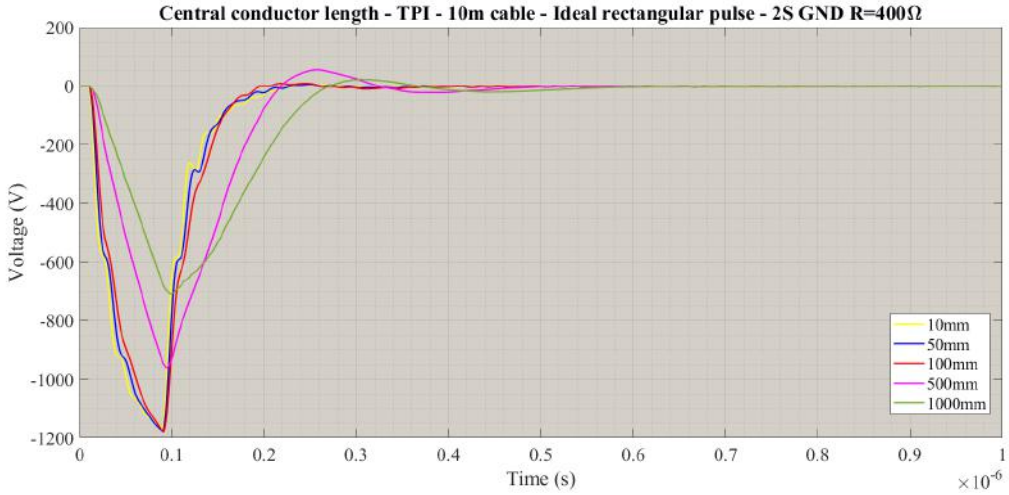

Figure 5.25: TPI - length of measurement segment - 10 m mini-cable - double side grounded cable screen through a 400 Ω resistor (PSCAD simulations)

5.2.4 Termination parameters

In this part, influence of changes in the termination parameters like capacitance and inductance are analyzed. Changes in V_{pea} by manipulating the termination resistance is evaluated in combination with mini-cable screen grounding.

5.2.4.1 Capacitance

Effect of change in the termination capacitance in V_{pea} is assessed in simulations 5.26, 5.26, 5.26 and 5.26. This test is repeated for 1, 2, 4 and 8 nF capacitors for all the setups when their cable screen is floated.

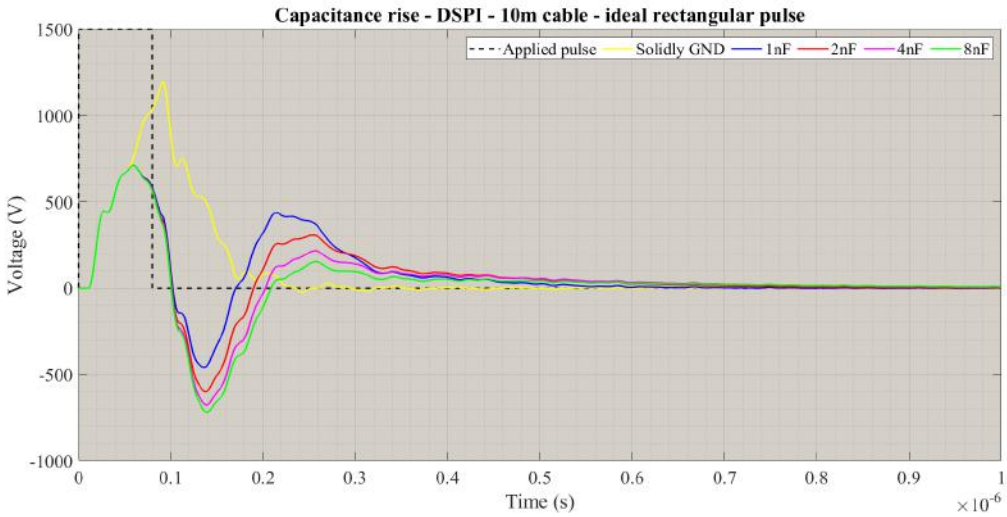

Figure 5.26: DSPI - Response of 5 m cable to ideal rectangular pulse, at different capacitor values (PSCAD simulations)

Figure 5.26 reveals that increase in termination capacitor leads to increase in the post-pulse undershoot magnitude for a 10m mini-cable test, while the post-pulse overshoot is forced to be damped simultaneously. Change in capacitor values has almost no effect on the oscillation frequency, as it maintains a value of $5.14MHz$ for the all capacitor values. Graph 5.27 related to SSPI simulations agrees precisely our findings regarding to DSPI simulations. It is also conspicuous that, in DSPI and SSPI setups, $\left|\widehat{V}_{pea}\right|$ rockets, whereas the post-pulse undershoot/overshoot disappear completely. Moreover, in this case PW_{pea} is almost doubled, negatively effecting resolution of the detection procedure.

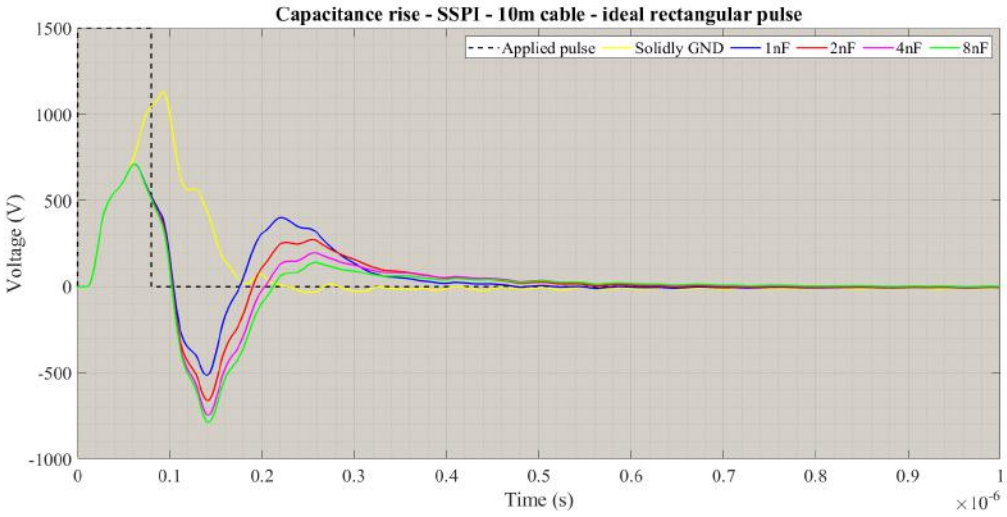

Figure 5.27: SSPI - Response of 5 m cable to ideal rectangular pulse, at different capacitor values (PSCAD simulations)

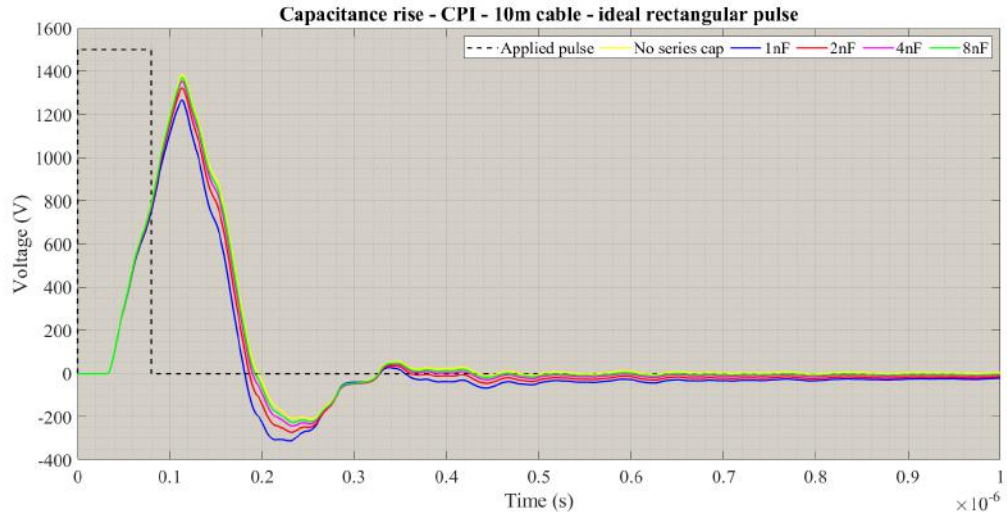

Figure 5.28: CPI - Response of 5 m cable to ideal rectangular pulse, at different capacitor values (PSCAD simulations)

In CPI setup (graph 5.28), where unlike the other practices the capacitor is deployed in the injection circuit, change in the capacitance is not very deterministic in the output voltage waveshape. The only sensible changes are a gentle downshift in the local extrema by the capacitance rise and moderate horizontal compression of the pulse shape.

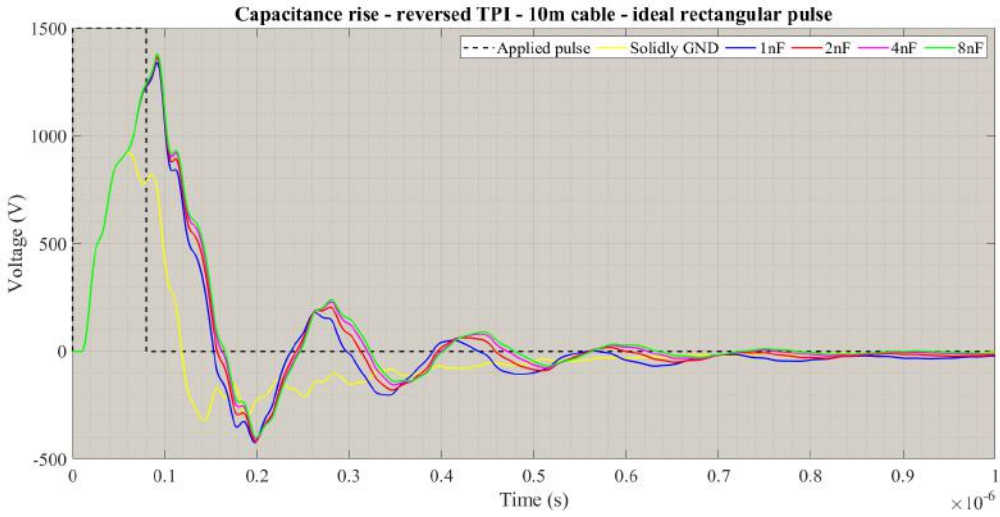

Figure 5.29: TPI - Response of 5 m cable to ideal rectangular pulse, at different capacitor values (PSCAD simulations)

Similar to CPI, TPI also experiences no considerable variation by changing the capacitance, however in contrary to CPI, its shift orientation is upward. Apparently, in the setups with higher capacitance the post-pulse oscillations lead those with lower capacitance. In addition, if the termination is solidly grounded, the main post-pulse oscillation disappears, whereas the high frequency components maintain in the system and after the reaching a local minimum the pulse starts being gradually damped out. Strong decay in $\widehat{V}_{pea}$ as well as pulse width plunge can be cited as the other significant consequences of the capacitor elimination.

5.2.4.2 Stray inductance

In this stage, by changing the termination values from 0 to $8\mu H$, deformation of the output pulsed voltage is analyzed.

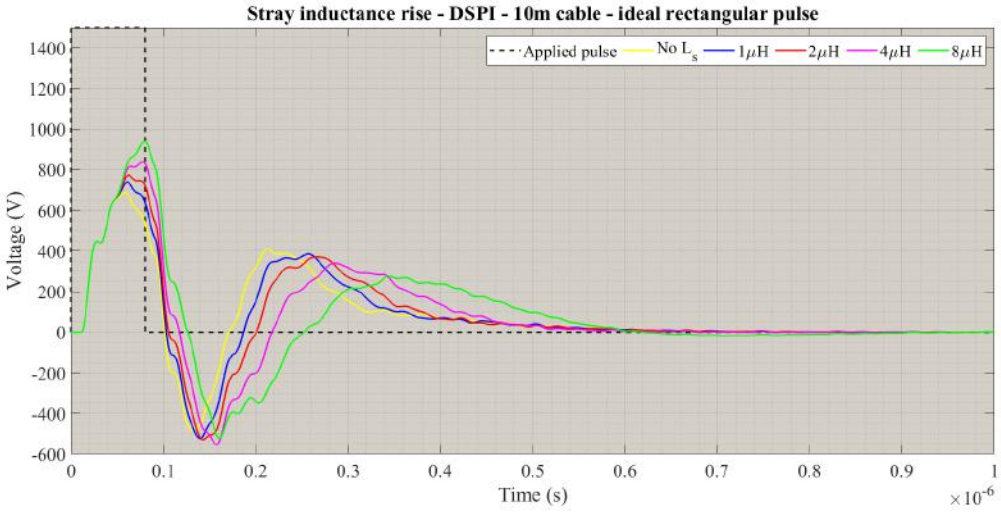

Figure 5.30: DSPI - Response of 5 m cable to ideal rectangular pulse, at different stray inductance values (PSCAD simulations)

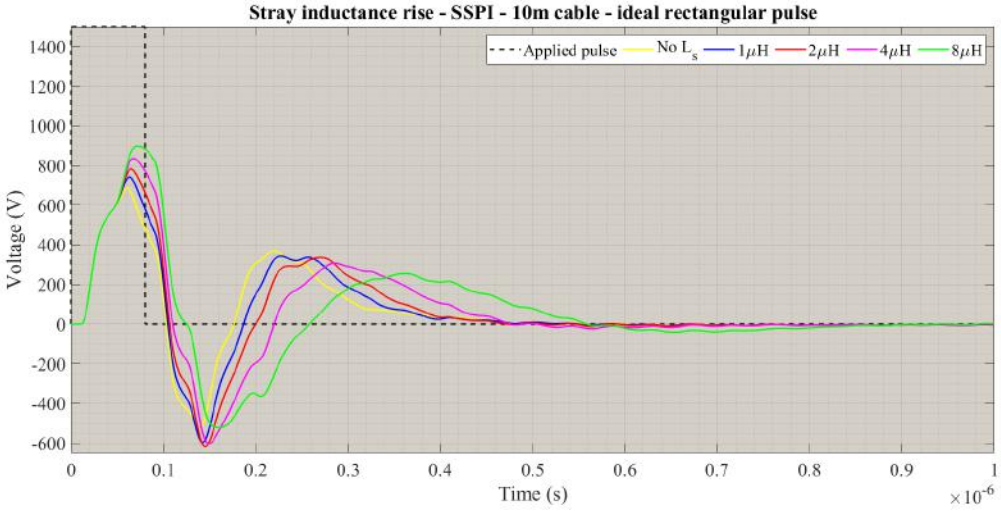

Figure 5.31: SSPI - Response of 5 m cable to ideal rectangular pulse, at different stray inductance values (PSCAD simulations)

Figures 5.30, 5.31, 5.32 and 5.33 imply that by inductance rise,

— In DSPI and SSPI, $\hat{V}_{pea}$ increases, while contrariwise it drops considerably in TPI and moderately in CPI.

— In all setups, PW_{pea} is stretched.

— The oscillation frequency decreases and the pulse is settled. This effect is less intense in CPI.

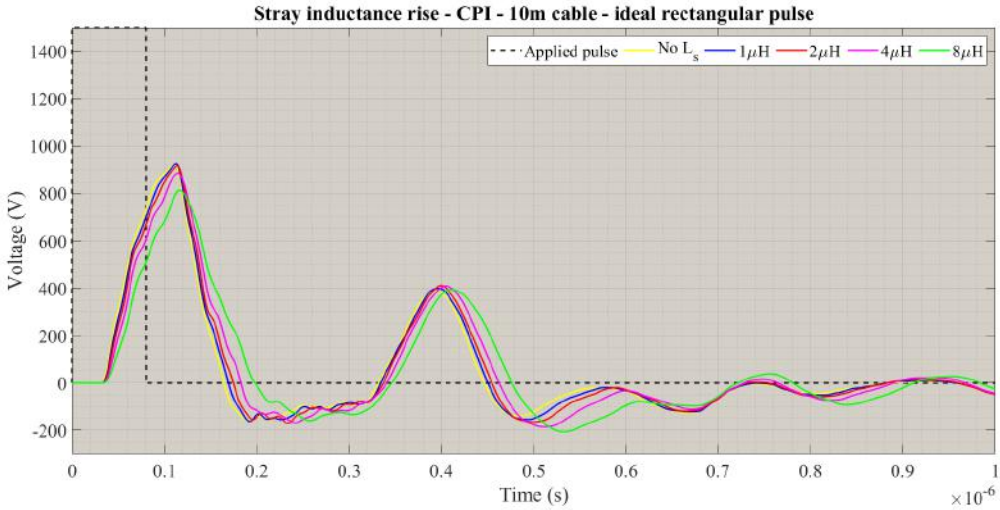

Figure 5.32: CPI - Response of 5 m cable to ideal rectangular pulse, at different stray inductance values (PSCAD simulations)

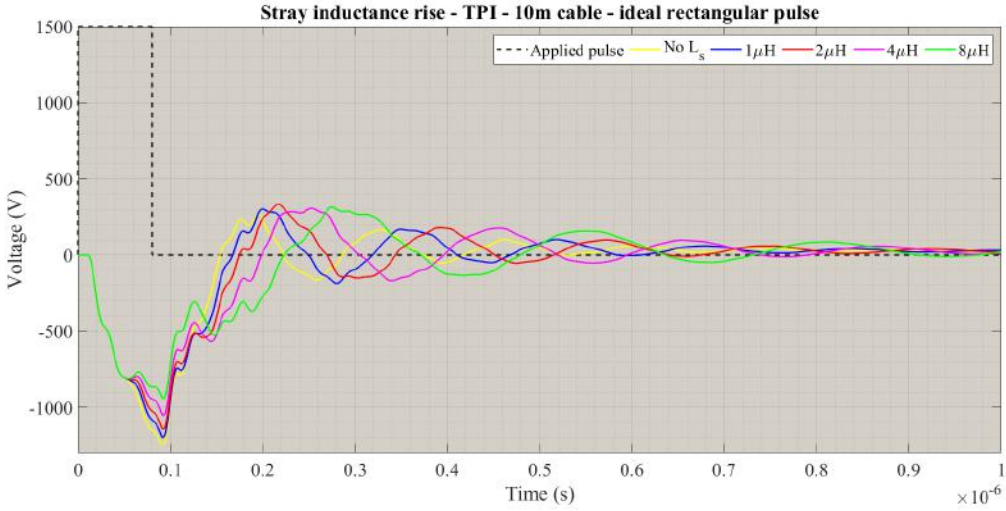

Figure 5.33: TPI - Response of 5 m cable to ideal rectangular pulse, at different stray inductance values (PSCAD simulations)

5.2.5 Mini-cable permittivity

The fundamental properties of a dielectric, such as relative permittivity ($\epsilon_{r,xlpe}$) and conductivity ($\sigma_{r,xlpe}$), usually are altered under influence of thermal and electrical stresses, aging and degradation, etc. As in an ultra-short test, change in conductivity of the insulation is negligible, the sensitivity analysis is only performed for XLPE permittivity. The simulations are repeated for relative permittivity values of 2, 2.38, 3 and 4.

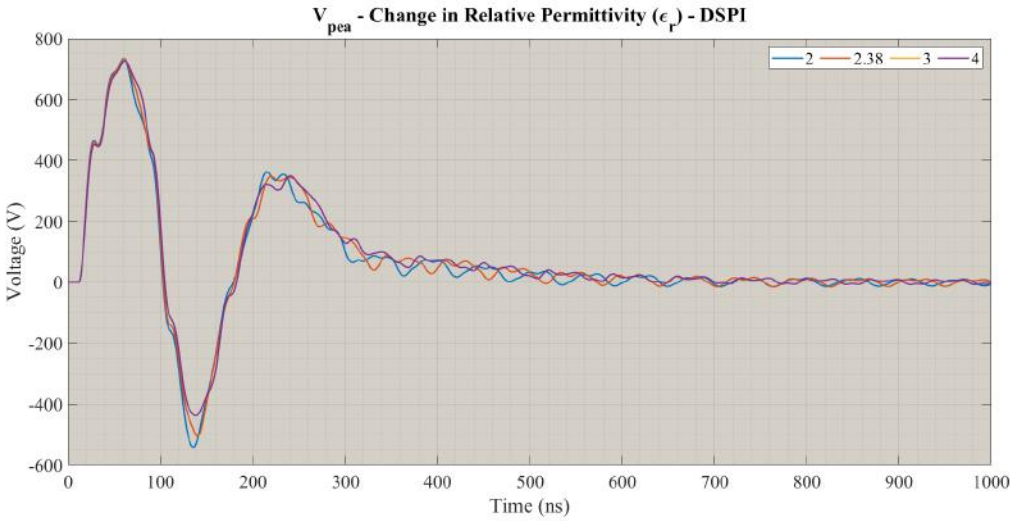

Figure 5.34: DSPI - sensitivity analysis of dielectric permittivity (PSCAD simulations)

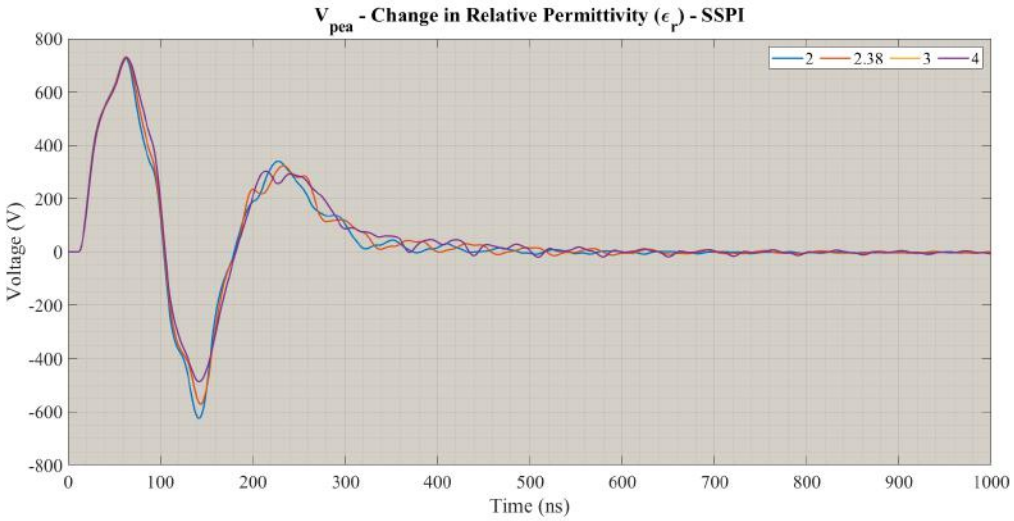

Figure 5.35: SSPI - sensitivity analysis of dielectric permittivity (PSCAD simulations)

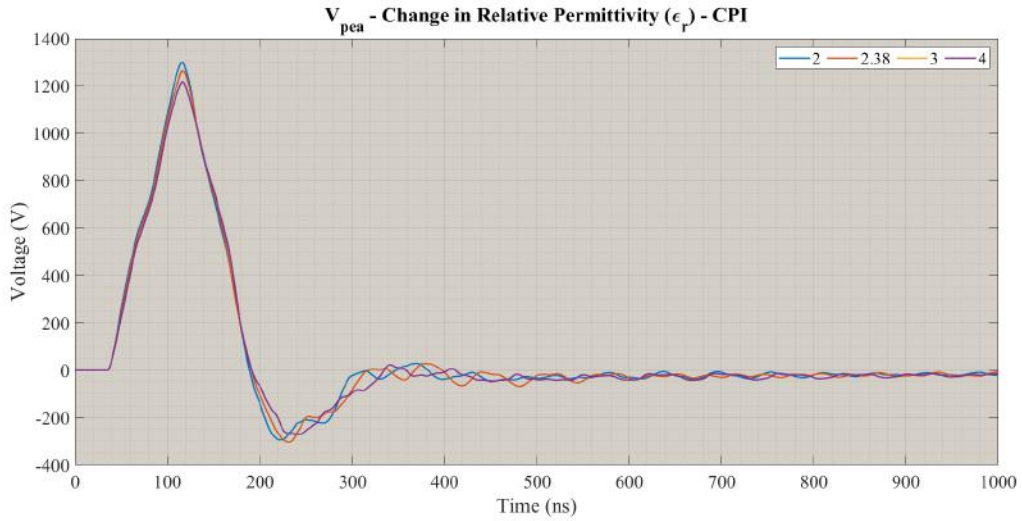

Figure 5.36: CPI - sensitivity analysis of dielectric permittivity (PSCAD simulations)

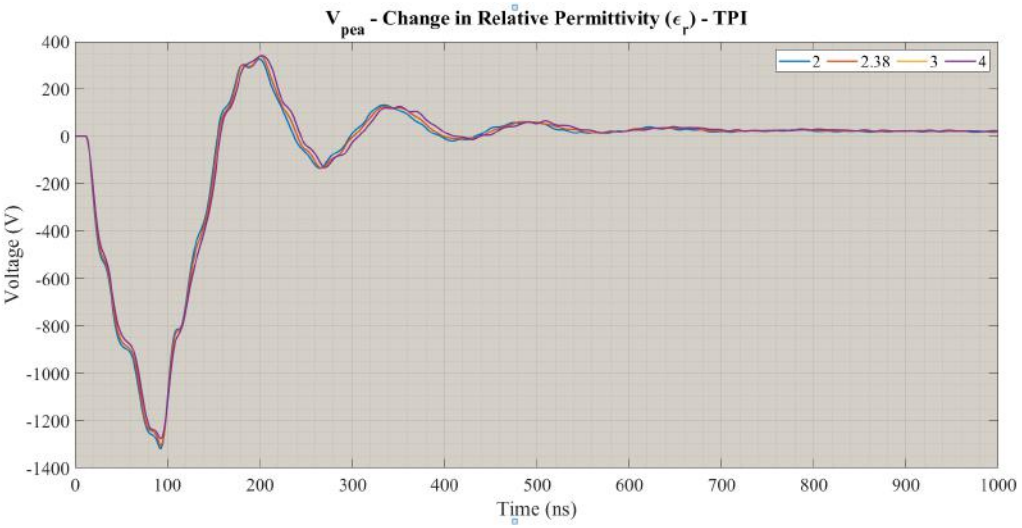

Figure 5.37: TPI - sensitivity analysis of dielectric permittivity (PSCAD simulations)

According to graphs 5.34, 5.35, 5.36 and 5.37, by raising the dielectric permittivity the following items are concluded,

— Generally, change in V_{pea} is not significant and deterministic

— Slightly higher damping ratio and lower oscillation frequencies are observed

— In DSPI and SSPI, the post-pulse undershoot magnitude declines.

— Influence on $\widehat{V}_{pea}$ in all cases are negligible, except of CPI in which the value drops by almost $100\,V$ by changing ϵ_r from 2 to 4.

5.3 Grounding practices

In this section, influence of change in grounding configuration, both for the mini-cable screen and PEA table, is evaluated.

5.3.1 Mini-cable screen

In design of systems working at high frequencies, a quality grounding is of crucial importance. An inferior grounding may lead to various problems, such as rise in insertion dissipation, impedance mismatches, superfluous reactive/resistive loading, change in system's electrical length, noises, etc. Moreover, some references [77] cited that leaving a transmission line ungrounded may result in much lower operational frequency interval, contributing to oscillatory behaviour of the system. In some practices like DSPI and SSPI, the screen conductor can not be directly connected to earth in proximity of the injection spot. In such a case all the injected pulse would propagate straight into earth without contribution in potential development across the target insulation. Some others [78] discuss inevitability of coaxial cable grounding at high frequencies (greater than 100 kHz), especially when the line is 20 times as long as the applied signal wavelength or more[78]. In our case When frequency rises sufficiently high, the current will make a path to earth through stray capacitances, contributing to common mode loops, which act as sources for noise. Th following group of graphs assess effect of screen grounding for a 10 m mini-cable.

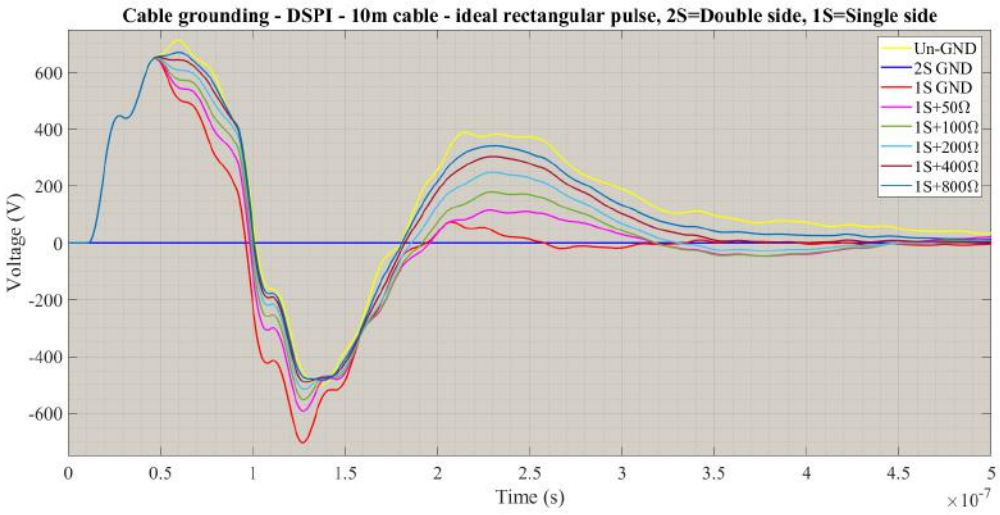

Figure 5.38: DSPI - Grounding of screen conductor - 10 m mini-cable (PSCAD simulations)

Graphs 5.38 and 5.39 reveal that, in DSPI and SSPI setups, by grounding both sides (2S) of the mini-cable no voltage is developed across the target dielectric, but by earthing only a single spot adjacent to the termination (1S) some important findings are obtained,

— the second peak diminishes significantly

— Earth path resistance is directly proportional to the second crest amplitude

— Earth path resistance is also directly proportional to the main pulse width

— Although by floating the screen a higher $\widehat{V}_{pea}$ is achieved, it contributes significantly to the post-pulse oscillations and pulse width extension

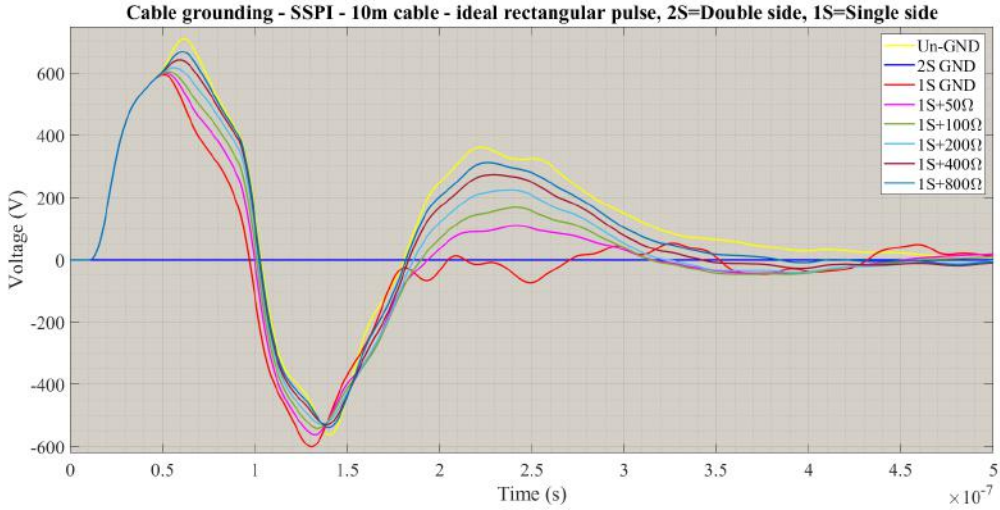

Figure 5.39: SSPI - Grounding of screen conductor - 10 m mini-cable (PSCAD simulations)

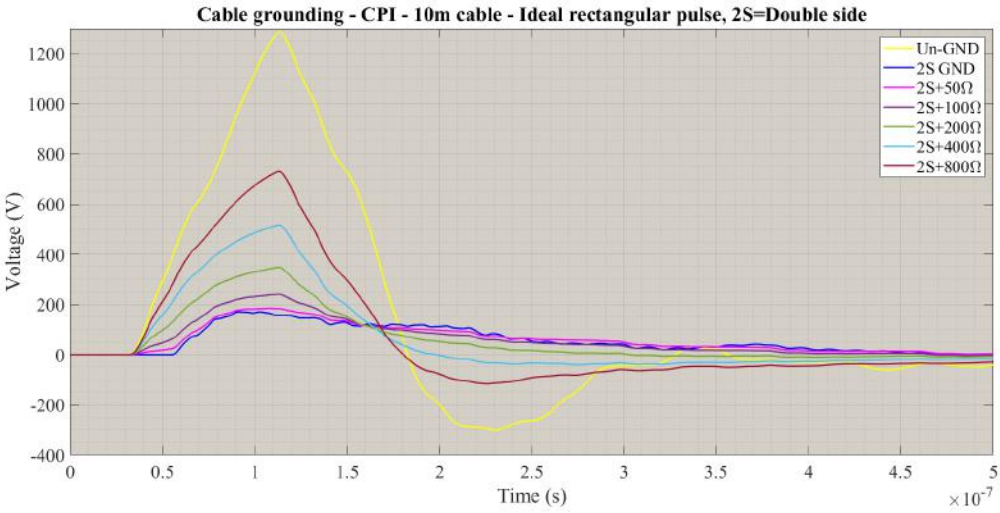

Figure 5.40: CPI - Grounding of screen conductor - 10 m mini-cable (PSCAD simulations)

Unlike DSPI and SSPI, it seems grounding of the cable's screen can not be a good option for CPI, since in this case $\widehat{V}_{pea}$ drops dramatically. According to the simulations, more isolated screen from earth yields better results for CPI. The simulations for different configurations of $1S$ grounding for CPI, shows also the same results.

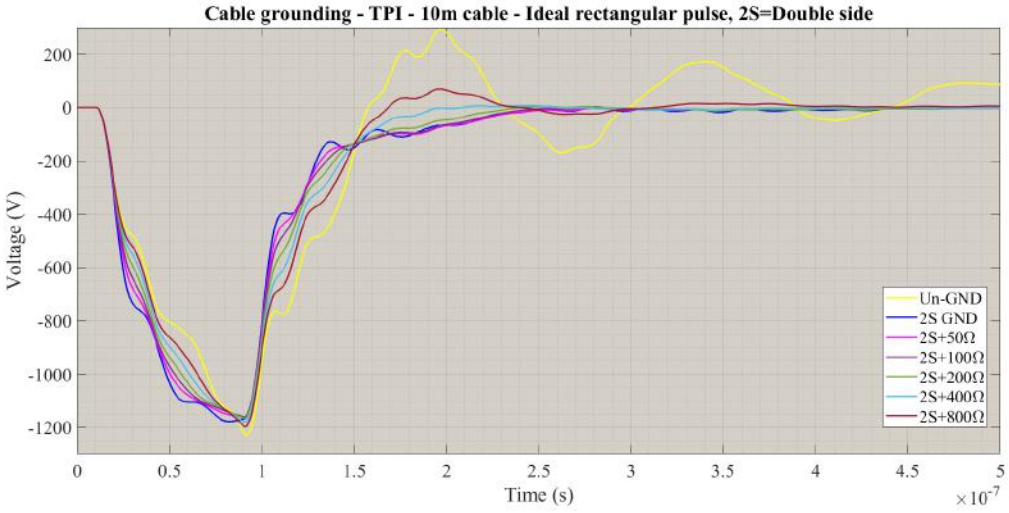

Figure 5.41: TPI - Grounding of screen conductor - 10m mini-cable - Both sides of the cable is grounded (PSCAD simulations)

A different scenario takes place for TPI practice as illustrated in graph 5.41. The TPI oscillatory behaviour is refined by coupling the screen conductor to earth potential (both 1S or 2S configurations). In fact, it gives rise to the system damping. A series resistance also may help smoothing the wave shape by damping out of the high frequency partial oscillations. The value of this resistor needs to be carefully selected, as excessive resistance leads to extra post-pulse undershoot (assuming absolute value of the voltage).

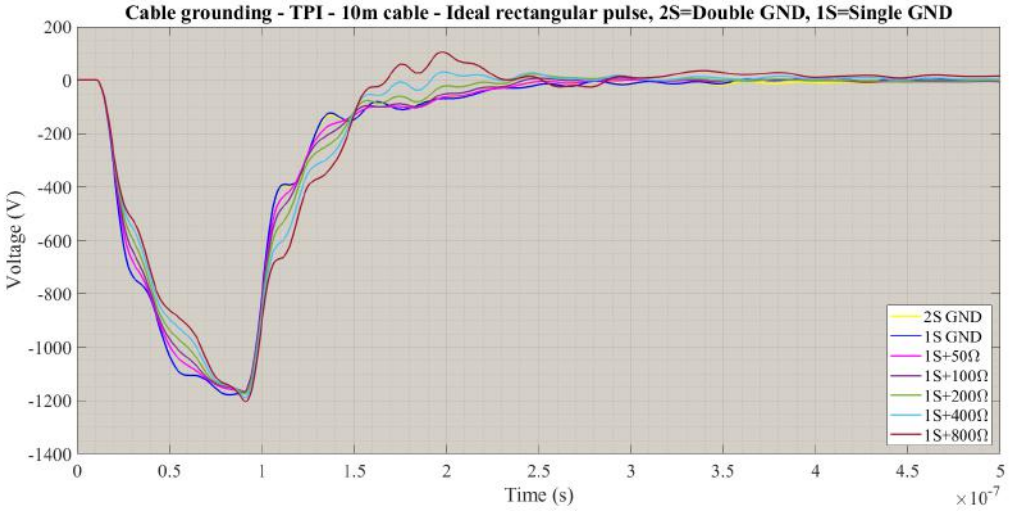

Figure 5.42: TPI - Grounding of screen conductor - 10m mini-cable - Only one side (in measurement table proximity) is grounded (PSCAD simulations)

Graph 5.42 show that a better result in terms of pulse width and oscillations is obtained when a single spot in proximity of the central exposed parts is grounded for each cable half through a

resistance, as slightly lower oscillations than 2S practice is achieved.

5.3.2 Table

Figures 5.43, 5.44, 5.45 and 5.46 uncovers a drop in output pulse magnitude ($\widehat{V}_{pea}$), for DSPI and SSPI, by increasing the resistance, whether the mini-cable is connected to earth or not. By increasing the earth resistance in all cases the slew rates also decline, which is not desirable.

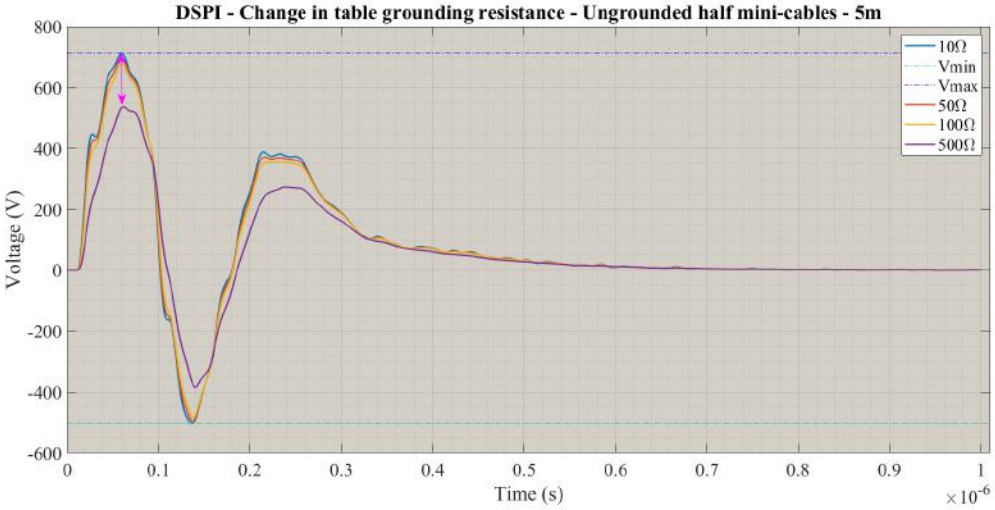

Figure 5.43: DSPI - change in table grounding resistance - floated half cables (PSCAD simulations)

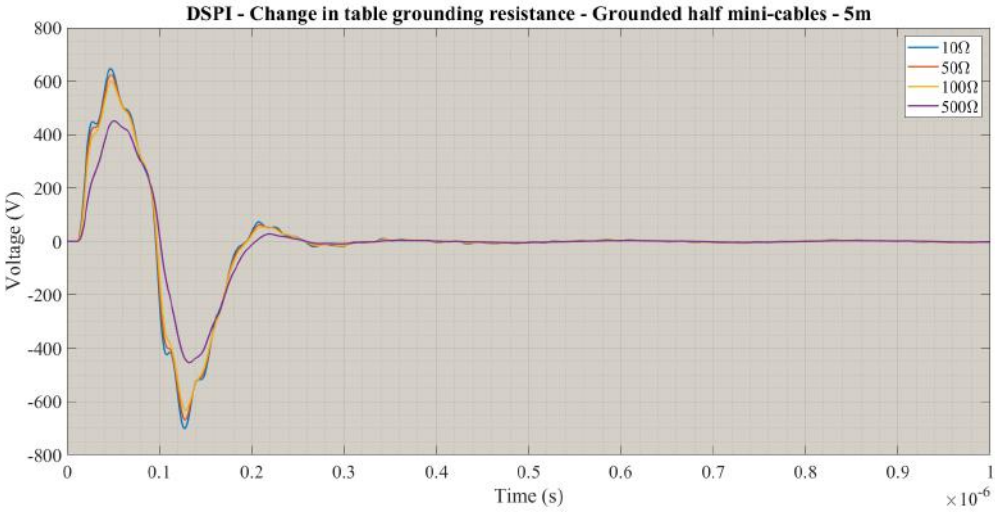

Figure 5.44: DSPI - change in table grounding resistance - grounded half cables (PSCAD simulations)

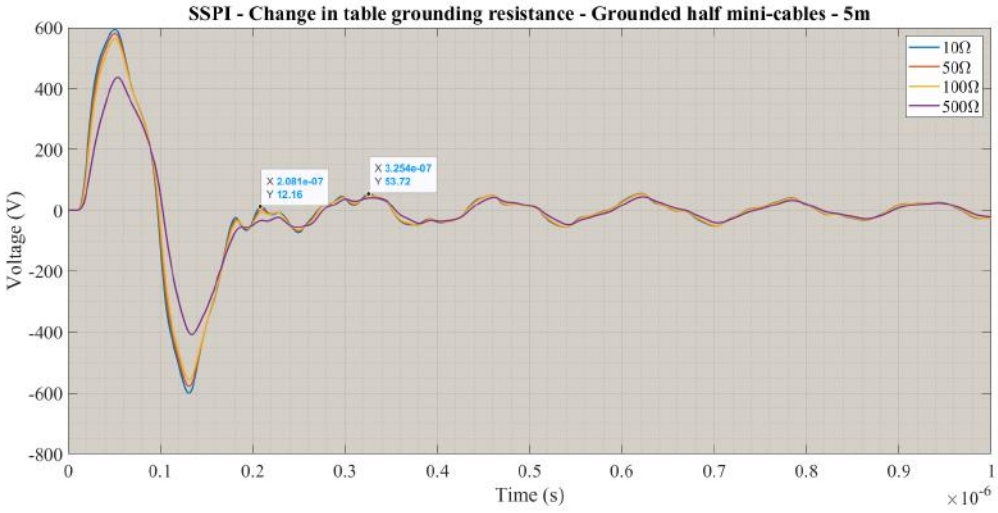

Figure 5.45: SSPI - change in table grounding resistance - GND half cables (PSCAD simulations)

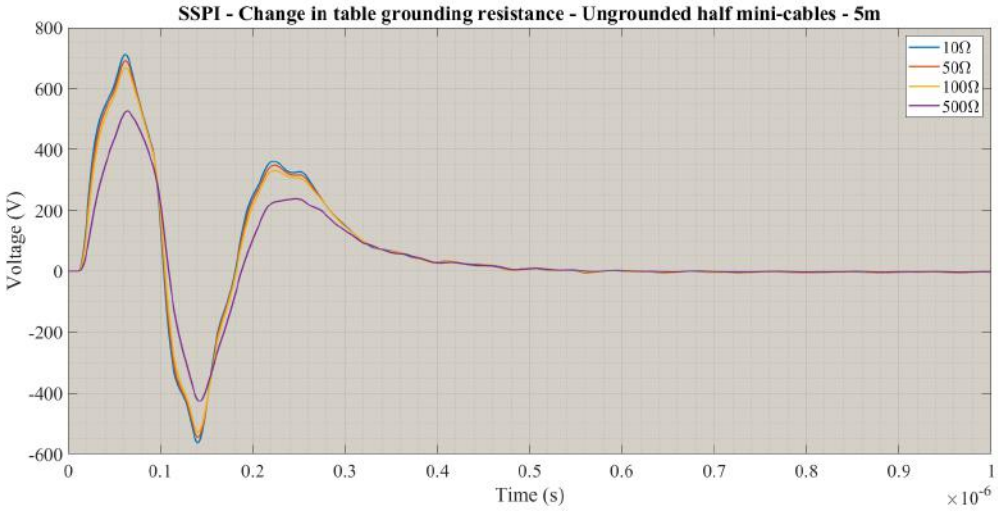

Figure 5.46: SSPI - change in table grounding resistance - FLT half cables (PSCAD simulations)

In CPI, similar to the recent cases, by increasing the resistance $\hat{V}_{pea}$ drops, although the rate of descent is lower than the recent cases. At higher resistance values the down-drop is more sensible, falling from just above 1285 V to 1027 V for 10 Ω and 0.5 $k\Omega$ accordingly. Similar to DSPI and SSPI, in CPI high grounding resistance values have negative impact on the pulse rise time.

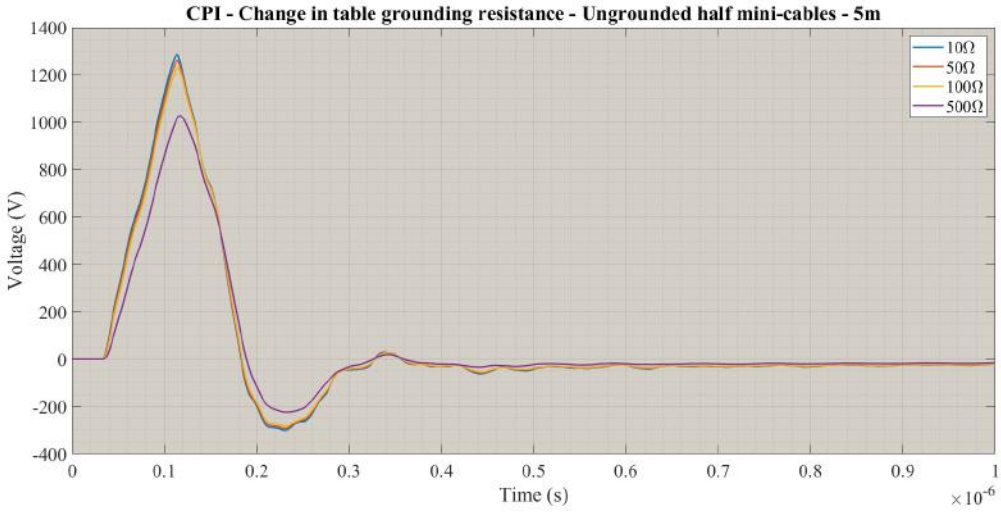

Figure 5.47: CPI - change in table grounding resistance - floated half cables (PSCAD simulations)

A rather high collapse, in output voltage, is seen when both half cable parts are grounded, forming a non-practical configuration that also produces high frequency noises. Increase in the resistance, helps damping the noises, despite a minor drop in the peak and rise time.

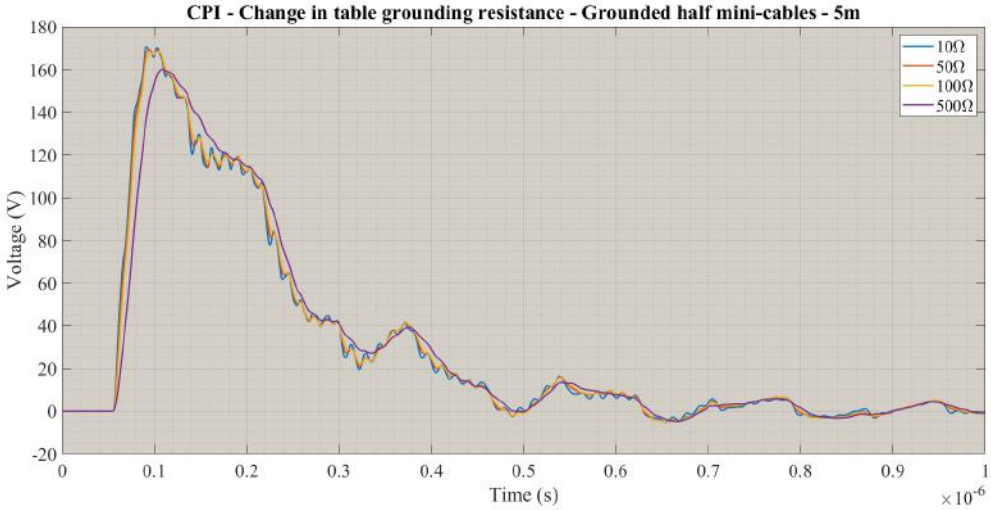

Figure 5.48: CPI - change in table grounding resistance - grounded half cables (PSCAD simulations)

As expected, in TPI, the table earthing is not favourable at all as illustrated in graphs 5.49 and 5.50. A rather high fall in the peaks is sensed by resistance decrease depending on the resistor value. The results are independent of mini-cable screen grounding practice. Having said that, very high resistance grounding helps suppression of the noises, both on the main pulse bulk and the tail oscillations to a large extent.

The most important finding of the current section is reported by figure 5.50. It can be observed that a combined effect of 1S mini-cable grounding and a highly resistive table ground yields

an almost square shaped pulsed voltage at the output with sufficiently high slew rate and well damped oscillations, however the crest drops moderately.

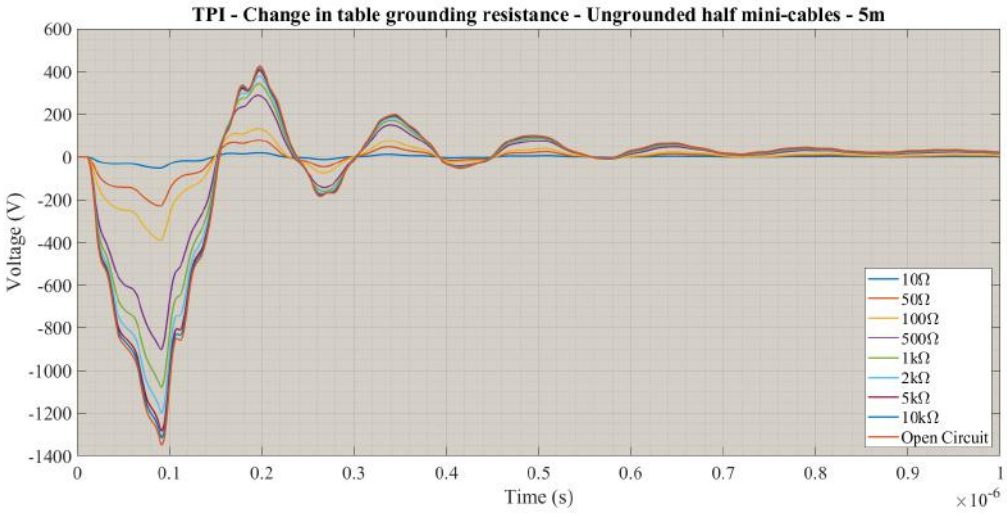

Figure 5.49: TPI - change in table grounding resistance - floated half cables (PSCAD simulations)

Figure 5.50: TPI - change in table grounding resistance - grounded half cables (PSCAD simulations)

5.4 Step response

From Heaviside step response of a system some important metrics like, delay, rise time, time duration to maximum overshoot, peak value of overshoot/undershoot, settling time, oscillation frequency, stability, etc. can be known. In other words, step response gives us a good insight into general behaviour of the system.

5.4.1 SSPI & DSPI

Graph 5.51 compares voltages and currents of SSPI and DSPI setups whether the mini-cable pieces are grounded ($1S$) or floated. Graphs 5.52 and 5.53 also simulate time-domain phase angles between the voltage and current vectors at the insertion spot.

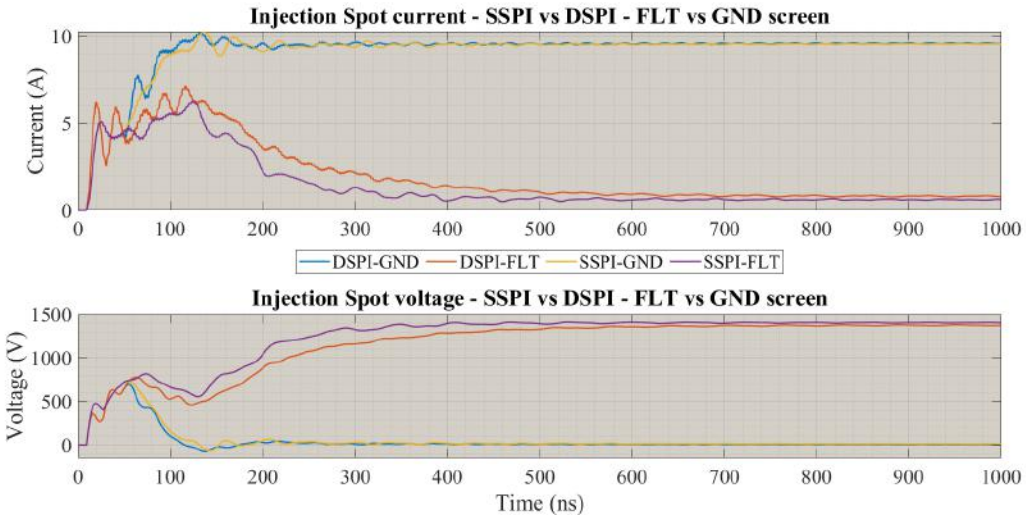

Figure 5.51: DSPI vs SSPI - Heaviside step response at injection spot - 10 m mini-cable - FLT & GND Halves (PSCAD simulations)

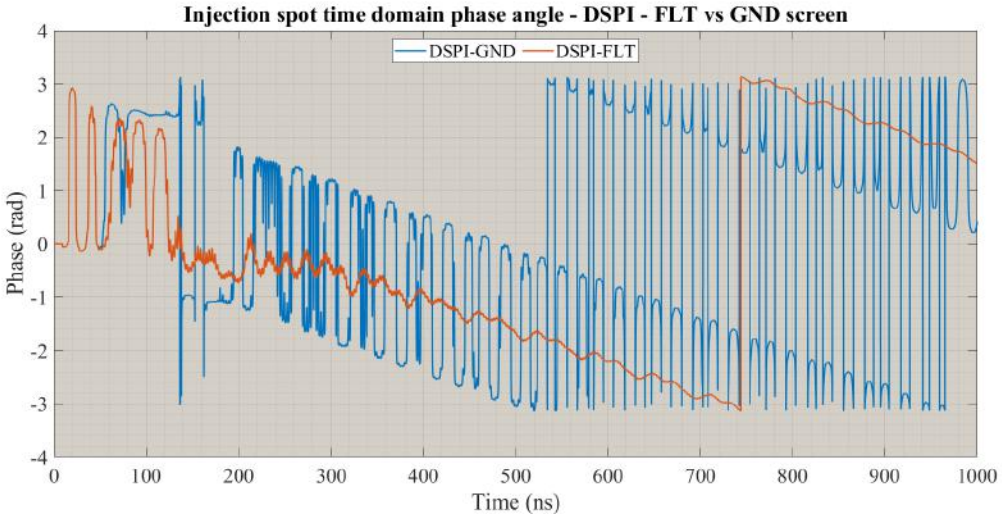

Figure 5.52: DSPI - Heaviside step input - Time-domain phase angle between instantaneous injection voltage & current - 10 m mini-cable - FLT vs GND (PSCAD simulations)

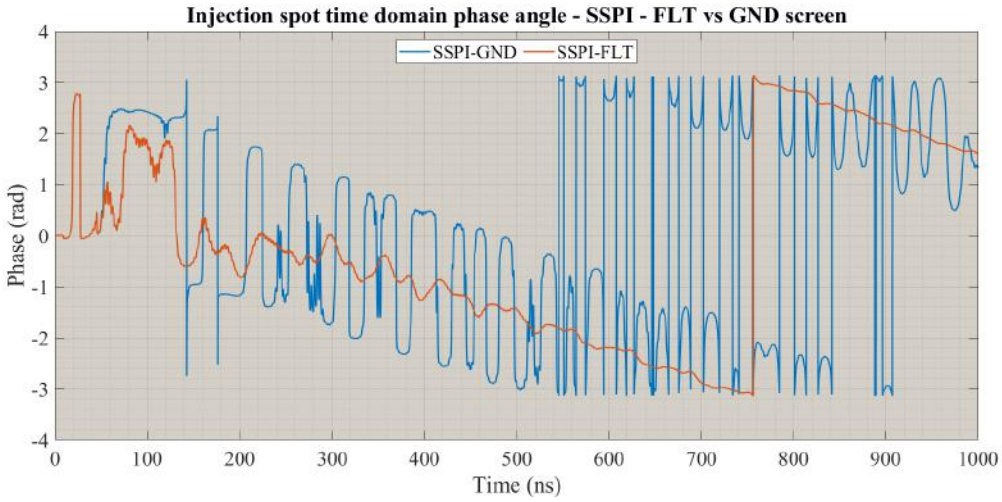

Figure 5.53: SSPI - Heaviside step input - Time-domain phase angle between instantaneous injection voltage & current - 10 m mini-cable - FLT vs GND (PSCAD simulations)

From the graphs above show that,

— The voltage drops to zero after an initial overshoot when the cable is grounded. In ungrounded case, after the overshoot a considerable dig is observed.

— Naturally, the currents behaves precisely opposite to the voltages. In fact in the both setups grounded practices, the currents converge to a rather fixed value after the initial overshoot and subsequent undershoot, while for floated cases only the initial overshoot appears and it maintains zero value for the rest of the time period.

— Figures 5.52 and 5.52 prove that,

a) **First region:** the system initially behave mainly inductive, therefore an sharp rise in current and voltage magnitude is observed. The crest oscillation implies underdamped behaviour of the system in this region.

b) **Second region:** in this region, after an initial violent phase shift (around 140 ns and 120 ns for FLT and GND cases respectively), which shows itself as a significant voltage dig in the FLT case, equivalent capacitance of the system starts being charged. The figures show much more underdamped behaviour for the GND case than its alternative. The charging time period for the GND case is much shorter than the FLT one (approximately 200 ns shorter).

c) **Third region:** in the GND case the current flows into earth through the coaxial cable. The extreme phase alteration is likely to be because of series inductance and parallel capacitance of the transmission line. Therefore, no voltage is established across the target insulation anymore. In contrast to the recent case, in the FLT system

the cumulative capacitance starts being discharged with a slow time constant giving an slight rise to inductive current. Additionally, the voltage across the dielectric is conserved, as the capacitor is permanently being charged by the tail DC component of the Heaviside step input.

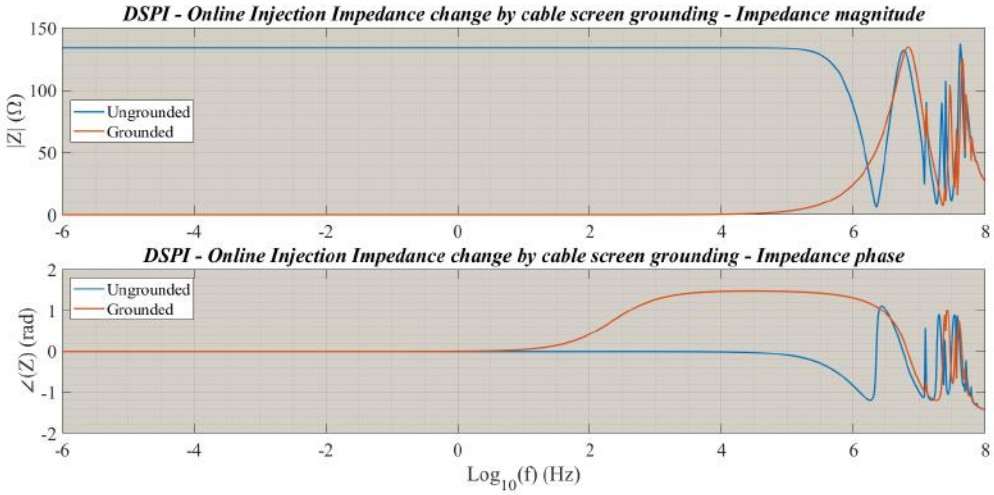

Figure 5.54: DSPI -Injection spot frequency dependent impedance - step response (PSCAD simulations)

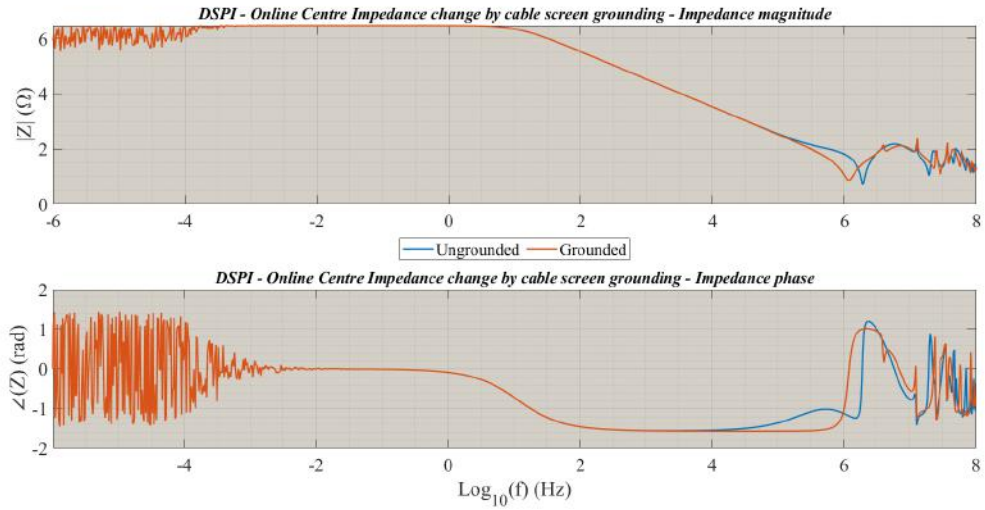

Figure 5.55: DSPI -Central spot frequency dependent impedance - step response (PSCAD simulations)

Graphs 5.54 and 5.55 show frequency scan of the Thevenin impedances seen from the injection and central spots respectively, for DSPI. Graph 5.54 implies that if the mini-cable is grounded,

— The Thevenin impedance seen from injection junction shows an inductive behaviour from almost $1\,kHz$ to just below $10\,MHz$, where the phase changes to capacitive.

— The impedance is at very low value close to zero, however at resonance frequency it escalates to around 140 Ω. Therefore, only the frequency components of the injected pulse in the resonance bandwidth contribute to the voltage formed at the injection spot.

Very similar trends as DSPI are also resulted for SSPI. On the other hand, if the screen is left ungrounded (1S) in DSPI and SSPI,

— Unlike the grounded case, if the mini-cable pieces are left floated, at lower frequencies up to 100 kHz, the system shows a resistive behaviour. Above 100 kHz the impedance becomes first capacitive, where the impedance magnitude drops to a bit higher than zero, and afterwards the phase shifts back to inductive, being recovered to 140 Ω again.

— In contrary to the grounded case, low frequency components participate in voltage formation at the injection spot.

— Similar to the grounded practices, beyond the system natural frequency, multiple resonances occur.

Figures 5.56 and 5.57 evaluate the cable segments length extension influence on the time-domain step response for DSPI and SSPI setups when the mini-cable halves screen are disconnected from earth.

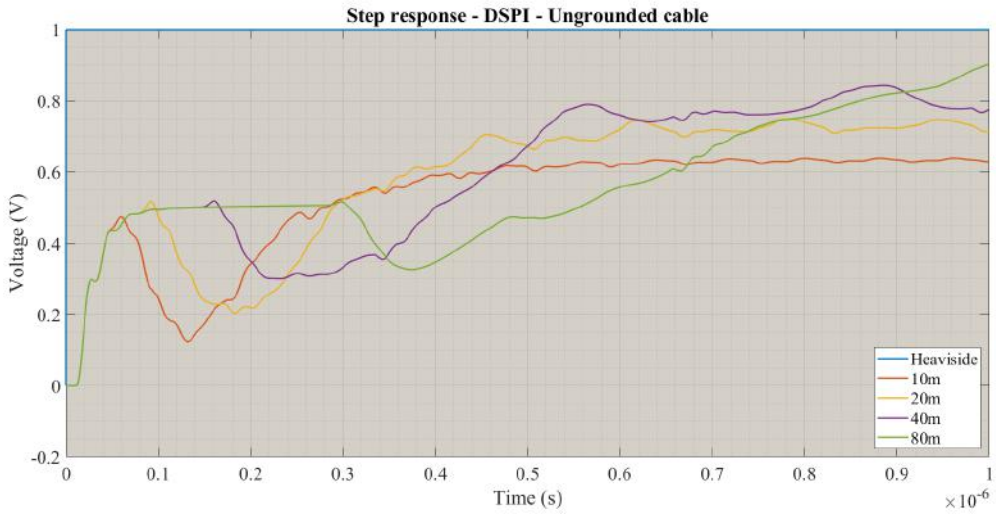

Figure 5.56: DSPI - 10 m mini-cable, Heaviside step response - Floated Halves (PSCAD simulations)

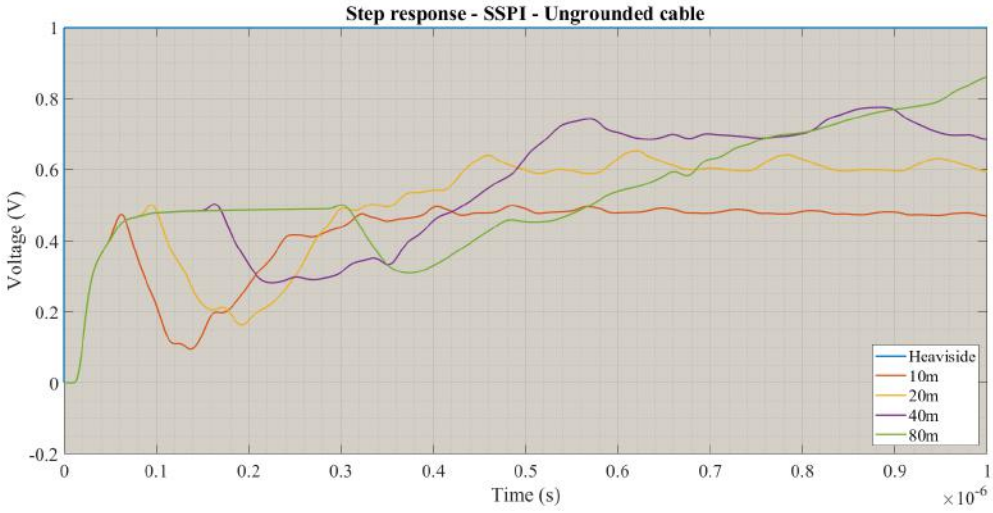

Figure 5.57: SSPI - 10 m mini-cable, Heaviside step response - Floated Halves (PSCAD simulations)

Figures 5.56 and 5.57 imply that,

— By cable enlargement, wider peak and much longer rise time and lower slew rate, are resulted.

— Decay rate in the pulse tail and system damping declines.

— SSPI and DSPI hold more energy in the system when the cable is not grounded, it is still magnified at higher cable length extension.

— The recorded overshoot amplitude does not deviate significantly from the original value by the cable enlargement.

— The voltage gain practically flaps between 43% and 52% for DSPI, and 39%-50% for SSPI

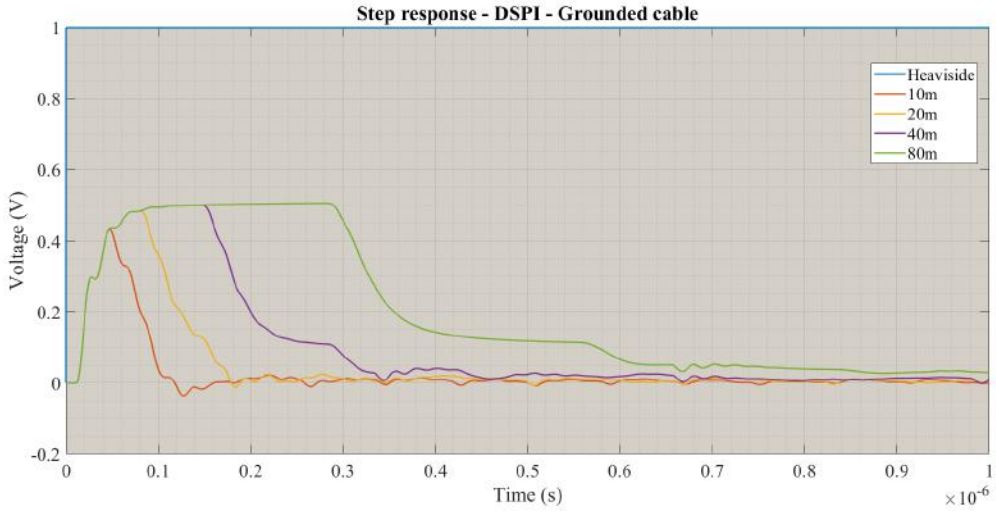

Figure 5.58: DSPI - 10 m mini-cable, Heaviside step response - Grounded Halves (PSCAD simulations)

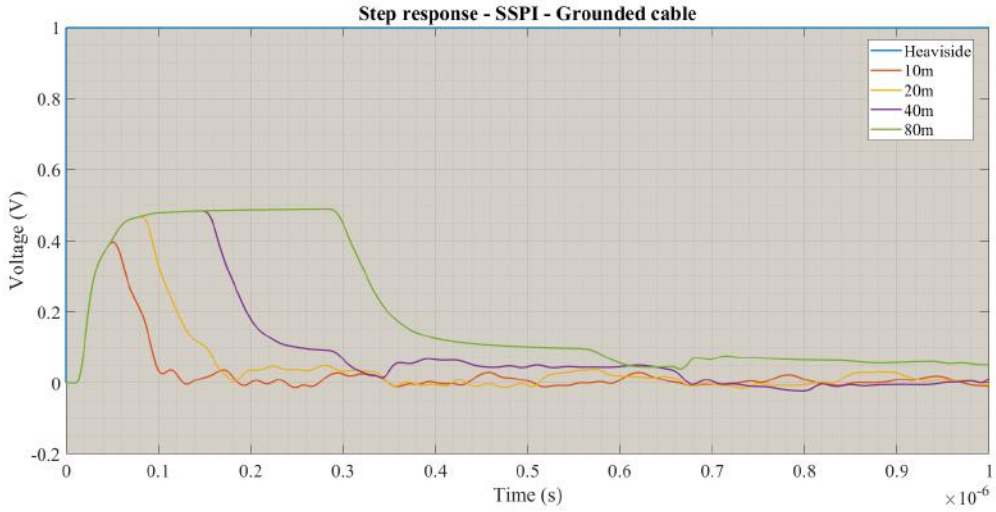

Figure 5.59: SSPI - 10 m mini-cable, Heaviside step response - Grounded Halves (PSCAD simulations)

The same simulations are also run when the cable parts are connected to earth. The results are depicted in graphs 5.58 and 5.59. The followings are concluded,

— Similar to the FLT cases, the voltage crest width is directly proportional to the transmission line length. By expanding the cable from 20 m to 80 m the crest widths also becomes four times larger.

— The line extension gives rise to the post pulse DC offset.

— Less high frequency oscillations are gained at higher lengths

— it seems application of step function while grounding the single side screen is not a good option for impulse shaping at the output when at longer cable samples due to the fact that the pulse width would not be acceptable anymore.

5.4.2 CPI

The simulations are also repeated for CPI. Graphs 5.60 and 5.61 represent the injection point voltage, current and phase angle in time-domain.

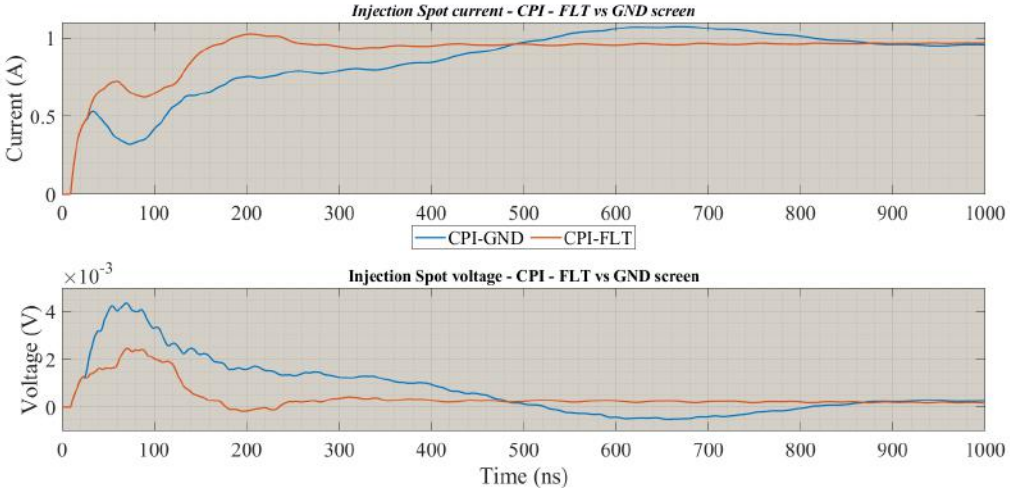

Figure 5.60: CPI - Heaviside step response at injection spot - 10 m mini-cable - FLT & GND Halves (PSCAD simulations)

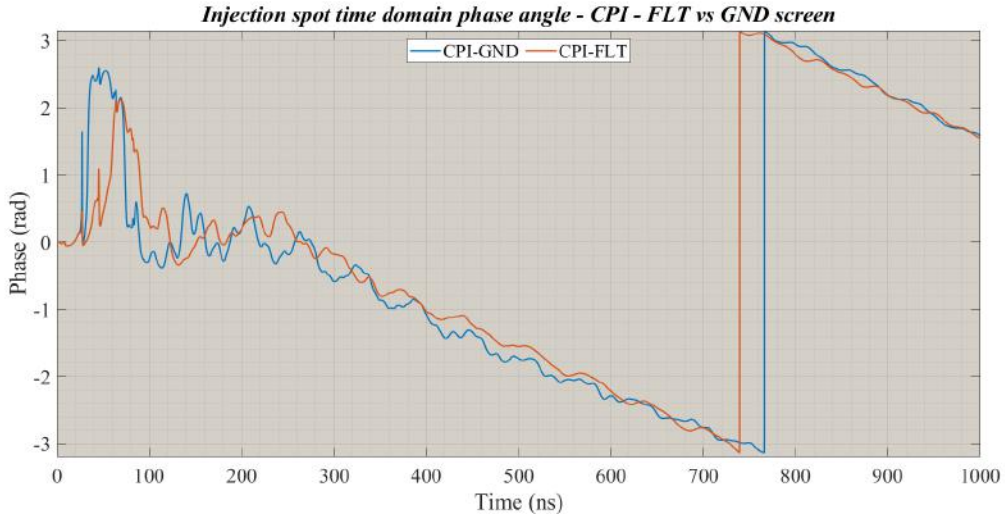

Figure 5.61: CPI - Heaviside step input - Time-domain phase angle between instantaneous injection voltage & current - 10 m mini-cable - FLT vs GND (PSCAD simulations)

The followings are concluded from the graphs above,

— Grounding of the mini-cable sections leads to overall rise of injected voltage while current drops in the transient period.

— Both the voltage and current waves are settled later in the GND case.

— The system damping is higher in FLT case.

— Generally, the screen floated voltage and current waveshapes resemble those of DSPI and SSPI.

— In the GND case, after approximately 500 ns, the voltage falls below and the current exceeds those of the FLT case.

— The initial overshoot in the GND case has much sharper leading and trailing edges than those of the GND practice.

— The phase shift from capacitive to inductive in the GND structure lags its alternative by approximately 40 ns, implying higher total capacitance of the former.

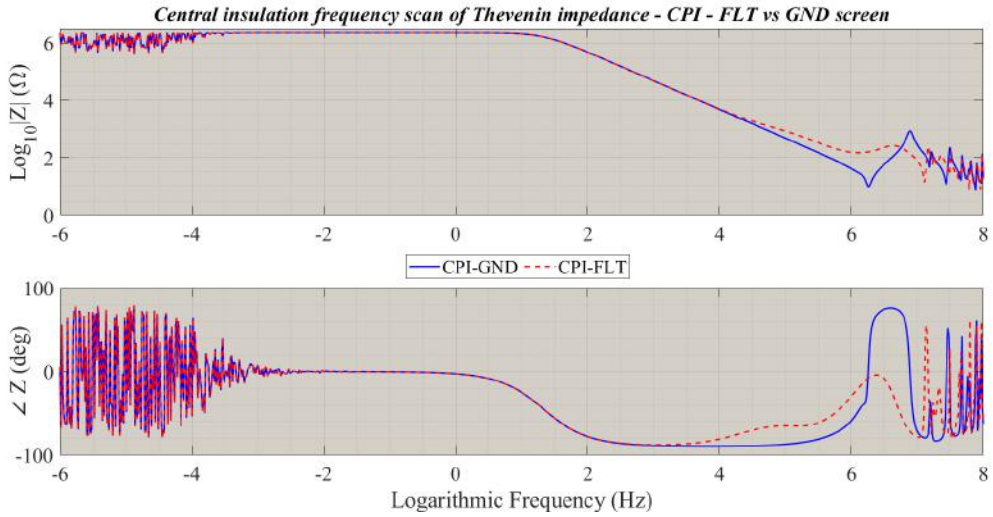

Figure 5.62: CPI -Central spot frequency dependent impedance scan- step response (PSCAD simulations)

Figure 5.62 shows the frequency-dependent Thevenin impedance seen by the target insulation. Apparently, between 13 kHz and 63 MHz, the floated practice sees higher impedance. It means all the frequency components inside this interval participate in voltage creation. Graph 5.63 shows by the mini-cable screen grounding the initial overshoot is almost vanished, $\widehat{V}_{pea}$ collapses and an oscillating current appears at the measurement location.

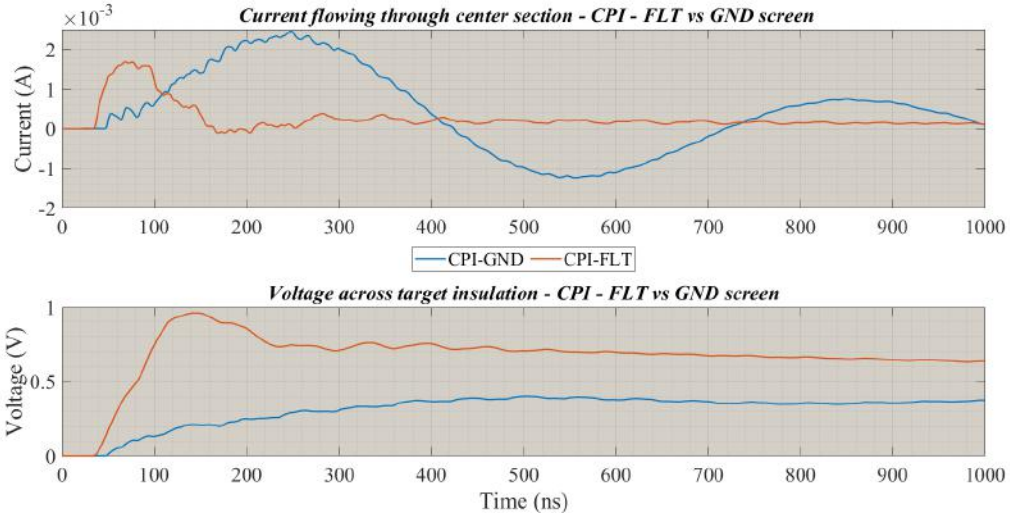

Figure 5.63: CPI - Heaviside step response at center spot - 10 m mini-cable - FLT & GND halves (PSCAD simulations)

Figures 5.64 and 5.65 analyze the cable length extension impact on the output waveshape (V_{pea}).

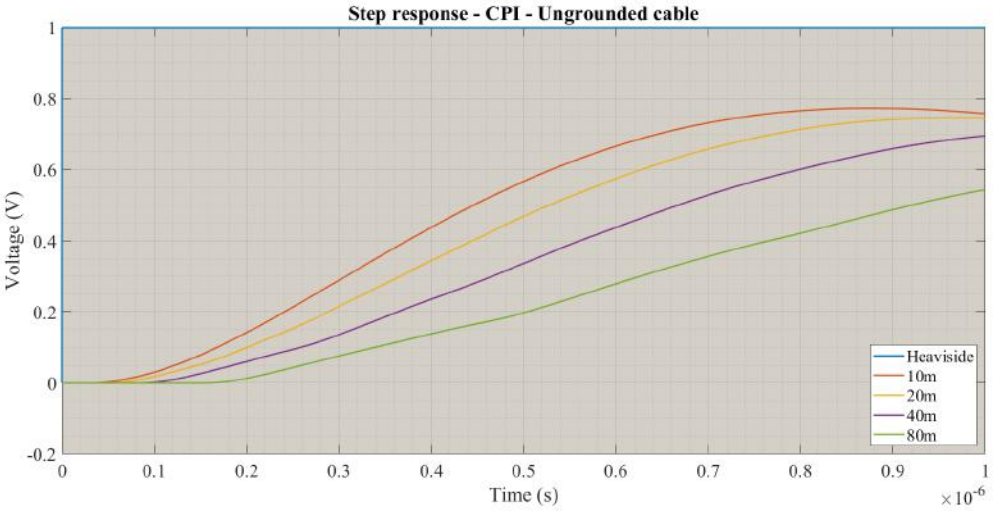

Figure 5.64: CPI - 10 m mini-cable, Heaviside step response - Floated Halves (PSCAD simulations)

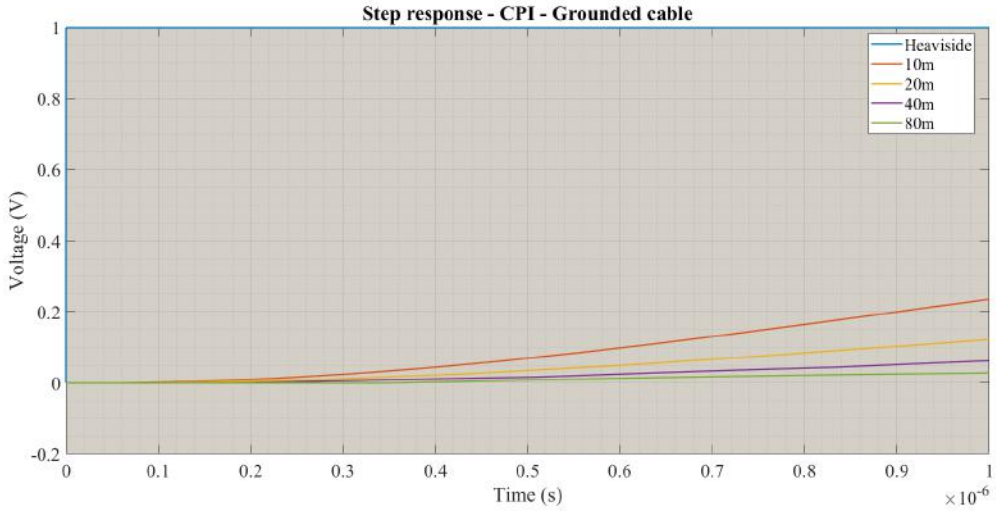

Figure 5.65: CPI - 10 m mini-cable, Heaviside step response - Grounded Halves (PSCAD simulations)

In CPI, the normalized peak value reaches to 77%, (for 10m test cable), however the rise time is much longer, negatively affecting the resolution. It is apparent that the system voltage response is overdamped, for both the GND and FLT screen practices. The damping ratio increases significantly by the screen grounding and length expansion. In response to a unit step input, $\widehat{V}_{pea}$ drops from $0.7\,V$, for the ungrounded case (figure 5.64), to just above $0.2\,V$ (figure 5.65), when the screens are connected to earth. Effect of the cable enlargement is so intense that for $80\,m$ cable simulation, almost no voltage arrives to the target spot. In conclusion, Heaviside step response of CPI setup imparts two important achievements, **a)** in CPI, screen grounding is pointless in terms of voltage gain transfer function and **b)** in practice, for full cable testing (long samples) CPI is inapplicable.

5.4.3 TPI

Similar to the previous items, the time-domain injection spot voltage, current and phase are simulated (Graphs 5.66 & 5.67).

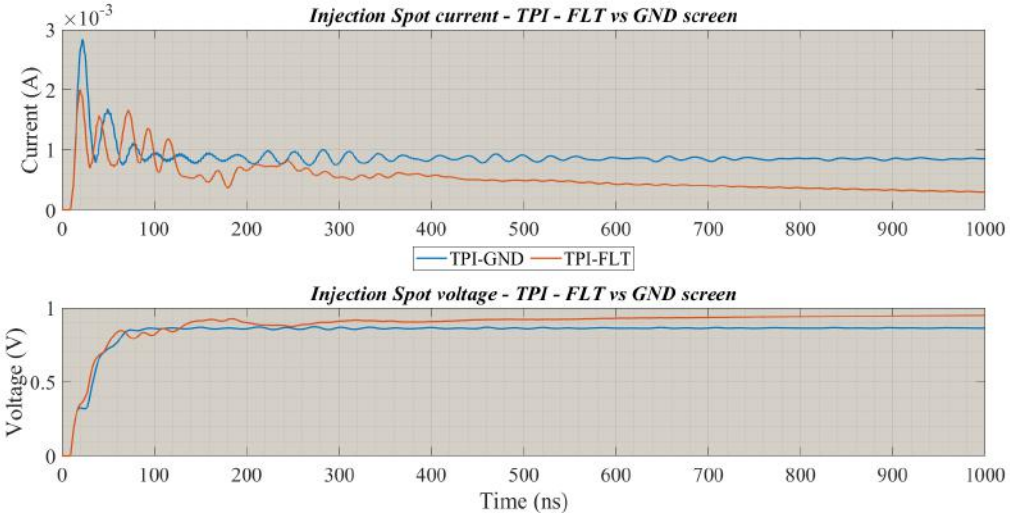

Figure 5.66: TPI - Heaviside step response at injection spot - 10 m mini-cable - FLT & GND Halves (PSCAD simulations)

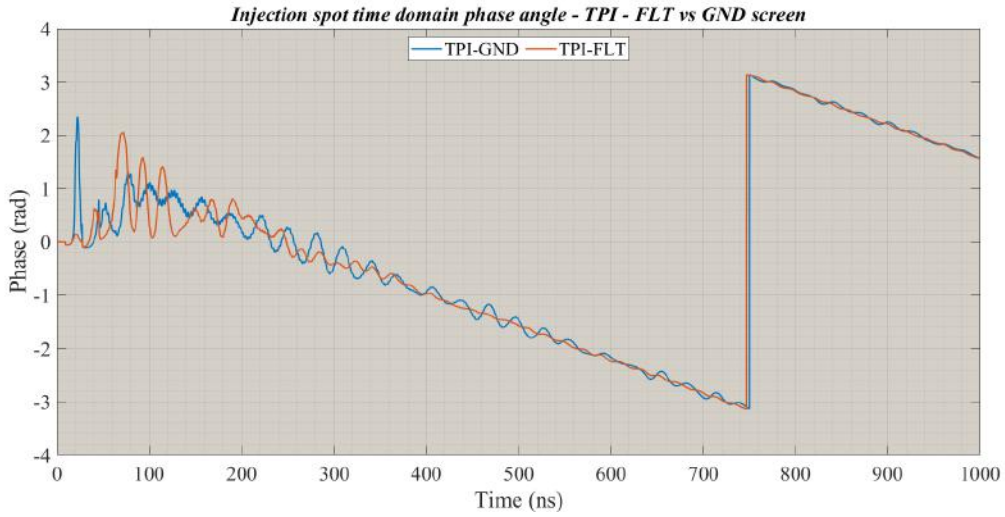

Figure 5.67: TPI - Heaviside step input - Time-domain phase angle between instantaneous injection voltage & current - 10 m mini-cable - FLT vs GND (PSCAD simulations)

From the graphs above, the following findings come out,

— In contrary to CPI, grounding of the mini-cable sections leads to overall rise of injected current, while the voltage declines.

— Very low injection current can be considered as an advantage in TPI, as a great deal of the injected power participate in the voltage waveshape forming. That is the reason why the voltage gain until the injection point is higher in TPI, to be in order of 85% of the source voltage peak ($\widehat{V}_{src}$), compared to the other setups.

— In the GND practice, the initial overshoot is higher, compared to its alternative. The mini-cable grounding helps damping of transient oscillations, although the high frequency post tail oscillations increase. The tail oscillations are also damped slower in comparison with the FLT case. Having said that the mentioned vibrations remain in the acceptable limits for the entire path.

— The rising slew rate in the GND practice is marginally lower.

— The curves on figure 5.67 shows that in the transient period the FLT practice shows more oscillatory behaviour. On the other hand, as grounding of the system contributes to the total system inductance, more oscillations are observed when the system capacitance is charged or discharged.

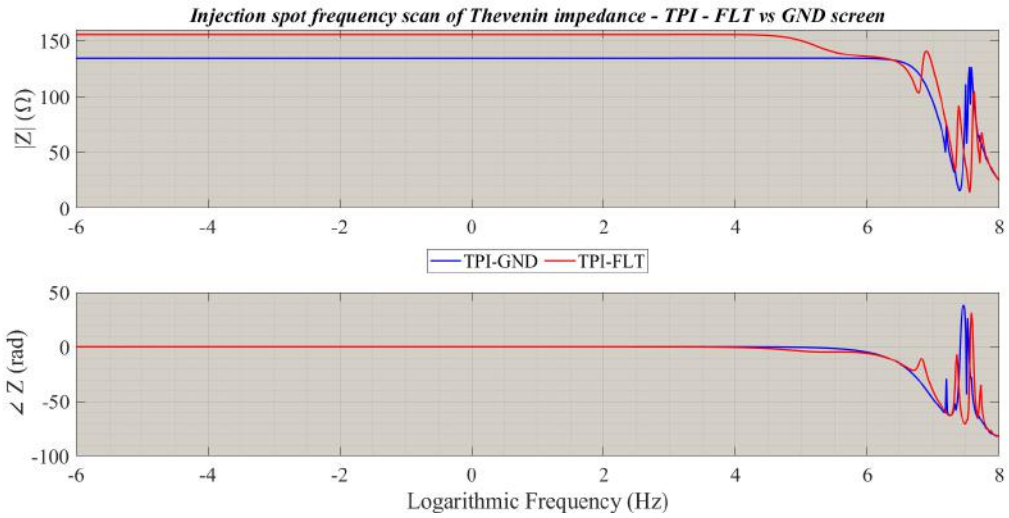

Figure 5.68: TPI -Injection spot frequency dependent impedance scan - step response (PSCAD simulations)

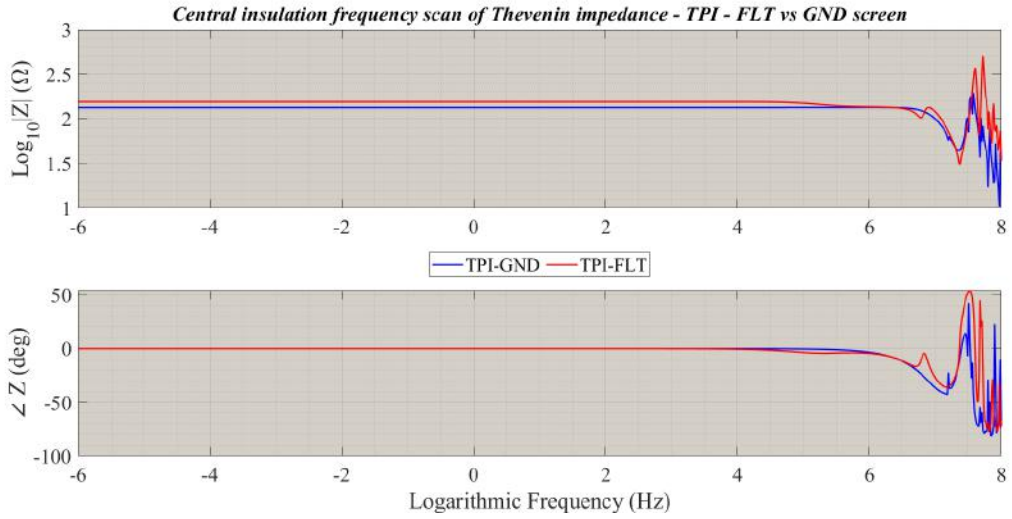

Figure 5.69: TPI -Central spot frequency dependent impedance scan- step response (PSCAD simulations)

Graph 5.68 implies that the impedance seen from the injection point in the GND case is higher than that of the FLT at up to almost 1 MHz, where both values become equal. At high frequencies the FLT practice shows more oscillatory trend with many partial resonances that leads to many noises in the output parameter. As the pulse is directly injected into the target insulation, its Thevenin impedance scan is almost the same as that seen from the injection spot (graph 5.69). Figure 5.70 compares the output voltage and current for the screen grounded and ungrounded TPI setups.

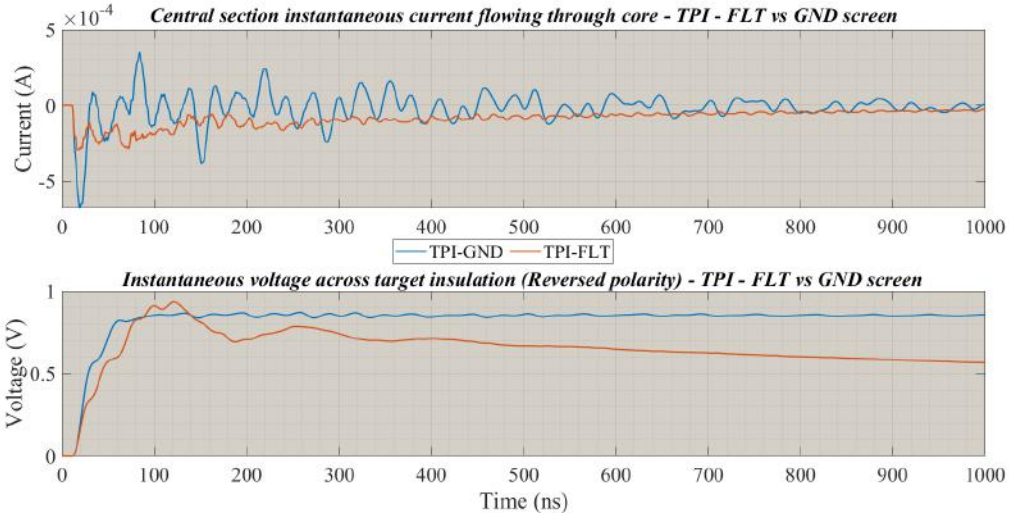

Figure 5.70: TPI - Heaviside step response at central section, core current & net potential difference between screen & core - 10 m mini-cable - FLT & GND Halves (PSCAD simulations)

Figure 5.70 explains that screen grounding of the mini-cable is beneficial in terms of rise time (RT_{pea}) and leading slew rate ($\tau_{r,pea}$) of V_{pea}, however it can be a source for partial high

frequency noises in the circuit and it pushes the peak value of the output voltage down (from 91% to 81% of the input voltage peak). Damping of the system also increases when the screen conductor is coupled into earth. The figures 5.71 and 5.72 evaluate impact of line extension on the TPI output voltage for floated and grounded screen conductors accordingly.

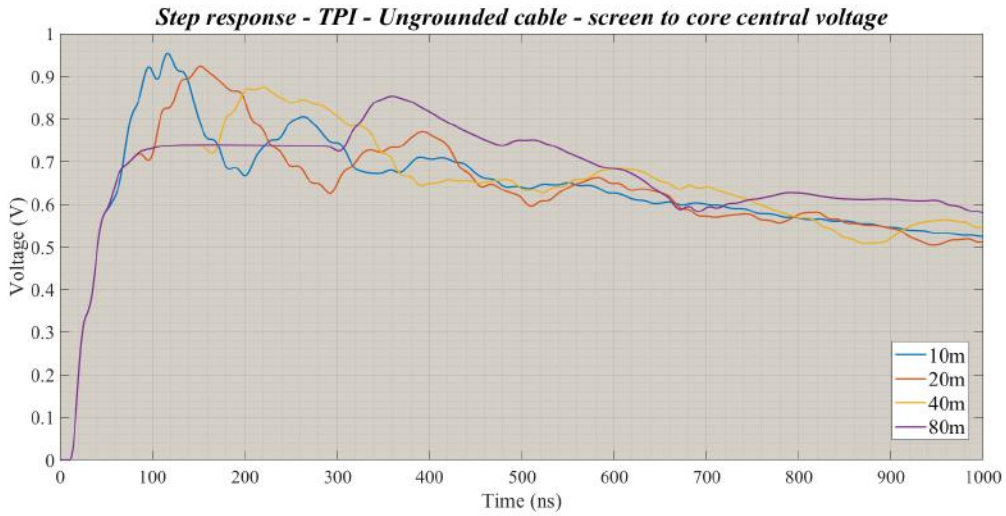

Figure 5.71: TPI - 10 m mini-cable, Heaviside step response - Floated Halves (PSCAD simulations)

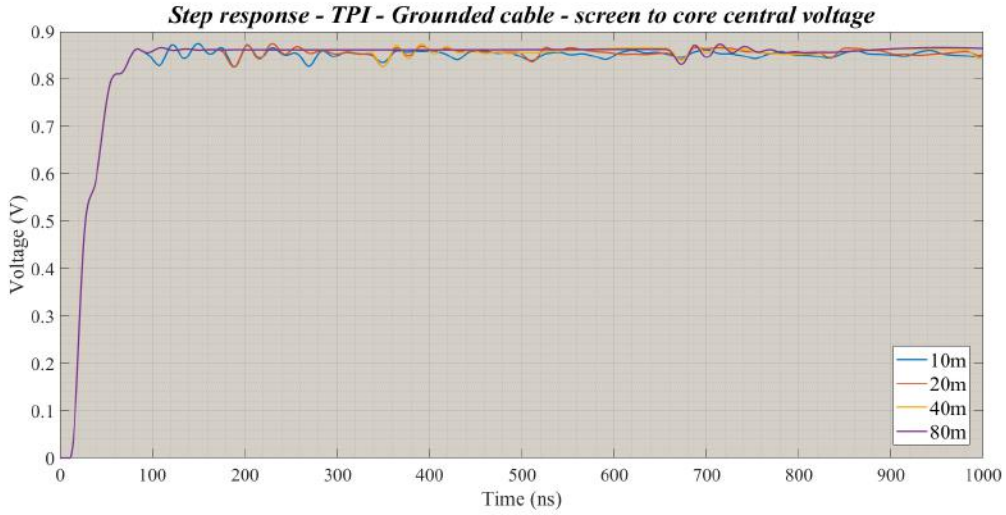

Figure 5.72: TPI - 10 m mini-cable, Heaviside step response - Grounded Halves (PSCAD simulations)

From the figures above it can be concluded that,

- As it is already discussed, slope of the screen grounded TPI is much sharper than that of the ungrounded case.

- The cable length extension is totally ineffective on rise time and slew rate of the GND case, but in the FLT case, due to shift in the overshoot the rise time and slew rate decrease.
- The length extension contributes to the system damping in FLT configuration. The magnitude and frequency of oscillations also drops when DUT becomes longer. For instance, by the sample enlargement from 10m to 20m, frequency of oscillation drops from 6.8 MHz to 4.1 MHz respectively. The GND configuration contains only high frequency partial oscillations.
- By length extension the GND configuration maintains the original voltage gain value (around 86%), while the voltage gain value drops when the floated cable is expanded. Therefore, the screen grounded TPI seems to be a good option for long samples.

5.5 Insertion inductance

In this section, change in unit step and 80 ns wide square wave circuit responses of different setups by manipulating the insertion inductance magnitude from 80 ns to 4 μs is analyzed. The simulations are repeated for grounded and ungrounded mini-cable screen.

5.5.1 DSPI & SSPI

Figures 5.73 and 5.74 shows the step responses for DSPI. The screen conductor of both mini-cable halves are grounded at the far end with reference to the injection spot in the latter.

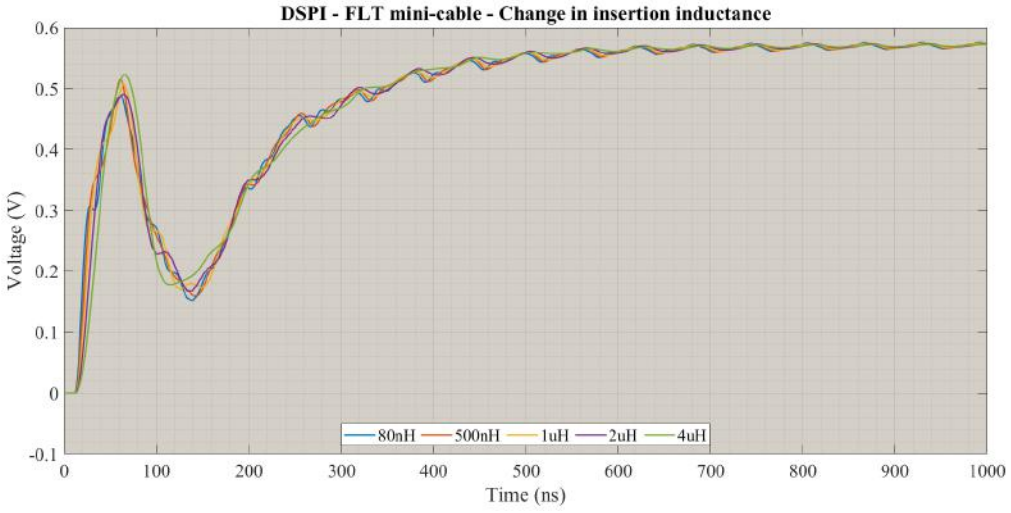

Figure 5.73: DSPI - 10 m mini-cable, Heaviside step response - FLT screens (PSCAD simulations)

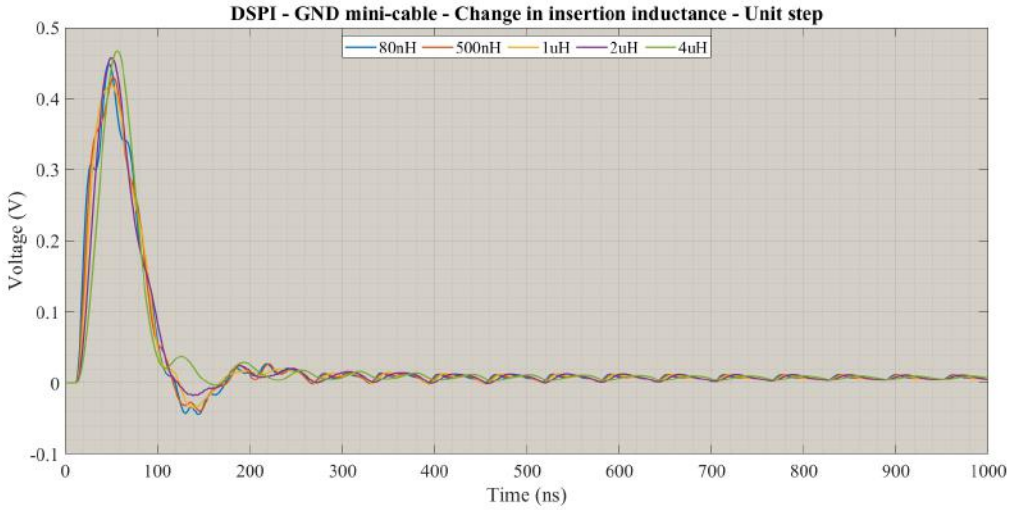

Figure 5.74: DSPI - 10 m mini-cable, Heaviside step response - Far end GND screens (PSCAD simulations)

a) Reduction in oscillations, **b)** more smooth waveshape specially at front and trailing edges and **c)** change in the output voltage magnitude are resulted in the both cases, although **d)** an negligibly low increase in rise time is also observed. One must pay attention to the fact that any increase in the inductance would not necessarily lead to the crest rise, specially in the grounded case, since by the inductance rise in the latter case the peak experiences an initial drop, thereupon it starts rising again exceeding the initial value. The other important issue to which a particular attention should be paid is gradual change in the post pulse undershoot polarity. In fact, at higher inductance value the undershoot starts being mirrored forming an overshoot instead. It seems 1 μH inductance shows the best combined result among all values.

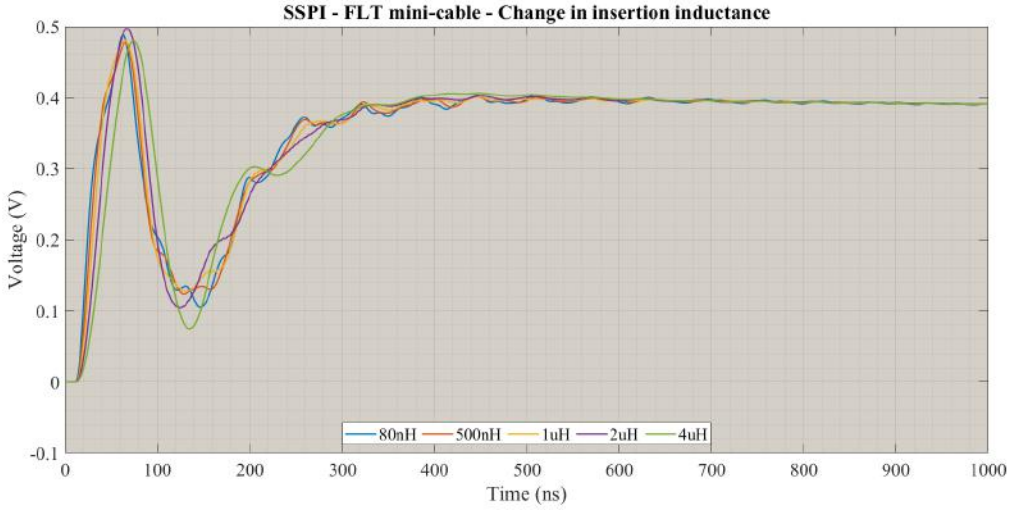

Figure 5.75: SSPI - 10 m mini-cable, Heaviside step response - FLT screens (PSCAD simulations)

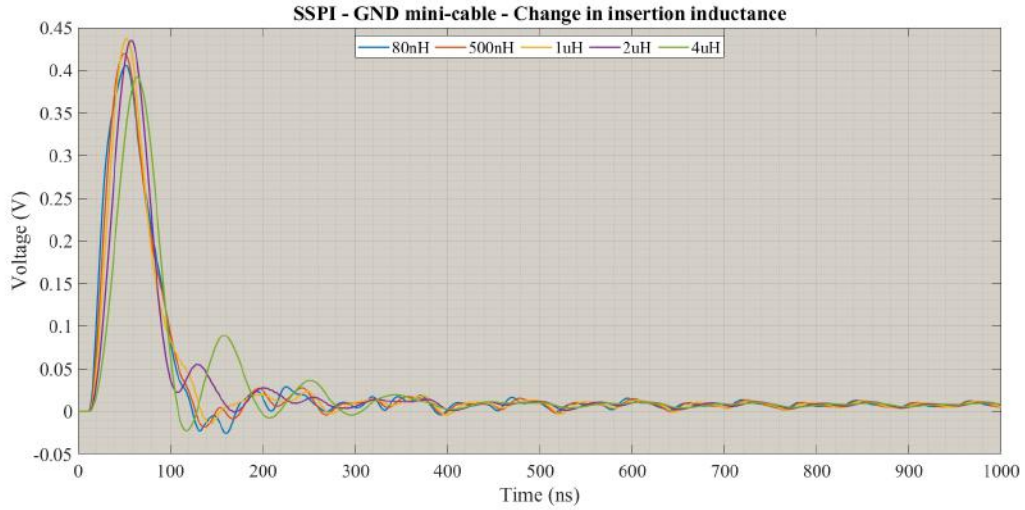

Figure 5.76: SSPI - 10 m mini-cable, Heaviside step response - Far end GND screens (PSCAD simulations)

The difference between SSPI and DSPI simulations is that tin DSPI, the insertion inductance is applied to both injection connections. Graphs 5.75 and 5.76 show the same results also for SSPI, with the only difference that the ultimate inductance value triggers rather high oscillations, while pushes the peak down simultaneously. The efficient inductance value in this case is estimated to be a value between 1 and 2 μH, according to graph 5.76.

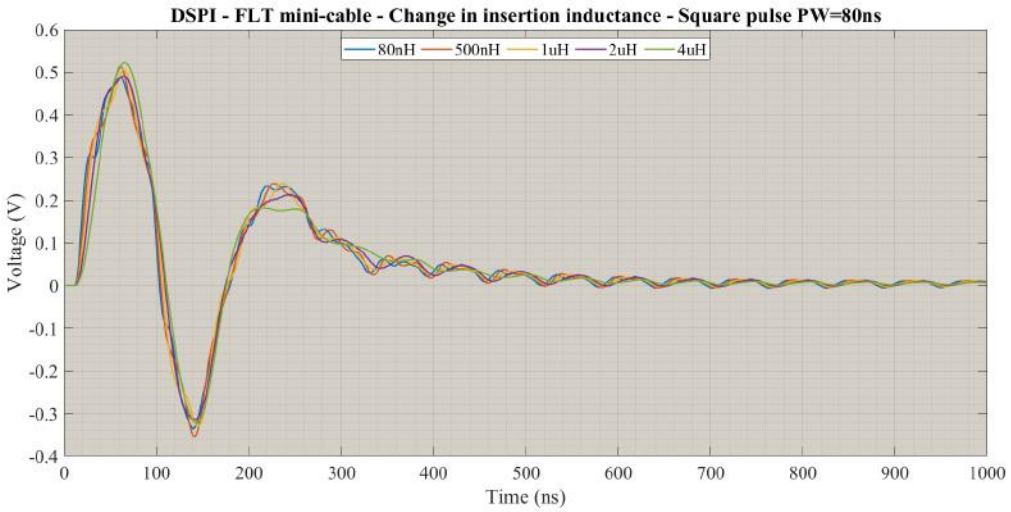

Figure 5.77: DSPI - 10 m mini-cable, 80 ns pulse width square pulse response - FLT screens (PSCAD simulations)

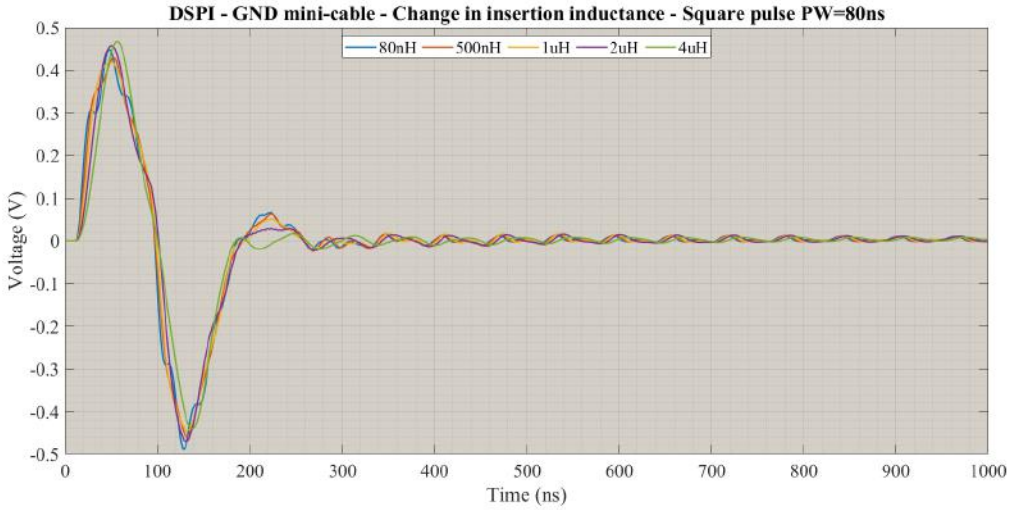

Figure 5.78: DSPI - 10 m mini-cable, 80 *ns pulse width square pulse response - Far end GND screens (PSCAD simulations)*

Similar to the step response, DSPI response to an ideal square wave (refer figures 5.77 & 5.78) also offers smoother waveshape at higher insertion inductances with slight rise in the local extrema. Unlike the step response, in this case, obviously rise in the inductance never leads to drop in the crests. Its damping impact on the post pulse overshoot is the other interesting finding of this set of simulations. In contrary to DSPI, SSPI simulations prove that exceeding the inductance from a certain value will not achieve desirable results, specially in terms of overshoot damping (figures 5.79 & 5.80).

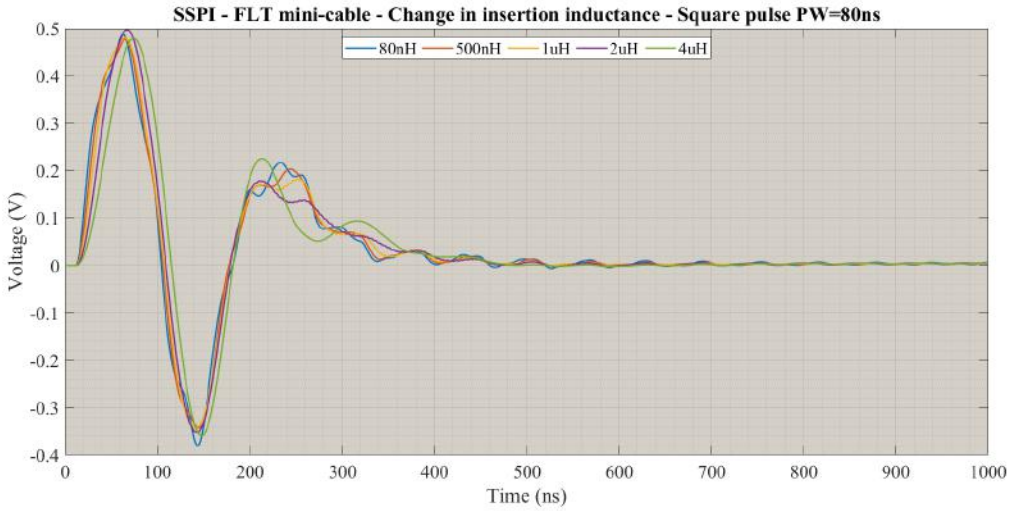

Figure 5.79: SSPI - 10 m mini-cable, 80 *ns pulse width square pulse response - FLT screens (PSCAD simulations)*

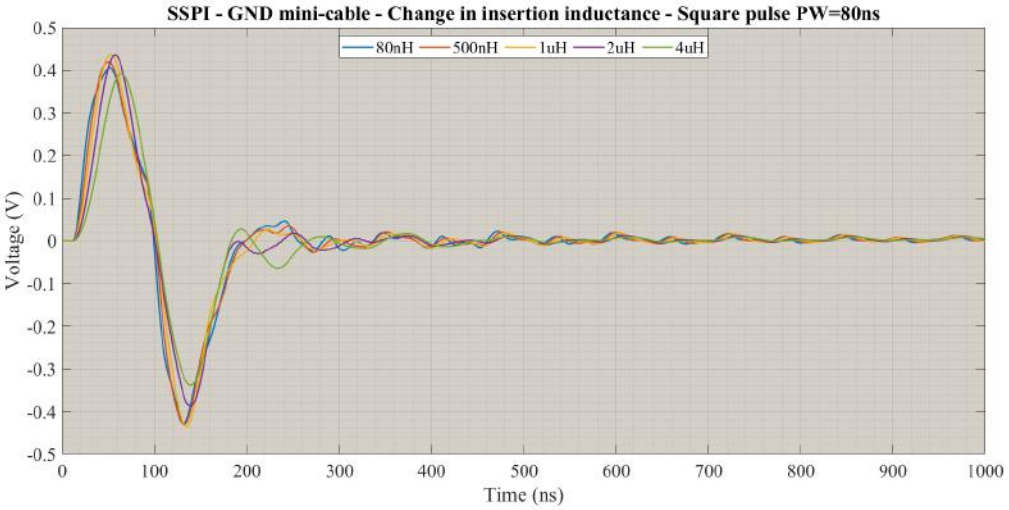

Figure 5.80: SSPI - 10 m mini-cable, 80 ns pulse width square pulse response - GND screens (PSCAD simulations)

5.5.2 TPI

Simulations 5.81 and 5.82, clue us in the fact that rise in the insertion inductance improves the outcome efficiently. Sufficient rise in the insertion inductance lifts the crest value up to almost 100% of the injected voltage that is a considered as a magnificent result, despite making the front edge a bit tilted, imposing a little longer rise time to the system. The outcome is seen for both grounding practices. Comparing two different grounding patterns reveals that grounding the near end of the shield helps maintaining the potential difference between the electrodes and preventing gradual rise in the second electrode potential. Nevertheless, a rather larger post-crest undershoot at high inductances can be considered as a drawback for this enhancement approach.

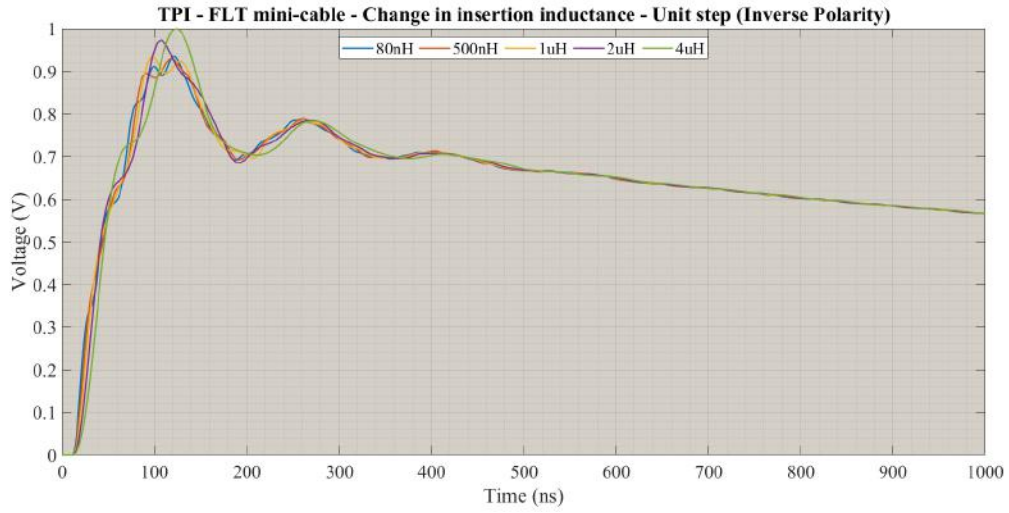

Figure 5.81: TPI - 10 m mini-cable, Heaviside step response - FLT screens (PSCAD simulations)

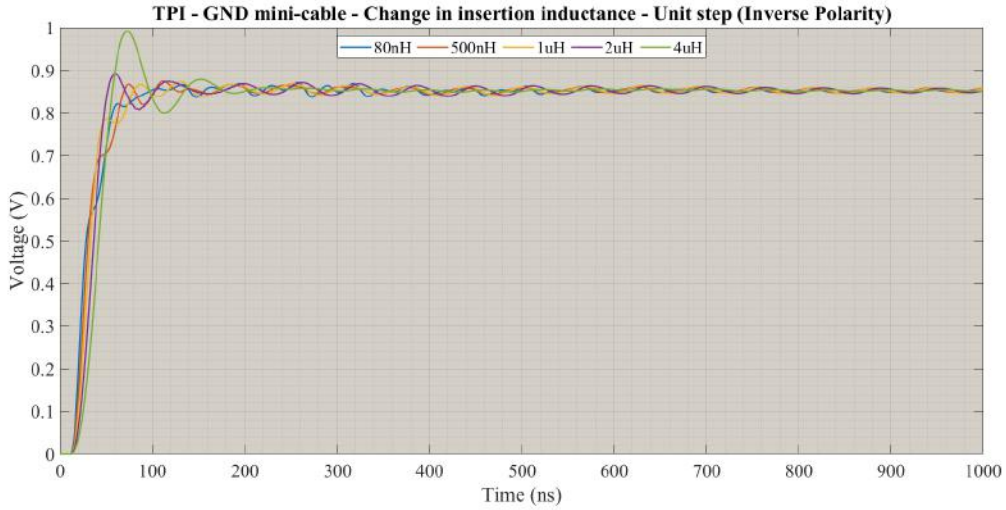

Figure 5.82: TPI - 10 m mini-cable, Heaviside step response - Near end GND screens (PSCAD simulations)

Although, insertion inductance rise seems to be pointless when screen conductor is floated as depicted ,figure 5.83 clarifies that a very nice pulse is delivered at the output when insertion inductance rise is combined by coupling the near end screens to earth. In the latter case, by increasing the inductance from 80 nH to 4 μH, the peak rises from 84% to just above 99%, which is desirable. Moreover, the crest oscillation is effectively damped out, however at high inductance values a post-pulse undershoot appears that should be somehow compensated.

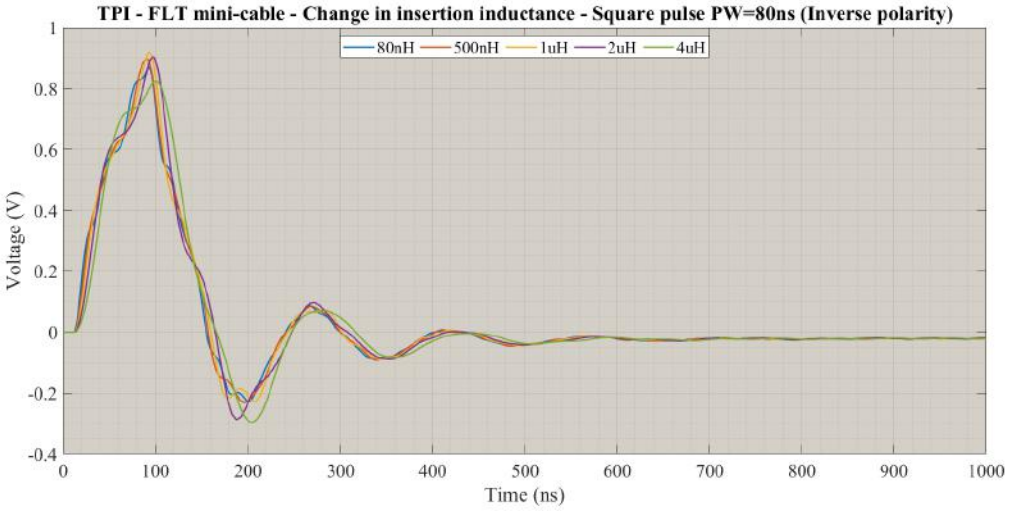

Figure 5.83: TPI - 10 m mini-cable, 80 *ns pulse width square pulse response - FLT screens (PSCAD simulations)*

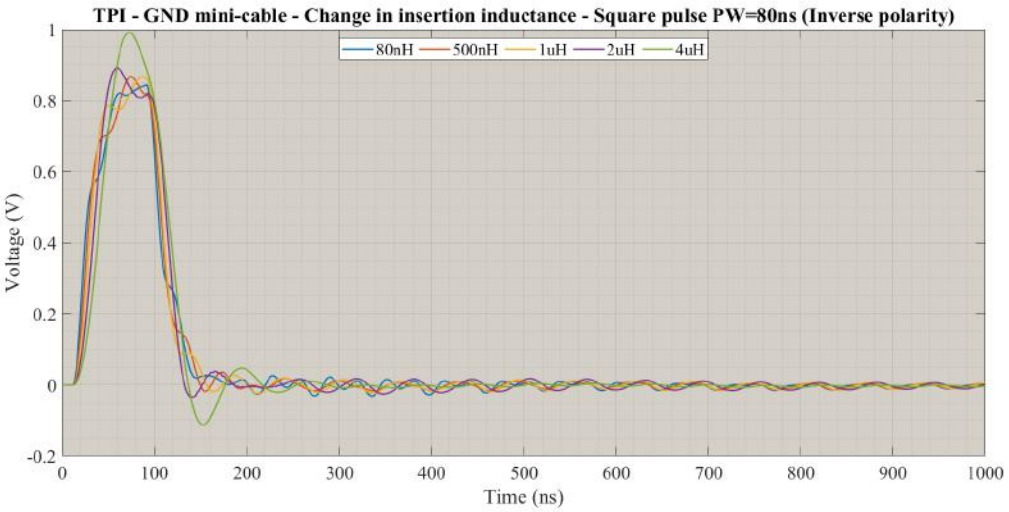

Figure 5.84: TPI - 10 m mini-cable, 80 ns pulse width square pulse response - GND screens (PSCAD simulations)

5.5.3 CPI

As it is already discussed, grounding of the screen conductors has no justification in terms of the system voltage gain. Both figures 5.86 and 5.88 agree this idea, as the delivered pulse crest values collapse to around 38% and 19% for the step and square input respectively when the screen conductors are earthed. Graph 5.88 also indicates that by increasing the insertion inductance the drop becomes even more intense reaching just above 16% of the input maximum value. It is also notable that both grounded cases show much more oscillatory behaviour than their floated alternatives.

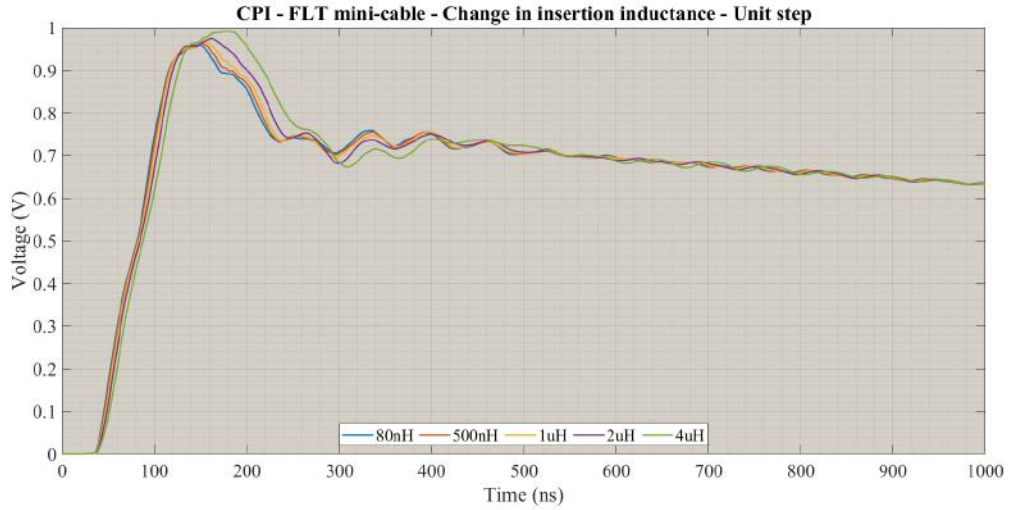

Figure 5.85: CPI - 10 m mini-cable, Heaviside step response - FLT screens (PSCAD simulations)

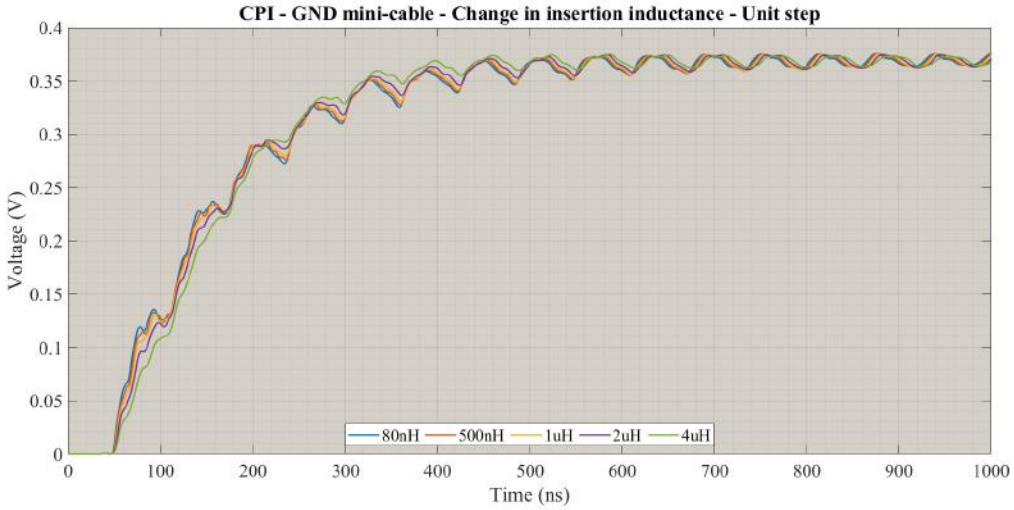

Figure 5.86: CPI - 10 m mini-cable, Heaviside step response - GND screens (PSCAD simulations)

In the floated cases, unlike other setups, increase in the insertion inductance can not help too much. In spite of a modest magnitude rise in response to a unit step input (from 98% to marginally above 99% for 80 nH & 1 μH accordingly), the voltage falls down at lower slew rate. On the other hand, in response to a square wave even this slight rise is not seen anymore, being substituted by a drop instead. Therefore, it can be concluded that change in the insertion inductance can not improve the results in CPI practice, independent of the screen grounding pattern.

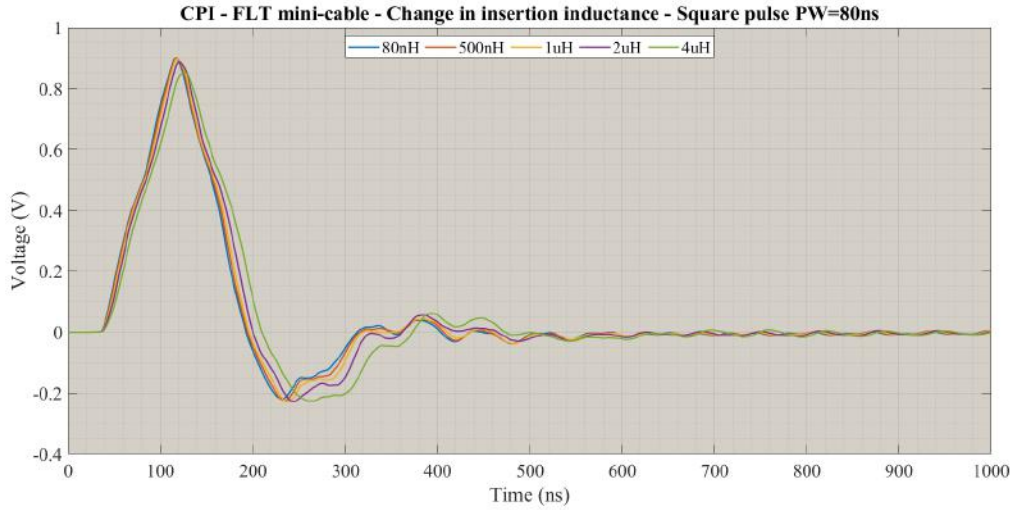

Figure 5.87: CPI - 10 m mini-cable, 80 ns pulse width square pulse response - FLT screens (PSCAD simulations)

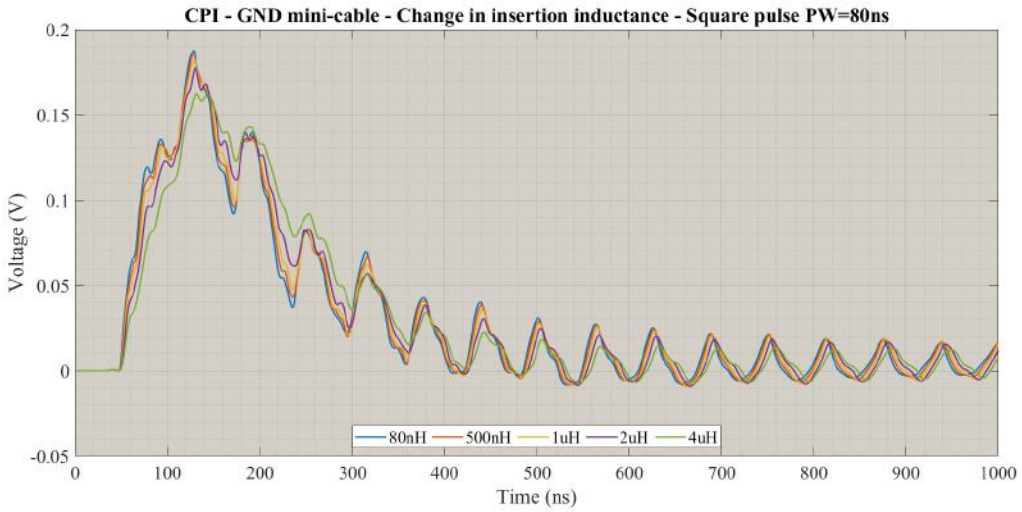

Figure 5.88: CPI - 10 m mini-cable, 80 ns pulse width square pulse response - GND screens (PSCAD simulations)

5.6 Optimization

In this section, based on the accomplished experiments, simulations and the relevant findings a few recommendations are provided to improve functionality of the setups for mini-cable scale tests. Initially, a set of general recommendation that are applicable for all of the setups are introduced. In the next stage, setup-specified recommendations are provided and finally the output of the optimized circuits are compared to each other.

5.6.1 General considerations

For all setups it is suggested that **a)** the central uncovered sections must be effectively long and **b)** the central electrode must be efficiently short, **c)** any unnecessary cable unshielding and **d)** signal splitting must be avoided. In SSPI and DSPI the exposed sections and central electrode lengths are chosen to be 100 mm (each side) for all cases and 50 mm and 100 mm for DSPI/SSPI/CPI and TPI accordingly.

5.6.2 SSPI/DSPI

1. **First approach - by step voltage input**
   The followings are recommended in order to enhance DSPI and SSPI setups, when a step voltage is injected instead of square wave,

   (a) Single side of the cable screen should be earthed ($1S$) at the far end adjacent to the central exposed part.

   (b) A step voltage ($\widehat{V}_{src} = 1500\,V$) is applied by the generator.

(c) An efficient value for the insertion inductor is selected. In this case, for SSPI, $L_{in} = 2\,\mu H$. In DSPI if the inductor is inserted into both sides of the splitter, $L_{in} = 3.2\,\mu H$ yields the optimal result, while in the case that the inductor is inserted before the splitter the same value as SSPI must be applied.

(d) The minor post-pulse overshoot also can be damped out by adding an insertion resistor (R_{in}) in series to the insertion inductor, although it imposes a drop to the crest value.

(e) the mini-cable screens are assumed to be solidly grounded. Every increase in the ground resistance would contribute to post pulse DC offset.

Figures below indicate the optimized DSPI and SSPI output voltages.

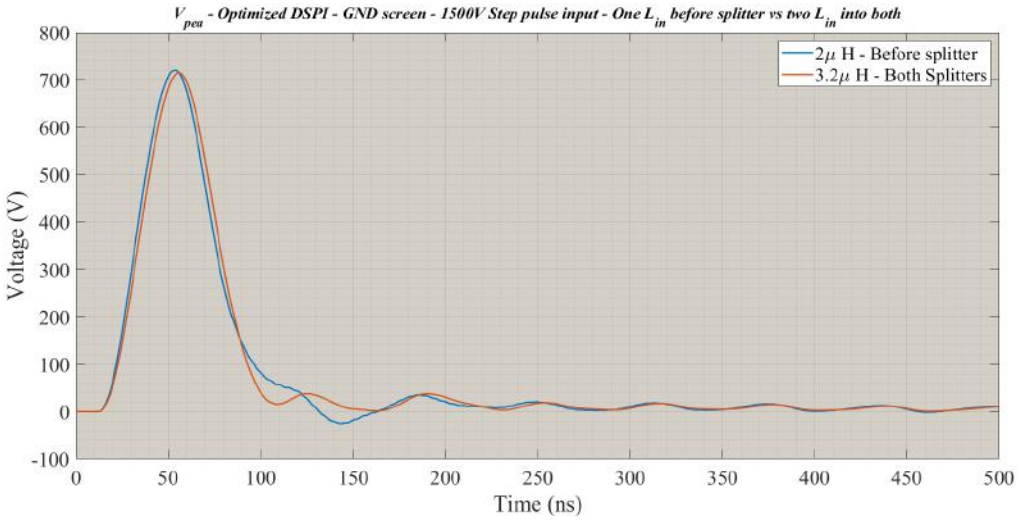

Figure 5.89: DSPI - Optimized V_{pea} - 1S far end GND screen & step voltage input of 1500 V peak (PSCAD simulations)

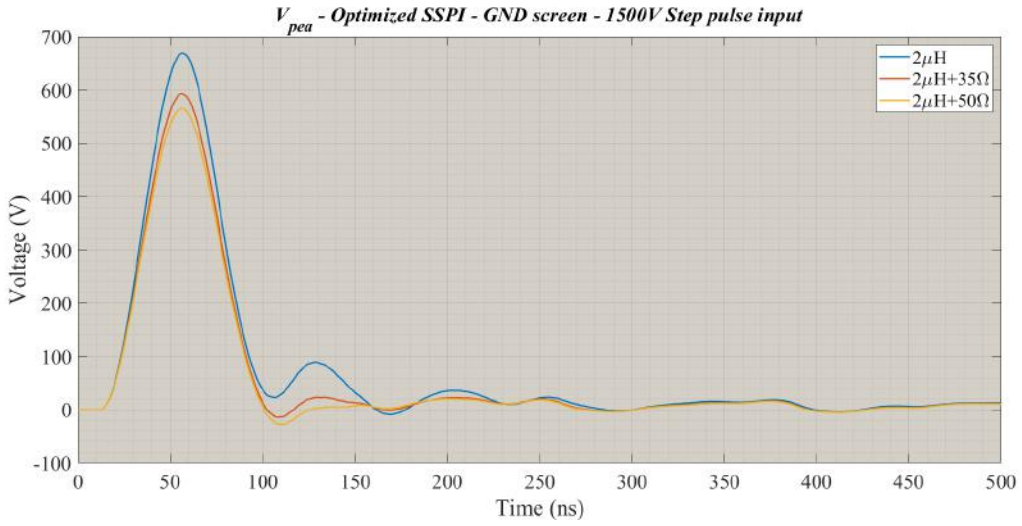

Figure 5.90: SSPI - Optimized V_{pea} - 1S far end GND screen & step voltage input of 1500 V peak (PSCAD simulations)

Figures 5.91 and 5.92 compare the voltage response before and after optimization for SSPI and DSPI. It is notable that the input voltage for non-optimized practice is an ideal square wave with 80 ns pulse width.

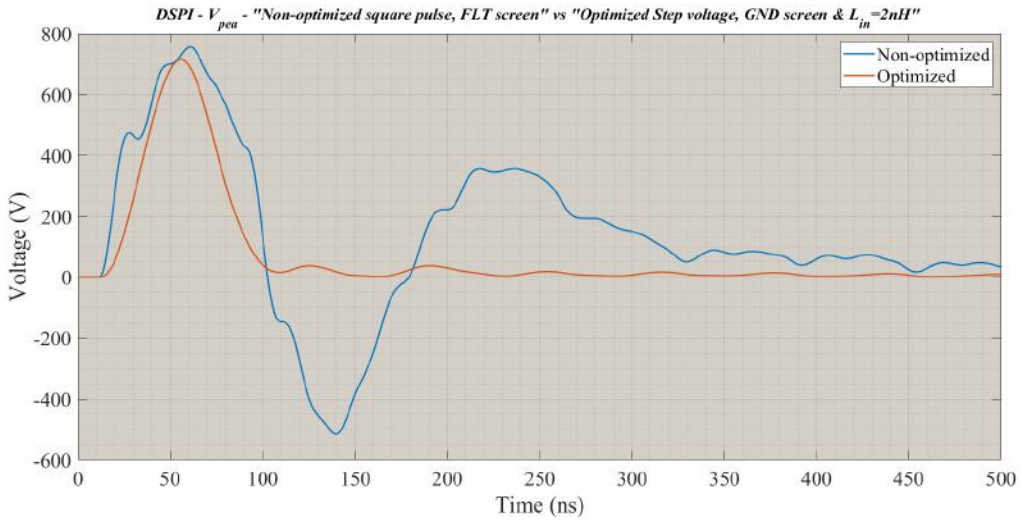

Figure 5.91: DSPI - V_{pea} - "Optimized 1S far end GND screen, $L_{in} = 2\ \mu H$, $R_{in} = 0$ before splitter & step voltage input of 1500 V peak" vs "Non-optimized, ideal square input, PW=80 ns, FLT screen" (PSCAD simulations)

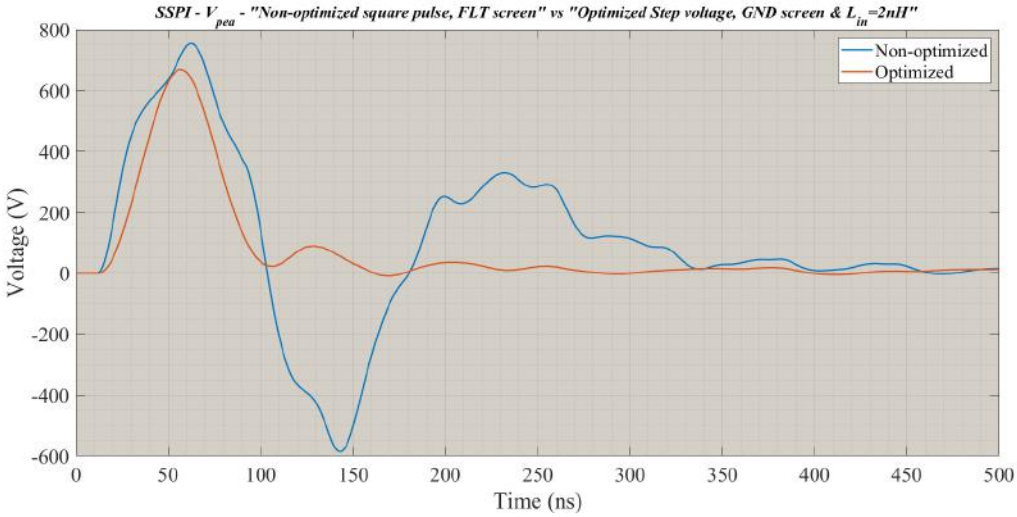

Figure 5.92: SSPI - V_{pea} - "Optimized 1S far end GND screen, $L_{in} = 2\,\mu H$, $R_{in} = 0$ & step voltage input of 1500 V peak" vs "Non-optimized, ideal square input, PW=80 ns, FLT screen" (PSCAD simulations)

As indicated in figures above, both SSPI and DSPI have been enhanced significantly from different aspects like pulse width, rise time, slew rate and so forth. The most important enhancement is with respect to oscillations. In fact neither bulk oscillation nor considerable post-pulse overshoot or undershoot is observed on the optimized curves, although the voltage experiences a drop with reference to the original case. The drop for SSPI (from 755 V to 667 V) is more important than that of DSPI (from 757 V to 722 V).

2. **Second approach - by square pulse** The followings are recommended in order to enhance DSPI and SSPI setups, when a square pulse of 80 ns is applied,

   (a) Very high increase in the termination resistance, for instance in SSPI $R_{trm} = 10\,k\Omega$

   (b) We add an inductor at the termination entrance. This helps rising the output voltage peak significantly, whereas the undershoot and overshoot disappear perfectly.

   (c) Increase in the insertion inductor leads to reduction in the waveshape distortion while $\widehat{V}_{pea}$ rises simultaneously.

   (d) Increase in the insertion resistor to a few tens of Ohm, although contributes to quenching the post pulse remained oscillations effectively, brings about a crest downfall.

   (e) Value of the termination capacitor is almost futile, since by re-valuing from 1.2 nF to 0.5 nF, no change is sensed in the waveshape at all.

   (f) One must avoid earthing the screen conductors in this approach, since it results in reviving the post-pulse local extrema.

Figures 5.91 and 5.92 compare the voltage response before and after optimization for SSPI and DSPI. It is notable that the input voltage for non-optimized practice is an ideal square wave with 80 ns pulse width.

Figure 5.93: DSPI - V_{pea} - "Optimized FLT screen, $L_{in} = 2\,\mu H$, $R_{trm} = 10\,k\Omega$ before splitter & square voltage input, $PW = 80\,ns$, 1500 V peak" vs "Non-optimized, same square input, FLT screen" (PSCAD simulations)

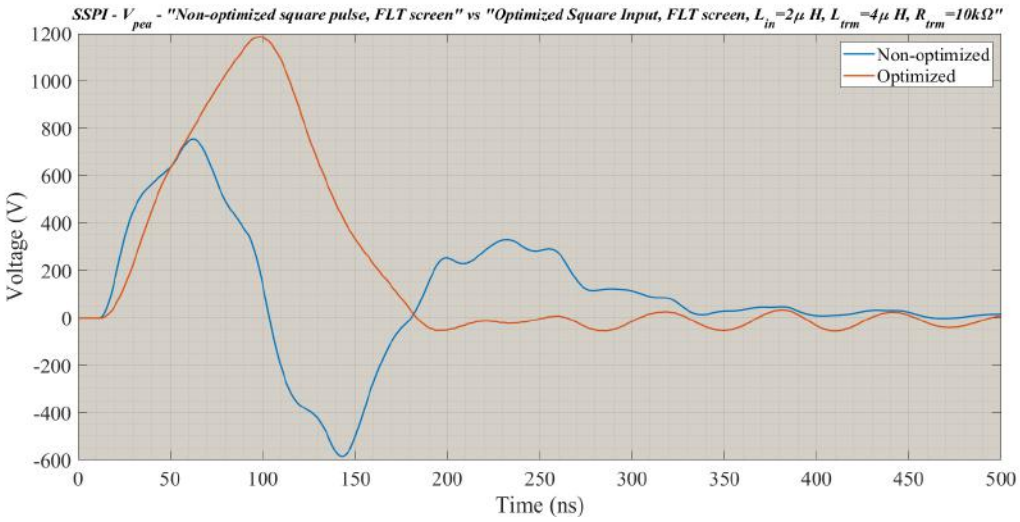

Figure 5.94: SSPI - V_{pea} - "Optimized FLT screen, $L_{in} = 2\,\mu H$, $R_{trm} = 10\,k\Omega$ & square voltage input, $PW = 80\,ns$, 1500 V peak" vs "Non-optimized, same square input, FLT screen" (PSCAD simulations)

Graphs 5.91 and 5.92 indicates a very efficient voltage gain optimization for both practices escalating from 50%, for non-optimized cases, to 79% and 83% for enhanced SSPI and DSPI respectively. Having said that in this approach the pulse widths are much higher than those

regarding the first approach, being 86 ns and 88 ns for SSPI and DSPI accordingly, however compared to the injected pulse width, which is in order of 80 ns, it seems to be very good result.

5.6.3 TPI

In TPI, the best results are obtained when,

(a) The insertion inductor has high values in order of 3.8 μH. In fact, L_{in} is directly proportional to the peak value and even can amplify the voltage gain beyond the input crest value, however it is not beneficial since it gives rise to the post-pulse oscillations at the same time.

(b) The simulations have shown that grounding the near end screen of the mini-cables through an resistor, in order of $100 - 150\,\Omega$, can help damping the post-pulse oscillations.

(c) Unlike DSPI and SSPI, shrinking the PEA electrode to 50 mm distorts the results, thus a 100 mm electrode is assumed in this case.

(d) The termination parameters are totally ineffective in this method of optimization.

Figure 5.95: TPI - V_{pea} - "Optimized 1S-GND near end screen through 150 Ω *resistor, $L_{in} = 3.8\,\mu H$ & square voltage input, $PW = 80\,ns$, 1500 V peak" vs "Non-optimized, same square input, FLT screen" - Polarity reversed (PSCAD simulations)*

Graph 5.95 implies an outstanding result for this approach, offering a voltage gain beyond 99% of the input crest, while it already was just below 87% for the non-optimized case, effectively damped oscillations and marginally narrower pulse width (78 ns) with reference to both the non-optimized setup (84 ns) and even the injected square wave (80 ns).

5.6.4 CPI

For CPI when a square wave is applied,

(a) A quality isolation from earth both at the cable screen and at the termination contributes to the output voltage quality. It mean the screen conductor of the both mini-cable halves must be disconnected from earth.

(b) Deploying shorter central measurement electrode (here 50 mm) and longer central exposed parts (here 100 mm) are beneficial.

(c) Rise in series insertion capacitance forces the peak value up, however by exceeding a certain effective value its becomes totally ineffective. In this case 7 nF capacitor is applied instead of 1.2 nF.

(d) The use of an insertion resistor in order of 100 Ω can help effective damping of the post pulse undershoot, however it pushes $\widehat{V}_{pea}$ downwards.
However, basically CPI always offer a high voltage gain in mini-cable tests, usually above 90%, a serious post-pulse undershoot in order of 200 to 300 V always appear in the output that is very probable to negatively influence detection and monitoring procedure. Hence, it is worthy to compensate it through an insertion resistor even in expense of 15 to 20% voltage drop at the output.

(e) The higher the insertion capacitor is, the lower insertion resistor is required in order to compensate the post-pulse undershoot.

Through a set of simulations, it is tried to find optimal values for C_{in} and R_{in}. Graph proves that the optimal value for the capacitor and resistor are 7 nF and 100 Ω respectively.

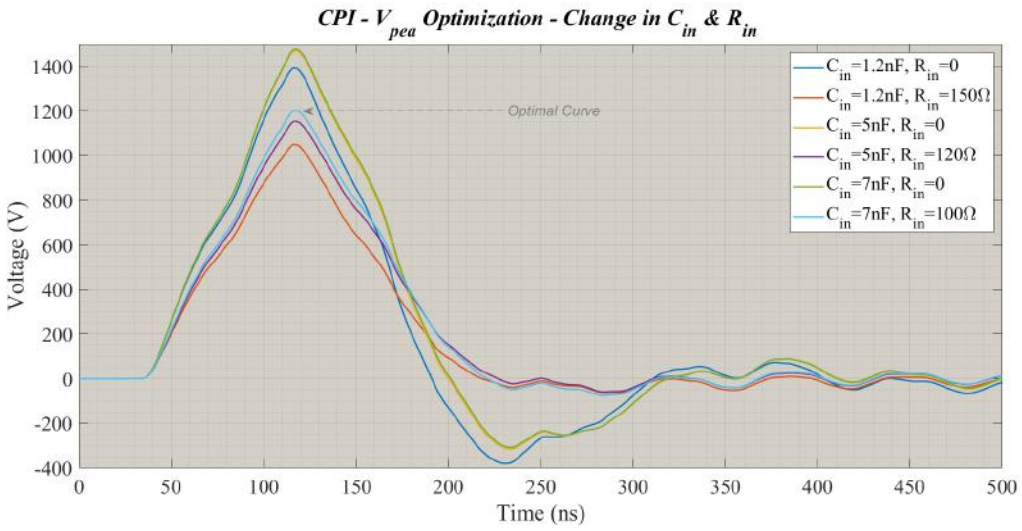

Figure 5.96: CPI - Ideal square pulse injection 80 *ns pulse width,* 1500 *V peak - V_{pea} Optimization - FLT screen, inspection of optimal values for C_{in} & R_{in} (PSCAD simulations)*

5.6.5 Optimized setups comparison

Graph 5.97 compares the resultant output voltage V_{pea}) for all recommended optimized setups. The simulations are executed for 10 m mini-cable sample.

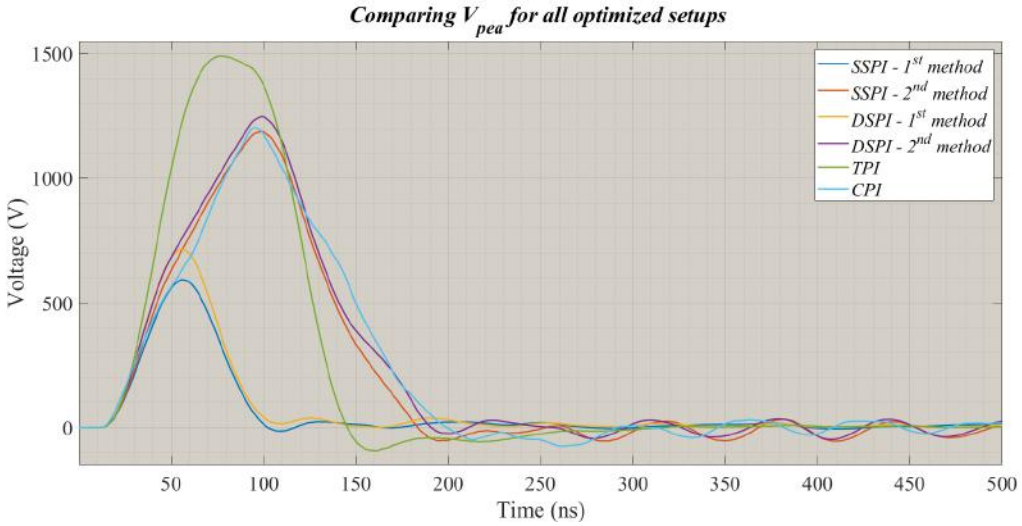

Figure 5.97: Comparing different setups after improvement (PSCAD simulations)

The most important parameters of the optimized curves are summarized in table 5.7 for comparison purposes. It is worthy to mention that for rise time calculation, $0-100\%$ rule is applied instead of $30-90\%$ that we formerly used, due to absence of bottom and crest oscillations and smooth waveshapes.

Setup	$\widehat{V}_{pea}$	PW_{pea}	τ_r	SR_r	Under/Overshoot	Oscillation
	V	ns	ns	V/ns	V	MHz
1^{st} DSPI	720	41.7	44.4	16.22	+38	Damped-out
1^{st} SSPI	592	44.4	44.8	13.22	-14	Damped-out
2^{nd} DSPI	1247	87.7	87.2	14.3	-23	12
2^{nd} SSPI	1188	86	86.5	14.02	-52	17
CPI	1202	91.1	83.4	14.41	-48	17
TPI	1489	76.3	64.6	19.44	-90	Damped-out
✗	1^{st} SSPI	CPI	2^{nd} DSPI	1^{st} SSPI	TPI	2^{nd} SSPI & DSPI
✓	TPI	1^{st} DSPI	1^{st} DSPI	TPI	1^{st} SSPI	TPI&1^{st} S-DSPI

Table 5.7: Comparison of most important parameters between all optimized circuits

5.7 Chapter highlights & Discussion

- **Setups comparison for 10 m mini-cable:** the simulations indicate that in terms of peak value ($\widehat{V}_{pea}$), CPI and TPI offer the best results. In DSPI and SSPI, intense post-pulse oscillations are seen in response to ideal square pulse. DSPI and CPI offer the best results in terms of rising slew rate, while TPI stands at the last stage due to crest oscillation that imposes a delay to reach the crest value. With regard to reflection at the pulse insertion spot, it seems SSPI and TPI lose greater part of the pulse energy than their alternatives, while CPI sees the least injection mismatch among all, however the values are not very far from each other. The simulations also have shown that CPI and TPI practices are vary susceptible to stored energy inside, that might have disturbing impact on the detection and monitoring procedure. The step responses of the different setups shows an underdamped oscillation for TPI, while SSPI and DSPI experience a considerable post-pulse undershoot, it is immediately damped out though. CPI curve show, contrastingly, an overdamped trend and a smooth step response. To sum up, generally, it seems CPI and TPI, at least for short samples, offer better voltage gain. SSPI and DSPI results can not be sufficiently reliable due to high post oscillations, despite the fact that from some resolution-related aspects, like high slew rate and low quality factor and more importantly narrow pulse width, they are higher-ranking.

- **Sensitivity analysis:** the cable length extension simulations proves a large drop in CPI magnitude at longer samples, while length is less influential in other cases. Having said that at much longer samples in order of 80 m, results for CPI are still as good as those of DSPI and SSPI. TPI shows the least susceptibility to length extension among all, making it the most competent option for a real size cable test.
  The simulations also suggest exposing longer cable section adjacent to the probing location in order to obtain higher voltage gain, despite the fact that in all cases magnitude of the post-pulse oscillations rise at the same time. In contrast to the semicon section length, any

extension in the measurement electrode brings about rough distortion in the output voltage, hence it is recommended to choose for the lowest possible electrode, the least limit for the electrode size is yet to be tested and determined.
Assessment of the termination parameters shows that change in the capacitance has minor effect on the test circuit quality, except for a slight post-pulse overshoot suppression in DSPI and SSPI. Moreover, an intentional rise in the termination inductance looks pointless for CPI and even disruptive for TPI, while in two other cases the peak value is improved at higher inductance values. The termination resistance, however, contributes to damping of the reflected waves at the cable-termination intersection in DSPI, SSPI and TPI, for CPI it is irrelevant though.
Dielectric permittivity sensitivity analysis shows that, in general, change in permittivity is not very deterministic in the voltage gain efficiency. The most considerable drop in the voltage peak is resulted for CPI, although the drop would not exceed 8% even by permittivity reduction to half. The most serious outcome of the test series comes out in DSPI and SSPI where deeper local minima and more oscillatory post-pulse local maxima are resulted, implying that the cable capacitance play a role in the post-pulse local extrema magnitude.

- **Grounding practices:** assessments have confirmed that in DSPI and SSPI grounding of the mini-cable screen conductor at both terminals (far and near end, $2S$) and/or only at the near end port are practically impossible, since the output voltage would collapse approaching zero. On the other hand, $1S$ screen grounding at the far end seems to be advantageous in terms of suppression of the post-pulse oscillations. The best results are obtained at low ground resistance values. Although some partial oscillations appear on the curves when the screen is solidly grounded, those can be damped effectively by adding a low ground resistor. In TPI, $2S$ and near end $1S$ grounding configurations yield equally effective pulse-shape improvement, particularly in terms of the pulse rise time and slew rate. It has also been shown that low ground resistances can help reducing the oscillations at sharp edges. By grounding the mini-cable screen in TPI, the pulse is also re-shaped from Gaussian to square, whose importance should be evaluated in further researched on the acoustic detection and monitoring phase of PEA test circuit. In contrary to DSPI, SSPI and TPI, for CPI any screen grounding of the sample must be avoided, as it would lead to an extreme plummet in the output voltage magnitude. Turn to the measurement table and screen electrode grounding, the results do not indicate any considerable optimization in the waveshape, except of a moderate damping effect on the pulse trailing edge oscillations and post-pulse overshoot. In the same case, low values of resistance would push absolute value of the output voltage down, thus they are not recommended.

- **Step response:** the most valuable finding regarding DSPI and SSPI practices are achieved by the step input injection, where we found out that by applying a step voltage while $1S$ far

port grounding of the mini-cable screen at the same time the problematic severe post-pulse undershoot and overshoot are both vanished completely, while $\widehat{V}_{pea}$ would not change considerably. The resultant pulse width, however, seems to be directly proportional to the mini-cable length, what must be taken into special consideration, when using this approach for long samples. The only notable outcomes for CPI are smooth step response, drop in the voltage gain for both grounded and ungrounded cases. In TPI, however, *s* grounding apparently leads to faster rise time and generally much better voltage gain are obtained, which are of vital importance beneficial. The simulations also show another important result which is applicability of TPI for long DUT. In fact, TPI perfectly maintains its quality by enlarging the sample.

- **Insertion inductance:** For DSPI and SSPI it has been seen that if the near end of the mini-cable screen is grounded, at an effective value for the insertion inductance the voltage gain reaches an optimal value whereas the post pulse undershoot is compensated efficiently. However, manipulation of the insertion inductance has no justification, in TPI we observe an outstanding result in terms of the voltage gain, despite the fact that at the optimal value an undershoot appears immediately after the pulse tail.

- **Optimization:** The first optimization approach for DSPI and SSPI offers a very smooth Gaussian-shaped pulse across the target insulation. This approach seems to be suitable for samples with low diameters as well as for the cases where high detection resolution is required, thanks to very narrow pulse widths and absence of oscillations. Low voltage gain, however, is considered as the most significant drawback of this method. In contrast to the first method, sufficiently high peak is obtained by the second approach with acceptable pulse width. TPI gains the best results in terms of peak value among all. As the optimized TPI output, is hardly affected by the cable enlargement, it even can be deployed for actual size cable space charge tests. The output pulse width that is optimized TPI is formed is even shorter than that of the injected pulse. The optimized version of CPI also offers a very substantial voltage gain, specially when the post-pulse undershoot is not compensated by means of an insertion resistor, nevertheless the waveform enhancement in CPI setup still needs more researches, since according to the simulations not many circuit are influential on its output. Having said that even after undershoot compensation the setup's voltage gain hardly drop below 80%. Higher pulse widths is counted as the principal pitfall of this method.

6

CONCLUSION

"The pendulum of the mind oscillates between sense and nonsense, not between right and wrong."

Carl. G. Jung

6.1 Summary & Discussion

This chapter highlights the key challenges and findings, and discusses how they were addressed throughout this thesis.

6.1.1 Injection methods & setups

As it was discussed in section 2.1, the previous researches on PEA method recommended three different injected methods of DSPI (Double-side Pulse Injection), TPI (Table Pulse Injection) and CPI (Core Pulse Injection). The lab tests showed that pulse injection into only one mini-cable half yields not much different results as into both sides, therefore, in order to avoid complexity and minimize disturbing effect of reflections, an auxiliary setup of SSPI (Single-side Pulse Injection) was introduced (figure 2.3) on which a group of tests were performed. We also took advantage of the practice for validation of the models. Although the main focus of the thesis is on application of PEA method for medium-voltage mini-cables, in order of a few meters, some simulations also were performed on longer cable samples in order to assess applicability of the setups for longer samples or sensitivity of the results to the sample enlargement.

6.1.2 Modeling

Necessity for modeling of the circuits is felt due to the fact that,

(a) Lack of accessibility

(b) Possible Damages to DUT

(c) Cost, time, material & labour conservation

(d) NOT all desired tests are executable in practice

Chapter 2 evaluated dependency of the cable parameters on frequency. Considering frequency-independence of the lumped models, making them inapplicable for transient and high-frequency analysis, it seems distributed models like the well-know phase model might be better option in our case. Section 3.1 also explained other restricting factor, prohibiting us from application of such models, namely cascading-related unwanted oscillations and neglecting some important factors like skin effect.
Below, it is listed a few of the obstacles, which were surmounted for modeling the setups,

- Difficulty in stray parameters estimation (see section 2.2.10)
- Unpredictable behaviour of the defect sections like the screen removed mini-cable parts
- Non-ideality of some components such as the termination capacitor (discussed in section 3.3.2)
- Very difficult approximation of frequency-dependent behavior of CB-XLPE (Carbon Black Cross-Linked Polyethylene) compound
- Enormous number of reflections and oscillations in the circuit that makes causality much trickier and sometimes impossible (see section 2.2.10.1).
- Approximation methods, used by PSCAD/EMTDC, for computation simplification, such as the issues that are already discussed for the cable permittivity (figure 3.9 & equation 3.1), group velocity inside the materials, neglecting delay and assuming light speed for travelling wave for wires and so forth.
- Imperfections in the real-world circuit, e.g. bad contacts, sample degradation, etc.

6.1.3 Model validation

In spite of the above-mentioned barriers, according to the simulations in chapter 3, it was proved that PSCAD phase model yields acceptable results, despite some shortcomings. The measured parameters for validation purposes are injection voltage and termination current, since these points are the only deterministic accessible spots in the circuit. The model was validated for both SSPI and DSPI.
A critical review on the validation chapter reveals,

(a) The simulations (section 3.3.1) of the injected circuit, with the mini-cable removed, indicate almost an identical voltage waveshape as that of the measurements, despite minor drop in the crest and pulse widths. The errors trigger the following hypothesis for possible causes,

— Miscalculation of characteristic impedance

— Phase constant error

— Attenuation constant error

— Human-error in TL length approximation

The first three all imply error in the cable primary parameters miscalculation. Although, the real reason behind this error needs more assessment, the author through a tentative, but theoretical, argumentation, in section 3.3.1, suggests the core twist ignored by the model as the most probable reason.

(b) Sections 3.3.4 and 3.3.6 show sufficiently good waveshapes at the output in terms of amplitude and trend for DSPI and SSPI when the table is grounded. The model shows better functionality for SSPI than DSPI. The reason for error in amplitude and phase are explained comprehensively in the same section. Then again, the reason introduced ignoring of twisting of the cable core, that implies lower current flow inside the cables in the simulations compares to that of measurements. The voltage and current graphs show higher error in DSPI than SSPI, both for current and voltage waveforms.

(c) Graph 5.51 reveals higher current flow for DSPI setup than SSPI. In addition, by disconnecting the PEA table from earth, we practically force the energy to flow towards the termination. Higher current flow is interpreted to more voltage drop, specially when travelling twice the path from injection point to the termination, which contributes to inaccuracy of the model (see graph 3.26). By comparing the DSPI and SSPI current graphs (figures 3.32 & 3.27) in sections 3.3.7 and 3.3.5 higher current, the idea is further firmed up.

(d) The lab measurements (Graphs 3.16 & 3.17) for square pulse tests on different capacitors, in section 3.3.2, imply imperfection of the applied high voltage capacitor and existence of stray inductance and resistance that cab be an origin for the reflected wave at the termination.

6.1.4 Mini-cable parameters

In Chapter 2 most of the relevant primary and secondary parameters of mini-cable were theoretically calculated and frequency-dependency of some of them were assessed. The most significant highlights of the assessment are,

(a) Skin depth of both core and screen conductor drop dramatically by frequency. This affects characteristic parameters of the cable (graph 2.38).

(b) As a result of skin depth reduction at high frequencies, the series line resistance rises while a huge reduction in the series inductance is observed (graph 2.39). This means the series primary parameters of the cable are very dependent on frequency.

(c) In spit of the fact that the shunt primary parameters also change with frequency rise, the shunt conductance high-frequency value is still in range of tens of fS/m and can be neglected. Initial drop in real part of the permittivity provokes rise of the shunt capacitance, however beyond a certain frequency, in order of tens of Hz, it becomes almost settled (graph 2.40).

(d) Hence, the secondary parameters, which are functions of the primary parameters, are frequency-dependent. Their frequency-dependence heavily rely on the transmission line series inductance and shunt capacitance rather than the other two. The calculations declare drop in characteristic impedance, phase and attenuation constants and contrarily rise in velocity factor by frequency rise.

(e) In PSCAD phase model permittivity applies a geometrical correction factor Θ (equation 3.2 & drawing 3.9) in order to take the semiconducting layers' effect into account, as in real size transmission lines for which the PSCAD/EMTDC is designed the semiconducting layer is not of importance. The new effective values reveal lower characteristic impedance and higher series capacitance, attenuation and phase constants with respect to the geometrical values. This is be contributed to justification of the model error.

6.1.5 CB-XLPE dilemma

Section 2.4.2 explained properties of Carbon Black Cross-Linked Polyethylene (CB-XLPE) compound, which is one of the most serious barriers in the circuit modeling. This thesis was not intended to inquire deeply into the topic, as it is far beyond the thesis scope, although developing an estimative model for the exposed parts seems to be inevitable. Properties of the material are extremely dependent on multiple factors like current intensity, temperature, filler size and distance, physical length and so forth. Any change in the factors would have a huge impact on the so-called percolation zone (see figure 2.26), which is a transition region in which the material changes its phase from resistive to capacitive and the resistivity drops dramatically. The commonly applied model is shown in figure 2.32 and the semiconductor complex permittivity was calculated based on the well-known Debye equation 2.18 and the initial values were selected both experimentally and through the literature. Graphs 2.33 and 2.37 illustrate non-linear nature of the permittivity and conductivity of the material.
In section 4.3.4, influence of the semiconducting material was evaluated through change in the central exposed parts. Slight drop in the injection voltage (graph 4.22) and rise in the injection current measured in the lab hint flow initiation of current flow at high frequencies, where the layers impedance magnitude drops (graph 4.24), through the outer semicon layer into earth. Ringing of the shortened case waveshape at the sharp edges signifies increase in leakage current at high frequencies. Simulations in section 5.2.2 also confirm our experimental findings. Diagrams 5.15-5.18, apparently denote positive impact of the central part enlargement on quality of the

delivered voltage across the target insulation, in terms of both magnitude rise and reduction in oscillations.

6.1.6 Reflections

As reported in sections 4.1 and 4.2, reflection is considered as a serious source for disturbances in the circuits (equations 4.1 and 4.2). The most susceptible spots are **a)** injection point (graph 4.16), **b)** termination entrance (refer graph 4.10), **c)** intersections between uncovered and healthy parts of the mini-cable (see drawing 4.11 & graph 4.12).

6.1.7 HVDC generator

In section 4.3.2, it was argued that due to very high series resistor of HVDC source, negligibly low current flows through the mentioned branch. Figure 4.18 shows that elimination of HVDC source and the series resistor has minor influence on the results, therefore the tests and simulations can be performed with disconnected DC source, however one must notice that in the actual cases the target inevitably must be fed by adequate HVDC voltage, otherwise PEA testing circuit does not function properly.

6.1.8 Termination

The tests and simulations proved leakage inductance and ohmic dissipation (see tests in section 3.3.2), into which coupling, ground and common mode stray inductances are added. Section 4.2 theoretically explicated frequency dependency of the termination impedance, reflection at the cable-termination crosspoint and influence of change in the termination parameters on the first two items. The following observations were attained,

(a) **Impedance:** generally, the impedance magnitude drops by frequency rise. The impedance magnitude underwent a substantial phase shift at the resonance frequency (graph 4.4).

(b) **Capacitance:** effect of capacitor value on the wave shape is very dependent on the current density flowing into the circuit as well as circuit configuration. Normally, a comparison between the solidly and capacitively grounded termination tests (figure 4.41) expresses reduction in injection current flow and rise in voltage in the latter, however graph 4.36 implies change in the table grounding practice from grounded to floated entirely inverses the trend. As long as the table is grounded an slight rise is observed on the first peak of the injection voltage, while the reflected wave amplitude decreases. Furthermore, figure 4.36 and demonstrates that the resonance frequency is shifted back to lower values whereas higher system damping is achieved (4.15) by capacitance increase in the termination. Graphs 5.27-5.29 also apparently indicate ineffectiveness of change in the termination capacitor on quality of the voltage across the central dielectric.

(c) **Inductance:** graph 4.25 verifies that the termination inductance is the main origin for the second peak on the injection voltage wave. Frequency scan of the termination also shows that the main resonance of the system is eliminated as soon as the termination is disconnected from earth (refer 4.26). Similar to the termination capacitance, the inductance rise shifts the oscillation frequency back to lower values. According to equation 4.14, inductance is the most influential parameter on the resonance bandwidth. Section 5.2.4.2 evaluated effect of the termination inductance change on the output voltage. The results show the voltage amplitude boost for SSPI and DSPI by the inductance growth, it is not advantageous for the other two setups though.

(d) **Resistance:** figures 4.3, 4.8 and 4.9 state that,

— resistance helps smoothing the phase transition at resonance frequency,

— the local minimum (for series resonance) and local maximum (for parallel resonance) are defined by the dynamic resistance of the system, thus in our case higher resistance results in an uplift in the resonance dig, in this way reflection at the termination crosspoint can be controlled. The lab experiments in sections 4.3.5.5 and 4.3.5.6 are the best examples for what we discussed above. Higher damping obtained in both cases reduction in the second peak magnitude can be seen, although a special care has to be taken since **NOT** every increase in the resistance would necessarily contribute to suppression of the reflected wave (see graph 4.9).

6.1.9 Non-optimized setups comparison

According to table 5.6 and graph 5.2, in spite of the fact that DSPI and SSPI offer unique results in terms of the output voltage bandwidth, rise time and slew rate, due to the extreme post-pulse undershoot and overshoot, if we exclude them in oscillation analysis, prohibits us from applying them in actual tests. This implies that in practice CPI offers the best resolution-related parameters. Moreover, beside the mentioned parameters, CPI provides us with a smooth waveshape, being almost free of oscillations with the least post-pulse ringing. In terms of the output voltage crest, still CPI presents the best results. Although TPI also yields acceptable values, its underdamped oscillatory behaviour affects its quality.

6.1.10 Sensitivity analysis

This research also analyzed sensitivity of the setups to a few important parameters. The key observations are listed below,

(a) **Cable length extension:** in DSPI and SSPI, it seems the first peak is not affected considerably by the cable length extension. Despite an slight initial drop in the simulated $\widehat{V}_{pea}$ for TPI, after reaching a certain value it stays stable. This makes TPI is good option

for real-size cable testing. Among all, CPI experiences the highest decrease in the voltage amplitude.

(b) **Central uncovered length:** in all cases enlargement of the central exposed parts are beneficial in terms of the output voltage amplitude. The reason is probably, reduction in current leakage through the outer semiconducting layer into earth that leads to decrease in the injection current while boosting the injection voltage at the same time. However, by the section enlargement post-pulse overshoot also escalates in DSPI and SSPI and a considerable undershoot appears on the CPI curve. TPI, however, is affected more than the rest as post-pulse oscillations are intensified significantly, due to the fact that the pulse would see much higher Thevenin impedance in this case.

(c) **Measurement electrode length:** it has disrupting effect in all cases since it reduces the impedance of the central part, therefore voltage across the target dielectric falls down.

(d) **Cable dielectric permittivity:** aging and degradation of the cable, specially when the cable is subjected to many tests, prompts changes in the dielectric permittivity. Graphs 5.34-5.37 explain that in DSPI, SSPI and CPI lower permittivity values cause more post-pulse oscillations and deeper undershoot, while TPI is hardly impacted by change in permittivity.

6.1.11 Screen ground practice

During the thesis (specifically sections 5.3.1 & 5.4), the cable screen grounding and its impact on the key parameters were comprehensively assessed. We understood that grounding of the screen conductor is one of the most critical issues in the circuits enhancement process. We saw that for DSPI and SSPI grounding the near end port (adjacent to the exposed part) of the mini-cable screen is practically impossible and must be avoided, however, grounding of the far end can be advantageous in terms of suppression of post-pulse ringing (graphs 5.38 & 5.39). The same graphs also justifies that higher earth connection resistance gives rise to the ringing magnitude. The screen grounding is specifically crucial in the method introduced based on step voltage injection (1^{st} approach for DSPI & SSPI in section 5.6.2). In TPI, near end grounding and double terminal grounding both contribute to slope sharpening of the leading and trailing edges, which the former showing slightly better results. TPI is the only case in which minor values of ground resistance can be beneficial in terms of small oscillation damping, selection the right value for this resistance is very important as high values would again distort the waveshape. Step response of TPI, discussed in section 5.4.3, shows that specifically in TPI case, grounding can provide us with the higher and more stable output voltage magnitude and considerable reduction in rise time (hence higher slew rate) and higher oscillation damping. In contrast to the the explained cases, cable screen grounding in CPI setups has no logical justification. As demonstrated in sections 5.4.2 and 5.3.1 the cable screen grounding in CPI causes a extreme collapse in the output voltage magnitude.

6.1.12 PEA measurement table grounding

Excluding TPI, in which the pulse-voltage is injected directly into the table hence the table must be kept isolated from earth, the thesis assessed influence of the table ground isolation for the rest (refer section 5.3.2). Graphs 5.43 to 5.44 indicate lower voltage gain by the ground resistance increase in DSPI, SSPI and CPI for both grounded and floated screen conductor practices.

6.1.13 Setups optimization

In the last stage, based on the performed tests, simulations and analyses, the thesis optimized the setups. For DSPI and SSPI two methods were proposed, each of which functions with different type of the input voltage (step or square). In the step-based DSPI and SSPI setups the use of insertion inductor and a series resistor as well as low resistance screen grounding at the far end are inevitable. Table 5.7 shows very nice resolution-relation parameters for the designed method, however its voltage gain is much lower than its alternatives. On the other hand, as explained in section the 2^{nd} optimization approach is based on manipulation of the termination parameters in order to compensate the extreme post-pulse ringing (figures 5.93 & 5.94). The results are further explained in the conclusion section.

6.2 Conclusion

Coming back to the research questions, the followings were resulted in this thesis,

- **Applicability of PSCAD phase model:** PSCAD/EMTDC software and its phase model can sufficiently accurate model the PEA testing circuits for mini-cable geometry sample with a length in order of $10\,m$.
- **Single- & Double-side screen pulse injection (SSPI & DSPI):** the research indicated that SSPI and DSPI yield very similar results. Therefore, SSPI can be considered as another practice for pulse injection into a mini-cable in PEA tests. Having said that the SSPI and DSPI original designs (non-optimized) are practically inapplicable for PEA testing due to severe post-transition undershoots and overshoots and demand for optimization.
- **SSPI & DSPI optimization:** both practices can be optimized by either applying square or step voltage, as proven in this research. The latter, however, still needs calibration and experimental validation.
- **Main reflection sources:** the thesis introduced impedance mismatches at injection spot, cable-termination interface and uncovered parts of the cable as the main origins for reflections in the setups, that contribute to the output waveform distortion.

- **Key parameters for optimization:** Grounding configurations, insertion and termination parameters, lengths of central exposed parts and central electrode, and the applied voltage wave shape are among key parameters for the circuits' optimization, by fine tuning of which both the output pulse amplitude and resolution-related parameters of the delivered pulsed voltage can be optimized.
- **Grounding practices:** the best grounding practices for measurement table/PEA cell assembly are those recommended by the original designs. In DSPI and SSPI, when a square pulse is applied, far end screen grounding is beneficial in terms of the output pulse-width and damping of the post-pulse overshoot. Although in combination with other optimization key parameters floating of the screen conductor is the best option. On the other hand, in case of step voltage application in SSPI and DSPI, far end screen conductor earthing is inevitable. In CPI any grounding of the screen conductor leads to considerable drop in the output pulsed-voltage amplitude and must be avoided. In connection with TPI, whose original setup recommended screen grounding at the far end, the simulations implied that ground connection at near end as well as at both near end and far end, yield better results.
- **Central sections:** longer central uncovered sections (removed screen) and shorter central measurement electrode (central sound section) lead to acquiring the better output pulse shapes. The former brings about the higher output pulse magnitude and the latter is advantageous in terms of both the output pulse peak and pulse-width.
- **Best injection setup(s):** CPI and TPI offer the best cumulative results regarding the delivered pulsed-voltages across the target insulation among all original and optimized setups, accordingly.

6.3 Recommendations

The author recommends the followings for further researches,

1. A more accurate model for CB-XLPE compound is crucial that would take more role-playing parameters into account.
2. The origins for low frequency noises that appear specially in the impedance frequency scans must be found through simulations and experimental tests.
3. It is important to invent an optimization approach for CPI that does not lead to drop in voltage magnitude while damping of the post-pulse undershoot is intended.
4. The output pulse-width of CPI still might be reduced by some techniques like pulse compression.

5. The role of possible common mode currents and ground bounce-back on the output-pulse distortion have to be investigated.

6. Accuracy of the PSCAD model might be a good topic for further researches in connection with this topic.

7. The first optimization approaches for DSPI and SSPI (based on step voltage injection), still need to be calibrated and experimentally validated in the lab.

BIBLIOGRAPHY

[1] M. A. Noras, "Charge detection methods for dielectrics–overview," *Trek Application Note*, no. 3005, pp. 1–13, 2003.

[2] A. Imburgia, P. Romano, M. Caruso, F. Viola, R. Miceli, E. Riva Sanseverino, A. Madonia, and G. Schettino, "Contributed review: Review of thermal methods for space charge measurement," *Review of Scientific Instruments*, vol. 87, no. 11, p. 111501, 2016.

[3] A. Imburgia, R. Miceli, E. R. Sanseverino, P. Romano, and F. Viola, "Review of space charge measurement systems: acoustic, thermal and optical methods," *IEEE Transactions on Dielectrics and Electrical Insulation*, vol. 23, no. 5, pp. 3126–3142, 2016.

[4] H. Hussaini, A. Ahmad, and A. A. Susan, "Review of space-charge measurement using pulsed electro-acoustic method: Advantages and limitations," *J. Eng. Research Applications*, vol. 5, pp. 90–95, 2015.

[5] J. S. Chahal and C. C. Reddy, "Modeling and simulation of pulsed electroacoustic measurement method," *IEEE Systems Journal*, vol. 8, no. 4, pp. 1283–1292, 2013.

[6] T. Takada, T. Maeno, and H. Kushibe, "An electric stress-pulse technique for the measurement of charges in a plastic plate irradiated by an electron beam," *IEEE transactions on electrical insulation*, no. 4, pp. 497–501, 1987.

[7] N. Othman, M. Piah, Z. Adzis, and N. Ahmad, "Comparative study on space charge distribution measurements using pea and pwp methods on high voltage insulation," *Jurnal Teknologi (Sciences & Engineering)*, vol. 64, pp. 43–47, 2012.

[8] R. Bodega, "Space charge accumulation in polymeric high voltage dc cable systems," 2006.

[9] Y. Li, M. Yasuda, and T. Takada, "Pulsed electroacoustic method for measurement of charge accumulation in solid dielectrics," *IEEE Transactions on Dielectrics and Electrical Insulation*, vol. 1, no. 2, pp. 188–195, 1994.

[10] T. Takada and T. Sakai, "Measurement of electric fields at a dielectric/electrode interface using an acoustic transducer technique," *IEEE Transactions on Electrical Insulation*, no. 6, pp. 619–628, 1983.

[11] H. Kitajima, Y. Tanaka, and T. Takada, "Measurement of space charge distribution at high temperature using the pulsed electro-acoustic (pea) method," in *Dielectric Materials, Measurements and Applications, Seventh International Conference on (Conf. Publ. No. 430)*. IET, 1996, pp. 8–11.

[12] X. Chen, X. Wang, K. Wu, Z. Peng, Y. Cheng, and D. Tu, "Space charge measurement in lpde films under temperature gradient and dc stress," *IEEE Transactions on Dielectrics and Electrical Insulation*, vol. 17, no. 6, 2010.

[13] M. A. A. L. Arnaout, "Acoustic wave propagation in a pulsed electro acoustic cell," in *Wave Propagation Theories and Applications*. InTech, 2013.

[14] G. Mazzanti and M. Marzinotto, *Extruded cables for high-voltage direct-current transmission: advances in research and development*. John Wiley & Sons, 2013, vol. 93.

[15] B. Sanden, J. Matallana, J. Parpal, A. Macphail, D. Wald, T. Kvarts, L. Benard, E. Zaccone, S. Hirano, J. Kim *et al.*, "Recommendations for testing dc extruded cable systems for power transmission at a rated voltage up to 500 kv," in *CIGRE Colloquium on HVDC and Power Electronic Systems*, vol. 3, 2012.

[16] T. Takada, "Acoustic and optical methods for measuring electric charge distributions in dielectrics," in *Electrical Insulation and Dielectric Phenomena, 1999 Annual Report Conference on*. IEEE, 1999, pp. 1–14.

[17] T. Takeda, N. Hozumi, H. Suzuki, K. Fujii, K. Terashima, M. Hara, Y. Mutrata, K. Wantanabe, and M. Yoshida, "Space charge behavior in full-size 250 kv dc xlpe cables," *IEEE Transactions on Power Delivery*, vol. 13, no. 1, pp. 28–39, 1998.

[18] K. Terashima, H. Suzuki, M. Hara, and K. Watanabe, "Research and development of 250 kv dc xlpe cables," *IEEE Power Engineering Review*, vol. 17, no. 7, pp. 45–45, 1997.

[19] www.facebook.com/people/Chris Yel, "Measuring space-charge in hvdc cables," Feb 2017. [Online]. Available: https://www.ee.co.za/article/measuring-space-charge-hvdc-cables.html

[20] R. Liu, T. Takada, and N. Takasu, "Pulsed electro-acoustic method for measurement of space charge distribution in power cables under both dc and ac electric fields," *Journal of Physics D: Applied Physics*, vol. 26, no. 6, p. 986, 1993.

[21] F. Zheng, Y. Zhang, Z. An, C. Liu, J. Dong, and C. Lin, "Thermal pulse method with an applied field," in *Solid Dielectrics (ICSD), 2013 IEEE International Conference on*. IEEE, 2013, pp. 427–430.

[22] T. Muronaka, Y. Tanaka, T. Takada, S. Maruyama, and H. Mutou, "Measurement of space charge distribution in xlpe cable using pea system with flat electrode," in *Electrical Insulation and Dielectric Phenomena, 1996., IEEE 1996 Annual Report of the Conference on*, vol. 1. IEEE, 1996, pp. 266–269.

[23] M. Yasuda, M. Ito, and T. Takada, "Measurement of charge distributions in coaxial cable using the pulsed electroacoustic method," *Japanese Journal of Applied Physics*, vol. 30, no. S1, p. 71, 1991.

[24] H. Zheng, "Application of pea technique to space charge measurement in cylindrical geometry hv cable systems," Ph.D. dissertation, Department of Engineering, 2015.

[25] *The Pulsed Electro-Acoustic (PEA) Space Charge Measurement Systems at TU Delft*, Delft University of Technology, feb 2011.

[26] Fast high voltage transistor switches. [Online]. Available: http://www.behlke.com/pdf/80-20-uf.pdf

[27] Product group b3 - mosfet, fixed on-time, high di/dt and ultrafast. [Online]. Available: http://www.behlke.com/gallery.htm

[28] K. Schon, *High impulse voltage and current measurement techniques*. Springer, 2013.

[29] L. BRANČÍK, "Techniques of time-domain simulation of transmission lines based on laplace transformation methods," Ph.D. dissertation, Thesis for Habilitation, BUT Brno, 1999.

[30] Z. Zhao, L. Yuan, H. Bai, and T. Lu, *Electromagnetic Transients of Power Electronics Systems*. Springer, 2019.

[31] Matlab. Matlab signal analyzer app. [Online]. Available: https://nl.mathworks.com/help/signal/ug/using-signal-analyzer-app.html

[32] P. Morshuis and M. Jeroense, "Space charge in hvdc cable insulation," in *Electrical Insulation and Dielectric Phenomena, 1997. IEEE 1997 Annual Report., Conference on*, vol. 1. IEEE, 1997, pp. 28–31.

[33] (2003) Test equipment solutions datasheet - lecroy waverunner 6000series. [Online]. Available: http://www.testequipmenthq.com/datasheets/LECROY-WAVERUNNER%206050-Datasheet.pdf

[34] M. Luo, D. Liu, and H. Luo, "Real-time deflection monitoring for milling of a thin-walled workpiece by using pvdf thin-film sensors with a cantilevered beam as a case study," *Sensors*, vol. 16, no. 9, p. 1470, 2016.

[35] M17/74 - rg 213 (rg 213/u). [Online]. Available: http://www.caledonian-cables.co.uk/Coaxia_Cable/M17_RG/RG213.html

[36] Rg 213 u - rg coaxial cable according to mil-c-17. [Online]. Available: http://halleycables.com/en/coaxial-audio-video/105-rg-213-u-rg-coaxial-cable-according-to-mil-c-17.html

[37] M17/mil-c-17 coaxial cable specifications. [Online]. Available: https://www.timesmicrowave.com/documents/resources/TL16p29m17specs.pdf

[38] Mil-c-17 coaxial cables - including m17/176-00001 twinaxial data bus cable. [Online]. Available: http://www.farnell.com/datasheets/1701739.pdf

[39] Rg213/u coaxial cable 50 ohms according to mil-c-17. [Online]. Available: http://www.wimo.de/download/RG-213U-milc17.PDF

[40] [Online]. Available: http://www.caledonian-cables.co.uk/Coaxia_Cable/M17_RG/RG213.html

[41] [Online]. Available: https://www.tek.com/high-voltage-probe-manual/p6015a

[42] Coaxial cables and terminations. [Online]. Available: https://www.physics.rutgers.edu/grad/506/coaxial%20cables.pdf

[43] Rectangular inductance calculator. [Online]. Available: https://cecas.clemson.edu/cvel/emc/calculators/Inductance_Calculator/rectgl.html

[44] Triangular inductance calculator. [Online]. Available: https://cecas.clemson.edu/cvel/emc/calculators/Inductance_Calculator/e-triangl.html

[45] Triangular inductance calculator. [Online]. Available: https://cecas.clemson.edu/cvel/emc/calculators/Inductance_Calculator/circular.html

[46] J. BUENO BARRACHINA, C. S. Cañas Peñuelas, S. Catalán Izquierdo, and F. Cavallé Sesé, "Capacitance evaluation on perpendicular plate capacitors by means of finite elemental analysis," *Renewable Energy and Power Quality Journal*, vol. 1, no. 7, pp. 617–621, 2009.

[47] D. R. King. (2012, jun) Lc resonant circuits. [Online]. Available: http://www.eng.utoledo.edu/~rking/Circuits2/LCresonance.pdf

[48] Europacable. (2016) Best practice for the installation of medium voltage cable accessories. [Online]. Available: https://www.ensto.com/globalassets/brochures/underground-cable-networks/europacable-position-paper-best-practices-for-installation-of-medium-voltage-cable-accessories.pdf

[49] Nexans. (2009, mar) 6-36kv medium voltage underground power cables xlpe insulated cables. [Online]. Available: https://www.sis.se/api/document/preview/567177/

[50] Caledonian. (2016) Caledonian medium voltage cables. [Online]. Available: http://www.caledonian-cables.co.uk/DdFls/MV/Medium%20Voltage%20Cables.pdf

[51] K. Jäger and L. Lindbom, "The continuing evolution of semiconductive materials fro power cable application," *IEEE Electrical Insulation Magazine*, vol. 21, no. 1, pp. 20–34, 2005.

[52] R. Rothon, *Fillers for polymer applications*. Springer, 2017.

[53] T. Liu, "Dielectric spectroscopy of very low loss model power cables," Ph.D. dissertation, University of Leicester, 2010.

[54] G. Bahder and F. Garcia, "Electrical characteristics and requirements of extruded semiconducting shields in power cables," *IEEE Transactions on Power Apparatus and Systems*, no. 3, pp. 917–925, 1971.

[55] R. Heinrich, S. Bonisch, D. Pommerenke, R. Jobava, and W. Kalkner, "Broadband measurement of the conductivity and the permittivity of semiconducting materials in high voltage xlpe cables," 2000.

[56] ABB. (2016, feb) Abb mv cable accessories products & technical presentation. [Online]. Available: http://www02.abb.com/global/seitp/seitp202.nsf/0/0d5d9f975e292672c1257f760013e66d/\protect\T1\textdollarfile/ABB+MV+CA+Products++Technical+presentation-ver1.pdf

[57] IEC. (2005) International standard - iec 60502-2. [Online]. Available: https://www.sis.se/api/document/preview/567177/

[58] I. E. Commission *et al.*, "Iec 60228: Conductors of insulated cables," *Edition*, vol. 3, pp. 2004–11, 2004.

[59] A. J. Thomas and T. K. Saha, "The analysis of dc and ac conductivity in the detection of water tree degradation in xlpe cables," in *IEEE Power Engineering Society General Meeting, 2005*. IEEE, 2005, pp. 87–94.

[60] R. Jobava, R. Heinrich, D. Pommerenke, W. Kalkner, and A. Gheonjian, "Efficient fdtd simulation of fields in coaxial cables with multi-layered insulation partially formed by dispersive layers of extremely high permittivity," in *Proceedings of the 7th International Seminar/Workshop on Direct and Inverse Problems of Electromagnetic and Acoustic Wave Theory*. IEEE, 2002, pp. 91–94.

[61] A. F. BURHANUDDIN and H. VISWANATHAN, "Measurement and simulation of cable impedance parameters in 600 v system."

[62] P. Wagenaars, P. Wouters, P. Van der Wielen, and E. Steennis, "Approximation of transmission line parameters of single-core xlpe cables," in *Conference Record of the 2008 IEEE International Symposium on Electrical Insulation*. IEEE, 2008, pp. 20–23.

[63] S.-W. Song, Z. Li, H. Zhao, P. Zhang, B. Han, M. Fu, and S. Hou, "Electric field control in dc cable test termination by nano silicone rubber composite," *AIP Advances*, vol. 7, no. 7, p. 075105, 2017.

[64] D. Fynes-Clinton, "Pd characteristics of typical mv xlpe power cable termination defects at vlf and power frequency test voltages," Ph.D. dissertation, 2016.

[65] A. Hoshmeh and U. Schmidt, "A full frequency-dependent cable model for the calculation of fast transients," *Energies*, vol. 10, no. 8, p. 1158, 2017.

[66] *Transient Analysis for PSCAD Power System Simulation - User's guide - A comprehensive resource for EMTDC*, Manitoba Hydro International Ltd, May 2018.

[67] D. K. Misra, *Radio-frequency and microwave communication circuits: analysis and design*. Wiley Online Library, 2004.

[68] *Energy Storage in Capacitor Banks*. John Wiley Sons, Ltd, 2017, pp. 331–368. [Online]. Available: https://onlinelibrary.wiley.com/doi/abs/10.1002/9781118886502.ch7

[69] K. Kurokawa, *An introduction to the theory of microwave circuits*. Elsevier, 2014.

[70] P. V. Nikitin, K. S. Rao, S. F. Lam, V. Pillai, R. Martinez, and H. Heinrich, "Power reflection coefficient analysis for complex impedances in rfid tag design," *IEEE Transactions on Microwave Theory and Techniques*, vol. 53, no. 9, pp. 2721–2725, 2005.

[71] C. Poole and I. Darwazeh, *Microwave active circuit analysis and design*. Academic Press, 2015.

[72] B. Datta and S. Chatterjee, "Simulation of bewley's lattice diagram using matlab," in *2013 IEEE 1st International Conference on Condition Assessment Techniques in Electrical Systems (CATCON)*. IEEE, 2013, pp. 11–16.

[73] D. M. Pozar, *Microwave engineering*. John wiley & sons, 2009.

[74] J. F. White, *High frequency techniques*. Wiley Online Library, 2003.

[75] T. A. Note, "Tdr impedance measurements: A foundation for signal integrity," 2004.

[76] J. Lehr and P. Ron, *Foundations of pulsed power technology*. John Wiley & Sons, 2017.

[77] E. Holzman, *Essentials of RF and microwave grounding*. Artech House Norwood, MA, 2006.

[78] H. W. Ott, *Electromagnetic compatibility engineering*. John Wiley & Sons, 2011.

[79] T. Van de Graaf, K. Bond *et al.*, "A new world: The geopolitics of the energy transformation," 2019.

[80] G. Mazzanti and M. Marzinotto, *Fundamentals of HVDC Cable Transmission*. Wiley-IEEE Press, 2013, pp. 384–. [Online]. Available: http://ieeexplore.ieee.org/xpl/articleDetails.jsp?arnumber=6558604

[81] E. W. Kimbark, *Direct current transmission*. John Wiley & Sons, 1971, vol. 1.

[82] P. S. C. of Wisconsin. (2011, may) Underground electric transmission lines. [Online]. Available: https://psc.wi.gov/Documents/Under%20Ground%20Transmission.pdf

[83] F. Alonso and C. Greenwell, "Underground vs. overhead: Power line installation-cost comparison and mitigation," *Electric Light & Power*, 2013.

[84] R. Sellick, J. Sullivan, Q. Chen, and C. Calebrese, "Future improvements to hvdc cables through new cable insulation materials," in *AC and DC Power Transmission (ACDC 2017), 13th IET International Conference on*. IET, 2017, pp. 1–6.

[85] H. Ghorbani, M. Jeroense, C.-O. Olsson, and M. Saltzer, "Hvdc cable systems—highlighting extruded technology," *IEEE Transactions on Power Delivery*, vol. 29, no. 1, pp. 414–421, 2014.

[86] A. Siemens, "High voltage direct current transmission-proven technology for power exchange," *Energy Sector, Germany. Accessed at http://www. siemens. com/sustainability/pool/en/environmental-portfolio/products-solutions/power-transmission-distribution/hvdc_proven_technology. pdf*, 2011.

[87] T. Worzyk, *Submarine power cables: design, installation, repair, environmental aspects*. Springer Science & Business Media, 2009.

[88] R. Bartnikas and K. Srivastava, *Power and communication cables*. McGraw-Hill Companies, 2000.

[89] J. Kassakian, R. Schmalensee *et al.*, "The future of the electric grid, an interdisciplinary mit study, 2011."

[90] J. H. T. S. G. B. P. D. Michael Milligan, Erik Ela, "Renewable electricity futures study - volume 4: Exploration bulk electric power systems: Operations and transmission planning," *National Renewable Energy Laboratory*, 2014.

[91] S. Eckroad *et al.*, "Program on technology innovation: a superconducting dc cable," *Electric Power Research Institute, Final Report*, vol. 1020458, 2009.

[92] P. Group. Submarine cable systems. [Online]. Available: https://www.prysmiangroup.com/sites/default/files/business_markets/markets/downloads/datasheets/SUBMARINE-29-07_A4_3_0.pdf

[93] T. L. Hanley, R. P. Burford, R. J. Fleming, and K. W. Barber, "A general review of polymeric insulation for use in hvdc cables," *IEEE Electrical Insulation Magazine*, vol. 19, no. 1, pp. 13–24, 2003.

[94] U. Cable, "Xlpe insulated power cables."

[95] C. C. Reddy, "Theoretical maximum limits on power-handling capacity of hvdc cables," *IEEE Transactions on Power Delivery*, vol. 24, no. 3, pp. 980–987, 2009.

[96] T. Electronics. Te´s raychem high voltage cable accessories up to 245 kv. [Online]. Available: http://www.te.com/content/dam/te-com/documents/energy/global/productdocuments/HV%20Cable%20Accessories/energy-hvca-catalogue-en.pdf

[97] T. C. T. Electronics. Raychem high voltage cable accessories up to 170 kv. [Online]. Available: http://www.filkab.com/files/category_files/file_3064_bg.pdf

[98] I. Pleşa, P. V. Noţingher, S. Schlögl, C. Sumereder, and M. Muhr, "Properties of polymer composites used in high-voltage applications," *Polymers*, vol. 8, no. 5, p. 173, 2016.

[99] A. L. C. Challenges and Solutions. Polymers—materials adapted from nature. [Online]. Available: https://www.learner.org/courses/chemistry/text/text.html?dis=U&num=Ym5WdElURS9OQ289&sec=YzJWaklUQS9OeW89

[100] S. Gubanski, "Emerging nanocomposite dielectrics," *Electra*, no. 226, pp. 24–32, 2006.

[101] M. F. Frechette, M. L. Trudeau, H. Alamdar, and S. Boily, "Introductory remarks on nanodielectrics," *IEEE Transactions on Dielectrics and Electrical Insulation*, vol. 11, no. 5, pp. 808–818, 2004.

[102] T. Lewis, "Nanometric dielectrics," *IEEE Transactions on Dielectrics and Electrical Insulation*, vol. 1, no. 5, pp. 812–825, 1994.

[103] T. Kravchenko, S. Khorolskaya, L. Polyansky, and E. Kipriyanova, *Nanocomposites: Synthesis, Characterization and Applications*. Nova Science Publishers, Inc., 2013.

[104] S. NISHIKAWA, K.-i. SASAKI, K. AKITA, M. SAKAMAKI, T. KAZAMA, and K. SUZUKI, "Xlpe cable for dc link," *SEI TECHNICAL REVIEW*, no. 84, p. 59, 2017.

[105] Y. Murata, M. Sakamaki, K. Abe, Y. Inoue, S. Mashio, S. Kashiyama, O. Matsunaga, T. Igi, M. Watanabe, S. Asai *et al.*, "Development of high voltage dc-xlpe cable system," *SEI technical review*, vol. 76, pp. 55–62, 2013.

[106] J. Han and R. Garrett, "Overview of polymer nanocomposites as dielectrics and electrical insulation materials for large high voltage rotating machines," in *NSTI-Nanotech*, vol. 2, 2008, pp. 727–732.

[107] F. H. Kreuger, "Industrial high dc voltage: 1. fields, 2. breakdowns, 3. tests," 1995.

[108] G. Chen and Z. Xu, "Charge trapping and detrapping in polymeric materials," *Journal of Applied Physics*, vol. 106, no. 12, p. 123707, 2009.

[109] L. A. Dissado and J. C. Fothergill, *Electrical degradation and breakdown in polymers*. IET, 1992, vol. 9.

[110] B. Han, X. Wang, Z. Sun, J. Yang, and Q. Lei, "Space charge suppression induced by deep traps in polyethylene/zeolite nanocomposite," *Applied physics letters*, vol. 102, no. 1, p. 012902, 2013.

[111] I. A. Tsekmes, "Electrical characterization of polymeric dc mini-cables by means of space charge & conduction current measurements," *BEng Thesis, Delft University of Technology*, 2012.

[112] C. C. Reddy and T. Ramu, "On the computation of electric field and temperature distribution in hvdc cable insulation," *IEEE Transactions on Dielectrics and Electrical Insulation*, vol. 13, no. 6, pp. 1236–1244, 2006.

[113] X. Chen, X. Wang, K. Wu, Z. Peng, Y. Cheng, and D. Tu, "Effect of voltage reversal on space charge and transient field in ldpe films under temperature gradient," *IEEE Transactions on Dielectrics and Electrical Insulation*, vol. 19, no. 1, pp. 140–149, 2012.

[114] M. Fu, L. A. Dissado, G. Chen, and J. C. Fothergill, "Space charge formation and its modified electric field under applied voltage reversal and temperature gradient in xlpe cable," *IEEE Transactions on Dielectrics and Electrical Insulation*, vol. 15, no. 3, 2008.

[115] R. Bartnikas, "Performance characteristics of dielectrics in the presence of space charge," *IEEE transactions on dielectrics and electrical insulation*, vol. 4, no. 5, pp. 544–557, 1997.

[116] Y. Zhang, J. Lewiner, C. Alquie, and N. Hampton, "Evidence of strong correlation between space-charge buildup and breakdown in cable insulation," *IEEE Transactions on Dielectrics and Electrical Insulation*, vol. 3, no. 6, pp. 778–783, 1996.

[117] S. Buddhawar, "Dc characterization of silicon insulation material," 2018.

[118] K. C. Kao, *Dielectric phenomena in solids*. Elsevier, 2004.

[119] B. Alijagic-Jonuz, "Dielectric properties and space charge dynamics of polymeric high voltage dc insulating materials," Ph.D. dissertation, TU Delft, Delft University of Technology, 2007.

[120] A. Morched, B. Gustavsen, and M. Tartibi, "A universal model for accurate calculation of electromagnetic transients on overhead lines and underground cables," *IEEE Transactions on Power Delivery*, vol. 14, no. 3, pp. 1032–1038, 1999.

[121] T. Noda, N. Nagaoka, and A. Ametani, "Phase domain modeling of frequency-dependent transmission lines by means of an arma model," *IEEE Transactions on Power Delivery*, vol. 11, no. 1, pp. 401–411, 1996.

[122] O. Ramos-Leaños, J. L. Naredo, and J. A. Gutierrez-Robles, "An advanced transmission line and cable model in matlab for the simulation of power-system transients," in *MATLAB-A Fundamental Tool for Scientific Computing and Engineering Applications-Volume 1*. InTech, 2012.

[123] B. Gustavsen and C. Heitz, "Modal vector fitting: A tool for generating rational models of high accuracy with arbitrary terminal conditions," *IEEE Transactions on Advanced Packaging*, vol. 31, no. 4, pp. 664–672, Nov 2008.

[124] L. M. Wedepohl, "Electrical characteristics of polyphase transmission systems with special reference to boundary-value calculations at power-line carrier frequencies," *Proceedings of the Institution of Electrical Engineers*, vol. 112, no. 11, pp. 2103–2112, November 1965.

[125] Frequency dependent models. [Online]. Available: https://hvdc.ca/webhelp/EMTDC/Transmission_Lines/Frequency_Dependent_Models.htm

[126] R. M. D. B. K. K. B. Gustavsen, G. Irwin, "Transmission line models for the simulation of interaction phenomena between parallel ac and dc overhead lines," *IPST - International Conference on Power Systems Transients*, June 1999.

[127] R. Iracheta-Cortez, N. Flores-Guzman, and R. Hasimoto-Beltran, "Implementation of the frequency dependent line model in a real-time power system simulator," *Ingeniería e Investigación*, vol. 37, no. 3, pp. 61–71, 2017.

[128] A. R. Blythe, T. Blythe, and D. Bloor, *Electrical properties of polymers*. Cambridge university press, 2005.

[129] C. Bishop, "The relationship between loss, conductivity, and dielectric constant," *Adv. Eng. Electromagn*, 2001.

[130] Pulse definition. [Online]. Available: http://www.rfcafe.com/references/electrical/pulse-definition.htm

[131] S. I. University. (2017, jun) Characteristics of pulse and square waves. [Online]. Available: https://www.engr.siu.edu/staff/spezia/Web150/website/handouts/lesson17_characteristics.pdf

[132] J. Ardizzoni, "High-speed time-domain measurements—practical tips for improvement," *Analog Dialogue*, vol. 41, no. 1, pp. 13–18, 2007.

APPENDIX A - SPACE CHARGE ACCUMULATION IN HVDC COAXIAL CABLES

A.1 HVDC transmission

Considerable enhancements in power electronics and energy conversion devices in recent decades have given rise to High-Voltage Direct Current (HVDC) application.

Some vast countries such as China, India and Brazil having super-fast-developing economies play leading role in this revolutionary turnaround. Huge need for energy in order to turn heavy wheels of these countries' economy have led to a widespread investigation on HVDC technology, building up new lines and systems as well as development, expansion and upgrading the existing lines.

Another important stimulants driving HVDC technology expansion is urge for transformation of energy supply pattern to Renewable Energy (RE) as a political, economical and technical reliable source of energy. The key arguments that are usually cited are [79],

- Higher energy efficiency factor of countries' economy that implies obtaining higher Gross Domestic Product (GDP) with lower energy import to a country
- Ever-increasing accessibility to RE production technology due to cost reduction, investment-driven innovations in technology, sharp rise in learning curve by many projects implementation, etc.
- Recently-developed diversity of RE consumption category like electric cars and smart grids, some part of which are dependent on DC/HVDC technology, such as HVDC relays, AC/DC converters, HVDC transmission systems, and so forth.
- Geopolitical energy shift due to climate change based international conventions & politically unreliable fossil fuel cut-down
- Ever-fluctuating and unstable prices of main energy carriers
- Insecure energy carrier transportation corridors

HVDC transmission lines (TL) offers solutions to overcome many conventional energy transmission/integration barriers like capacitive/resistive dissipation, frequency synchronization in interconnected power grids and so on. To put it differently, taking critical selection between HVDC and HVAC[1] energy transmission is contingent upon a number of diverse factors from technical to economic and even environmental.

A.2 HVDC Cables

The HVDC cable use is an appealing approach for underground transmission in crowded regions[2] where large amount of load is concentrated[80, 81]. This technology is more eco-friendly in comparison with overhead lines and helps clearing unpleasant visual impact up in urban areas. This is absolutely the most realistic and practicable choice for long submarine transmission links. Right-of-way-related political and local issues are other motivations justifying deployment of HVDC cabling system, however most of the commercially available cables are much more expensive than overhead lines at the same power capacity and same voltage level[3]. This might contribute to complexity of decision-making process in best TL selection.

Despite many pros offered by cabling systems, some regularly cited cons are high need for restoration and repair expenses[4] due to intense insulation deterioration under physical stresses, tedious MTTR[5] bringing about outages and ultimately low accessibility demanding for very laborious grid enhancement and repair[83]. HVDC cables are usually classified based on the type of the applied insulating material[8, 80, 84, 85] as stated stated below.

- Oil-Paper Insulated
  - Mass-Impregnated Non-Draining (MIND) [86–88]: Still most of the available HVDC cabling infrastructure all over the world is formed by the MIND cables.
  - Oil Filled (OF)
    - Low pressure OF (LPOF, SCOF[6], SCFF)
    - High pressure OF (HPOF)
- Polypropylene-Laminate Paper (PPLP) or Polypropylene Paper Laminate (PPL)
- Gas filled cables

[1] High Voltage Alternating Current

[2] In metropolitan regions having more underground installations like motorway tunnels and subway infrastructure, the application of underground HVDC cables seems to be more beneficial[80]

[3] From 4 to 14 times more costly[82]

[4] The total costs including fault detection, ditching, connecting of the cables, re-installation, etc are estimated from 5 to 10 times higher than that of overhead lines[83]

[5] Mean Time to repair

[6] Self-Contained Oil-Filled cables also called Emanueli cables

- Extruded cables(XLPE, thermoplastic, N-EPR[7])
- High Temperature Super-Conducting cables (HTSC)[82, 88–91]

figure A.1 clarifies that cable type selection in submarine applications is highly dependent on line length and voltage-level [92].

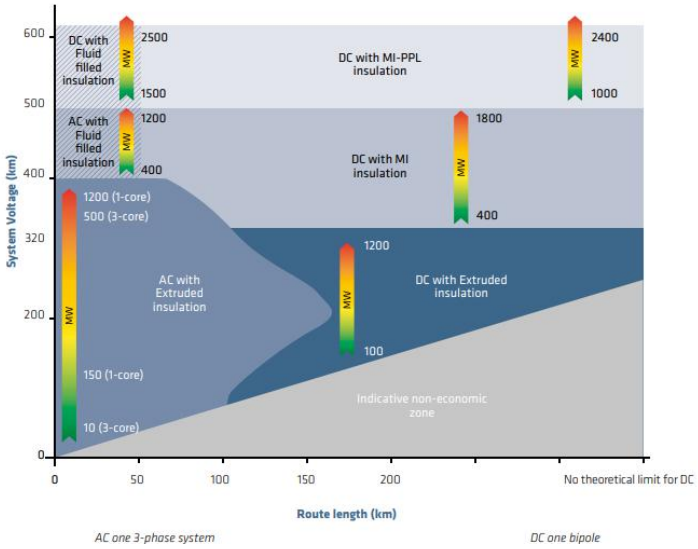

Figure A.1: Choosing cable technology based on voltage level and depth in undersea applications[92]

A.3 Cross-Linked Polyethylene HVDC Cables (XLPE)

Space charge accumulation is a significant problem in XLPE HVDC cables. The main reason for vulnerability of polymer insulations, such as XLPE, is existence of amorphous regions and energy traps usually due to non-homogeneity of the polymer and subsequent non-uniform cristallinity rate. Because of ever-expanding XLPE extruded cable class deployment in recent decades, many researches have been focused on their technological enhancement. The use of extruded HVDC cables can cut down the expenses of the new line construction considerably [8]. However the HVDC cabling systems bulk is still formed by MIND cables, considering recent advances in HVDC-XLPE cable technology, a shift towards extruded cables is observable.

A.4 XLPE application as insulating material

Elimination of oil as insulation is very advantageous from all economical, technical and environmental aspects. Cost reduction driven by less armour demand leads to frugality in entire cabling

[7]by taking *nanoclay particles* in charge in order to strengthen a commonly used insulation in AC cables that is EPR(Ethylene Propylene Robber)[84]

system expenses. In fact, because of physical robustness of XLPE under mechanical tensions, compared to the alternatives, less or even in some circumstances no armour is required in such cables.
The most important restricting factor in HVDC cables is operating temperature due to maximum thermal voltage limitation. From this aspect, HVDC cables again offer a better result compared to their AC alternative. Indeed, more efficient cross-sectional conductor utilization leads to least ohmic dissipation, hence lower temperature gradient across insulation.
Beside the frequency, insulating material also plays an important role in transmission capacity. XLPE cables offer higher operating temperature than other HVDC cable technologies like MIND at the same voltage level. This can practically be interpreted in higher transmission capacity.
XLPE cables maintenance, in contrast to other types of HVDC cables especially oil-filled, is rather simple. The components can be replaced easily considering recent advances in smart insulating materials.
XLPE cable system is less hazardous for environment in long-term use [93] because of no oil-leakage problem. The moisture barrier in case of XLPE cables is reduced significantly and this allows for less weight of the cables [93].
In conclusion, many references [94] cited superior electrical/physical characteristics, being competence in high-current electricity transportation, being convenience in installation, no height restriction, low need for maintenance, thinner metal-sheath and thus less sheath failures as other features that give an upper-hand to this technology compared to the others.
As it is already discussed, in spite of benefits that are met by means of XLPE, still significant part of the HVDC grid is formed by mass-impregnated cables; considering that cabling system has a large share of total expenses of an HVDC system, re-building procedure and substituting the oil-based existing cables with extruded types is very costly and time-consuming [8, 84, 93, 95–97].
Polyethylene (PE) is a thermoplastic polymer that has been the most commonly used material for transmission cables for decades due to satisfactory electrical, mechanical and rheological properties. The cross-linking process and adding nano-fillers into polymer lattice improves mechanical and electrical properties of PE. XLPE insulation is classified into AC-XLPE and DC-XLPE. The latter yields higher volume resistivity and dielectric strength under DC electric field, less space charge accumulation, higher operating temperature, hence longer life-cycle compared to the alternative.

A.5 XLPE morphology

The micro- and nano-composites are commonly used for high voltage purposes. In general, the polymers are classified into three different types based on their properties as follows:

- Thermoplastics
- Thermosets

- Elastomers

The polyethylene(PE)(see figure A.2) insulation as a *Thermoplastic* polymer has been the most popular material for transmission cables for many years due to rather good electrical, mechanical and rheological properties that it offers. After reporting of many failures and break-downs due to the poor quality and moisture diffusion, a large part of the system was substituted by XLPE[8] which offers much better performance compared to that of its alternative[98].

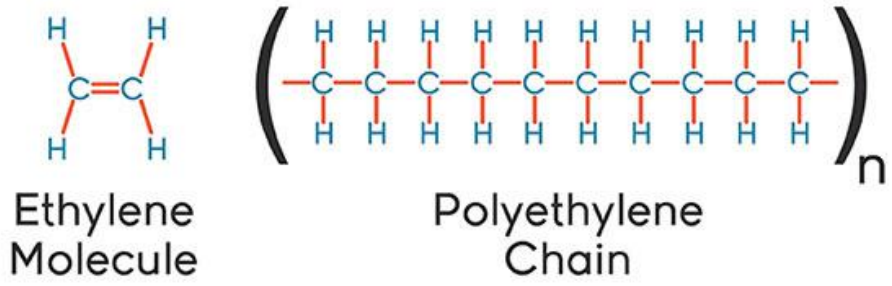

Figure A.2: Ethylene molecule and Polyethylene chain
[99]

After cross-linking process, inorganic nano-fillers[9](A.4) are homogeneously added to the polymer matrix in order to improve the operating temperature as well as the mechanical performance of the material; the resultant material is called nano-metric dielectric or nano-dielectric that presents different properties than those of the bulk polymer. The nano-particles are connected physically and chemically into the surrounding polymeric network[101, 102, 102] and enhance its properties. The synthesis of a nano-composite usually follows two different approaches containing bottom-up and top-down methods as shown in the figure below(see figure A.3)[98]. In the literature[98, 103] these approaches as well as principal methods aiming the distributing the nano-fillers into the polymer web are explained comprehensively.

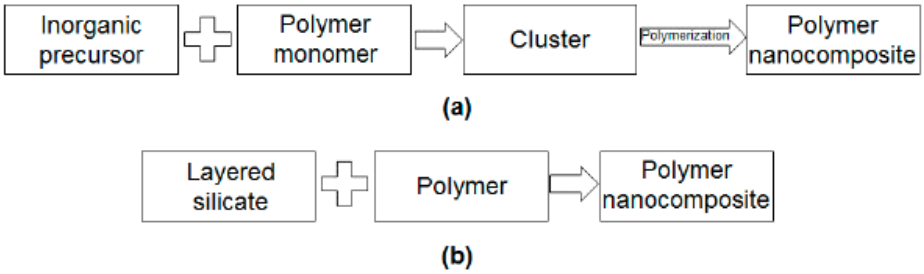

Figure A.3: Approaches for nano-composite synthesis
[98]

[8]Constructed by adding some cross-linking bonds to *crystalline or semi-crystalline thermoplastic* LDPE(Low Density Polyethylene) that forms a *Thermoset*type of polymer

[9]Like *layered silicate (LS)*, SiO_2, TiO_2 and Al_2O_3[100]

This polymer is usually categorized into two different classes consisting of AC-XLPE and DC-XLPE. Although, XLPE has been used successfully in AC cables for many years, the *Space Charge Accumulation* as a very considerable problem makes its application in DC-cables difficult[104]. Having said that, cross-linked polyethylene has superiority over other insulating materials from many aspects which cannot be neglected easily justifying the recent investments to improve its performance under DC current. DC-XLPE shows a better performance in terms of electrical volume resistivity, space charge accumulation, life-time, dielectric strength[10] under DC-voltage and operating temperature compared to its AC version. The AC-XLPE includes amorphous structure[11] that allows for space charge aggregation, this amorphous region must be minimized for DC applications. In order to achieve better insulation performance, which is translated into more resistance against electric stresses[12] and being compact[13] at the same time, the polymer needs to become purified with homogeneous particles distribution. The best quality is gained when inorganic filler nano-particles are injected and very evenly dispersed within the polymer[98, 105].

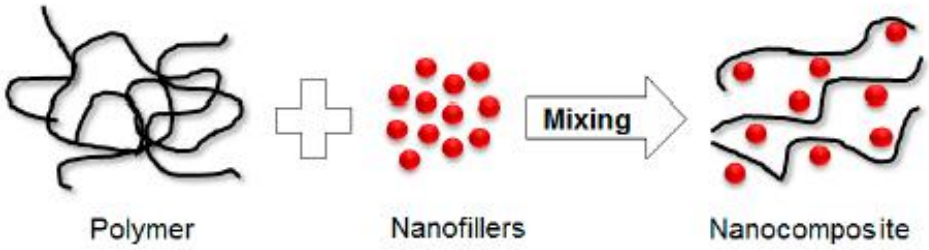

Figure A.4: construction process of a non-composite
[106]

A.6 Space Charge

A.6.1 Space charge as a problem

Space charge accumulation is considered as one of the most important origins for HVDC cables degradation and breakdown. When a cable is subjected to AC voltage, due to quick polarity alteration, space charges do not usually have enough time to be collected in the dielectric, although this is not the case for DC stresses. According to the general continuity equation any interruption in flow of charge carriers in a dielectric arose from non-homogeneity of the material, which implies current density divergence (see equation A.1), gives rise to local charges.

$$\vec{\nabla}.\vec{J} + \frac{\partial \rho}{\partial t} = \sigma_{gnr} \tag{A.1}$$

[10] Also known as break-down strength
[11] Arbitrary paths through the crystalline chain of polyethylene[32]
[12] higher voltage level
[13] miniaturizing process

$\vec{J}$ stands for density vector, ρ is volume charge density and σ_{gnr} shows per unit volume space charge generation, whose positive and negative values denote source and sink. Otherwise speaking, by combining microscopic from of Ohm's law and the general continuity equation, it is concluded that formation of space charges is a function of abrupt change in permittivity and conductivity of that regards inhomogeneity of the material (equation A.4).

$$J = \sigma E = n_e v_d \tag{A.2}$$

$$\sigma = \sum n_e q \mu \tag{A.3}$$

$$\rho + \frac{\epsilon}{\sigma}\frac{\partial \rho}{\partial t} = \vec{J} \cdot \vec{\nabla}\frac{\epsilon}{\sigma} \tag{A.4}$$

n, q, μ and σ are charge concentration, elementary charge, mobility of charge particle and conductivity accordingly. These charges, that in some cases remain for long time inside the material, stimulate changes in electric field profile and subsequently an unwanted energy is stored in the system. Poisson's law explains how space charges alter local electric filed flux,

$$\vec{\nabla}\vec{E} = \frac{\rho}{\epsilon} \tag{A.5}$$

$$\epsilon = \epsilon_r \epsilon_0 \tag{A.6}$$

where $\vec{E}$, ϵ, ϵ_r, ϵ_0 are electric field generated by space charge and the material, relative and vacuum permittivities respectively. The stored energy is in direct proportionality with squared magnitude of the space charge driven electric field.

$$W_e = \frac{\epsilon E^2}{2} \tag{A.7}$$

Release of the stored energy may result in the system's malfunction. The resultant local electric field superposition into the applied DC electric field[14] especially in drastically fluctuating conditions such as polarity reversal and temperature gradient(see figure A.5) can lead to severe stresses with disruptive consequences [108–113].

[14]Applied DC electric field is non-ideal and always contains an AC part, usually originated from switching actions during energy conversion [32, 107]

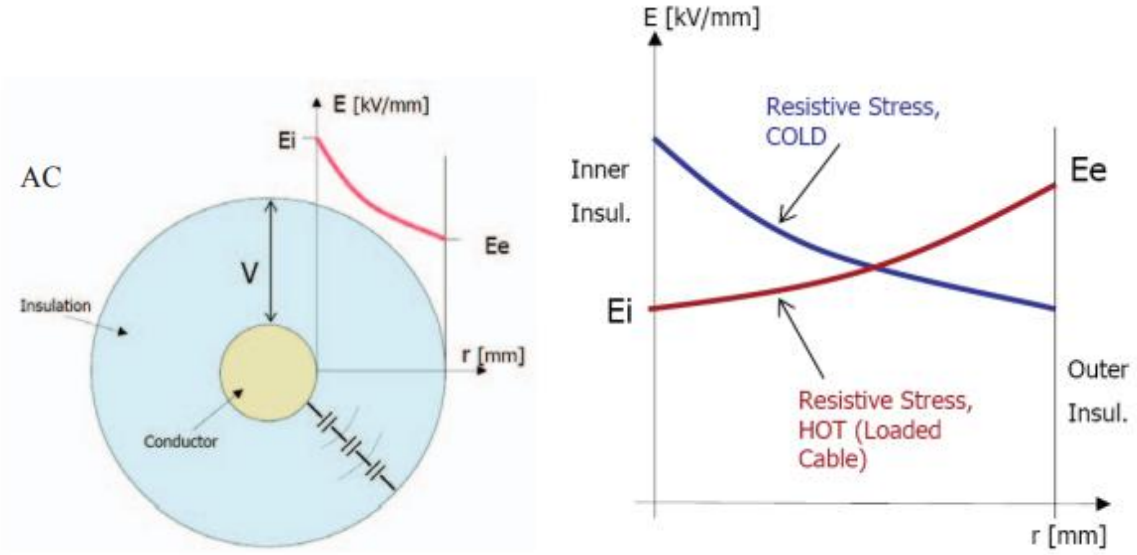

(a) Dielectric stress of AC cable

(b) Dielectric stress of DC cable and its relation with temperature

Figure A.5: A comparison between dielectric stresses of AC and DC cables [84]

Although AC-XLPE ordinarily shows excellent performance under AC voltage, some of its advantageous features (e.g. low carrier mobility and high trapping rates) maybe considered as drawbacks in specific circumstances when being exposed to DC-stresses [114]. The space-charges-driven electric field enhancement, which creates premature failures, through partial discharges and treeing process, acts as stimulant for rapid-aging and break-down in cables [114–116].
The space charge accumulation process, which is predominantly attributed to the polymer micro-structure and energy trap distribution, is massively dependent on dielectric charge trapping mechanism. There is still no model in order to anticipate the trap distribution and their energy depth accurately. A random process dictates whether the depths and traps are distributed evenly or discretely.
The space charge accumulation issue, in polymer substances as a type of homogeneous material, is totally different from the procedure that oil-paper insulated[15] cables follow. In order to analyze space charges trapped within the polymer, three concepts of conduction[16], injection and trapping need to be taken into account[107].

[15] Taped insulated
[16] The ease of the charged particles transportation through the dielectric which follows the Ohm's law

A.6.2 Space charge phenomenon

Formation of space charges can be explained from either macroscopic or microscopic points of view.

A.6.2.1 Macroscopic rationale

This aspect, principally, attributes space charge accumulation to change of permittivity and conductivity at interfaces, temperature gradient, change in the material homogeneity due to additives and impurity and finally morphological inhomogeneity or in other words change crystallinity of the medium[111].

1. **Interfaces between dielectric and conductors:** if quantity of injected or extracted charge carriers from the electrode deviates from potential of the dielectric for charge transportation, homo or hetero charges are collected close to the electrode.

$$|\overrightarrow{J_{inj,ext}}| \neq |\vec{J_{trs}}| \tag{A.8}$$

$J_{inj,ext}$ and J_{trs} are injection/extraction and transport current densities respectively.

- *Poor Injection:* presuming that negative charge carriers (electrons) are conveniently conducted in the dielectric, so that it exceeds the rate of charge injection by the cathode, a layer of holes is formed in the vicinity of the negative electrode.

$$|\overrightarrow{J_{inj,ext}}| < |\vec{J_{trs}}| \tag{A.9}$$

  The built-up space charge carrier sheet is also called hetero-charges, because its polarity is opposite to the electrode dominant charge carriers. The hetero-charge layer magnifies electric field in vicinity area, consequently electron emission from the cathode is accelerated until an equilibrium is achieved. An analogous phenomena also takes place close to the anode where a wall of negative hetero charges is constructed, pushing the local electric field direction towards the created wall, thus a negative peak is formed in electric field profile (extraction process). Again this results in extraction of holes from anode towards the negative wall until the negative potential is cancelled out. To sum up, high charge carrier mobility within the dielectric is the main reason behind hetero-charge layer creation.

- *Excessive Injection:* On the other hand if the amount of supplied negative charge carriers (electrons) exceeds what the dielectric carrier conductivity allows for, a wall of homo-charges, having the same polarity as the electrodes (both cathode and anode) dominant charge carrier, will appear.

$$|\overrightarrow{J_{inj,ext}}| > |\vec{J_{trs}}| \tag{A.10}$$

Those disturb, similar to the previous case, the local field distribution and act as barriers declining the electric field intensity leading to less electron injection or hole extraction.

2. **Surface charge between two dielectrics:** in accordance with Maxwell-Wagner theory, development of the surface charge accumulated on the interface between two different materials is governed by the characteristic properties of the two media, like permittivity and conductivity (to put it another way $\vec{\nabla}(\frac{\epsilon}{\sigma}) \neq 0$), as well as the applied electric field[111, 117].

$$\kappa = \frac{\sigma_b \epsilon_a - \sigma_a \epsilon_b}{d_b \sigma_a + d_a \sigma_b} U_0 \left(1 - e^{\frac{-t}{\tau}}\right) \tag{A.11}$$

where ϵ_a, ϵ_b, σ_a, σ_b, d_a, d_b stand for permittivities, conductivities and thicknesses of the first and second medium, κ is growth rate of the surface charge and τ is a time constant, defined as follows,

$$\tau = \frac{d_b \epsilon_a + d_a \epsilon_b}{d_b \sigma_a + d_b \sigma_a} \tag{A.12}$$

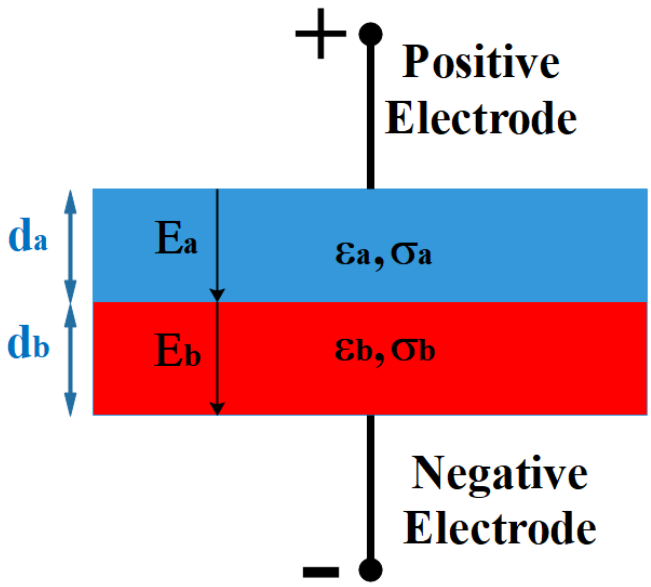

Figure A.6: Maxwell capacitor

3. **Temperature gradient:** assuming constant applied voltage across the insulation, by intensifying the temperature profile slope between the conductors, conductivity decreases and a rise in homo-charges is observed. This occurs naturally in the operating systems. As time passes Joule losses ($P \propto I^2 R$) lead to heating up of the conductor, subsequently temperature gradient is formed across the electrodes. According to the equation below, the

developed space charge is proportional to the current density and change rate (gradient) of the factor $\frac{\epsilon}{\sigma}$,

$$\rho = \vec{J} \cdot \vec{\nabla} \frac{\epsilon}{\sigma} \tag{A.13}$$

4. **Physical/Chemical inhomogeneity:** Chemical additives, such as anti-oxidants and fillers, that usually are added in order to manipulate electrical and physical characteristics of the dielectric as well as physical impurities and by-products form manifold regional interfaces where the local electric field experiences abrupt change in permittivity and conductivity. Such phenomena results in change in electric field profile and considered as a stimulant for space charge accumulation.

5. **Change in material crystallinity:** Morphological inhomogeneity also lead to change in local characteristics of the dielectric. Interfaces among amorphous and crystalline zones in the bulk of a polymer dielectric are susceptible areas to space charge accumulation. This vulnerability can be minimized by the polymer cross-linking process as well as adding appropriate fillers.

There are also some external conditions that contribute to acceleration of space charge accumulation,

1. **Applied electric field:** Electric field increases the dielectric conductivity. When electric field is applied across an insulation, conductivity of the material changes inhomogeneously, with inverse proportion to radius. Therefore, charge carriers move faster and more convenient close to positive electrode, whereas the dielectric conductivity remains high close to ground electrode. In case of non-homogeneous conductivity of the material, by boosting the applied electric field, accumulated space charge quantity rises, since injection and extraction processes become accelerated.

2. **Polarity reversal/abrupt change in applied field:** this is one of the most extreme stresses that insulation may confront. During polarity reversal the electric field reaches a maximum of 1.6 times greater than the Laplacian field. This can be justified by the electric field originated from space charges congestion inside the matter.

3. **Ambient temperature:** similar to temperature gradient if the insulation is warmed up, conductivity declines leading to less electron injection or hole extraction and homo-charges are formed.

A.6.2.2 Microscopic rationale

The other reasoning method by means of which space charge aggregation can be explained is microscopic according to which the phenomenon is attributed to trapping, injection/extraction or conduction of the positive or negative charge carriers.

1. **Trapping mechanism:** the energy traps are explained by means of Niels-Bohr atomic band model. Niels-Bohr model defines three principal energy levels for an atom including valence (E_v), conduction (E_c) and bang gap (E_g), that in the latter charge carriers are not allowed to remain. If, due to existence of physical defects/impurities or chemical additives, the band gap region in the vicinity of the valence band is doped with superfluous electrons or from those in the vicinity of conduction band electrons are extracted, hence extra holes are created, two trap states are formed. The new quasi-stable energy states (dangling bands), forming local electric fields, resist against convenient conduction of the charge carriers, and they spend long time in the traps (figure A.7).

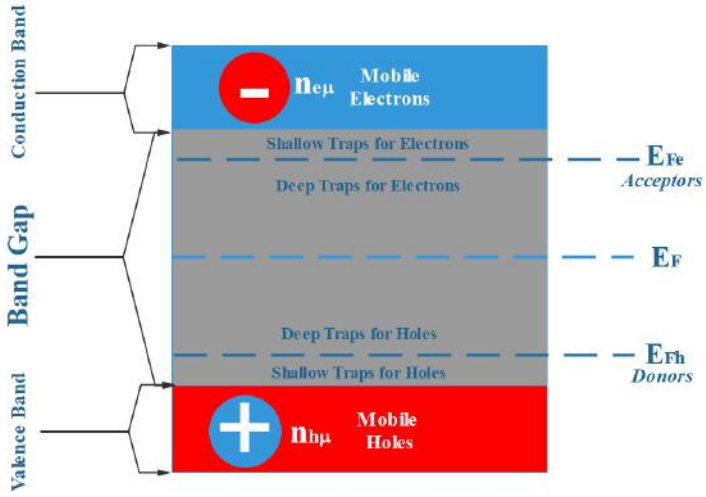

Figure A.7: Niels-Bohr Energy Band & traps states of polymer insulator

2. **Injection/extraction mechanism at metal-dielectric interface:** the electrons govern conduction/emission mechanism in the polymeric insulators, meaning that either the electrons are injected into the cathode or extracted from the anode. At an electrical contact like electrode-dielectric, electric charge carrier start moving from one medium to the another. The process continues until an equilibrium condition is fulfilled, that is determined by the Fermi-levels of the media. Net stream of the charge carriers at the interface leads to creation of two charge walls with different polarities. The set of the two walls form a potential barrier at the interface producing an electric field that withstand against further flow of the charges [118].

   Hence, for the electrons a certain value of energy (ϕ_{brr}) is required in order to trespass the barrier, which is dependent on the conductor work function (ϕ_{mtl}) and insulator affinity (χ_{ins}),

$$\phi_{brr} = \phi_{mtl} - \chi_{ins} \tag{A.14}$$

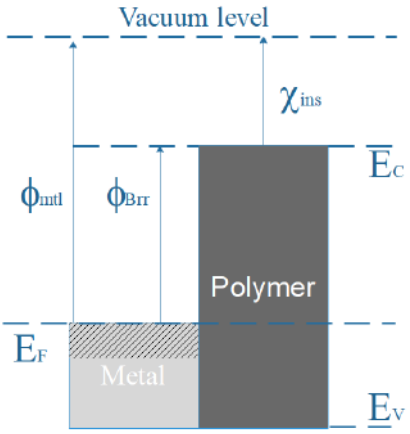

Figure A.8: Energy barrier at electrode-dielectric interface without applied electric field and space charge effect

The injection process usually follows two main mechanisms, dependent on the applied electric field intensity,

- Schottky injection mechanism: at medium electric fields (usually $E < 100kV/mm$), the potential barrier drops by the factor $\Delta\phi$[118].

$$\Delta\phi = -q\sqrt{\frac{qE}{4\pi\epsilon_0\epsilon_r}} \tag{A.15}$$

According to the equation of Richardson lines,

$$J = A_G T^2 exp\left(-\frac{\phi_{brr}}{k_B T}\right) \qquad \frac{A}{m^2} \tag{A.16}$$

therefore slope of the line is $-\frac{\phi_{mtl}}{k}$.

$$A_G = \lambda_r A_0 \tag{A.17}$$

Thus, Thermionic emission relation after applying the limited electric field is derived,

$$J = A_G T^2 exp\left(-\frac{\phi_{brr} - \Delta\phi}{k_B T}\right) \qquad \frac{A}{m^2} \tag{A.18}$$

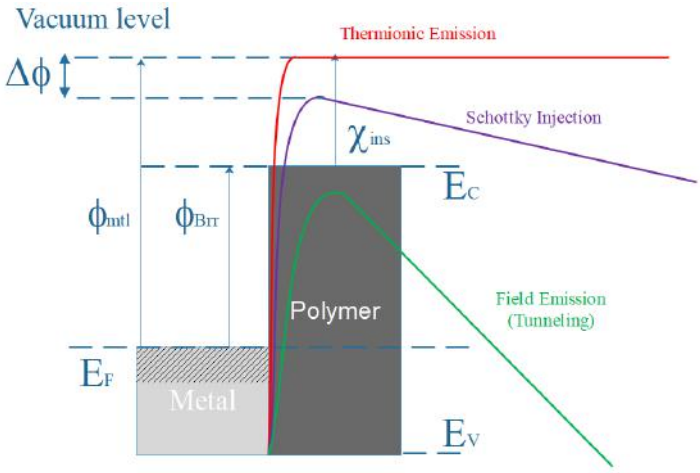

Figure A.9: Metal-dielectric interface, injection mechanisms

- Fowler-Nordheim: as indicated in figure A.9, when the applied electric field is sufficiently high (commonly $E > 100kV/mm$), the injection mechanism will become independent of temperature and the barrier width and height drop considerably[109]. This method is called field emission or tunneling. The current density at the interface, in this case is derived as follows,

$$J = BE^2 exp\left(-\frac{-C\phi\prime^{1.5}}{E}\right) \qquad \frac{A}{m^2} \tag{A.19}$$

$$\phi\prime = \phi_{brr} - E_F \tag{A.20}$$

Richadson's constant	A	$-$
Practical constants	$B\&C$	$-$
Boltzmann constant	k_B	J/K
Metal-specified corrected constant	A_G	A/m^2K^2
Metal-specified correction factor	λ_r	$-$
Elementary charge	q	C
Electric field	E	V/m
Temperature	T	K
Metal work function	ϕ	eV
Barrier height	ϕ_{brr}	eV

3. **Charge carrier transportation mechanism:** the term conduction refers to drifting of the charged particles like electrons, holes or ions, resulted by a force exerted as a result of an electric field or diffusion of them towards a region with lower charge concentration of that type. In insulating material, existence of shallow and deep traps affects the charge carrier transportation regime considerably.

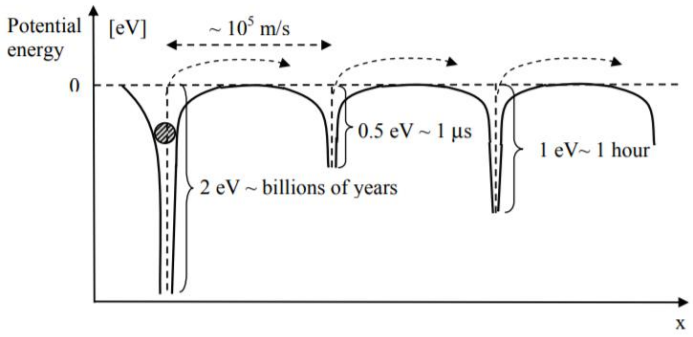

Figure A.10: Traps inside dielectric[119]

As it is already discussed, the space charge trapping mechanism is contingent upon both geometrical and potential, in the matter of energy depth and distribution of the traps. Therefore conduction mechanism of the carriers inside the medium is also limited in terms of time and velocity by the mentioned factors. The deeper the trap energy is, the longer time the charge carrier has to spend in order to be deliberated from the traps, contributing to the conduction process. The most important mechanisms in carrier conduction inside a dielectric medium are cited below [14, 109, 117].

a) *Space-Charge Limited Conduction (SCLC):* This mechanism, is mainly valid for the cases where the dielectric is very narrow (thin film) with quality metal contact so that the electrons can be injected conveniently to the insulation. An abrupt change in mobility of charge carriers when entering the dielectric material leads to formation of a space charge sheet through the dielectric in vicinity of the electrode, interrupting further charge injection.

In trap-free dielectrics with a perfect ohmic contact and in absence of thermally-produced charge carriers, the charge density (electrons) is summation of intrinsic and injected charges[14], leading to double term equation for current density.

$$n_{ch} = n_0 + n_1 \tag{A.21}$$

$$J = \overbrace{\underbrace{\frac{n_0 q \mu V}{d}}_{\text{Ohmic term }, J_{Ohm}} + \underbrace{\frac{1.125 \epsilon \mu V^2}{d^3}}_{\text{SCLC term, } J_{SCLC}}}^{\text{Net current density}} \tag{A.22}$$

when the applied voltage exceeds a certain value, so-called transition voltage (V_{tr}), the second term becomes the dominant mechanism for current density, therefore Mott-Gurney square law determines the relationship between current density and applied voltage.

If the dielectric contains shallow energy traps, in spite of almost same contribution of the injected charge carriers in space charge formation inside the material, only

an infinitesimal fraction ($10^{-10} < \theta < 10^{-6}$) of that will be involved in conduction procedure. The new SCLC current density, hence, is defined as follows,

$$J'_{SCLC} = \theta J_{SCLC} \tag{A.23}$$

$$\theta = \frac{n_c}{n_t} \tag{A.24}$$

By further increase in the applied voltage (V_{TFL}), the traps reach a fill-up level, where injected electron concentration (n_c) equals the trap concentration (n_t), and the SCLC current density escalates at the same voltage value and the coefficient θ reaches to one. By further increasing the applied voltage, the current density shows again the SCLC behaviour, being proportional to the the voltage squared ($J \propto V$) (see graph A.11).

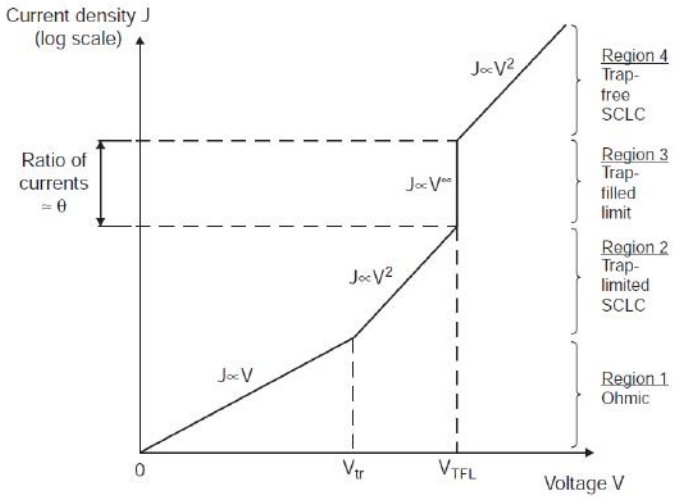

Figure A.11: J-V curve of polymer dielectric and SCLC conduction[14]

b) *Poole-Frankel de-trapping effect*: in case of high electric field application, in depletion regions (either donor or acceptor) where the charged carriers are trapped, the potential barrier is reduced in height, facilitating hopping mechanism. The resultant current density due to Poole-Frankel effect is derived as follows,

$$J = \sigma_0 E exp\left(-\frac{q\phi' - \beta\sqrt{E}}{2k_B T}\right) \tag{A.25}$$

where σ_0 is the material intrinsic conductivity and β is a constant.

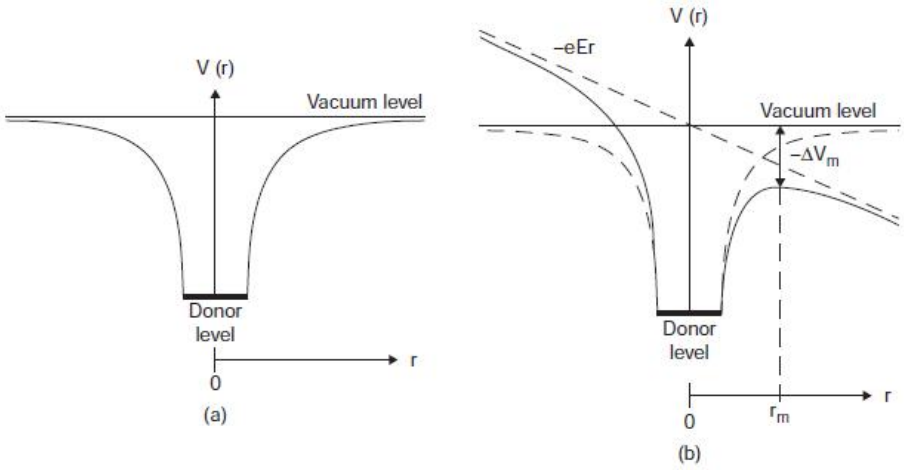

Figure A.12: ***a)*** *electron potential diagram at no or low field* ***b)*** *at high field (ΔV_m implies potential deviation from the utmost barrier height)[14]*

c) *Thermally-excited hopping:* The phenomenon is defined based on the concept of mobility gap. In the energy band gap model, no energy state is allowed to exist in the band gap of the material ($N(E) = 0$) and on the band edges borders the state concentration sees a sudden change. But in reality, the mobility-gap governs the process. In this model the band tails have a gradual rise and fall, and the band edges are extended towards the Fermi-level, with low concentration, though. Redundant delocalized states are placed above (below) the conduction (valence) band edge, between which the energy barriers barely exceed $k_B T$. The band tails together with the traps form a set of localized states along the mobility gap in which the charge carriers are permitted to acquired a certain value of energy (equi-energetic). These states are separated by the barriers having a few kT. Thermal excitation of the polymer lattice allows the charge carriers to either jump over the barriers or tunnel through them in order to reach the next energy state, although the hopping process is not very probable in reality[109].

The space charge trapping mechanism is contingent upon both geometrical and potential[17] distribution of the traps. The reason behind spatial space charge distribution lies in the fact that the insulating material may undergo various phenomena[18] to which the external layer of the insulation is more likely to get exposed[108]. The space charges injection is usually originated from two main sources, that are either electrodes[19] or ionization within the material.

[17] In the matter of energy depth
[18] chemical, physical, thermal, etc.
[19] Due to many mechanisms like Schottky injection and tunneling[108]

APPENDIX B

APPENDIX B - PHASE MODEL

In this appendix, Phase Model or Universal Line Model (ULM), used for the cable simulation in the developed PSCAD model is briefly introduced.

B.0.1 PSCAD/EMTDC phase model

This model was first introduced by Morched et al.[120], thanks to the algorithm Noda et al. 1996 [121] introduced to solve transmission line's equations directly in phase domain. In contrary to Noda algorithm, Morched applied the Gustavsen's vector fitting tool for implementation of rational function approximation. In this approach, the characteristic admittance matrix $[Y_c]$ is fitted in phase domain, since it is smoothly dependent on frequency, while calculation of the propagation matrix $[H]$ is processed in the modal domain, due to the fact that the modal delay changes dramatically, hence a unique time delay is defined for each mode. In other words, the poles and times delays are derived in modal domain and then the fitting procedure is done in phase domain by means of these values, then using least square method the residues are calculated.

It is worth to know that in the mode model, the frequency dependency of modal matrices $[T_v]$ and $[T_i]$ is ignored, however in the phase model, these matrices are considered as functions of frequency [120]. According to [122, 123] the admittance matrix is approximated by means of rational functions as follows,

$$\boldsymbol{Y_c} = \boldsymbol{G_0} + \sum_{i=1}^{N_y} \frac{\boldsymbol{G_i}}{s - q_i} \tag{B.1}$$

where N_y represents fitting order of the admittance matrix, G_i is a matrix for the rational function residues and G_0 indicates matrix of residues when frequency tends to infinity.

The fitting process for the transfer function fitting is more complicated. As it is already mentioned in this chapter and also cited in the literature [124], every mode for each conductor may have different time delay, however we need to define a single delay for the propagation function $\boldsymbol{H}$.

$$\boldsymbol{H} = \boldsymbol{M}\boldsymbol{H}_m\boldsymbol{M}^{-1} \tag{B.2}$$

The eigenvalues matrix of $\boldsymbol{H}$ includes propagation constants for every mode on its diagonal,

$$\boldsymbol{H}_m = diag\Big[\exp(-\gamma_1 L), \exp(-\gamma_2 L), \ldots, \exp(-\gamma_N L)\Big] \tag{B.3}$$

where similar to the mode model γ is defined as follows,

$$\gamma = \sqrt{\boldsymbol{YZ}} \tag{B.4}$$

hence if,

$$\boldsymbol{D} = \boldsymbol{M}\boldsymbol{M}^{-1} \tag{B.5}$$

$$\boldsymbol{H} = \sum_{i=1}^{N} \boldsymbol{D}_i \exp(-\gamma_i) L \tag{B.6}$$

using minimum phase shift theorem,

$$\boldsymbol{H} = \sum_{i=1}^{N} \boldsymbol{D}_i \exp(-\tilde{\gamma}_i L) \exp(-s\tau_i) \tag{B.7}$$

where τ_i is the i^{th}-mode delay. If there would exist N_g groups with almost similar time delays the equation cab be written as follows:

$$\tilde{\boldsymbol{H}} = \sum_{k=1}^{Ik} \boldsymbol{D}_k \exp(-\tilde{\gamma}_k L) \exp(-s\tau_k) \tag{B.8}$$

where Ik is the number of modes for each group. In order to make groups, a minimum phase shift is determined (usually 10°) and all group elements are considered to have similar time delay. Using this method a single time delay is approximated for each transfer function group, hence the k^{th} element of the matrix $\tilde{\boldsymbol{H}}$ can be defined as a rational function. Ultimately, the original transfer function is approximated as follows:

$$\boldsymbol{H} = \sum_{k=1}^{N_g} \exp(-s\tau_k) \sum_{i=1}^{Nh(k)} \frac{\boldsymbol{R_{k,i}}}{s - p_{k,i}} \tag{B.9}$$

Having the transfer function, the transmission line equations can be defined[120, 125].

$$\boldsymbol{Y_c}.\boldsymbol{V_k} - \boldsymbol{I_k} = 2\boldsymbol{H^T}.\boldsymbol{I_{m,r}} = 2\boldsymbol{I_{k,i}} \tag{B.10}$$

$$\boldsymbol{Y_c}.\boldsymbol{V_m} - \boldsymbol{I_m} = 2\boldsymbol{H^T}.\boldsymbol{I_{k,r}} = 2\boldsymbol{I_{m,i}} \tag{B.11}$$

where the indices $i\&r$ stand for incident and reflected parameters. The phase model is illustrated in the drawing below.

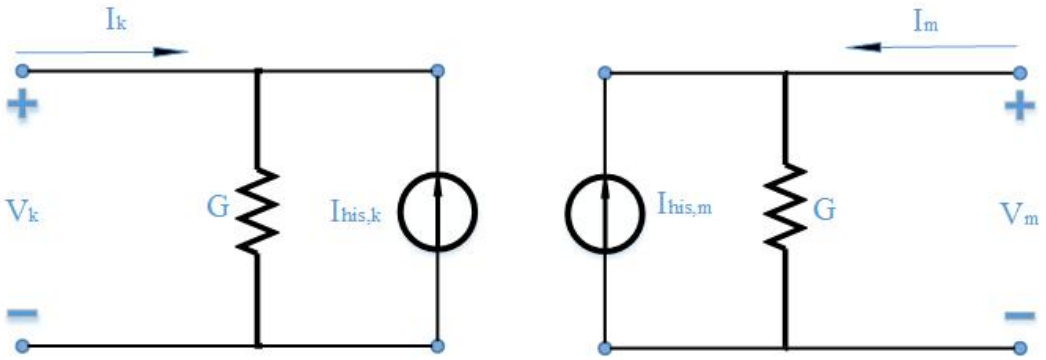

Figure B.1: Frequency-dependent phase model

According to the algorithm that PSCAD/EMTDC proposed for frequency dependent cable models the history vales of current sources $\boldsymbol{I_his,k}$ and $\boldsymbol{I_his,m}$ are renewed per time step [125–127].

$$\boldsymbol{I_k}(n) = \boldsymbol{G}.\boldsymbol{V_k}(n) - \boldsymbol{I_{his,k}} \tag{B.12}$$

$$\boldsymbol{I_{k,r}}(n) = \boldsymbol{I_k}(n) - \boldsymbol{I_{k,i}}(n) \tag{B.13}$$

$$\boldsymbol{I_{k,i}}(n+1) = \boldsymbol{H} \circledast \boldsymbol{I_{m,r}}(n-\tau) \tag{B.14}$$

$$\boldsymbol{I_{his,k}}(n+1) = \boldsymbol{Y_c'} \circledast \boldsymbol{V_k}(n) - 2\boldsymbol{I_{k,i}}(n+1) \tag{B.15}$$

The approach and computer implementation process are explained perfectly in the literature [122, 126].

APPENDIX C

APPENDIX C - PARAMETERS

In this Appendix, some important formula concerning min-cable parameter calculation are introduced.

C.1 Complex permittivity

According to literature [53, 128], the highest value of relative permittivity is represented by static permittivity (ϵ_s) if and only if time duration is sufficiently plentiful. This parameter is also known as dielectric constant. Elseways, is time is not sufficient in order to allow dipole formation inside the medium, instantaneous relative permittivity (ϵ_∞) determines the apparent permittivity. Between the two severe conditions, there exists a dispersion time interval in which the dipole behaviour is very frequency-dependent. If we assume an alternating electric field of $E = E_0 \cos(\omega t)$, by the angular frequency escalation, the dipole orientation vector would lag the electric field vector by δ . In this case, the electric displacement is defined as follows:

$$\begin{aligned} D &= D_0 \cos(\omega t - \delta) \\ &= D_0 \cos(\omega t)\cos(\delta) + D_0 \sin(\omega t)\sin(\delta) \end{aligned} \tag{C.1}$$

Moreover, the following equation shows instantaneous relationship between electric displacement and electric field.

$$D(\omega) = \epsilon(\omega) E(\omega) \tag{C.2}$$

Hence, real and imaginary parts of complex relative permittivity are derived which are origins for loss and charging current through a capacitor accordingly.

$$\epsilon_r' = \frac{D_0 \cos(\delta)}{\epsilon_0 E_0} \tag{C.3}$$

$$\epsilon_r'' = \frac{D_0 \sin(\delta)}{\epsilon_0 E_0} \tag{C.4}$$

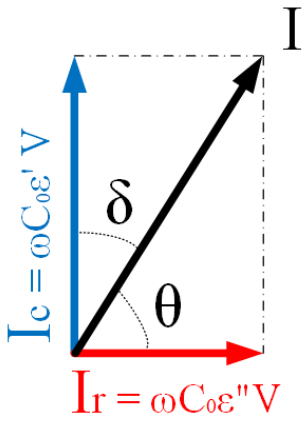

Figure C.1: Penetrating current through dielectric

A combined quantity is introduced that describes behaviour of dielectric medium.

$$\epsilon_r^*(\omega) = \epsilon_r'(\omega) - j\epsilon_r''(\omega) \tag{C.5}$$

Loss tangent ($\tan\delta$), considering both AC and DC conduction, which practically are not distinguishable in dielectric evaluation, is defined as follows:

$$tan\delta = \frac{\epsilon_r'' + \frac{\sigma_{DC}}{\omega\epsilon_0}}{\epsilon_r'} \tag{C.6}$$

This factor is a measure that shows ratio of energy dissipated per cycle and the total applied energy. Equation C.6 takes both AC-influenced polarization and DC dissipation into account. The mmost important approaches for relaxation of dielectrics are:

- Debye
- Havriliak-Negami
- Cole-Cole
- Davidson-Cole

Debye equation is the most fundamental equation that describes relaxation process in a dielectric material. This method represents ideal dielectric response, while neglecting any interaction between the dipoles.

$$\epsilon_r^*(\omega) = \epsilon_\infty + \frac{\epsilon_s - \epsilon_\infty}{1 + j\omega\tau} \tag{C.7}$$

ϵ_∞ and ϵ_s are initial high frequency and static relative permittivities respectively and τ is the relaxation time period.

By enhancing Debye equation for encountering asymmetry and breadth of the medium dispersion graph, Havriliak-Negami equation is derived. The coefficients α and β stand for asymmetry and width of the curve accordingly.

$$\epsilon_r^*(\omega) = \epsilon_\infty + \frac{\epsilon_s - \epsilon_\infty}{(1+(j\omega\tau)^\alpha)^\beta} \tag{C.8}$$

Cole-Cole and Davidson-Cole equations are basically special cases of Havriliak-Negami, taking only one of the coefficients into account, while assuming the other equal to one.
Cole-Cole assumes asymmetry to be a variable in the complex permittivity equation (see C.9).

$$\epsilon_r^*(\omega) = \epsilon_\infty + \frac{\epsilon_s - \epsilon_\infty}{1+(j\omega\tau)^\alpha} \tag{C.9}$$

On the other hand, the additional variable encountered in Davidson-Cole is the dispersion graph breadth (see C.10).

$$\epsilon_r^*(\omega) = \epsilon_\infty + \frac{\epsilon_s - \epsilon_\infty}{(1+j\omega\tau)^\beta} \tag{C.10}$$

C.2 Conductivity

Under influence of frequency, conductivity of dielectric material alters, adding up a second term to the conductivity equation [59, 129].

$$\begin{aligned}
\sigma_e^*(\omega) &= \sigma_s(\omega) + \sigma_a(\omega) \\
&= \Big(\sigma'(\omega) + \sigma_{DC}(\omega)\Big) + j\sigma"(\omega) \\
&= j\omega\epsilon^*(\omega) \\
&= j\omega\epsilon'(\omega) + \omega\epsilon"(\omega)
\end{aligned} \tag{C.11}$$

where σ_e, σ_s and σ_a stand for effective, static and alternating conductivity of the material. The loss tangent can similarly be decomposed.

$$\tan\delta_e = \tan\delta_s + \tan\delta_a \tag{C.12}$$

where,

$$\tan\delta_s = \frac{\sigma_{DC}}{\omega\epsilon_0\epsilon_r'} \tag{C.13}$$

and,

$$\tan\delta_a = \frac{\epsilon_r''}{\epsilon_r'} \tag{C.14}$$

Complex permittivity	$\epsilon^*(\omega)$	F/m
Real part of complex permitivitty	$\epsilon'(\omega)$	No.
Imaginary part of complex permitivitty	$\epsilon"(\omega)$	No.
Complex relative permittivity	$\epsilon_r^*(\omega)$	Complex No.
Real part of complex relative permitivitty	$\epsilon_r'(\omega)$	No.
Imaginary part of complex relative permitivitty	$\epsilon"_r(\omega)$	No.
Vacuum permittivity	ϵ_0	F/m
Effective conductivity	$\sigma_e(\omega)$	S/m
Static (DC) conductivity	$\sigma_s(\omega)(\sigma_{DC}(\omega))$	S/m
Alternating (AC) conductivity	$\sigma_a(\omega)(\sigma_{AC}(\omega))$	S/m
Angular frequency	ω	rad/s

C.3 Helical correction factor

Usually a helical correction factor of F_{hl} is applied to v_p that provides an estimation covering some issues like charge transfer facilitation between conductors due to semiconducting layer existence, stranding of wires and deviation of the cable axis angle from the wire axis.

$$F_{hl} = \sqrt{\frac{1}{1+\left(\frac{2\pi r_{os}}{l_{cable}}\right)^2 . \frac{1-(r_i-r_{os})^2}{2ln(r_{os}/r_i)}}} \tag{C.15}$$

The propagation velocity changes with reference to its value at previous frequency.

$$v_g(\omega) = \frac{\partial \omega}{\partial \beta} \tag{C.16}$$

C.4 Pulse parameters

calculation of a non ideal pulse parameters are of crucial importance. In this appendix the most common rule in order to determine the three parameters of each pulse including *pulse width(t_p)*, *rise time(t_r)* and *fall time or tail(t_f)* is explained[130–132].

C.4.1 Pulse Width

The required time for any pulse to move from 50% of peak in rising edge to the same value in the falling edge.

C.4.2 Rise Time

The time required for each pulse to rise its amplitude from 10% of the crest to 90% of that.

C.4.3 Fall Time

The time required for each pulse to drop from 90% of the crest amplitude to 10% of that.

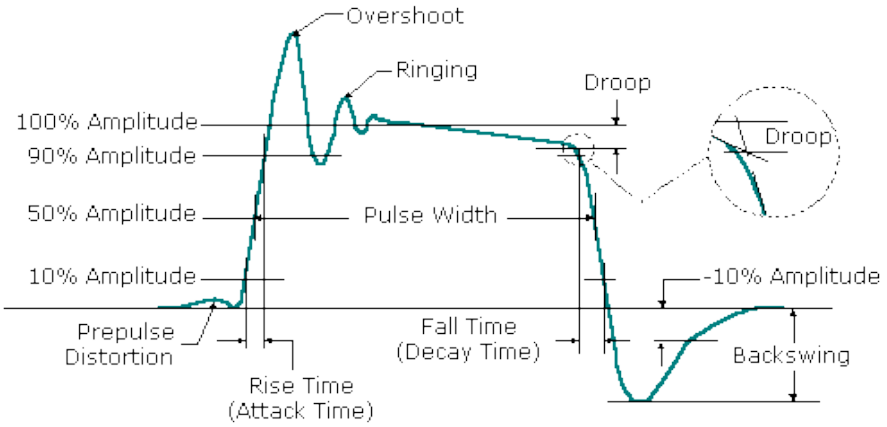

Figure C.2: Non-ideal pulse waveshape and parameters[130]

Notice:for an ideal pulse having rising and falling tilt the definitions are a bit different meaning that all values of 10% and 90% change to 0%and 100%. *Notice*:if the ceiling is tilted the average of two extreme values is assumed to be the crest.

$$V_{crest} = \frac{V_1 + V_2}{2} \tag{C.17}$$

Where V_1 is the highest value at the rising edge and V_2 is the highest value at the falling edge.